Modeling and Control of Flexible Link Manipulators

Dipendra Subedi

UiA University of Agder

Doctoral Dissertations at the University of Agder 373

Dipendra Subedi

Modeling and Control of Flexible Link Manipulators

Doctoral Dissertation for the degree *Philosophiae Doctor (PhD)* at
the Faculty of Engineering and Science, Specialisation in Mechatronics

University of Agder
Faculty of Engineering and Science
2022

Doctoral Dissertations at the University of Agder 373
ISSN: 1504-9272
ISBN: 978-82-8427-083-8

Printed by 07 Media
Kristiansand

Preface

The work presented in this doctoral thesis was carried out between February 2019 and July 2022 at the Department of Engineering Sciences, University of Agder. Associate Professor Ilya Tyapin and Professor Geir Hovland from the Department of Engineering Sciences at the University of Agder were respectively the main supervisor and co-supervisor of this work. The project received funding from the Research Council of Norway through the centre SFI Offshore Mechatronics (project 237896) and the University of Agder.

Acknowledgments

I would first like to thank my thesis supervisor, Associate Professor Ilya Tyapin of the Department of Engineering Sciences at the University of Agder. The door to his office was always open whenever I ran into a problem or had a question, steering me in the right direction whenever he thought I needed it.

I am sincerely grateful to my thesis co-supervisor, Professor Geir Hovland of the Department of Engineering Sciences at the University of Agder, for his very valuable comments throughout my PhD.

A special thank goes to my colleague, Jan Christian Bjerke Strandene, for the help and support in the lab. I also want to acknowledge Ajit Jha, Sondre Sanden Tørdal, Atle Aalerud, Teodor Nilsen Aune, Arild Bergesen Husebø, and Gulshan Noorsumar for their support and for providing valuable feedback.

I must express my very profound gratitude to my parents, brothers, sisters, and friends for providing me with unfailing support and continuous encouragement throughout my years of study and through the process of researching and writing this thesis. This accomplishment would not have been possible without them. In particular, I am grateful to my wife, Asha, for her incredible love and support throughout my research. To my son, Aadip, thank you for being such a great kid, and for being my source of happiness even at tough times full of stress and self-doubt. Thank you.

Finally, I would like to acknowledge the Norwegian Research Council, center SFI Offshore Mechatronics, and the University of Agder for the funding without which this research project would have never been possible.

Dipendra Subedi
Grimstad, Norway
July 2022

Abstract

Autonomous maritime navigation and offshore operations have gained wide attention with the aim of reducing operational costs and increasing reliability and safety. Offshore operations, such as wind farm inspection, sea farm cleaning, and ship mooring, could be carried out autonomously or semi-autonomously by mounting one or more long-reach robots on the ship/vessel. In addition to offshore applications, long-reach manipulators can be used in many other engineering applications such as construction automation, aerospace industry, and space research. Some applications require the design of long and slender mechanical structures, which possess some degrees of flexibility and deflections because of the material used and the length of the links. The link elasticity causes deflection leading to problems in precise position control of the end-effector. So, it is necessary to compensate for the deflection of the long-reach arm to fully utilize the long-reach lightweight flexible manipulators.

This thesis aims at presenting a unified understanding of modeling, control, and application of long-reach flexible manipulators. State-of-the-art dynamic modeling techniques and control schemes of the flexible link manipulators (FLMs) are discussed along with their merits, limitations, and challenges. The kinematics and dynamics of a planar multi-link flexible manipulator are presented. The effects of robot configuration and payload on the mode shapes and eigenfrequencies of the flexible links are discussed. A method to estimate and compensate for the static deflection of the multi-link flexible manipulators under gravity is proposed and experimentally validated. The redundant degree of freedom of the planar multi-link flexible manipulator is exploited to minimize vibrations. The application of a long-reach arm in autonomous mooring operation based on sensor fusion using camera and light detection and ranging (LiDAR) data is proposed.

Sammendrag

Autonom maritim navigasjon og offshore operasjoner har i nyere tid fått oppmerksomhet med fokus på reduksjon av operasjonskostnader samt forbedring av pålitelighet og sikkerhet. Offshore operasjoner, som for eksempel inspeksjon av vindparker, rensing av oppdrettsanlegg og fortøyning av fartøy, kunne ha blitt utført autonomt eller semi-autonomt ved å montere en eller flere roboter med lang rekkevidde på et offshore fartøy. I tillegg til offshore operasjoner så kan manipulatorer med lang rekkevidde benyttes i mange anvendelser innen for eksempel i byggebransjen samt luft og romfartsindustrien. Noen anvendelser krever design av lange og slanke mekaniske strukturer med en viss grad av fleksibilitet og defleksjon på grunn av materialvalg og lengden på lenkene. Elastistet i lenkene fører til defleksjon som igjen fører til problemer forbundet med presis posisjonsstyring av verktøyet montert ved håndleddet til roboten. Derfor vil det være nødvendig å kompensere for defleksjon av slanke lenker for å få full utnyttelse av elastiske, lettvektsmanipulatorer med lang rekkevidde.

Denne avhandlingen har som mål å presentere en forent forståelse av modellering, styring og anvendelse av elastiske manipulatorer med lang rekkevidde. Forskjellige moderne dynamiske modelleringsteknikker og reguleringskonsepter av FLMs blir diskutert sammen med deres meritter, begrensninger og utfordringer forbundet med disse. Kinematikk og dynamikk av en planar elastisk manipulator med flere lenker presenteres. Effekten av robot konfigurasjon og last på svingemoduser og egenfrekvenser av de elastiske lenkene diskureres. En metode for å estimere og kompensere for statisk defleksjon av elastiske manipulatorer med flere lenker påvirket av tyngdekraften foreslås og valideres eksperimentelt. Den redundante frihetsgraden til en planar elastisk manipulator med flere lenker blir utnyttet for å minimere vibrasjoner. Anvendelse av en arm med lang rekkevidde i autonome fartøyningsoperasjoner basert på fusjon av sensordata fra kamera og LiDAR presenteres.

Publications

Included Works

The following papers are included as a part of this thesis. They have been published in peer-reviewed conference proceedings and journals. The versions included in this dissertation differ only in formatting compared to the original published versions.

Paper A Dipendra Subedi, Ilya Tyapin and Geir Hovland. Review on Modeling and Control of Flexible Link Manipulators. *Modeling, Information and Control*, 41(3):141–163, 2020. doi: 10.4173/mic.2020.3.2.

Paper B Dipendra Subedi, Ilya Tyapin and Geir Hovland. Modeling and Analysis of Flexible Bodies Using Lumped Parameter Method. *2020 IEEE 11th International Conference on Mechanical and Intelligent Manufacturing Technologies (ICMIMT)*, pages 161–166, 2020. doi: 10.1109/ICMIMT49010.2020.9041188.

Paper C Dipendra Subedi, Ilya Tyapin and Geir Hovland. Dynamic Modeling of Planar Multi-Link Flexible Manipulators. *Robotics*, 10(2):70, 2021. doi: 10.3390/robotics10020070.

Paper D Dipendra Subedi, Teodor Nilsen Aune, Ilya Tyapin and Geir Hovland. Static Deflection Compensation of Multi-Link Flexible Manipulators Under Gravity. *IEEE Access*, 10:9658-9667, 2022. doi: 10.1109/ACCESS.2022.3144404.

Paper E Dipendra Subedi, Ilya Tyapin and Geir Hovland. Control of Redundant Flexible Manipulators with Redundancy Resolution. *2022 8th International Conference on Mechatronics and Robotics Engineering (ICMRE)*, pages 116–121, 2022. doi: 10.1109/ICMRE54455.2022.9734097.

Paper F Dipendra Subedi, Ajit Jha, Ilya Tyapin and Geir Hovland. Camera-LiDAR Data Fusion for Autonomous Mooring Operation. *2020 15th IEEE Conference on Industrial Electronics and Applications (ICIEA)*, pages 1176-1181, 2020. doi: 10.1109/ICIEA48937.2020.9248089.

Additional Contributions

The author has contributed to the following papers as part of the research done at the centre SFI Offshore Mechatronics.

Paper G Ajit Jha, Dipendra Subedi, Per-Ove Løvsland, Ilya Tyapin, Linga Reddy Cenkeramaddi, Baltasar Lozano and Geir Hovland. Autonomous Mooring towards Autonomous Maritime Navigation and Offshore Operations. *2020 15th IEEE Conference on Industrial Electronics and Applications (ICIEA)*, pages 1171-1175, 2020. doi: 10.1109/ICIEA48937.2020.9248169.

Paper H Atle Aalerud, Joacim Dybedal and Dipendra Subedi. Reshaping Field of View and Resolution with Segmented Reflectors: Bridging the Gap Between Rotating and Solid-State LiDARs. *Sensors*, 20(12) 2020. doi: 10.3390/s20123388.

Contents

List of Figures

List of Tables

Abbreviations

2D two-dimensional. 16

3D three-dimensional. 5

AC alternating current. 29, 30

ADS automation device specification. 32

AMM assumed modes method. 8, 12

CLIK closed-loop inverse kinematics. xvii, 25, 26

CPU central processing unit. 31

DC direct current. 29, 31

DH Denavit-Hartenberg. xix, 14, 16

DoF degrees of freedom. 3, 11, 13, 25, 35

E-Stop emergency stop. 30, 31

EtherCAT ethernet for control automation technology. 29–32

FEM finite element method. 12

FLM flexible link manipulator. ix, xi, xv, xvii, 3–8, 11, 12, 19–27, 35, 36

FSoE failsafe over EtherCAT. 31

HMI human-machine interface. 32

IMU inertial measurement unit. 3, 19, 23, 27–29

LiDAR light detection and ranging. ix, xi, 6, 9

LPM lumped parameter method. 8, 12, 35

MCB miniature circuit breaker. 29, 30

MEMS micro-electromechanical systems. 29

P proportional. 23

PC personal computer. 29–32

PD proportional derivative. 23

PI proportional integral. 23

PID proportional integral derivative. 4, 23

PLC programmable logic controller. 29–32

TMM transfer matrix method. 13

Chapter 1

Introduction

1.1 Motivation and Problem Statement

The current world population of 7.7 billion is expected to reach 8.6 billion by 2030, 9.8 billion in 2050, and 11.2 billion in 2100 [1]. Satisfying the demands of 2.1 billion more people requires a leap in the food production levels. One of the solutions to this problem is to use robotic technology in fish farming and offshore industries, as this technology has the potential to revolutionize the aquaculture industry.

Currently, service vessels with several crew members on board are used to carry out day-to-day tasks including fish welfare monitoring, facility inspections, control of feed rationing, and lice counting on offshore fish farm facilities. To meet the production demands, the need of locating facilities in more hostile and hard-to-reach environments will soon rapidly increase the operational costs.

To meet the energy demands of the increasing population, offshore wind farms are one of the most suitable options. However, due to harsh environmental conditions, the costs of their installation, inspection, and maintenance will increase. So, offshore companies are looking for ways to reduce costs by minimizing employee costs and improving manufacturing efficiency and safety.

As the sea farms and offshore wind farms are situated in remote and isolated places, they pose a challenging environment for the human operator due to hazardous weather and an unfriendly atmosphere. A promising solution to obtain maximum productivity, efficiency, safety, and reduce labor costs is to utilize industrial robotics in the offshore environment for cleaning, manipulation, inspection, maintenance, and repair [2].

1.1.1 Autonomous Offshore Operations

Autonomous maritime navigation and offshore operations have increasingly become the focus of current research with the aim of reducing operational costs and in-

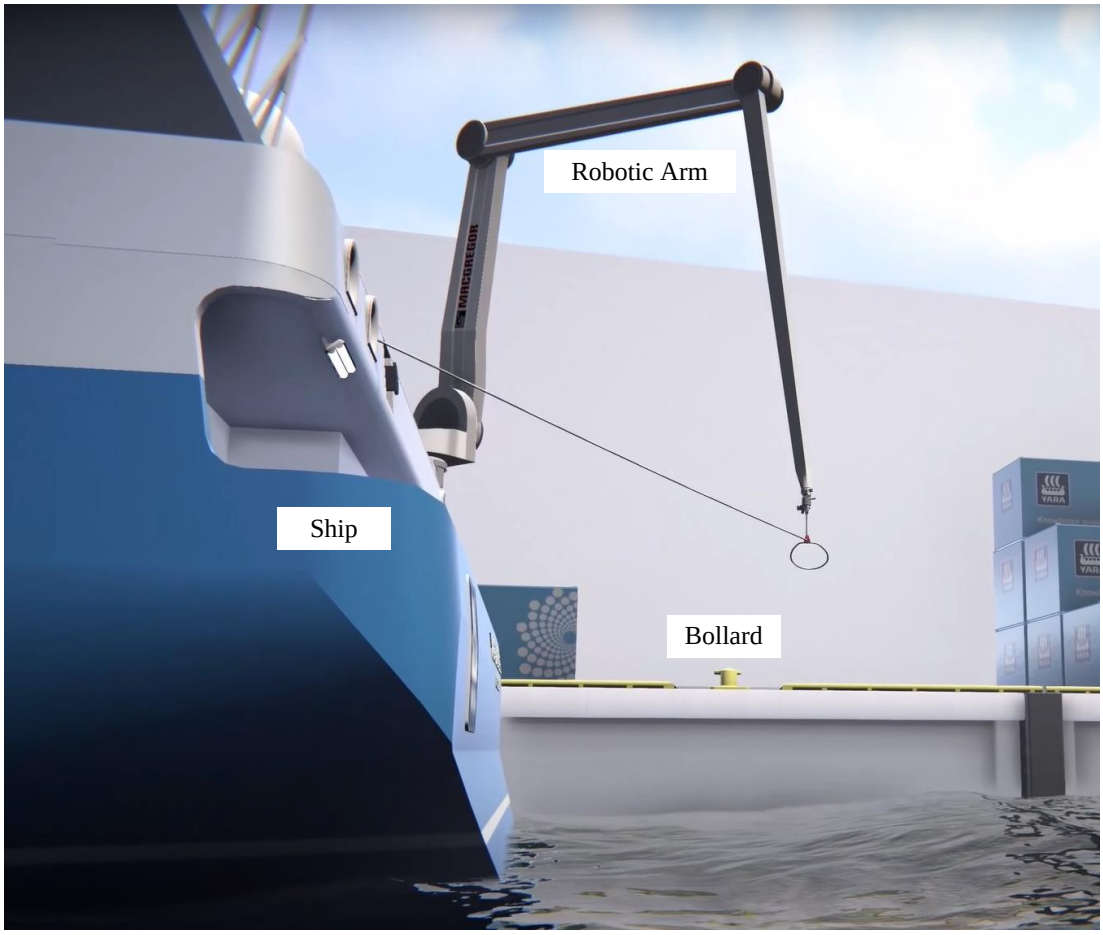

Figure 1.1: Autonomous mooring (with permission from MacGregor AS)[1].

creasing reliability and safety. They offer the opportunity to develop sustainable transportation and trade as they have the potential to reduce carbon footprint and facilitate environmental protection. Offshore operations, for example, wind farm inspection, sea farm cleaning, and ship mooring could be carried out autonomously or semi-autonomously by mounting one or more long-reach robots on the ship/vessel (see Figure 1.1). Autonomous operations rely on the accurate perception of the environment with several complementary sensory modalities. The use of onboard robotic manipulators equipped with the camera and LiDAR combination to carry out autonomous mooring operations is presented in paper F.

1.1.2 Long-Reach Manipulators

Many studies have been done to analyze the potential to apply robots in offshore environments for manipulation and inspection [3, 4].

In order to utilize robotics technologies in offshore environments, a number of challenges must be overcome that hardly exist in any other application area of

[1] `https://youtu.be/Co211gU_J5w`

robots [5]. As industries are looking for more automated platforms, specialized long-reach robot arms should be developed to be able to tolerate the harsh environments in offshore areas. Specifically, the control architecture designed for the manipulator should be able to reduce oscillations in the arms while following collision-free, pre-planned trajectories or while manipulating payloads with large areas subjected to wind forces.

For achieving minimum oscillation and good position accuracy, the conventional robots are designed with highly stiff materials which consequently require expensive, high-power drives [6]. However, the vibration of the end-effector at high speed and high load is still present due to elasticity. In this context, lightweight, flexible manipulators are better and cheaper alternatives, when the control architecture is designed to reduce the vibration of the end-effector to an acceptable range. The advantages of lightweight, flexible manipulators over conventional manipulators include the following [7]:

- Lower cost
- High payload-to-robot-weight ratio
- High operational speed
- Better transportability
- Safe operation due to reduced inertia.

In addition to offshore applications, the long-reach manipulators can be used in many other engineering applications such as construction automation, aerospace industry, and space research. Some applications require the design of long and slender mechanical structures which possess some degrees of flexibility and deflections because of the material used and the length of the links. The link elasticity causes deflection leading to problems in precise position control of the end-effector. So, it is necessary to compensate for the deflection of the long-reach arm to fully utilize the long-reach lightweight flexible manipulators.

Using only the kinematic information and joint encoder readings, it is not possible to control the position and orientation of the end-effector precisely enough to perform manipulation tasks in a long-reach flexible arm compared to more rigid industrial robots. To control the vibration of the flexible arm, additional sensors, for example, vision sensors and inertial measurement units (IMUs), can be added to the flexible arm control architecture to provide deflection/vibration measurement of the flexible link or the end-effector.

The highly nonlinear dynamics of the FLM with an infinite number of degrees of freedom (DoF) make their control more complicated compared to the conventional

industrial robot. An accurate model of the system aids the development of efficient and optimal model-based control algorithms for FLMs. In this context, it is desirable to build a mathematical model of the system incorporating flexible link dynamics in an accurate and computationally affordable way.

1.1.3 Research Questions

i. Can the closed-form dynamic model for a planar multi-link flexible manipulator be derived and used in the model-based control?

ii. Can the static deflection of a multi-link flexible manipulator be measured/estimated under gravity and compensated during motion from initial to goal pose?

iii. Is it possible to minimize oscillations in a flexible manipulator by exploiting redundancy?

1.2 State-of-the-Art

The study of modeling, control, and sensor systems for the application of flexible manipulators is of ongoing interest to researchers worldwide. With the recent advancement in technology, researchers are focusing on the development of an accurate dynamic model of flexible manipulators, controlling and applying them to different applications. Paper A presents a review of state-of-the-art dynamic modeling techniques and control schemes to control FLMs that were studied in recent literature along with their merits and limitations.

The review of the recent literature shows that most of the standard dynamic modeling approaches for FLMs assume small deflections in general. This can be a reasonable assumption for most robotic applications, but it can be violated in applications that require high accelerations, velocities, tip forces, and torques. Some studies consider moderate and large deformations to overcome the limitations of assuming small deflection [8–14].

Because of the difficulty in obtaining an accurate dynamic model of the FLMs, model-free control methods are used more often than model-based controllers: these types of controllers are popular because of their robustness to parameter uncertainty and disturbances in FLMs. However, only a few model-free methods, including proportional integral derivative (PID) control and iterative learning control, are used to control industrial robots, as other model-free methods need additional attention to solve the problem of low dynamic accuracy and/or unstable control caused by the non-collocated system. In order to solve the problem of individual controllers, two

or more control techniques are combined to achieve control performances that are better than using individual control techniques [15–18].

A recent boost in computing power and the emergence of machine learning algorithms have enabled scientists to apply intelligent control techniques or to combine learning-based control approaches with other methods to control FLMs. In addition, several recent control techniques proposed in the literature are based on neural networks and other learning-based algorithms [19–32].

The literature review (presented in paper A) on the state-of-the-art modeling and control techniques of FLMs reveals that most of the studies are limited to planar single-link and two-link flexible manipulators. More research studies are required for the modeling and control of multi-link flexible manipulators undergoing general three-dimensional (3D) motion.

1.3 Thesis Outline

Following the introduction in chapter 1, the thesis is divided into four main chapters, which are followed by the appended articles published in peer-reviewed conference proceedings and journals. The content of each chapter is summarized as follows:

Chapter 1 – Introduction

The chapter presents the research questions and motivation for this project. The state-of-the-art is briefly discussed. Finally, the dissertation outline is provided followed by a summary of the appended papers.

Chapter 2 – Modeling

The chapter summarizes different modeling techniques for FLMs and presents the kinematic and dynamic models of a planar three-link flexible manipulator used in this project.

Chapter 3 – Control

This chapter describes the challenges and complexities associated with the control of FLMs and highlights different control methods used for FLMs.

Chapter 4 – Experimental Setup

The chapter describes the experimental setup used in the thesis.

Chapter 5 – Concluding Remarks

The chapter summarizes and concludes the key outcomes of the project. Furthermore, research trends, further work, and the outlook on long-reach manipulators are discussed.

Appended Papers

The articles published in peer-reviewed conference proceedings and journals are appended at the end of the dissertation. The versions included in this thesis differ only in their formatting.

1.4 Contributions

The work done in this project has contributed to four main research areas of FLMs:

i. **Modeling:** Different methods of modeling FLMs are explored and discussed (presented in paper A). Lumped parameter method and assumed modes method of modeling FLMs are presented in papers B and C respectively.

ii. **Design and Prototyping:** A planar three-link flexible manipulator is designed, built, and commenced in the lab to carry out research in the field of FLMs. A detailed description of the experimental setup used in the project is presented in chapter 4.

iii. **Control:** Different model-based and model-free control methods used for controlling FLMs, that are studied in the literature, are reviewed in paper A. A strategy to compensate for the static deflection in planar multi-link flexible manipulators under gravity is proposed in paper D. The online control of a redundant FLM with redundancy resolution techniques to achieve minimum vibrations is discussed in paper E.

iv. **Application:** The application of a long-reach arm in autonomous mooring operation using camera-LiDAR data fusion is proposed and presented in paper F.

The main contributions of this work are summarized in Figure 1.2.

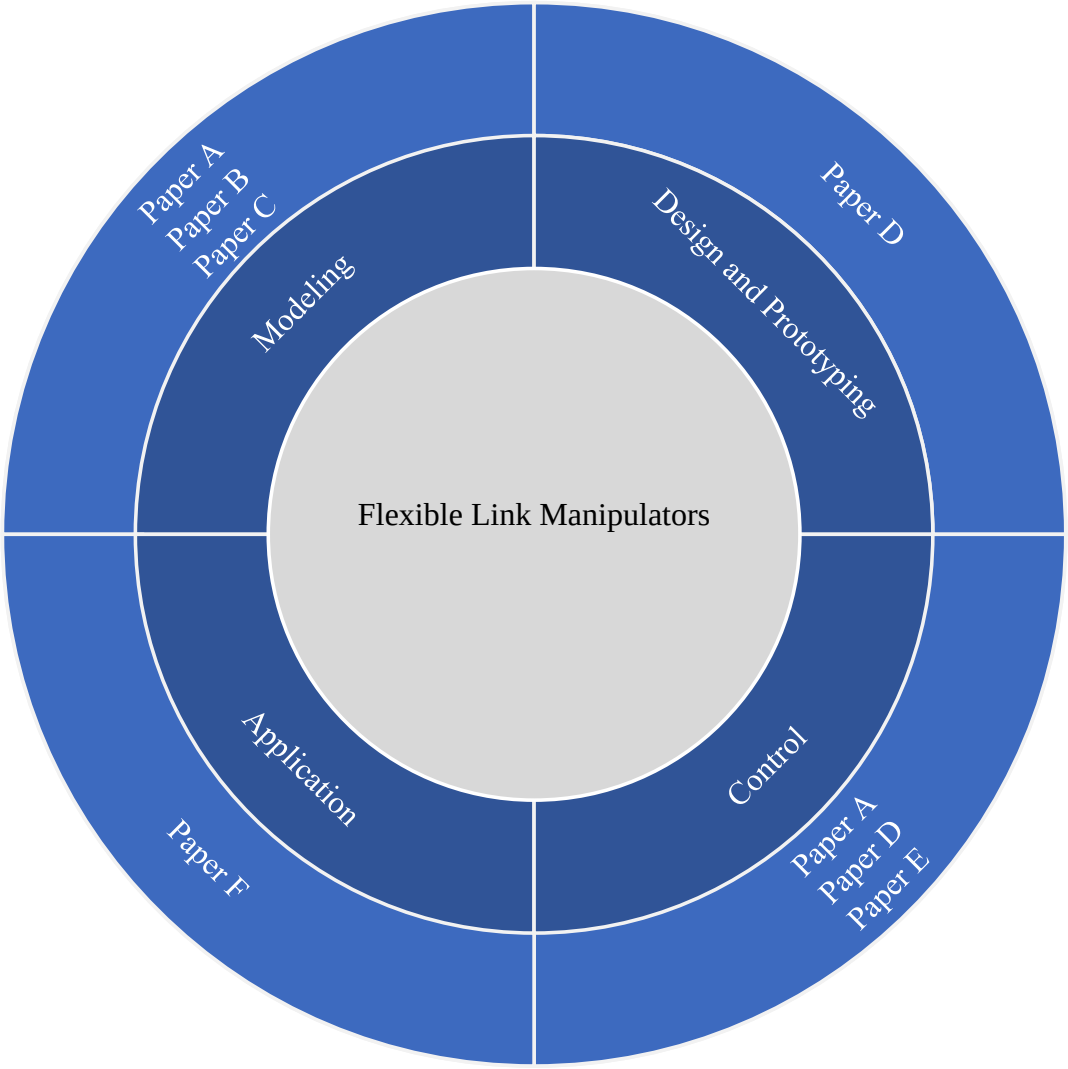

Figure 1.2: Thesis context and contributions.

The dissertation provides context to the contributions of the following papers:

Paper A – Review on Modeling and Control of Flexible Link Manipulators

This paper presents a review of dynamic modeling techniques and various control schemes to control flexible link manipulators (FLMs) that were studied in recent literature. The advantages and complexities associated with the FLMs are discussed briefly. A survey of the reported studies is carried out based on the method used for modeling link flexibility and obtaining equations of motion of the FLMs. The control techniques are reviewed by classifying them into two main categories: model-based and model-free control schemes. The merits and limitations of different modeling and control methods are highlighted.

Paper B – Modeling and Analysis of Flexible Bodies Using Lumped Para-

meter Method

The modeling, identification and analysis of a flexible beam is presented. The lumped parameter method is used to model a flexible beam. The use of camera measurements to identify lumped parameters, namely spring stiffness and damping coefficient, is described. The measurements of the tip oscillations using a high-speed camera and high-precision laser tracker are compared. The static and dynamic behavior of the flexible beam model is compared to the experimental results to show the validity of the model.

Paper C – Dynamic Modeling of Planar Multi-Link Flexible Manipulators

A closed-form dynamic model of the planar multi-link flexible manipulator is presented. The assumed modes method is used with the Lagrangian formulation to obtain the dynamic equations of motion. Explicit equations of motion are derived for a three-link case assuming two modes of vibration for each link. The eigenvalue problem associated with the mass boundary conditions, which changes with the robot configuration and payload, is discussed. The time-domain simulation results and frequency-domain analysis of the dynamic model are presented to show the validity of the theoretical derivation.

Paper D – Static Deflection Compensation of Multi-Link Flexible Manipulators Under Gravity

The static deflection compensation method of a planar multi-link flexible manipulator is proposed using the feedback from inertial sensors mounted at the tip of each link. The proposed compensation technique is validated experimentally using a high-precision laser tracker. The proposed strategy is experimentally verified using a three-link flexible manipulator. A strategy to compensate for the centripetal and tangential acceleration induced on the accelerometer mounted on the rotating link is proposed for correct inclination estimation. The improvement in the inclination estimation using the proposed compensation technique is verified both in simulation and experimental studies.

Paper E – Control of Redundant Flexible Manipulators with Redundancy Resolution

This paper deals with the online control of a redundant flexible link manipulator to achieve minimum oscillations using the redundancy resolution technique. Different redundancy resolution techniques proposed and used for rigid link manipulators are tested for their use in the case of flexible link manipulators. The simulation model of a planar three-link flexible manipulator is used in this study. The redundancy resolution using kinetic energy minimization techniques

is compared with the local joint acceleration minimization method to show the advantage of achieving minimum vibrations.

Paper F – Camera-LiDAR Data Fusion for Autonomous Mooring Operation

The use of camera and LiDAR sensors to sense the environment has gained increasing popularity in robotics. Individual sensors, such as cameras and LiDARs, fail to meet the growing challenges in complex autonomous systems. One such scenario is autonomous mooring, where the ship has to be tied to a fixed rigid structure (bollard) to keep it stationary safely. The detection and pose estimation of the bollard based on data fusion from the camera and LiDAR are presented here. Firstly, a single shot extrinsic calibration of LiDAR with the camera is presented. Secondly, the camera-LiDAR data fusion method using camera intrinsic parameters and camera to LiDAR extrinsic parameters is proposed. Finally, the use of an image-based segmentation method to segment the corresponding point cloud from the fused camera-LiDAR data is developed and tailored for its application in autonomous mooring operation.

Chapter 2

Modeling

This chapter describes briefly different modeling methods used for FLMs and presents the kinematic and dynamic models of a planar three-link flexible manipulator used in this project.

2.1 Flexible Link Model

A flexible link possesses infinite DoF which is mathematically complex to model. However, the flexible link system can be described with finite DoF by trading the accuracy for ease of use. The accuracy of the model depends on the assumptions made to simplify the complexity of the FLMs. However, all the dynamically relevant properties of the FLMs system such as flexibility effects, dynamic interactions, and coupling effects are important to represent accurately. The following assumptions are made for the development of the dynamic model of the FLMs throughout this thesis:

i. Link deflections are small.

ii. Each link of the manipulator can undergo bending deformations (transversal deflection) in the plane of motion.

iii. The torsional effects and shear deformations are neglected.

iv. All joints are rigid and revolute. This assumption is considered because of higher stiffness of the joint compared to the stiffness of the link.

This section provides a short introduction to different methods for modeling link flexibility. In addition to the methods discussed below, there are many other methods that are used for obtaining the dynamic model of the FLMs which include, but are not limited to, perturbation method, pseudo-rigid body method, global mode method, and modal integration method, as discussed in detail in paper A.

2.1.1 Lumped Parameter Method

In this method, the link flexibility is modeled by a set of mass, spring, and damper connected in series. Although lumped parameter method (LPM) is a simple and easy method to implement, its implementation relies on an accurate determination of the model parameters, namely spring stiffness and damping coefficients. Paper B discusses a systematic approach to accurately estimate model parameters using a camera and presents the use of LPM to model a flexible beam.

2.1.2 Assumed Modes Method

In this method, the link flexibility is represented by a combination of spatial mode shapes and time-varying generalized coordinates. The modal series is truncated to a finite dimension based on the assumption that the dynamics and overall motion of the link are dominantly governed by the first few low-frequency modes [33]. Among different modeling methods, assumed modes method (AMM) is more widely used in the literature. Paper C contains a detailed analysis of the AMM to model link flexibility and obtain a closed-form dynamic model of the planar multi-link flexible manipulator.

AMM has been used by many researchers to develop and experimentally verify a dynamic model of flexible mechanical systems [34–37]. The choice of proper boundary conditions is important while using AMM for modeling FLMs. Following four applicable boundary conditions, according to the general beam vibration theories, are detailed in [38, 39]:

i. Pinned-Pinned

ii. Clamped-Pinned

iii. Clamped-Free

iv. Clamped-Clamped.

It is also equally important to select compatible joint variables, deflection variables, and their corresponding mode shape functions [40, 41].

2.1.3 Finite Element Method

In finite element method (FEM), the flexible link is modeled as a combination of a finite number of elements interconnected at nodes. The displacement at any point of the continuous element is expressed in terms of the finite number of displacements at the nodal points multiplied by the polynomial interpolation functions [42]. The FEM is applicable for complex structures and can handle nonlinear and mixed

boundary conditions, but a large number of state-space equations involved makes it computationally expensive.

The finite element discretization of the flexible bodies introduces a large number of DoF resulting in computationally expensive simulation of the multi-body system. However, the number of DoF can be reduced using a model reduction procedure. This allows an efficient simulation of the multi-body system while keeping an accurate description of the predominant dynamic behavior. Model reduction involves a trade-off between the model order and the accuracy of the representation of the real plant dynamics. In other words, the order of the dynamic model should be suitable to use in real-time control and, at the same time, should not lead to a spill-over effect (the problem of un-modeled residual modes) that would destabilize the system.

The model reduction techniques discussed in the literature can be divided into three main categories [43, 44]:

i. Static condensation, substructuring, and modal truncation (Guyan reduction, dynamic reduction, component mode synthesis, improved reduction system method, and system equivalent expansion reduction process)

ii. Padé and Padé-type approximations (Krylov subspace method)

iii. Balancing-related truncation techniques.

The Craig-Bampton method (component mode synthesis technique) is one of the most frequently applied methods for the reduction of mechanical systems [45]. The quality of the reduced models depends on the selection of the right modes in complex systems, which needs an experienced user.

2.1.4 Transfer Matrix Method

In transfer matrix method (TMM), each element of the system is represented by a transfer matrix that transfers a state vector from one end of the element to the other. The individual element matrices are multiplied together to obtain the system transfer matrix [46]. The TMM is a frequency-domain technique, but it is difficult to include the interaction between the gross motion and the flexible dynamics of the manipulator [33].

2.2 Kinematics

The flexible body kinematics (presented in paper C) and the equivalent rigid body kinematics (presented in paper E) of a planar multi-link manipulator are summarized in this section.

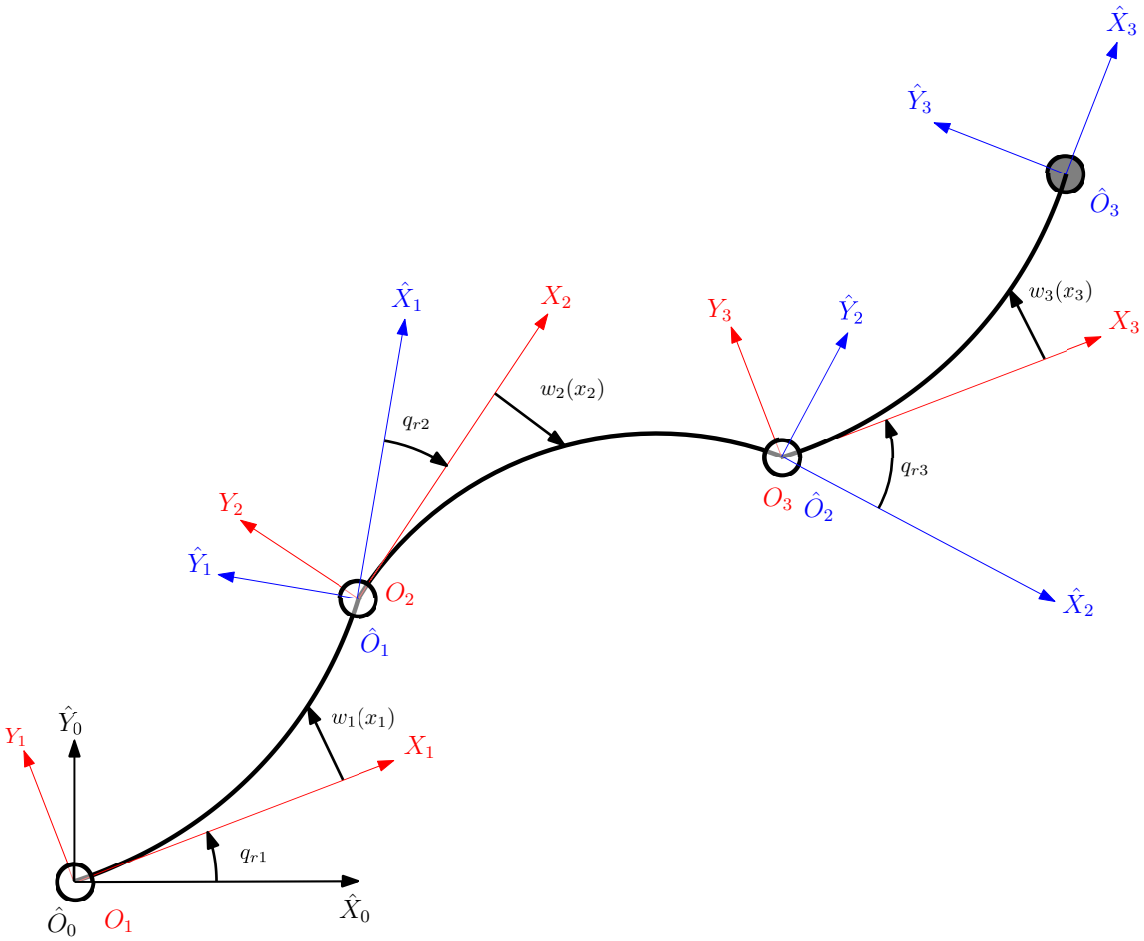

Figure 2.1: Planar three-link flexible manipulator.

2.2.1 Flexible Body Kinematics

Figure 2.1 shows a model of a planar three-link flexible manipulator. The direct kinematic model of the planar manipulator can be formulated in terms of displacement vectors and rotation matrices. The coordinate frames for the manipulator are assigned following a methodology similar to the Denavit-Hartenberg (DH) convention: the inertial frame $(\widehat{X}_0, \widehat{Y}_0)$, the rigid body moving frame associated with link i (X_i, Y_i) located at joint i, and the flexible body moving frame associated with link i $(\widehat{X}_i, \widehat{Y}_i)$ located at the tip of link i. The rigid motion of link i is represented by the joint i position q_{ri}, and the deflection at any point x_i along the link i is described by $w_i(x_i)$, where $0 \leq x_i \leq \ell_i$, and ℓ_i is the length of the link i.

The position of a point along the link i and its endpoint referred to frame (X_i, Y_i) are given by Equations (2.1) and (2.2) respectively. Here, ${}^i\boldsymbol{r}_{i+1}$ also denotes the position of the origin of frame (X_{i+1}, Y_{i+1}) with respect to frame (X_i, Y_i). The absolute positions of the aforementioned points referred to frame $(\widehat{X}_0, \widehat{Y}_0)$ are given by Equations (2.3) and (2.4) respectively, where $\boldsymbol{W}_i$ is the cumulative transformation from inertial frame $(\widehat{X}_0, \widehat{Y}_0)$ to frame (X_i, Y_i). $\boldsymbol{W}_i$ can be calculated recursively using Equations (2.5)–(2.7), where $\boldsymbol{A}_i$ represents the joint rotation matrix, and $\boldsymbol{E}_{i-1}$

represents the influence of the elastic deformation of the previous link $i-1$ in the orientation of link i. The orientations of frames (X_i, Y_i) and $(\widehat{X}_{i-1}, \widehat{Y}_{i-1})$ with respect to frame $(\widehat{X}_0, \widehat{Y}_0)$ are given by Equations (2.8) and (2.9) respectively.

$$ {}^{i}\boldsymbol{p}_i = \begin{bmatrix} x_i & w_i(x_i) \end{bmatrix}^T \tag{2.1} $$

$$ {}^{i}\boldsymbol{r}_{i+1} = {}^{i}\boldsymbol{p}_i\big|_{x_i=\ell_i} = \begin{bmatrix} \ell_i & w_{ie} \end{bmatrix}^T \tag{2.2} $$

$$ \boldsymbol{p}_i = \boldsymbol{r}_i + \boldsymbol{W}_i^i \boldsymbol{p}_i \tag{2.3} $$

$$ \boldsymbol{r}_{i+1} = \boldsymbol{r}_i + \boldsymbol{W}_i^i \boldsymbol{r}_{i+1} \tag{2.4} $$

$$ \boldsymbol{W}_i = \boldsymbol{W}_{i-1}\boldsymbol{E}_{i-1}\boldsymbol{A}_i = \widehat{\boldsymbol{W}}_{i-1}\boldsymbol{A}_i, \quad \boldsymbol{W}_0 = \widehat{\boldsymbol{W}}_0 = \boldsymbol{I} \tag{2.5} $$

$$ \boldsymbol{A}_i = \begin{bmatrix} cos(q_{ri}) & -sin(q_{ri}) \\ sin(q_{ri}) & cos(q_{ri}) \end{bmatrix} \tag{2.6} $$

$$ \boldsymbol{E}_i = \begin{bmatrix} 1 & -w'_{ie} \\ w'_{ie} & 1 \end{bmatrix}, \quad w'_{ie} = \frac{\partial w_i(x_i)}{\partial x_i}\bigg|_{x_i=\ell_i}, \quad \boldsymbol{E}_0 = \boldsymbol{I} \tag{2.7} $$

$$ \alpha_i = \sum_{j=1}^{i} q_{rj} + \sum_{k=1}^{i-1} w'_{ke}, \quad i \leq n \tag{2.8} $$

$$ \widehat{\alpha}_i = \sum_{j=1}^{i-1} q_{rj} + \sum_{k=1}^{i-1} w'_{ke}, \quad i \leq n+1 \tag{2.9} $$

The differential kinematics can be obtained using the time derivatives of the displacement and rotation as shown in Equations (2.10)–(2.19).

$$ {}^{i}\dot{\boldsymbol{p}}_i = \begin{bmatrix} 0 & \dot{w}_i \end{bmatrix}^T \tag{2.10} $$

$$ {}^{i}\dot{\boldsymbol{r}}_{i+1} = {}^{i}\dot{\boldsymbol{p}}_i\big|_{x_i=\ell_i} = \begin{bmatrix} 0 & \dot{w}_{ie} \end{bmatrix}^T \tag{2.11} $$

$$ \dot{\boldsymbol{p}}_i = \dot{\boldsymbol{r}}_i + \dot{\boldsymbol{W}}_i^i p_i + \boldsymbol{W}_i^i \dot{\boldsymbol{p}}_i \tag{2.12} $$

$$ \dot{\boldsymbol{r}}_{i+1} = \dot{\boldsymbol{r}}_i + \dot{\boldsymbol{W}}_i^i r_{i+1} + \boldsymbol{W}_i^i \dot{\boldsymbol{r}}_{i+1} \tag{2.13} $$

$$ \dot{\alpha}_i = \sum_{j=1}^{i} \dot{q}_j + \sum_{k=1}^{i-1} \dot{w}'_{ke} \tag{2.14} $$

$$\dot{\hat{\alpha}}_i = \sum_{j=1}^{i-1} \dot{q}_j + \sum_{k=1}^{i-1} \dot{w}'_{ke} \tag{2.15}$$

$$\dot{\boldsymbol{A}}_i = \boldsymbol{S}\boldsymbol{A}_i\dot{q}_i, \quad \boldsymbol{S} = \begin{bmatrix} 0 & -1 \\ 1 & 0 \end{bmatrix} \tag{2.16}$$

$$\dot{\boldsymbol{E}}_i = \boldsymbol{S}\dot{w}'_{ie} \tag{2.17}$$

$$\dot{\boldsymbol{W}}_i = \dot{\widehat{\boldsymbol{W}}}_{i-1}\boldsymbol{A}_i + \widehat{\boldsymbol{W}}_{i-1}\dot{\boldsymbol{A}}_i \tag{2.18}$$

$$\dot{\widehat{\boldsymbol{W}}}_{i-1} = \dot{\boldsymbol{W}}_{i-1}\boldsymbol{E}_{i-1} + \boldsymbol{W}_{i-1}\dot{\boldsymbol{E}}_{i-1} \tag{2.19}$$

2.2.2 Rigid Body Kinematics

The forward kinematics of a manipulator describing the pose of the end-effector as a function of the joint angles is given by Equation (2.20), where $\boldsymbol{x} \in \mathbb{R}^m$ is the vector representing the pose of the end-effector, and $\boldsymbol{q}_r \in \mathbb{R}^n$ is the vector of joint positions.

$$\boldsymbol{x} = f(\boldsymbol{q}_r) \tag{2.20}$$

For the planar three-link manipulator, $n = 3$ represents three joints and $m = 2$ represents the two-dimensional (2D) position of the end-effector. Figure 2.2 shows the equivalent rigid body schematic of a three-link manipulator with DH parameters given in Table 2.1.

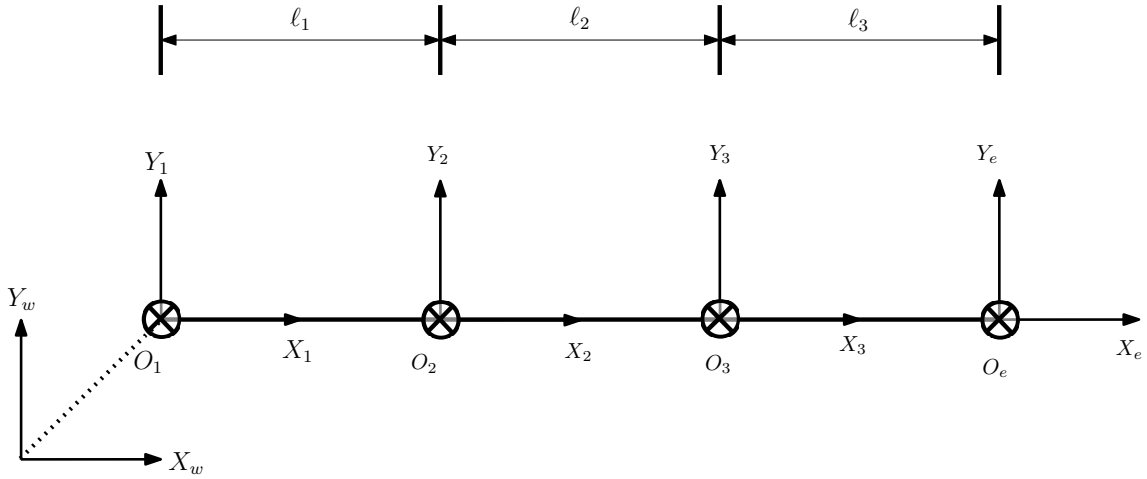

Figure 2.2: Equivalent rigid body kinematics.

Table 2.1: DH parameters.

Axis	**RotZ**	**TranZ**	**TranX**	**RotX**
1	q_{r1}	0.0	ℓ_1	0.0
2	q_{r2}	0.0	ℓ_2	0.0
3	q_{r3}	0.0	ℓ_3	0.0

Differentiating Equation (2.20) with respect to time, the relation between joint velocity and end-effector velocity is obtained as shown in Equation (2.21), which is called differential kinematics of the manipulator, where $\boldsymbol{J}(\boldsymbol{q}_r) \in \mathbb{R}^{m\times n}$ is the $m \times n$ Jacobian matrix.

$$\dot{\boldsymbol{x}} = \boldsymbol{J}(\boldsymbol{q}_r)\dot{\boldsymbol{q}}_r \tag{2.21}$$

Similarly, the relation between the joint acceleration and end-effector acceleration is obtained by differentiating Equation (2.21) with respect to time as shown in Equation (2.22).

$$\ddot{\boldsymbol{x}} = \boldsymbol{J}(\boldsymbol{q}_r)\ddot{\boldsymbol{q}}_r + \dot{\boldsymbol{J}}(\boldsymbol{q}_r, \dot{\boldsymbol{q}}_r)\dot{\boldsymbol{q}}_r \tag{2.22}$$

2.3 Dynamics

The dynamic model of the planar multi-link flexible manipulator derived using the assumed modes method is given by Equation (2.23), where $\boldsymbol{q} = \begin{bmatrix}\boldsymbol{q}_r & \boldsymbol{q}_f\end{bmatrix}^T$, $\boldsymbol{q}_r = \begin{bmatrix}q_{r1} & q_{r2} & \cdots & q_{rn}\end{bmatrix}^T$, $\boldsymbol{q}_f = \begin{bmatrix}q_{f11} & q_{f12} & \cdots & q_{f1n_f} \cdots & q_{fn1} & q_{fn2} & \cdots & q_{fnn_f}\end{bmatrix}^T$, q_{ri} represents the i^{th} joint position, q_{fij} represents the time-varying variable related to the spatial assumed mode shape of link i and mode of vibration j, n_f represents the total number of assumed modes of vibration, $\boldsymbol{M}(\boldsymbol{q})$ is the inertia matrix, $\boldsymbol{c}(\boldsymbol{q}, \dot{\boldsymbol{q}})$ is the vector of Coriolis and centripetal effects, $\boldsymbol{g}(\boldsymbol{q})$ is the gravity term, and $\boldsymbol{K}$ is the rigidity modal matrix (presented in paper C).

$$\boldsymbol{M}(\boldsymbol{q})\ddot{\boldsymbol{q}} + \boldsymbol{c}(\boldsymbol{q}, \dot{\boldsymbol{q}}) + \boldsymbol{g}(\boldsymbol{q}) + \boldsymbol{K}\boldsymbol{q} = \boldsymbol{\tau} \tag{2.23}$$

Joint viscous friction and link structural damping can be included by adding a damping matrix $\boldsymbol{D}$ as

$$\boldsymbol{M}(\boldsymbol{q})\ddot{\boldsymbol{q}} + \boldsymbol{c}(\boldsymbol{q}, \dot{\boldsymbol{q}}) + \boldsymbol{g}(\boldsymbol{q}) + \boldsymbol{K}\boldsymbol{q} + \boldsymbol{D}\dot{\boldsymbol{q}} = \boldsymbol{\tau}. \tag{2.24}$$

The dynamic equation can be written in another form separating rigid and flexible parts as in Equations (2.25)–(2.27).

$$\begin{bmatrix}\boldsymbol{M}_{rr} & \boldsymbol{M}_{rf} \\ \boldsymbol{M}_{rf}^T & \boldsymbol{M}_{ff}\end{bmatrix}\begin{bmatrix}\ddot{\boldsymbol{q}}_r \\ \ddot{\boldsymbol{q}}_f\end{bmatrix} + \begin{bmatrix}\boldsymbol{c}_r \\ \boldsymbol{c}_f\end{bmatrix} + \begin{bmatrix}\boldsymbol{g}_r \\ \boldsymbol{g}_f\end{bmatrix} + \begin{bmatrix}\boldsymbol{0} & \boldsymbol{0} \\ \boldsymbol{0} & \boldsymbol{K}_{ff}\end{bmatrix}\begin{bmatrix}\boldsymbol{q}_r \\ \boldsymbol{q}_f\end{bmatrix} + \begin{bmatrix}\boldsymbol{D}_{rr} & \boldsymbol{0} \\ \boldsymbol{0} & \boldsymbol{D}_{ff}\end{bmatrix}\begin{bmatrix}\dot{\boldsymbol{q}}_r \\ \dot{\boldsymbol{q}}_f\end{bmatrix} = \begin{bmatrix}\boldsymbol{\tau}_r \\ \boldsymbol{0}\end{bmatrix} \tag{2.25}$$

$$\boldsymbol{M}_{rr}\ddot{\boldsymbol{q}}_r + \boldsymbol{M}_{rf}\ddot{\boldsymbol{q}}_f + \boldsymbol{c}_r + \boldsymbol{g}_r + \boldsymbol{D}_{rr}\dot{\boldsymbol{q}}_r = \boldsymbol{\tau}_r \tag{2.26}$$

$$\boldsymbol{M}_{rf}^T\ddot{\boldsymbol{q}}_r + \boldsymbol{M}_{ff}\ddot{\boldsymbol{q}}_f + \boldsymbol{c}_f + \boldsymbol{g}_f + \boldsymbol{K}_{ff}\boldsymbol{q}_f + \boldsymbol{D}_{ff}\dot{\boldsymbol{q}}_f = \boldsymbol{0} \tag{2.27}$$

Chapter 3

Control

This chapter describes the challenges and complexities associated with the control of FLMs and highlights different control methods used for FLMs.

3.1 Overview of FLM Control

The control of FLMs is a challenging and ongoing field of robotics research and development. Different types of tasks and robot systems require a variety of robot controllers. This chapter presents a systematic overview of different methods of FLM control and introduces the research topics related to FLM control relevant to this project.

Unlike rigid manipulators, it is not possible to control the end-effector position and orientation of FLMs precisely by using joint encoders only. Additional sensors (e.g., inertial sensors and vision sensors) are required to sense deflections and oscillations. For the correct positioning of the end-effector in the FLM, the deflection should be estimated by using a suitable sensor system and should be compensated using the feedback control strategy of adjusting joint variables. Some commonly used sensors for deflection measurements and estimations in FLMs are [7]:

i. Strain gauges

ii. IMUs

iii. Optical/vision systems

iv. Position sensitive devices

v. Piezoelectric materials

vi. Ultrasonic sensors

vii. Range sensors.

Paper A presents challenges and complexities associated with the control of FLMs and provides a review of different model-based and model-free control methods studied in the literature. The common problems/complexities associated with the control of FLMs, as discussed in [39] and paper A, are as follows:

i. **Non-minimum phase:** It results from the system zeros located in the right half of a complex plane (s-plane).

ii. **Non-collocation:** It refers to the problem with the accurate end-effector position control of the FLM using non-collocated actuation/ torque input (at the joint).

iii. **Under-actuation:** The FLM system has fewer actuators (at joints) than the number of degrees of freedom. This is because the elastic links have infinite degrees of freedom.

iv. **Controller/observer spillover:** Control spillover is the excitation of the residual modes by the controller action and observation spillover is the contamination of sensor reading by the residual modes. This problem is due to model truncation and may lead to an unstable closed-loop system. Nevertheless, a model-free robust controller can be used to avoid controller/observer spillover problems caused due to model truncation [6].

Apart from the control complexities discussed above, there are other problems such as friction, backlash, and gear non-linearities that should be addressed by the control algorithms designed for FLMs. Main control problems that are studied in the literature for FLMs are categorized as follows (presented in paper A) [39] :

i. Tip position control [47, 48]

ii. Joint position control [49]

iii. Tip trajectory tracking control [50]

iv. Joint trajectory tracking control [51–53]

v. Vibration control [54]

vi. Motion control [55–57]

vii. Force control [58, 59]

viii. Hybrid control (position and force [60, 61], position and vibration [62], trajectory tracking and vibration [63], and other combinations).

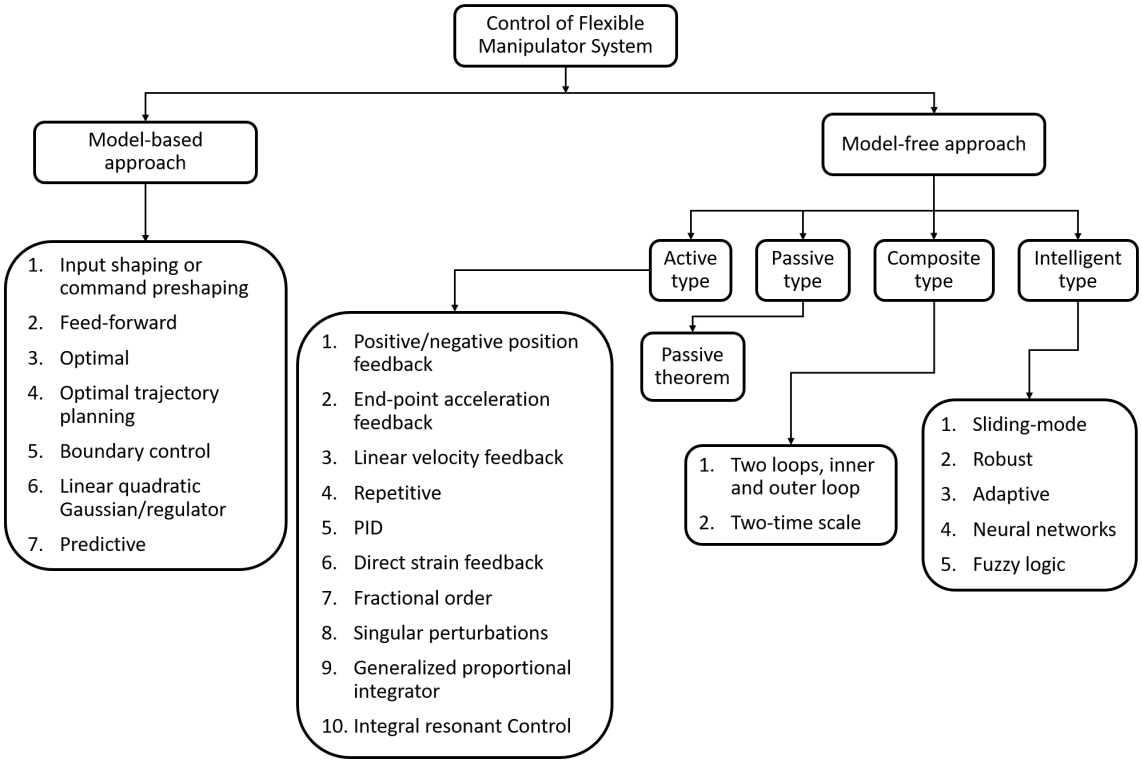

Figure 3.1: Model-based and model-free control schemes.

There are various control schemes reported in the literature, depending on the control problems. The control techniques can be broadly divided into two main categories: model-based control and model-free control, as shown in Figure 3.1 and discussed in detail in paper A.

i. **Model-Based Control:** In model-based control, the system's dynamic model is explicitly used to aid the controller design. The mathematical model is applied to calculate the controller response required to obtain the explicitly specified desired output response.

   Model-based control techniques (shown in Figure 3.1) include input shaping or command preshaping control, feed-forward control, optimal control, optimal trajectory planning, boundary control, linear quadratic Gaussian/regulator, predictive control, and (state) observer-based control [7].

   Since the controller is derived using the dynamic model of the system, to achieve good control performances, the parameters of the model should closely match the real system. The parameters of the FLM model are obtained by best fitting either to measured results of the excitation of the real robot or to an even more accurate model of the robot obtained, for example, using finite element modeling. Excitation is usually made in the same frequency range as it will be used for the control of the FLM. Most of the model-based controllers proposed in the literature use system identification techniques to determine

precise model parameters. Then the identified parameters are used to design the controller.

ii. **Model-Free Control:** Model-free control is a technique to control complex systems using a simplified representation of the system: subsequent algebraic estimation techniques are then used to design a simple and effective controller [64]. The controller does not rely on the precise mathematical model of the system, but it is solely based on the measurements obtained from the system.

Model-free control techniques (shown in Figure 3.1) include, but are not limited to, robust control, adaptive control, sliding mode control, intelligent control methods, composite control (inner/outer loop control, two-time scale control), PID control, singular perturbations technique, integral resonant control, generalized proportional integrator control, fractional order control, direct strain feedback control, repetitive control, passivity-based control, positive/negative position feedback control, end-point acceleration feedback control, and linear velocity feedback control [7].

Recently, there is a trend of using the combination of different control techniques to achieve better control performances than using individual control methods.

In this work, the control algorithms commonly designed for rigid-link manipulators are adopted with some modifications to use in the case of multi-link FLMs. In particular, the above-discussed problems (i.e., non-minimum phase, non-collocation, under-actuation, and controller/observer spillover) associated with FLMs are avoided, while still satisfying the requirements of the intended application of the long-reach manipulator (i.e., autonomous mooring) by assuming that deflections are slowly varying.

Joint space-based and task space-based controllers are the two common control schemes for robot manipulators.

3.2 Control in the Joint Space

Joint space is defined by a vector of joint positions. In this method, the robot is controlled to track the trajectory in joint space. In most robotic applications, the tasks are specified in the Cartesian space. Therefore, it is first necessary to solve the inverse kinematics problem to map the trajectories from the task space into the joint space before applying the joint space-based controllers.

Figure 3.2 shows a simplified architecture of the joint space-based controllers, where $\boldsymbol{x}_d$ is the desired Cartesian pose, $\boldsymbol{q}$ is the vector of joint positions, $\boldsymbol{q}_d$ is the vector of desired joint positions, and τ is the reference input torque command of the robot.

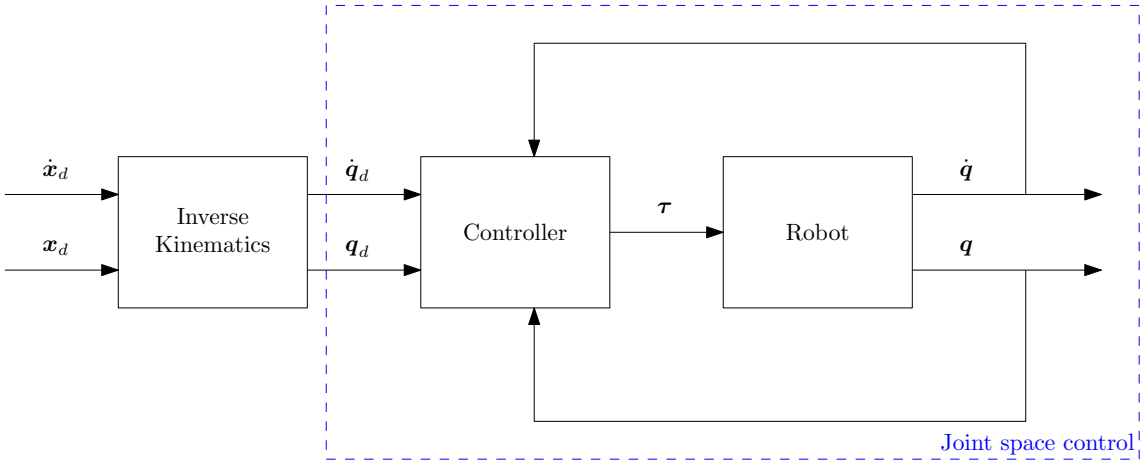

Figure 3.2: Block diagram of the joint space control.

Proportional derivative (PD), PID, and computed torque techniques are the common joint space-based control schemes.

The rigid body kinematics and joint position feedback are enough for the precise pose control of the rigid link manipulators. However, additional sensors are required to sense deflections and oscillations and should be compensated in the case of FLMs.

Independent Joint Control

An independent joint control strategy based on a cascaded architecture with deflection compensation for FLMs is presented in paper D and is shown in Figure 3.3. In Figure 3.3, q_{i_d} represents the desired joint i position, q_i is the actual joint i position, Δq_i is the static compensation angle or the angular deflection of link i at the tip, and θ_i is the inclination angle estimated using IMU i mounted on link i. The innermost loop is a proportional integral (PI) current controller. The next cascade level is a PI velocity control loop, the outermost cascade is a proportional (P) position controller, and the static deflection compensation action enters into the position cascade level.

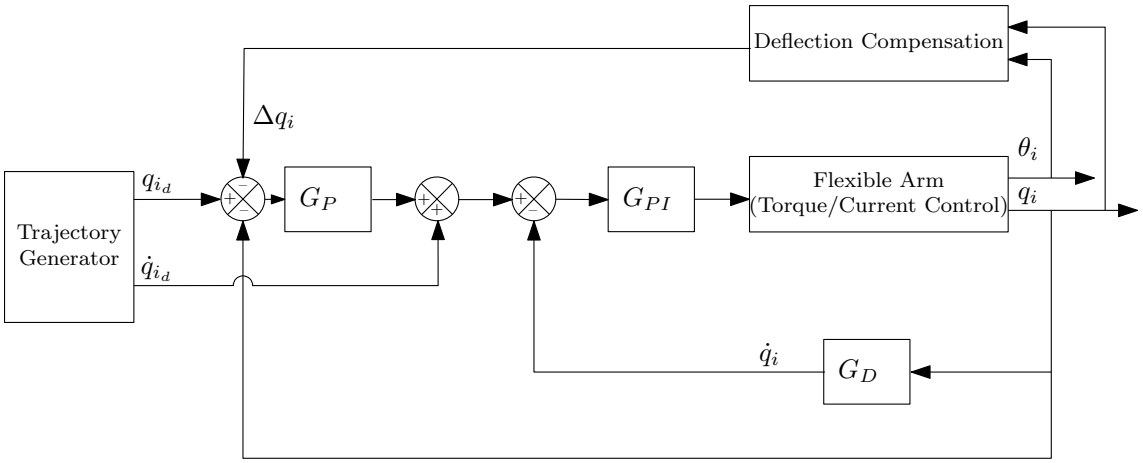

Figure 3.3: A general architecture for independent joint control with deflection compensation for FLM.

3.3 Control in the Cartesian Space

Cartesian space (or task space) is defined by the position and orientation of the end-effector of a robot. In this method, the robot is controlled to track the trajectory in the task space. The obvious strategy is to use inverse kinematic algorithms to convert task space variables into the corresponding joint space variables and then use joint space control. This approach is called *kinematic control*. Another strategy is to design a control scheme directly in the task space by reconstructing task space variables from measured joint space variables by using the kinematic mappings.

Figure 3.4 shows a simplified architecture of the task space-based controllers, where $\boldsymbol{x}$ is the actual Cartesian pose of the robot.

In the case of FLMs, the actual end-effector pose (i.e., task space variables) does not match the end-effector pose calculated using the rigid body kinematics due to deflection. This adds additional complexity to the task space control of FLMs. Although the task space variables could be measured using suitable sensor systems (for example, vision systems), the joint variables are still needed to evaluate the Jacobian matrix.

Although the direct task space control approach has the advantage to operate directly on the task space variables, the joint space behavior is difficult to predict and the feedback gains in tasks space are not intuitive. Furthermore, it does not allow easy management of the effects of singularities and redundancy and may become computationally demanding if, besides positions, also velocities and accelerations are of concern [65]. However, the kinematic control approach provides an easy way to analyze the important properties of kinematic mappings: singularities and redundancy.

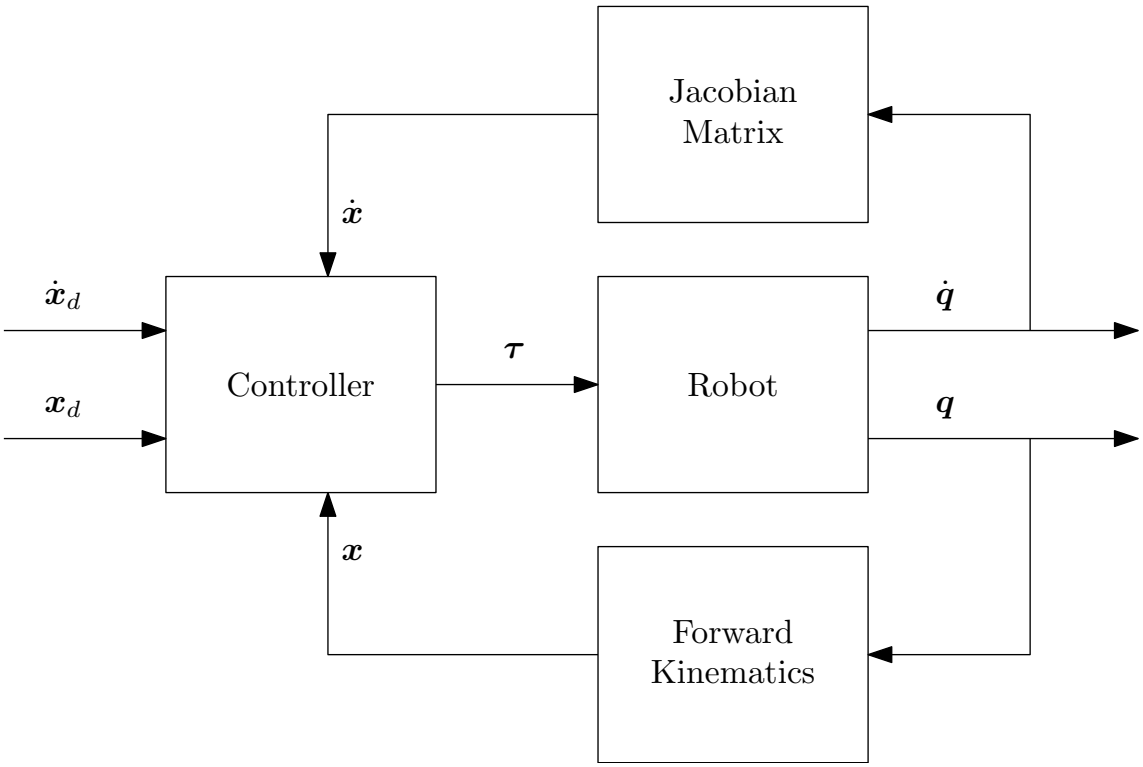

Figure 3.4: Block diagram of the task space control.

Redundancy Resolution

A kinematically redundant manipulator has more DoF than required to achieve the desired position and orientation of the end-effector. This redundancy of the manipulator can be exploited in a strategic manner that will improve its performance without affecting the validity of the solution. Different redundancy resolution methods are available in the literature for rigid link manipulators. Manipulator redundancy has been exploited in the literature to achieve different criteria, for example, joint limits avoidance [66, 67], minimization of kinetic energy [68], obstacles avoidance [69], singularity avoidance [70, 71], and minimization of joint torques [72]. However, their application in redundant FLMs has not been explored. Paper E explores different redundancy resolution methods and utilizes them to control redundant FLMs for achieving minimum vibrations.

In paper E, the closed-loop inverse kinematics (CLIK) algorithm with redundancy resolution at the acceleration level is used as shown in Figure 3.5, where $\boldsymbol{K}_p$ and $\boldsymbol{K}_v$ are symmetric positive definite matrices and their choices guarantee that the task-space position error ($\boldsymbol{e}_p = \boldsymbol{x}_d - \boldsymbol{x}$) and velocity error ($\boldsymbol{e}_v = \dot{\boldsymbol{x}}_d - \boldsymbol{J}\dot{\boldsymbol{q}}_r$) uniformly converge to zero.

The joint trajectories generated using the redundancy resolution techniques are used for the online control of the FLM. It is shown in paper E that the kinetic energy minimization approaches reduce the elastic vibrations compared to the local joint

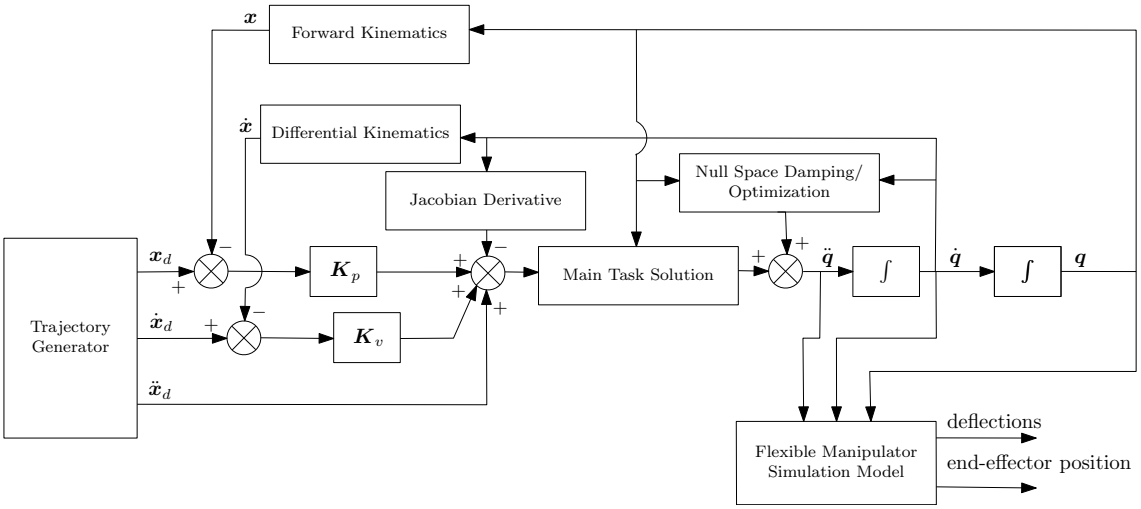

Figure 3.5: CLIK algorithm with redundancy resolution at the acceleration level applied to control FLM.

acceleration minimization method of redundancy resolution.

Chapter 4

Experimental Setup

This chapter describes the experimental prototype developed in the lab to carry out this research in the field of FLMs.

The experimental setup used in this work is shown in Figure 4.1. It consists of a planar three-link flexible manipulator with three revolute joints. Each joint consists of a hub, motor, and planetary gearbox. A STIM300 IMU sensor is mounted closer to the tip of each link and a Leica spherical reflector is mounted closer to the tip of the last link so that the precise position of the reflector can be tracked using a Leica AT960 laser tracker. The Leica tracker is used for validating the deflection compensation method proposed in paper D and it is calibrated with respect to the inertial frame $(\widehat{X}_0, \widehat{Y}_0)$ to measure the reflector position.

Hardware Architecture

The hardware architecture of the experimental setup is illustrated in Figure 4.2. It consists of the following main components:

i. **Manipulator:** The planar three-link flexible manipulator consists of the following:

   (a) **Links:** Each link of the manipulator is made of a hollow aluminium profile. The link dimensions are shown in Table 4.1.

   (b) **Motors and Gearboxes:** Each joint consists of a permanent magnet-excited three-phase synchronous motor and a planetary gearbox. The general specifications of the motors and gearboxes are shown in Table 4.2 and Table 4.3 respectively.

   (c) **IMUs:** The manipulator consists of three STIM300[1] IMU sensors mounted closer to the tip of each link. Each sensor contains three highly accurate

[1] `https://www.sensonor.com/products/inertial-measurement-units/stim300/`

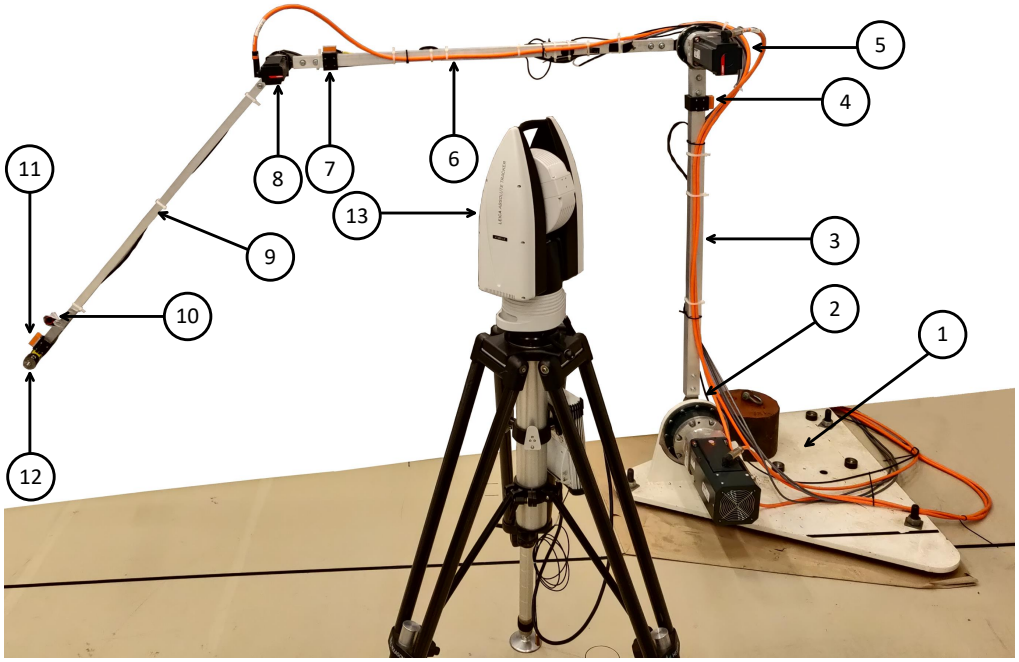

(**a**)

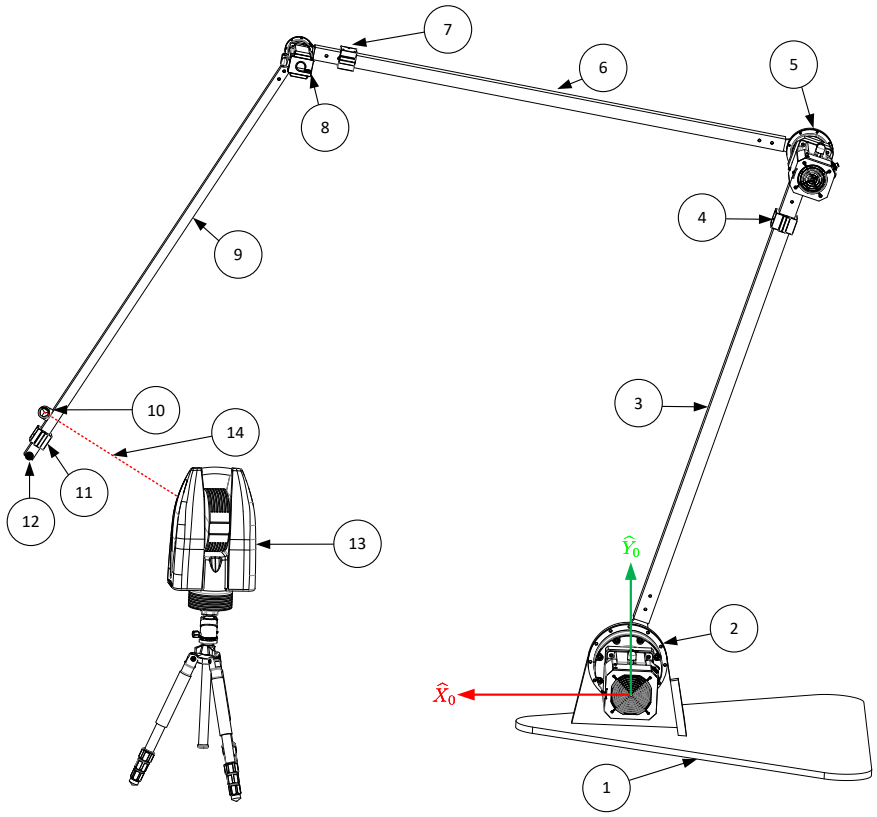

(**b**)

Figure 4.1: Experimental setup (1) Robot base, (2) Joint 1, (3) Link 1, (4) IMU 1, (5) Joint 2, (6) Link 2, (7) IMU 2, (8) Joint 3, (9) Link 3, (10) Leica spherical reflector, (11) IMU 3, (12) Payload, (13) Leica AT960 laser tracker, (14) Laser beam): (**a**) actual, (**b**) the schematic.

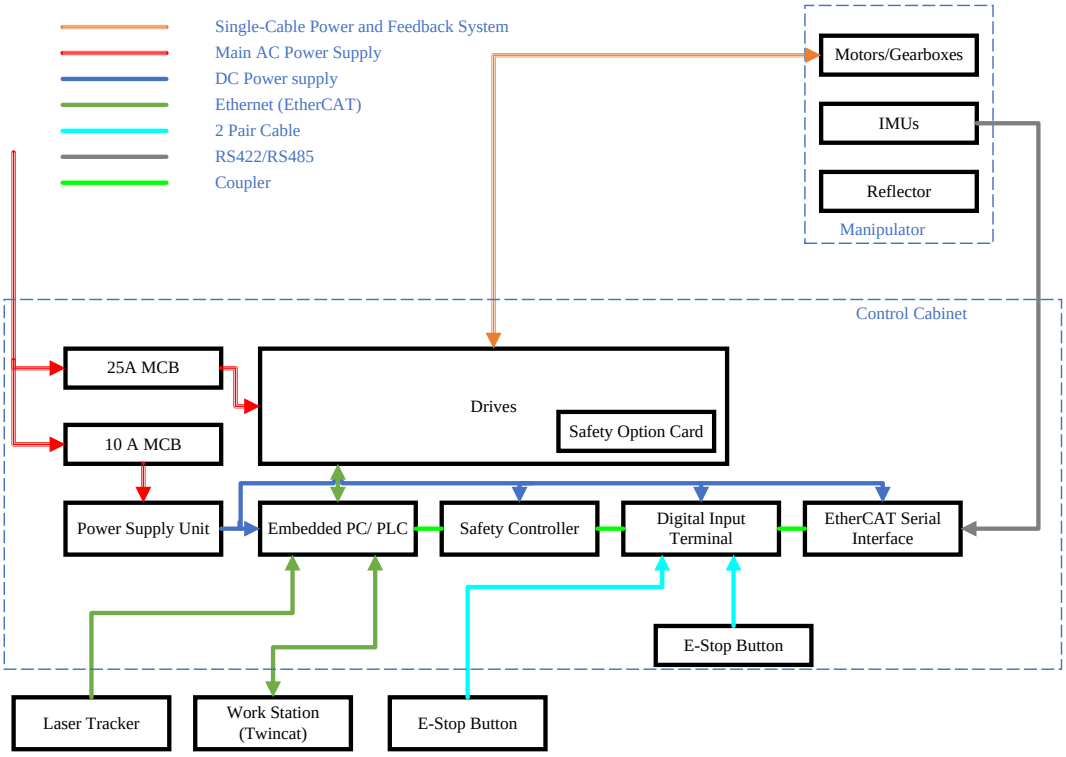

Figure 4.2: Hardware architecture.

micro-electromechanical systems (MEMS) gyros, three high stability accelerometers, and three inclinometers. All IMUs are factory calibrated and compensated over their entire operating temperature range.

(d) **Reflector:** A Leica spherical reflector[2] is mounted closer to the tip of the manipulator. The laser tracker can track the precise position of the reflector.

ii. **Control Cabinet:** The control cabinet is shown in Figure 4.3. It consists of the following components:

(a) **Power Supply:** A three-phase 400 V alternating current (AC) power supply is supplied to three servo drives via a 3-pole 25 A miniature circuit breaker (MCB). Moreover, a direct current (DC) power supply unit is protected with a 3-pole 10 A MCB. This makes it possible to run the DC circuit with the embedded personal computer (PC)/programmable logic controller (PLC) without switching on the drives. The DC power supply unit provides 24 V DC power to all the components in the control cabinet requiring DC power input including servo drives, embedded PC/PLC, safety controller, digital input terminal, and ethernet for control

[2] `https://leica-geosystems.com/products/total-stations/accessories/reflectors`

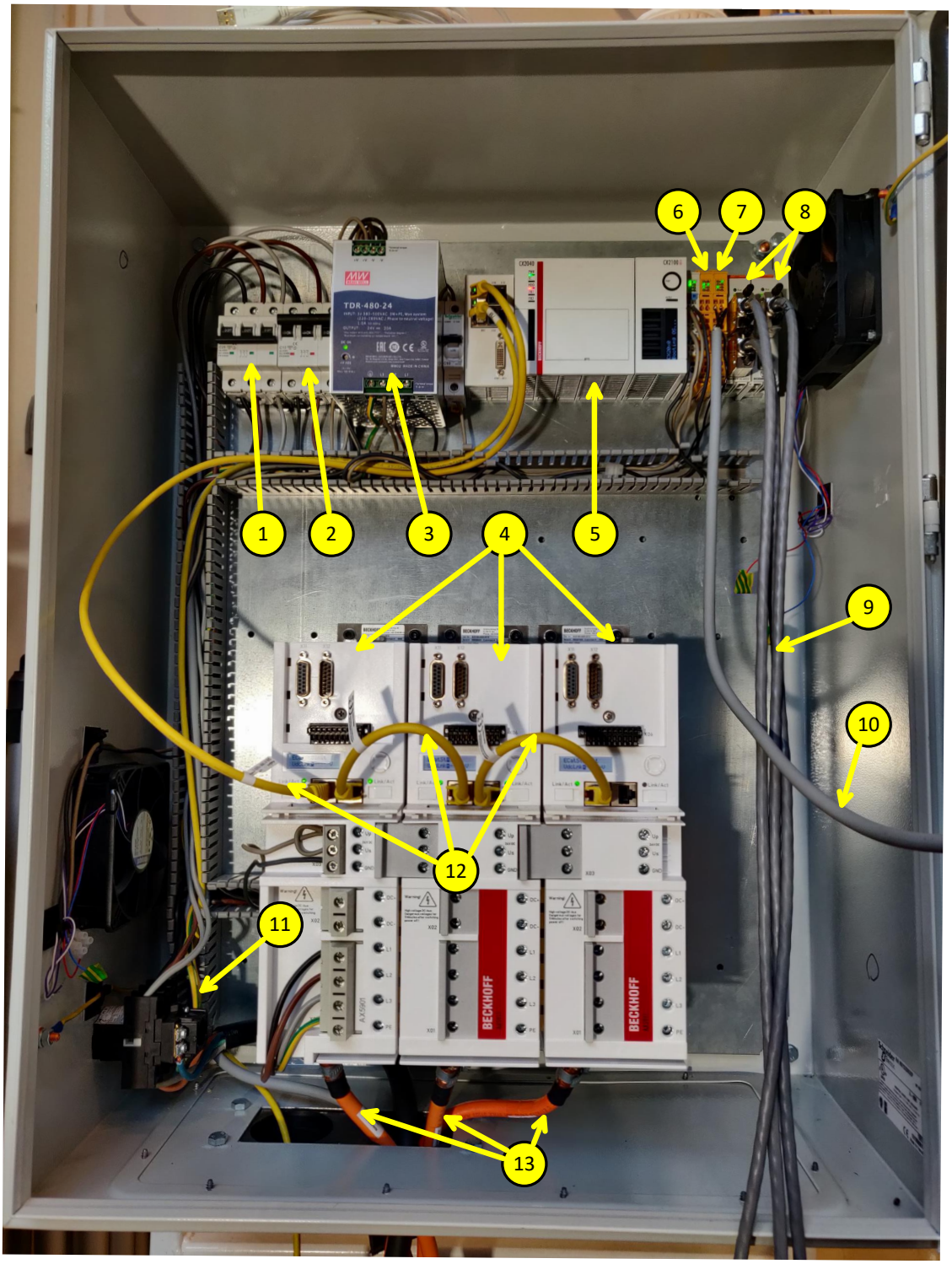

Figure 4.3: Control cabinet (① 25 A MCB, ② 10 A MCB, ③ Power supply unit, ④ Drives, ⑤ Embedded PC/PLC, ⑥ Safety controller, ⑦ Digital input terminal, ⑧ EtherCAT serial interface, ⑨ RS422/RS485 cable, ⑩ Two pair cable to connect E-Stop button, ⑪ Main AC power supply, ⑫ EtherCAT connectors, ⑬ Single-cable power and feedback system).

automation technology (EtherCAT) serial interface.

(b) **Embedded PC/PLC:** The embedded PC with a high-performance central processing unit (CPU) can be transformed into a powerful PLC by installing TwinCat automation software. It can communicate with drives, laser tracker, safety controller, digital input terminal, EtherCAT serial interface, and other devices compatible with EtherCAT communication protocol.

(c) **Drives:** There are three compact servo drives: one for each joint with a TwinSAFE[3] drive option card that provides drive integrated safety functions. All servo drives have a rated output current of 6 A, a peak output current of 13 A, and a max DC link voltage of 875 V. Three drives are connected to form a multi-axis system. The control loop has a cascaded structure and supports fast and highly dynamic positioning tasks. The drives can communicate with the embedded PC/PLC for allowing PC-based control via EtherCAT communication protocol.

(d) **Safety Controller:** A dedicated safety controller is connected to the PLC which is a TwinSAFE component used for the realization of safety-oriented applications on the basis of Boolean values. For this purpose, certified function blocks are available enabling the processing of safe input signals and the generation of safe output signals. The safety controller safely exchanges data via failsafe over EtherCAT (FSoE) with other devices including the TwinSAFE digital input terminal.

(e) **Digital Input Terminal:** A digital input terminal is a TwinSAFE component used for connecting sensors with potential-free contracts for 24V DC. It has four fail-safe inputs. The signals are transmitted via FSoE to a TwinSAFE Logic-capable component (safety controller) and can be used to evaluate them in terms of safety. Two E-Stop buttons are connected to the digital input terminal.

(f) **EtherCAT Serial Interface:** The EtherCAT serial interface enables the connection of devices with RS422/RS485 interfaces. This interface can communicate with the PLC via the coupler. Three IMUs are connected to this interface via RS422 cable.

(g) **E-Stop Buttons:** There are two emergency stop (E-Stop) buttons connected to the EtherCAT serial interface: one is placed on the control cabinet, while the other is freely movable and can be placed near the workstation.

[3] `https://www.beckhoff.com/en-en/products/automation/twinsafe/twinsafe-hardware/ax5805.html`

Table 4.1: Link dimensions.

	Length (m)	**Width (m)**	**Height (m)**	**Thickness (m)**
Link 1	1.5	50×10^{-3}	50×10^{-3}	4×10^{-3}
Link 2	1.5	40×10^{-3}	40×10^{-3}	3×10^{-3}
Link 3	1.5	30×10^{-3}	30×10^{-3}	2.5×10^{-3}

Table 4.2: Motor specifications.

Specifications	**Motor 1**	**Motor 2**	**Motor 3**
Standstill torque (Nm)	17.1	8.20	1.37
Rated torque (Nm)	16.1	7.50	1.34
Peak torque (Nm)	37.1	35.0	6.10
Rated speed (rpm)	1400	2000	3000
Rated power (kW)	2.36	1.57	0.42
Standstill current (A)	5.20	3.30	1.00
Peak current (A)	13.9	17.9	5.5
Torque constant (Nm/A)	3.30	2.48	1.37

iii. **Laser Tracker:** A Leica AT960 laser tracker is used to track the precise position of the Leica spherical reflector mounted at the tip of the manipulator. The tracker is connected with the PLC using the EtherCAT and can track the reflector at 1 kHz.

iv. **Workstation:** A workstation with TwinCAT 3.1 installed on the Windows 10 operating system is used to communicate with the embedded PC/PLC via EtherCAT communication protocol and to deploy software developed to control the manipulator. The human-machine interface (HMI) is developed using PyQt5[4] and pyads[5], which are based on Python 3[6], Qt[7], and TwinCAT automation device specification (ADS).

Table 4.3: Gearbox specifications.

Specifications	**Gearbox 1**	**Gearbox 2**	**Gearbox 3**
Gear ratio	61	50	35
Nominal output torque (Nm)	1100	304	40
Maximum acceleration torque (Nm)	1400	380	55

[4] `https://pypi.org/project/PyQt5/`
[5] `https://pypi.org/project/pyads/`
[6] `https://www.python.org/downloads/`
[7] `https://www.qt.io/`

Design Requirements

The selection of motors, gearboxes, drives, and links is done by considering the following design requirements:

i. Each link of the arm is 1.5 m long and made of elastic hollow aluminum profiles such that the total deflection of the arm should be less than 10% of the total length of the arm in the horizontal configuration with a payload of 2 kg at the end-effector, and the deflection of each link should be considerably visible.

ii. The end-effector of the arm can follow a circular trajectory with a radius of 1 m at the tangential speed of 2 m/s^2 with the center at $(2.5\ m, 1.5\ m)$.

iii. Inertia ratio $\lambda \leq 10$.

iv. The weight of the manipulator system is minimized.

v. The nominal output torque and maximum acceleration torque of the joints are maximized.

vi. The motion of the end-effector should be planar.

However, the motion of the end-effector is not perfectly planar because of the asymmetrical load at the joints. The problem of resonance or the effective operating bandwidth of the system may occur because of high inertia ratios $\lambda > 10$.

Chapter 5

Concluding Remarks

This chapter summarizes and concludes the key outcomes of the project. Furthermore, research trends, further work, and the outlook on long-reach flexible manipulators are discussed.

5.1 Conclusions

The work presented in this dissertation has contributed to the area of modeling, control, and application of long-reach flexible manipulators.

Different state-of-the-art modeling and control strategies of the FLMs, along with the challenges associated with them, have been discussed. The modeling and analysis of a flexible beam using the LPM have been presented and the use of the camera to identify the lumped parameters (i.e., stiffness and damping coefficient) of the flexible beam has been proposed and validated experimentally. A closed-form dynamic model for a planar multi-link flexible manipulator has been derived. The effect of robot configuration and payload on the mode shapes and eigenfrequencies of the flexible links are discussed. A method to estimate the static deflection of multi-link flexible manipulators under gravity has been proposed. A strategy to compensate for the static deflection by using a feedback control strategy of adjusting joint variables has been detailed and experimentally validated. The redundant DoF of the planar multi-link flexible manipulator have been exploited to minimize vibrations. One of the application areas of long-reach manipulators, i.e. autonomous mooring, has been explored and detailed.

5.2 Future Work

Although the closed-form dynamic model of the FLM has been derived for the multi-link flexible manipulator, because of high computational requirements, it is not

trivial to use the model to design model-based controllers in the case of manipulators with more than two links. However, the model can be used to study the effects of any control methods on the flexibility of the manipulator system.

Since the eigenfrequencies change with the changes in manipulator configuration and payload, the design of the model-based control using system identification techniques is difficult for multi-link manipulators with more than two links.

In spite of the fact that significant advancements have been made in many aspects of FLMs over the last few decades, there are many issues yet to be resolved, and simple, robust, reliable, and effective controls of FLMs still remain a challenge. Undoubtedly, further research efforts in this area would contribute significantly to the development of lightweight flexible manipulators for space research and long-reach manipulators for offshore industries to perform different robotic operations safely. The mooring operation could be executed autonomously by mounting long-reach arm/s on a ship. Cleaning, repair, and maintenance operations in offshore wind farms and sea farms could be carried out autonomously or semi-autonomously with the reduction of oscillations in the long-reach arm. Furthermore, the construction industry could utilize the long-reach manipulator for material handling and assembly tasks. Application-oriented studies on FLMs could be one of the possible future directions of research.

Bibliography

[1] Population Division United Nations, Department of Economic and Social Affairs. World Population Prospects: The 2017 Revision, Key Findings and Advance Tables. Working Paper No. ESA/P/WP/248., 2017. URL `https://population.un.org/wpp/Publications/Files/WPP2017_KeyFindings.pdf`.

[2] Heping Chen, Samuel Stavinoha, Michael Walker, Biao Zhang, and Thomas Fuhlbrigge. Opportunities and challenges of robotics and automation in offshore oil & gas industry. *Intelligent Control and Automation*, 5(3):136–145, 2014. doi: 10.4236/ica.2014.53016.

[3] Matthias Bengel, Kai Pfeiffer, Birgit Graf, Alexander Bubeck, and Alexander Verl. Mobile robots for offshore inspection and manipulation. In *2009 IEEE/RSJ International Conference on Intelligent Robots and Systems*, pages 3317–3322. IEEE, 2009. doi: 10.1109/IROS.2009.5353885.

[4] Kai Pfeiffer, Matthias Bengel, and Alexander Bubeck. Offshore robotics-survey, implementation, outlook. In *2011 IEEE/RSJ International Conference on Intelligent Robots and Systems*, pages 241–246. IEEE, 2011. doi: 10.1109/IROS.2011.6094661.

[5] Erik Kyrkjebø, Pål Liljebäck, and Aksel A Transeth. A Robotic Concept for Remote Inspection and Maintenance on Oil Platforms. In *ASME 2009 28th International Conference on Ocean, Offshore and Arctic Engineering*, pages 667–674. American Society of Mechanical Engineers, 2009. doi: 10.1115/OMAE2009-79702.

[6] Santosha Kumar Dwivedy and Peter Eberhard. Dynamic analysis of flexible manipulators, a literature review. *Mechanism and machine theory*, 41(7):749–777, 2006. doi: 10.1016/j.mechmachtheory.2006.01.014.

[7] Chang Tai Kiang, Andrew Spowage, and Chan Kuan Yoong. Review of control and sensor system of flexible manipulator. *Journal of Intelligent & Robotic Systems*, 77(1):187–213, 2015.

[8] F Boyer and N Glandais. Simulation of flexible manipulators with elastic non-linearities. In *Proceedings 1999 IEEE International Conference on Robotics and Automation (Cat. No.99CH36288C)*, volume 1, pages 759–766 vol.1, may 1999. doi: 10.1109/ROBOT.1999.770066.

[9] Akira Abe. Trajectory planning for residual vibration suppression of a two-link rigid-flexible manipulator considering large deformation. *Mechanism and Machine Theory*, 44(9):1627–1639, 2009. ISSN 0094114X. doi: 10.1016/j.mechmachtheory.2009.01.009.

[10] H R Heidari, M H Korayem, M Haghpanahi, and V Feliu Batlle. A new nonlinear finite element model for the dynamic modeling of flexible link manipulators undergoing large deflections. In *2011 IEEE International Conference on Mechatronics*, pages 375–380, apr 2011. doi: 10.1109/ICMECH.2011.5971314.

[11] Laura Celentano. Modeling of Flexible Robots with Varying Cross Section and Large Link Deformations. *Journal of Dynamic Systems, Measurement and Control, Transactions of the ASME*, 138(2):1–12, 2016. ISSN 15289028. doi: 10.1115/1.4032133.

[12] Ivan Giorgio and Dionisio D. Del Vescovo. Non-linear lumped-parameter modeling of planar multi-link manipulators with highly flexible arms. *Robotics*, 7(4): 1–13, 2018. ISSN 22186581. doi: 10.3390/robotics7040060.

[13] Habib Esfandiar, Moharam H Korayem, and Mohammad Haghpanahi. Large deformation modeling of flexible manipulators to determine allowable load. *Structural Engineering and Mechanics*, 62(5):619–629, 2017. doi: 10.12989/sem.2017.62.5.619.

[14] Bruno Scaglioni, Luca Bascetta, Marco Baur, and Gianni Ferretti. Closed-form control oriented model of highly flexible manipulators. *Applied Mathematical Modelling*, 52:174–185, 2017. ISSN 0307904X. doi: 10.1016/j.apm.2017.07.034.

[15] Bin Xu. Composite learning control of flexible-link manipulator using NN and DOB. *IEEE Transactions on Systems, Man, and Cybernetics: Systems*, 48(11): 1979–1985, nov 2017. ISSN 21682232. doi: 10.1109/TSMC.2017.2700433.

[16] Kshetrimayum Lochan, Binoy Krishna Roy, and Bidyadhar Subudhi. Use of memristive chaotic signal as a desired trajectory for a two-link flexible manipulator using contraction theory based on a composite control technique. *European Physical Journal: Special Topics*, 228(10):2215–2231, 2019. ISSN 19516401. doi: 10.1140/epjst/e2019-900038-5.

[17] Shiyuan Jia, Yinghong Jia, Shijie Xu, and Quan Hu. Maneuver and Active Vibration Suppression of Free-Flying Space Robot. *IEEE Transactions on Aerospace and Electronic Systems*, 54(3):1115–1134, 2017. ISSN 00189251. doi: 10.1109/TAES.2017.2775780.

[18] Chunyu Yang, Yiming Xu, Linna Zhou, and Yongzheng Sun. Model-free composite control of flexible manipulators based on adaptive dynamic programming. *Complexity*, 2018, 2018. ISSN 10990526. doi: 10.1155/2018/9720309.

[19] Hejia Gao, Wei He, Chen Zhou, and Changyin Sun. Neural Network Control of a Two-Link Flexible Robotic Manipulator Using Assumed Mode Method. *IEEE Transactions on Industrial Informatics*, 15(2):755–765, 2018. ISSN 15513203. doi: 10.1109/TII.2018.2818120.

[20] Yuncheng Ouyang, Wei He, and Xiajing Li. Reinforcement learning control of a singlelink flexible robotic manipulator. *IET Control Theory and Applications*, 11 (9):1426–1433, 2017. ISSN 17518652. doi: 10.1049/iet-cta.2016.1540.

[21] Changyin Sun, Wei He, and Jie Hong. Neural Network Control of a Flexible Robotic Manipulator Using the Lumped Spring-Mass Model. *IEEE Transactions on Systems, Man, and Cybernetics: Systems*, 47(8):1863–1874, 2016. ISSN 21682232. doi: 10.1109/TSMC.2016.2562506.

[22] C Sun, H Gao, W He, and Y Yu. Fuzzy Neural Network Control of a Flexible Robotic Manipulator Using Assumed Mode Method. *IEEE Transactions on Neural Networks and Learning Systems*, 29(11):5214–5227, nov 2018. ISSN 2162-2388. doi: 10.1109/TNNLS.2017.2743103.

[23] Wei He, Xiuyu He, and Changyin Sun. Vibration Control of an Industrial Moving Strip in the Presence of Input Deadzone. *IEEE Transactions on Industrial Electronics*, 64(6):4680–4689, 2017. ISSN 02780046. doi: 10.1109/TIE.2017.2674592.

[24] Zhi-cheng Qiu and Wen-zheng Zhang. Trajectory planning and diagonal recurrent neural network vibration control of a flexible manipulator using structural light sensor. *Mechanical Systems and Signal Processing*, 132:563–594, 2019. ISSN 10961216. doi: 10.1016/j.ymssp.2019.07.014.

[25] Zhi-cheng Qiu, Cheng Li, and Xian min Zhang. Experimental study on active vibration control for a kind of two-link flexible manipulator. *Mechanical Systems and Signal Processing*, 118:623–644, 2019. ISSN 10961216. doi: 10.1016/j.ymssp.2018.09.001.

[26] Fangfei Cao and Jinkun Liu. An adaptive iterative learning algorithm for boundary control of a coupled ODE–PDE two-link rigid–flexible manipulator. *Journal of the Franklin Institute*, 354(1):277–297, 2017. ISSN 00160032. doi: 10.1016/j.jfranklin.2016.10.013.

[27] Zhijie Liu and Jinkun Liu. Adaptive Iterative Learning Boundary Control of a Flexible Manipulator with Guaranteed Transient Performance. *Asian Journal of Control*, 20(3):1027–1038, 2018. ISSN 19346093. doi: 10.1002/asjc.1379.

[28] J Dong, B He, M Ma, C Zhang, and G Li. Open-Closed-Loop PD Iterative Learning Control Corrected With the Angular Relationship of Output Vectors for a Flexible Manipulator. *IEEE Access*, 7:167815–167822, 2019. ISSN 2169-3536. doi: 10.1109/ACCESS.2019.2930559.

[29] Y Yang, Z Liu, and G Ma. Adaptive Distributed Control of a Flexible Manipulator Using an Iterative Learning Scheme. *IEEE Access*, 7:145934–145943, 2019. ISSN 2169-3536. doi: 10.1109/ACCESS.2019.2946018.

[30] T Chen, M Li, and J Shan. Iterative learning control of a flexible manipulator considering uncertain parameters and unknown repetitive disturbance. In *2019 American Control Conference (ACC)*, pages 2209–2214, jul 2019. doi: 10.23919/ACC.2019.8815014.

[31] Tingting Meng and Wei He. *ILC for a Flexible Single-Link Manipulator*, pages 109–128. Springer Singapore, Singapore, 2020. ISBN 978-981-15-2784-5. doi: 10.1007/978-981-15-2784-5_5.

[32] Esmail Ali Alandoli, Tian Soon Lee, Y J Lin, and V Vijayakumar. Dynamic model and intelligent optimal controller of flexible link manipulator system with payload uncertainty. *Arabian Journal for Science and Engineering*, 46(8): 7423–7433, 2021. doi: 10.1007/s13369-021-05436-7.

[33] M Osman Tokhi and Abul K M Azad. *Flexible robot manipulators: modelling, simulation and control*, volume 68. Iet, 2008.

[34] A De Luca, L Lanari, P Lucibello, S Panzieri, and G Ulivi. Control experiments on a two-link robot with a flexible forearm. In *29th IEEE Conference on Decision and Control*, pages 520–527 vol.2, 1990. doi: 10.1109/CDC.1990.203651.

[35] Alessandro De Luca and Bruno Siciliano. Closed-Form Dynamic Model of Planar Multilink Lightweight Robots. *IEEE Transactions on Systems, Man and Cybernetics*, 21(4):826–839, 1991. ISSN 21682909. doi: 10.1109/21.108300.

[36] Franklyn Gerardo Duarte Vera. *Modeling and sliding-mode control of flexible-link robotic structures for vibration suppression.* PhD thesis, Clausthal University of Technology, Clausthal, nov 2016. URL `https://dokumente.ub.tu-clausthal.de/servlets/MCRFileNodeServlet/clausthal_derivate_00000188/Db112913.pdf`.

[37] Xuping Zhang, James K Mills, and William L Cleghorn. Dynamic Modeling and Experimental Validation of a 3-PRR Parallel Manipulator with Flexible Intermediate Links. *Journal of Intelligent and Robotic Systems*, 50(4):323–340, 2007. ISSN 1573-0409. doi: 10.1007/s10846-007-9167-4.

[38] H. N. Rahimi and M. Nazemizadeh. Dynamic analysis and intelligent control techniques for flexible manipulators: A review. *Advanced Robotics*, 28(2):63–76, 2014. ISSN 01691864. doi: 10.1080/01691864.2013.839079.

[39] K. Lochan, B. K. Roy, and B. Subudhi. A review on two-link flexible manipulators. *Annual Reviews in Control*, 42:346–367, 2016. ISSN 13675788. doi: 10.1016/j.arcontrol.2016.09.019.

[40] W J Book. Modeling, design, and control of flexible manipulator arms: a tutorial review. In *29th IEEE Conference on Decision and Control*, pages 500–506 vol.2, dec 1990. doi: 10.1109/CDC.1990.203648.

[41] Thomas R Kurfess. *Robotics and automation handbook.* CRC press, 1st editio edition, 2005. doi: 10.1201/9781315220352.

[42] Rex J. Theodore and Ashitava Ghosal. Comparison of the Assumed Modes and Finite Element Models for Flexible Multilink Manipulators. *The International Journal of Robotics Research*, 14(2):91–111, 1995. ISSN 17413176. doi: 10.1177/027836499501400201.

[43] P Koutsovasilis and M Beitelschmidt. Comparison of model reduction techniques for large mechanical systems. *Multibody System Dynamics*, 20(2):111–128, 2008. doi: 10.1007/s11044-008-9116-4.

[44] Renato Vidoni, Lorenzo Scalera, Alessandro Gasparetto, and Marco Giovagnoni. Comparison of model order reduction techniques for flexible multibody dynamics using an equivalent rigid-link system approach. In *Proceedings of the 8th EC-COMAS Thematic Conference on Multibody Dynamics, Prague, Czech Republic*, pages 19–22, 2017.

[45] L Wu, Paolo Tiso, and F van Keulen. A modal derivatives enhanced Craig-Bampton method for geometrically nonlinear structural dynamics. In *Proceedings of ISMA*, pages 3615–3624, 2016.

[46] R Krauss. An Improved Approach for Spatial Discretization of Transfer Matrix Models of Flexible Structures. In *2019 American Control Conference (ACC)*, pages 3123–3128, jul 2019. doi: 10.23919/ACC.2019.8814650.

[47] Umesh Kumar Sahu, Arun Mishra, Biswajeet Sahu, Prateek Priyaranjan Pradhan, Dipti Patra, and Bidyadhar Subudhi. Vision-Based Tip Position Control of a Single-Link Robot Manipulator. *SSRN Electronic Journal*, pages 1416–1422, 2019. doi: 10.2139/ssrn.3356203.

[48] N Singh and S Rajendran. Integral Fast Output Sampling control for Flexible Link Manipulators with LMI approach. In *2016 IEEE 1st International Conference on Power Electronics, Intelligent Control and Energy Systems (ICPEICES)*, pages 1–6, jul 2016. doi: 10.1109/ICPEICES.2016.7853698.

[49] Santanu Kumar Pradhan and Bidyadhar Subudhi. Position control of a flexible manipulator using a new nonlinear self-Tuning PID controller. *IEEE/CAA Journal of Automatica Sinica*, 7(1):136–149, 2020. ISSN 23299274. doi: 10.1109/JAS.2017.7510871.

[50] Kshetrimayum Lochan and Binoy Krishna Roy. Second-order SMC for tip trajectory tracking and tip deflection suppression of an AMM modelled nonlinear TLFM. *International Journal of Dynamics and Control*, 6(3):1310–1318, 2018. ISSN 21952698. doi: 10.1007/s40435-017-0371-1.

[51] Y Si, J Pu, and L Sun. A fast terminal sliding mode control of two-link flexible manipulators for trajectory tracking. In *2017 Chinese Automation Congress (CAC)*, pages 6387–6391, oct 2017. doi: 10.1109/CAC.2017.8243928.

[52] G Huan and W Q Xian. Observer based tracking control of flexible manipulator. In *2017 2nd International Conference on Advanced Robotics and Mechatronics (ICARM)*, pages 662–666, aug 2017. doi: 10.1109/ICARM.2017.8273241.

[53] Kshetrimayum Lochan, Jay Prakash Singh, and Binoy Krishna Roy. *Tracking control and deflection suppression of an AMM modelled TLFM using backstepping based adaptive SMC technique*, volume 581. Springer Singapore, 2020. ISBN 9789811394188. doi: 10.1007/978-981-13-9419-5_4.

[54] Mule Pala Prasad Reddy and Jeevamma Jacob. Vibration control of flexible link manipulator using SDRE controller and Kalman filtering. *Studies in Informatics and Control*, 26(2):143–150, 2017. ISSN 1841429X. doi: 10.24846/v26i2y201702.

[55] Ji Wang, Yangjun Pi, Yumei Hu, Zhencai Zhu, and Lingbin Zeng. Adaptive simultaneous motion and vibration control for a multi flexible-link mechanism

with uncertain general harmonic disturbance. *Journal of Sound and Vibration*, 408:60–72, 2017. ISSN 10958568. doi: 10.1016/j.jsv.2017.07.024.

[56] Xuping Zhang and Yue Qing Yu. Motion control of flexible robot manipulators via optimizing redundant configurations. *Mechanism and Machine Theory*, 36(7): 883–892, 2001. ISSN 0094114X. doi: 10.1016/S0094-114X(01)00020-9.

[57] Lianfang Tian, Jun Wang, and Zongyuan Mao. Constrained motion control of flexible robot manipulators based on recurrent neural networks. *IEEE Transactions on Systems, Man, and Cybernetics, Part B (Cybernetics)*, 34(3):1541–1552, 2004. doi: 10.1109/TSMCB.2004.826400.

[58] Gerasimos Rigatos and Krishna Busawon. *Flexible-Link Robots*, pages 271–300. Springer International Publishing, Cham, 2018. ISBN 978-3-319-77851-8. doi: 10.1007/978-3-319-77851-8_5.

[59] Ali Bazaei and Mehrdad Moallem. Improving force control bandwidth of flexible-link arms through output redefinition. *IEEE/ASME Transactions on Mechatronics*, 16(2):380–386, 2010. ISSN 10834435. doi: 10.1109/TMECH.2010.2046332.

[60] F Matsuno and K Yamamoto. Dynamic hybrid position/force control of a flexible manipulator. In *[1993] Proceedings IEEE International Conference on Robotics and Automation*, pages 462–467 vol.2, may 1993. doi: 10.1109/ROBOT.1993.291914.

[61] Baigeng Wang, Shurong Li, and Zhe Liu. Robust Adaptive Position/Force Control for Flexible-Link with Flexible-Joint Manipulator. In *Proceedings of the 11th International Conference on Modelling, Identification and Control (ICMIC2019)*, pages 1215–1227, Singapore, 2020. Springer Singapore. ISBN 978-981-15-0474-7. doi: 10.1007/978-981-15-0474-7_114.

[62] V K Singh and J Ohri. Simultaneous control of position and vibration of flexible link manipulator by nature-inspired algorithms. In *2018 IEEE 8th Power India International Conference (PIICON)*, pages 1–6, dec 2018. doi: 10.1109/POWERI.2018.8704403.

[63] O. A. Garcia-Perez, G. Silva-Navarro, and J. F. Peza-Solis. Flexible-link robots with combined trajectory tracking and vibration control. *Applied Mathematical Modelling*, 70:285–298, 2019. ISSN 0307904X. doi: 10.1016/j.apm.2019.01.035.

[64] Hebertt Sira-Ramírez, Alberto Luviano-Juárez, Mario Ramírez-Neria, and Eric William Zurita-Bustamante. Chapter 4 - Extensions of ADRC. In *Active*

Disturbance Rejection Control of Dynamic Systems, pages 109–172. Butterworth-Heinemann, 2017. ISBN 978-0-12-849868-2. doi: 10.1016/B978-0-12-849868-2.00004-6.

[65] B. Siciliano. Task space control. In *Theory of Robot Control*, pages 115–139. Springer London, 1996. ISBN 978-1-4471-1501-4. doi: 10.1007/978-1-4471-1501-4_3.

[66] Jingguo Wang, Yangmin Li, and Xinhua Zhao. Inverse kinematics and control of a 7-DOF redundant manipulator based on the closed-loop Algorithm. *International Journal of Advanced Robotic Systems*, 7(4):1–9, 2010. ISSN 17298814. doi: 10.5772/10495.

[67] Fabrizio Flacco, Alessandro De Luca, and Oussama Khatib. Control of Redundant Robots under Hard Joint Constraints: Saturation in the Null Space. *IEEE Transactions on Robotics*, 31(3):637–654, 2015. ISSN 15523098. doi: 10.1109/TRO.2015.2418582.

[68] A. Nedungadi and K. Kazerouinian. A Local Solution with Global Characteristics for the Joint Torque Optimization of a Redundant Manipulator. *Advanced Robotics: 1989*, 6(5):559–591, 1989. doi: 10.1007/978-3-642-83957-3_39.

[69] M Kirćanski and M Vukobratović. *Trajectory Planning for Redundant Manipulators in the Presence of Obstacles*, pages 57–63. Springer US, Boston, MA, 1985. ISBN 978-1-4615-9882-4. doi: 10.1007/978-1-4615-9882-4_6.

[70] Charles W Wampler. Manipulator Inverse Kinematic Solutions Based on Vector Formulations and Damped Least-Squares Methods. *IEEE Transactions on Systems, Man, and Cybernetics*, 16(1):93–101, 1986. doi: 10.1109/TSMC.1986.289285.

[71] C. Y. Chung, B. H. Lee, M. S. Kim, and C. W. Lee. Torque optimizing control with singularity-robustness for kinematically redundant robots. *Journal of Intelligent and Robotic Systems: Theory and Applications*, 28(3):231–258, 2000. ISSN 09210296. doi: 10.1023/A:1008152705719.

[72] John M. Hollerbach and Ki C. Suh. Redundancy resolution of manipulators through torque optimization. In *Proceedings - IEEE International Conference on Robotics and Automation*, pages 1016–1021, 1985. ISBN 0818606150. doi: 10.1109/ROBOT.1985.1087285.

Paper A

Review on Modeling and Control of Flexible Link Manipulators

Dipendra Subedi, Ilya Tyapin and Geir Hovland

This paper has been published as:

Dipendra Subedi, Ilya Tyapin and Geir Hovland. Review on Modeling and Control of Flexible Link Manipulators. *Modeling, Information and Control*, 41(3):141–163, 2020. doi: 10.4173/mic.2020.3.2.

Review on Modeling and Control of Flexible Link Manipulators

Dipendra Subedi, Ilya Tyapin and Geir Hovland

Department of Engineering Sciences
University of Agder
4879 Grimstad, Norway

Abstract **This paper presents a review of dynamic modeling techniques and various control schemes to control flexible link manipulators (FLMs) that were studied in recent literature. The advantages and complexities associated with the FLMs are discussed briefly. A survey of the reported studies is carried out based on the method used for modeling link flexibility and obtaining equations of motion of the FLMs. The control techniques are reviewed by classifying them into two main categories: model-based and model-free control schemes. The merits and limitations of different modeling and control methods are highlighted.**

A.1 Introduction

Link flexibility is present in manipulators because of two main reasons: the use of lightweight material and the long or slender design. It introduces static and dynamic deflections of the link and end-effector. Neglecting link flexibility in modeling and control of robots causes static and dynamic errors while carrying out any task. The static error includes a steady-state error, and dynamic errors include vibration and tracking error. These errors result in the degradation of the overall performance of the FLMs. From the control point of view, mechanical flexibility introduces an additional problem of non-collocation between the input commands and typical outputs to be controlled. So, it is crucial to consider link flexibility during modeling and control design of FLMs.

Major advantages of FLMs over rigid, bulky robots (designed with highly stiff materials) include, but are not limited to, low cost, smaller actuators, reduced energy consumption, high payload-to-robot-weight ratio, high operational speed, better transportability, and safer operation [1]. Because of these underlying advantages, the research interest in FLMs has increased significantly in recent years. FLMs can be used in many engineering applications for performing different robotic operations such as space research [2–4], construction automation [5], offshore applications (wind farm,

sea farm, fish farm, autonomous mooring), aerospace industry, robotic surgery [6, 7], and applications that require physical interaction [8] and human-robot collaboration.

In contrast to the rigid industrial robot, it is not possible to control the precise position and orientation of the end-effector of the FLMs to perform manipulation tasks using only the rigid body kinematic information and joint encoder readings. This is because link flexibility causes deflection of the links and unwanted oscillations, which causes problems in the precise position control of the end-effector and may even lead to an unstable system. To control the vibration of the FLMs, additional sensors like vision sensors, IMUs, are usually added to the FLMs control architecture to provide vibration measurement of the flexible links or the end-effector.

For achieving minimum oscillations and good position accuracy, the industrial robots are designed with highly stiff materials (like heavy steel with bulky design), which consequently require expensive high-power drives. However, the vibration of the end-effector at high speed and high load is still present due to industrial robot joint elasticity. In this context, lightweight flexible manipulators are better (cheaper) alternatives if the control architecture is designed to reduce the vibration of the end-effector to an acceptable range (depending on the application).

The nonlinear dynamics of the system with an infinite number of degrees of freedom make control of FLMs more complicated than the conventional industrial robots. In order to develop an efficient model-based control algorithms for the FLMs, it is necessary to construct a mathematical model of the system incorporating flexibility of the links. On the one hand, it is impractical to model the flexible link with infinite degrees of freedom for dynamic analysis and simulations, but on the other hand, it is challenging to describe the system with a finite degree of freedom and still being able to represent all the dynamically relevant flexibility effects. Nevertheless, the actual system behavior should be represented by a dynamically accurate and computationally affordable mathematical model to design a suitable (model-based) control algorithm. When designing an FLM, it is important to obtain dynamic features that avoid complex vibration modes, which will make it difficult to control the FLM. Therefore, modeling is essential for the model-based design of FLMs for optimal control performance. In general, additional generalized coordinates are introduced to describe flexibility in addition to the coordinates that are used to describe the rigid motion of the manipulator in a Lagrangian formulation. Because of the additional generalized coordinates, the FLMs have fewer actuators than the number of degrees of freedom. As a result of this type of under-actuation, it is more difficult to design suitable laws to control FLMs than to control rigid arm manipulator. Lochan et al. [9] described additional complexities involved in the flexible manipulator, including the problem of controller/observer spillover due to model truncation.

The study of modeling, control, and sensor systems for the application of FLMs are of on-going interest for researchers worldwide. With the recent advancement in technology and the emergence of newer robot applications, researchers are focusing on the accurate dynamic modeling of the FLMs, controlling and applying them into different applications.

Because of a huge number of research publications in FLMs, it is interesting to present an exhaustive review of different modeling techniques, dynamic models, control problems, control strategies, and complexities involved in FLMs that are studied by many researchers worldwide. Previously, the studies on FLMs were surveyed by Jing et al. [3], Sayahkarajy et al. [10], Alandoli et al. [11], Lochan et al. [9], Kiang et al. [1], Hussein [12], Rahimi and Nazemizadeh [13], Dwivedy and Eberhard [14], and Benosman and Le Vey [15].

Jing et al. [3] reviewed different dynamic stable control methods along with kinematic analysis of space flexible manipulators. The control strategies reviewed in the paper included linear feedback control, nonlinear control, and adaptive control. Furthermore, they pointed out several problems with modeling of dynamics and stable control of FLMs and presented some suggestions for the stable dynamic control. Sayahkarajy et al. [10] and Lochan et al. [9] surveyed different modeling methods and control schemes used for the two-link flexible manipulator. Alandoli et al. [11] presented a review of different mathematical modeling and control techniques for FLMs by grouping them based on the number of links: single-link, two-link, and multi-link manipulators. Kiang et al. [1] reviewed different modeling methods, control techniques, sensors used for FLMs, and flexible joint manipulators. Hussein [12] focused the survey on different vision-based control approaches for FLMs. Rahimi and Nazemizadeh [13] reported a literature survey on three commonly used dynamic modeling methods, namely lumped parameter, assumed model, and finite element methods, and three main intelligent control techniques, namely fuzzy logic, neural network, and genetic algorithm. Dwivedy and Eberhard [14] reviewed the literature related to dynamic analysis of flexible joint/link manipulators by classifying them based on modeling, control, and experimental studies. They further categorized papers based on the number of links (single-link, two-link, and multi-link manipulators) and method of analysis used in the studies (lumped parameter, assumed modes, finite element, and other methods). Benosman and Le Vey [15] surveyed different control strategies for one-link, two-link, and multi-link flexible manipulators based on the studies published until 2004.

Besides a lot of research done in the field of modeling and control of FLMs in recent years (from 2016 to present), a rigorous review of different modeling and control techniques is not available to report the current state of the art. This paper provides an extensive review of different modeling and control techniques for FLMs

available in literature up to 2020 and hence complements the earlier literature reviews. Besides, the merits and demerits of different modeling and control techniques are highlighted.

The paper is organized into four sections as follows. The various techniques for modeling FLMs, along with their advantages and disadvantages, are summarized in section A.2. A comprehensive review of different methods to control FLMs is presented in section A.3 by categorizing them into model-based and model-free techniques. Conclusions and discussions follow in section A.4, along with the suggestions on possible future directions for research on FLMs.

A.2 Modeling of FLMs

Some applications require the design of long and slender mechanical structures with infinite rigidity, which is always an ideal assumption. Such structures possess some degree of in-built flexibility, which is unavoidable because of the material used and length of the link. Moreover, in recent years, the use of lighter arms and cheaper gears by robot manufacturers is justifiable in order to compete with lower prices. In this context, it is necessary to incorporate the flexibility for accurate dynamic modeling of the system.

Apart from the complexities associated with modeling link flexibility with infinite degrees of freedom, there are other issues that are in common to rigid manipulators that need to be handled. One of them is Coulomb friction in actuators, gears, and other transmissions. Additionally, joint flexibility, non-linearities in gears as lost motion and backlash have to be included in the dynamic model of the FLM. This section emphasizes the research in modeling flexibility in the links of FLMs rather than general modeling issues in manipulators. A review of different methods commonly used to model flexible bodies and techniques to obtain equations of motion is presented.

A.2.1 Methods of dynamic modeling of flexible bodies

Different models of flexible bodies are available in the literature depending upon the assumptions and required complexity. The accuracy of the models depends on the assumptions made to simplify the complexity of the flexible link manipulator system. For example, the Euler-Bernoulli equation is often used to include bending of a flexible link that neglects the effects of shear deformation and rotary inertia, which results in an error in deflection estimation for high-frequency vibrations [16]. There are four main approaches that are commonly used in the literature: lumped parameter method (LPM), assumed modes method (AMM), finite element method

(FEM), and transfer matrix method (TMM). Apart from these common methods, there are other methods used for the development of the dynamic model of the FLMs which include, but are not limited to, perturbation method [17, 18], pseudo-rigid body method [19], global mode method [20], and modal integration method [21].

A.2.1.1 Lumped parameter method (LPM)

In this method, the flexible link is modeled as a set of mass, spring, and damper connected by a torsion spring joint [22]. Kim and Uchiyama [23] used this method to model FLM to clarify the vibration mechanism of a constrained, multi-DOF, flexible manipulator, and to devise the suppression method.

Recently, researchers used the LPM to model flexible arms of multi-link manipulators [24], the boom of a mobile concrete pump [25], and other flexible mechanical structures [26]. Lochan et al. [27] utilized LPM to model the dynamics of a two-link flexible manipulator. Sun et al. [28], Cambera and Feliu-Batlle [29], He et al. [30], and Cambera and Feliu-Batlle [31] modeled a single-link flexible manipulator system based on LPM. Pucher et al. [32, 33] described the elastic deflection of a 3-DOF robot with flexible links using LPM.

- Advantages
  (a) Simple method.
  (b) Easy implementation.
- Disadvantages
  (a) Less accurate [9].
  (b) Difficulty in determining spring constant (stiffness) [34].

A.2.1.2 Assumed modes method (AMM)

In AMM, the link flexibility is represented by a combination of separable mode shapes and time-varying generalized coordinates. The modal series is truncated to a finite dimension because the contribution of higher modes to the overall movement is negligible, and dynamics of the system are dominantly governed by only the first few (low frequency) modes [35]. This method is usually adopted when the global shape functions can be analytically computed, like in the case of links with simple geometries.

The proper choice of suitable boundary conditions must be made while using AMM. Rahimi and Nazemizadeh [13] and Lochan et al. [9] described four main boundary conditions that are applicable according to general beam vibration theories: pinned-pinned, clamped-pinned, clamped-free, and clamped-clamped. Ata et al. [36]

analyzed different combinations of boundary conditions and their effect on the elastic deflection and corresponding actuators' torques in a two-link FLM. If the inertia ratio of the lightweight link to the hub is small, the clamped (clamped-mass) boundary condition yields better results than pinned boundary conditions [37]. Clamped boundary conditions can be enforced by closing a feedback control loop around the joint [38]. Compatible joint variables and deflection variables and their corresponding shape functions must be selected [39]. If the joint angle is measured from the tangent of the preceding beam link to the tangent of the following beam link, clamped-free boundary conditions are a good choice for basis shapes, and if the angle between lines that connects successive joint axes of the arm is used as joint variables, pinned-pinned boundary conditions provide the necessary constraints and are good choices [40].

Effects of payload on the FLM modeled using AMM with clamped-mass boundary conditions were discussed by Ahmad et al. [41] and Moh. Khairudin [42]. Luca and Siciliano [38] used different payload conditions for modal analysis in a planar two-link FLM. Celentano and Coppola [43] proposed a computationally efficient method based on the AMM to model FLMs. Suarez et al. [8] used AMM to model a flexible link in a long-reach manipulator with a lightweight dual-arm. Gao et al. [44] used AMM to develop an n-dimensional discretized model of a two-link flexible manipulator where the dynamic behavior of the flexible link is derived from the Lagrangian and the Euler-Bernoulli beam theory. Saeed et al. [45] and Badfar and Abdollahi [46] modeled the dynamics of rigid-flexible manipulators using the AMM technique. Other recent works on single-link FLMs using AMM include, but are not limited to, the studies done by Ouyang et al. [47], Reddy and Jacob [48], Meng et al. [49], and Zhang et al. [50]. Furthermore, the AMM was used to model two-link FLMs by Lochan and Roy [51], Qiu et al. [52], and Lochan et al. [53].

- Advantages
  (a) The concept of natural frequencies is explicit.
  (b) A model derived with AMM is of low order that is advantageous for a control design [10].
- Disadvantages
  (a) In the AMM, it is difficult to calculate modes of the link with varying cross-sections [34].
  (b) The selection of an accurate set of boundary conditions (assumed modes) is challenging (error-prone) based on manipulator structure, payload, hub inertia, and natural modes of vibration [54].
  (c) The complexity of the model increases with the increase in the number of assumed modes [10].

A.2.1.3 Finite element method (FEM)

In FEM, the flexible link is modeled as a combination of finite number of elements, and the displacement at any point of the continuous element is expressed in terms of finite number of displacements at the nodal points multiplied by the polynomial interpolation functions [34]. Beres et al. [55] used Lagrange formulation, and Amirouche and Xie [56] developed a recursive formulation using Kane's equation to obtain the dynamic model of a multi-link flexible manipulator based on FEM. Zhang and Yu [57] modeled a spatial $4R$ manipulator with four flexible links using FEM. Korayem et al. [58] modeled planar two-link FLM using this method. Heidari et al. [59] proposed a nonlinear finite element model for the dynamic modeling of FLMs undergoing large deformations and tested the proposed approach in a single-link, very flexible arm. Recently, Singla and Singh [60] used FEM to model a two-link FLM where the elastic behavior of the link is modeled using Euler-Bernoulli Beam theory and Lagrange approach to derive equations of motion. Similarly, Sahu and Patra [61] used FEM to model a 2-DOF serial FLM. Furthermore, recent studies using FEM to obtain the mathematical model of single-link FLMs include the works by Tahir et al. [62], and Garcia-Perez et al. [63].

- Advantages
  (a) All the generalized coordinates are physically meaningful in FEM [9].
  (b) In FEM, the connection is supposed to be clamp-free with a minimum of two mode shapes per link [58].
  (c) Applicable for complex cross-sectional geometries [34].
  (d) FEM can handle nonlinear and mixed boundary conditions [35, 58].
  (e) Fewer mathematical operations are required for inertia matrix computation in the FEM model [34].
- Disadvantages
  (a) The use of FEM to approximate flexibility gives rise to an over-estimated stiffness matrix, which may lead to an unstable closed-loop response [34].
  (b) The FEM is computationally very expensive because of a large number of state-space equations [34, 54, 55].
  (c) The concept of natural frequency is not explicit [9].

A.2.1.4 Transfer matrix method (TMM)

In TMM, each element of the system is represented by a transfer matrix that transfers a state vector from one end of the element to the other, and the system transfer matrix

is obtained by multiplying the element transfer matrices together [64, 65]. Krauss and Book [64] developed Python software modules for modeling and control design of flexible robots using the TMM. Although the TMM can be used to model the FLMs without any spatial discretization or mode shape assumptions, it leads to infinite dimensional transfer functions involving transcendental expressions in the Laplace variable s and hence, it is limited to the linear system. It is impossible to compute inverse Laplace transform of the infinite dimensional transfer functions; therefore, it is difficult to perform the time domain simulations. This problem of traditional TMM is overcome by the discrete-time transfer matrix method (DT-TMM), allowing nonlinear systems to be analyzed and facilitating time-domain simulations Krauss and Okasha [66].

Li and Zhang [67] combined the discrete-time transfer matrix method with the finite segment method and proposed a computationally efficient method for the modeling of FLMs. Kivila et al. [68] elaborated a systematic method for finding natural frequencies and mode shapes for n-link spatial serial manipulators using TMM and validated the method by finite element analysis and experiments. An improved approach for spatial discretization of transfer matrix models of flexible structures was proposed by Krauss [69] for converting a TMM model to a state-space model for systems with significant actuator or zero dynamics. Apart from the capabilities of TMM in feedback control design using Bode plots, discretization approaches can be used to obtain a state-space form from a TMM model so that modern (state-space) control design techniques like pole-placement can be applied [69].

- Advantages

  (a) This approach avoids the possibility of modal spillover because a reduced-order model is never used [70].

  (b) The TMM is well suited to modeling FLMs when the model is used for control design because it is a frequency domain technique that outputs Bode plots, which makes it easy to incorporate feedback [64].

  (c) The establishment of global dynamic equations for modeling a system is not needed [67].

  (d) The orders of the matrices involved in the calculation always remain small regardless of the number of elements in the model, which significantly increases the computational speed [67].

- Disadvantages

  (a) It makes no allowance for interaction between the gross motion and

the flexible dynamics of the manipulator, nor can these effects be easily included in the model [35].

A.2.2 Methods of deriving equations of motion

There are three common methods to derive the governing equations of motion of the FLMs, which have their own merits and demerits: Newton-Euler equations, Lagrange equations, and Kane's method. Kane and Levinson [71] presented the comparison of different methods for deriving the equations of motion. In addition to these commonly used methods, other techniques to obtain equations of motion of FLMs includes, but are not limited to, Hamilton's principle [5, 72–77] and Gibbs-Appell formulation [78].

A.2.2.1 Newton-Euler formulation

In this formalism, the dynamic equations are written separately for each body/link. Boyer and Glandais [79] used the Newton-Euler formulation for obtaining the dynamic model of a spatial four degrees of freedom flexible manipulator. Sabatini et al. [2] modeled multi-body dynamics of flexible space manipulator using the Newton-Euler approach. Subedi et al. [22] used the Newton-Euler technique with LPM to derive equations of motion for a flexible cantilever beam. Bascetta et al. [80] developed a closed-form model of three-dimensional flexible manipulator with links of general shape using the Newton-Euler formulation. Scaglioni et al. [81] used the Newton-Euler method to obtain a closed-form control-oriented model of the highly flexible manipulators.

- Advantages

  (a) Simple formulation because the equations of motion will always have the same form independently of the geometry, inertia, or constraints of motion of a rigid body [82].

  (b) Inverse dynamics is in real-time because the equations are evaluated in a numeric and recursive way.

  (c) It may be considered better than the Lagrangian method for the implementation of model-based control schemes because the equations can be implemented by numerical programming methods.

- Disadvantages

  (a) Workless constraint forces or torques must be determined, which is difficult when the system is composed of many bodies [82].

A.2.2.2 Lagrange formulation

The Lagrange method eliminates interaction forces between adjacent links and provides a systematic method for developing the equations of motion of the entire system. In this formalism, the symbolic closed-form equations are obtained directly. Ahmad et al. [41], Moh. Khairudin [42], Abe [16], Celentano and Coppola [43], Ouyang et al. [47], Ouyang et al. [47], Reddy and Jacob [48], Meng et al. [49], Sun et al. [83], Badfar and Abdollahi [46], Lochan et al. [84], Qiu et al. [52], Qiu and Zhang [85], Saeed et al. [45], Pradhan and Subudhi [86], and Boucetta et al. [87] used the Lagrange formulation for obtaining the mathematical model of the FLMs with AMM.

Other recent studies using the Lagrange method for deriving equations of motion of the FLMs includes, but are not limited to, Singh and Rajendran [88], Si et al. [89], Dong et al. [90], Mehria and Foruzantabarb [91], Singla and Singh [60], and Agrawal et al. [92].

- Advantages
  (a) Eliminates workless constraint forces to obtain constraint-free differential equations [82].
  (b) It may be considered better than the Newton-Euler method for the study of dynamic properties and analysis of control schemes because the closed-form symbolic equations are obtained directly.
- Disadvantages
  (a) Complicated derivatives of Lagrangians (energy functions), which often results in complex formulation [71].
  (b) Lengthy equations.
  (c) Computationally inefficient [93].

A.2.2.3 Kane's method

Concepts of generalized speeds, angular velocities, and partial velocities are the key elements of Kane's method [94]. The equations of motion derived from Kane's method are superior (simpler form and requires a minimum of labor to derive) to Lagrange's equations for the formulation of equations governing modal coordinates [71].

Buffinton [95] used AMM and an alternative form of Kane's method to formulate the equations of motion of a two-degree-of-freedom manipulator (like Stanford Arm) with a translational flexible beam. Amirouche and Xie [56] derived equations of

motion of a two-link robot manipulator with a rigid link and a flexible link based on Kane's equation and the general matrix representation of the partial velocities and partial angular velocities. They used a recursive formulation based on FEM. Meghdari and Fahimi [96] used Kane's method in conjunction with improved assumed modes technique to obtain first-order decoupled equations of motion of the two-link flexible manipulator in conjunction with choosing a proper congruency transformation between derivatives of generalized coordinates and generalized speeds. Zhang and Zhou [97] used Kane's method to derive the equations of motion of the flexible robots and showed the effects of flexibility on the dynamics of the robot with two flexible links and one rigid link connected by three flexible joints. They used AMM to describe the deformation of the flexible links.

Recently, Ren et al. [98] used Kane's method to establish the dynamic equations of motion of a two-link manipulator with two flexible joints/flexible links. Jia et al. [99] used Kane's method to derive the coupled dynamics of the multi-link flexible system(with two flexible links and two rigid links) and a singular perturbation approach to decouple the dynamics of the whole system into a fast subsystem and a slow subsystem. Additionally, other relevant studies using Kane's method for modeling FLMs includes Malvezzi et al. [82], Bian et al. [100], and Bian and Gao [101].

- Advantages

  (a) Kane's method leads to simpler equations of motion [40].

  (b) Differentiation scalar energy function is not required [71].

  (c) Computationally efficient [40].

  (d) Eliminates constraints forces that ultimately do not contribute to the equations of motion to obtain constraint-free differential equations [40, 82].

  (e) It can be used for solving the dynamics of robots containing closed-chains without cutting the closed-chain open [102].

  (f) It allows the use of motion variables (generalized speeds) that permit the selection of these variables as not only individual time-derivatives of the generalized coordinates but any convenient linear combinations of them [40].

- Disadvantages

  (a) It is necessary to calculate the acceleration of the center of mass of each body (in the Lagrangian formulation, it is only necessary to calculate only the velocities of the center of mass of each body).

A.2.3 Modeling FLMs undergoing small, moderate, and large deflections

Link flexibility in FLMs can be modeled assuming either small, moderate, or large deflections. Most of the standard dynamic modeling approaches for FLM assume small deflections in general. This can be a reasonable assumption for most of the robotic applications but can be violated in some applications which require high accelerations, velocities, tip forces, and torques. Some studies consider moderate and large deformations to overcome the limitations of assuming small deflection. Luca and Siciliano [38] used the Lagrangian approach with AMM to derive the closed-form equations of motion for multi-link planar FLM under small deflection assumption where the links are modeled as Euler-Bernoulli beams with proper clamped-mass boundary conditions. Boyer and Glandais [79] proposed the dynamic model of FLMs derived using the Newton-Euler method premised on an exact nonlinear Euler-Bernoulli field that can model moderate deformations or some second-order effects which appears in some limit cases as high velocities, accelerations, or tip forces and torques. Abe [16], Heidari et al. [59], Celentano [103], Giorgio and Del Vescovo [24], Esfandiar et al. [104], and Scaglioni et al. [81] developed the dynamic model of FLMs under the hypothesis of large link deformations.

A.2.4 Partial differential equation (PDE) vs. ordinary differential equation (ODE) models

The majority of the works done in FLMs rely on ODE models, which are derived by either LPM, AMM, or FEM. The finite dimensional ODE approximation of the PDE dynamic model is not precise enough to describe the distributed states of the FLMs, specifically because the FLMs are linear PDE models inherently [105]. Conventional control techniques can be used with finite dimensional ODE models [106]. Although the ODE models are simple for control design and analysis, they may cause problems such as spillover instability, a high order of controllers, and difficulty in engineering implementation [107].

To avoid the problems associated with ODE models, the PDE dynamic models are studied, which are derived without any truncation of vibration modes and are precise enough to describe the distributed states. Commonly, Hamilton's principle is used to derive governing equations of the FLMs modeled using PDE.

The resulting PDE models are infinite dimensional avoiding spillover errors and the errors caused due to mode shape truncation and simplification of the boundary conditions [106]. In the case of the rigid-flexible manipulator, coupled ODEs-PDEs can be used to obtain the dynamic model of the system [108].

However, the control design using PDE models is more challenging compared to ODE models [109, 110], and accurate simulation of a nonlinear PDE is itself a very complex problem [73].

Zhang et al. [106] compared typical PDE and ODE models for the two-link flexible manipulators. Although, the PDE modeling and control strategies require design insights for simplifications and are theoretically involving, it is claimed that the PDE models are much more attractive from the stability and robust control design perspectives with guaranteed stability properties [106]. Zhang et al. [109] derived a PDE model for a two-link flexible manipulator, and experimental hardware setup was used to validate the analytical PDE model. Recently, Dogan and Morgül [73], Zhang and Liu [111], Zhang and Liu [107], Zhang and Liu [112], Zhang and Liu [113], Yang et al. [105], Jiang et al. [114], Liu et al. [110], Liu et al. [115], Yang et al. [74], Yang and Tan [75], Zhang et al. [116], Cao and Liu [117], Yang et al. [76], Li et al. [118], Cao and Liu [5], and Meng and He [77] used PDE models for relevant studies of FLMs.

A.3 Control of FLMs

Although the FLMs have many advantages for their use in a wide range of applications, the problem of control for damping out oscillations quickly and effectively is challenging. The control complexities associated with FLMs include, but are not limited to, non-minimum phase in the system, non-collocation, and under-actuation [9]. Moreover, some of the complexities like controller/observer spillover arise because of the choice of the dynamic model of the FLMs. If a finite dimensional representation of a distributed parameter system (i.e., FLMs) is used (based on LPM, AMM, or FEM) to design the control system, some of the unmodeled dynamics present in the dynamic model of the system cause control and observation spillover. This may lead to an unstable closed-loop system. Thus, it is necessary to consider the complexities associated with the control of the FLMs while carrying out mathematical modeling of the system. Nevertheless, a model-free robust controller can be used to avoid controller/observer spillover problem caused due to model truncation [14]. In addition to vibrations due to link flexibility, there are other problems such as friction, backlash, and gear non-linearities that should be addressed by the control algorithm designed for FLMs.

One of the critical steps in the controller design is the tuning of the control parameters. Global controller tuning for the whole workspace and for different loads is challenging in both model-based and model-free controllers. Moreover, model parameters may need tuning, even if model identification has been made. Different methods for tuning FLM controller gains include the Ziegler-Nichols method

[92, 119], LMI approach [119], dynamic particle swarm optimization method [92], self-tuning method using the artificial neural network [120], self-tuning method based on nonlinear autoregressive moving average with exogenous-input (NARMAX) model of the FLM [86], soft computing based tuning method [121], and self-tuning method based on generalized minimum variance [52]. Compared to the standard Ziegler-Nichols tuning method, the recent self-tuning methods have shown superior performance in the control of FLMs [92].

Main control problems that are studied in the literature for FLMs are categorized as follows [9]:

(a) Tip position control [88, 122]

(b) Joint position control [86]

(c) Tip trajectory tracking control [51]

(d) Joint trajectory tracking control [53, 89, 123]

(e) Vibration control [48]

(f) Motion control [57, 124, 125]

(g) Force control [126, 127]

(h) Hybrid control (position and force [128, 129], position and vibration [121], trajectory tracking and vibration [63], and other combinations).

There are various control schemes reported in the literature, depending on the control problems. Jing et al. [3] presented a state-of-the-art review on kinematic analysis and dynamic stable control of space flexible manipulators and pointed out existing problems and suggestions on dynamic stable control. Lochan et al. [9] surveyed different control schemes for joint position control, tip position control, joint trajectory tracking control, and tip trajectory tracking control problems for the two-link flexible manipulators. The control schemes reported are categorized into classical control, robust control, intelligent control, and hybrid control techniques. Alandoli et al. [11] presented different control methods for regulating the motion and suppressing the vibration of single-link, two-link, and multi-link flexible manipulators. The review showed the effectiveness of model predictive control with/without piezoelectric actuators, a combination of the robust nonlinear and fuzzy compensator, linear quadratic regulator, and fuzzy logic controllers for the control and vibration suppression of FLMs. Sayahkarajy et al. [10] reviewed different control techniques for FLMs, including classical linear control, optimum control, inversion-based control, command shaping techniques, trajectory optimization, force

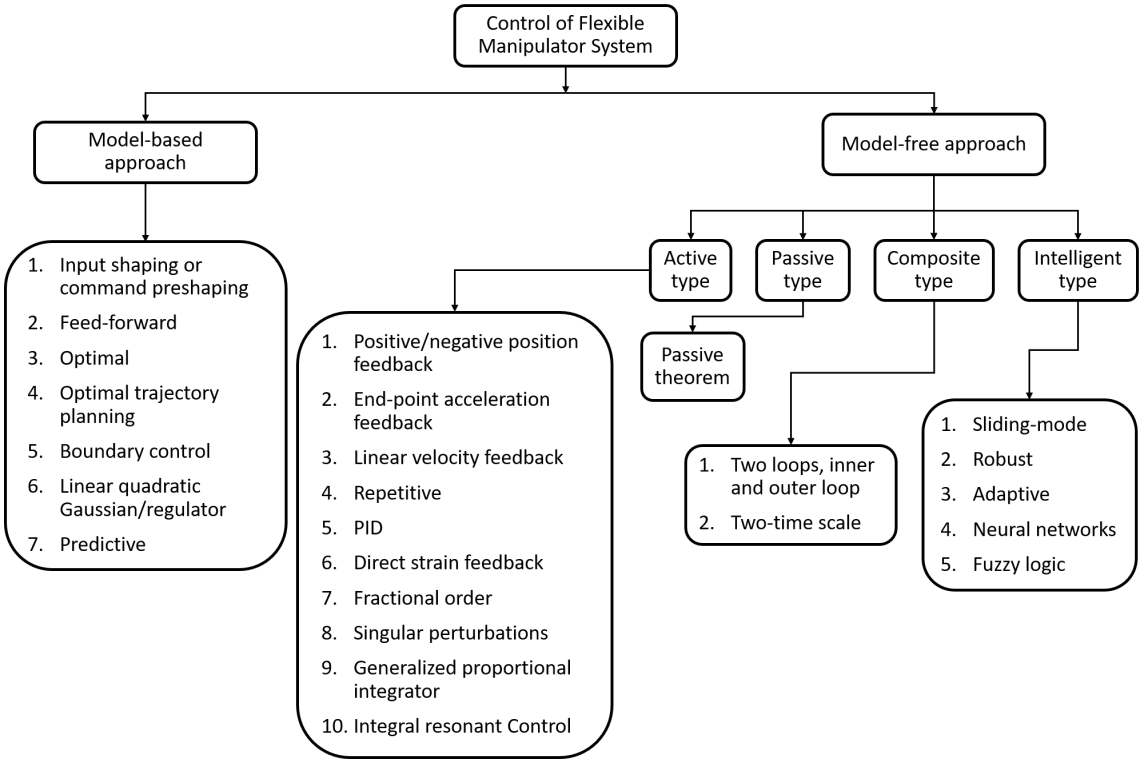

Figure A.1: Control schemes

control, intelligent control techniques (using fuzzy logic, neural networks, and genetic algorithm), and robust control. Kiang et al. [1] summarized the advantages and disadvantages associated with different control techniques used for FLMs, which are represented diagrammatically in figure A.1. Closed-loop control of the flexible manipulator system requires some forms of feedback signals to apply any suitable control strategies. The feedback control signals for the flexible manipulator system could include, but are not limited to, tip's acceleration, tip displacement, and strain along the link. Different sensors used in the control of flexible manipulators are reviewed in [1], which include strain gauges, accelerometer, vision systems (cameras), position-sensitive devices, piezoelectric materials, ultrasonic sensor, and range sensors. Hussein [12] reviewed different approaches of flexible robot control using visual servoing along with their advantages, disadvantages, and comparisons. Rahimi and Nazemizadeh [13] reported a review of different intelligent control techniques of flexible manipulators by categorizing them into fuzzy logic, neural network, and genetic algorithm approaches and pointed out that intelligent control strategies, which do not need a priori knowledge of system dynamics, may provide a better way to approach control of FLMs. Benosman and Le Vey [15] presented a survey study of different control methods used for FLMs including PD control, input-output linearization via static state feedback-the computed torque, adaptive control, neural network based control, lead-lag control, output redefinition, singular perturbations, sliding mode control, stable inversion in the frequency domain, stable inversion in

the time domain, algebraic control, poles placement, optimal trajectory planning, optimal control, robust control, mechanical wave approach, input shaping, boundary control, and exact linearization via dynamical state feedback.

The purpose of this section is to present the review of different control schemes for the control of FLMs that are published recently (mostly from 2016 to 2019). The control techniques are divided into two main categories: model-based control and model-free control.

A.3.1 Model-based control techniques

In model-based control, we use the system's dynamic model explicitly to aid in the controller design. The mathematical model is applied to calculate the controller response required to obtain the explicitly specified desired output response. Model-based control techniques (see figure A.1) include input/command shaping control, feed-forward control, optimal control, optimal trajectory planning, boundary control, linear quadratic gaussian/regulator, predictive control, and (state) observer-based control [1].

Since the controller is derived using the dynamic model of the system, the parameters of the model should closely match the real system to achieve good control performance. The parameters of the FLM model are obtained by best fit to measurements made during the excitation of the real robot or even a more accurate model of the robot (for example, the FEM design model). Excitation is usually made in the same frequency range as it will be used for the control of the FLM. Most of the model-based controller proposed in the literature use system identification techniques to determine precise model parameters. Then the identified parameters are used to design the controller. Krauss [70] used an optimization algorithm to find values for the FLM system parameters that minimize the error between the experimental Bode plots and those from symbolic TMM analysis. Mohamed et al. [119] performed system identification to obtain a set of linear models of a two-link flexible manipulator. Lou et al. [130] proposed a reduced-order transfer function with relocated zeros and added a first-order inertia element to the model to precisely identify the system model. Ripamonti et al. [131] identified model parameters using the Prony method and a minimization of the error between the numerical and experimental frequency response function (FRF) in the frequency domain. Cambera and Feliu-Batlle [29] identified the parameters of the motor subsystem using the velocity-time response of the motor, and that of the flexible link subsystem using the frequency response of the system. Comi et al. [4] and Subedi et al. [22] used experimental measurements to identify lumped parameters of the flexible manipulators. Qiu and Zhang [85] identified the locally controlled autoregressive moving average (CARMA) model of

the flexible manipulator through experiments. Pradhan and Subudhi [86] used a recursive least square (RLS) algorithm to identify the parameters of the nonlinear autoregressive moving average with exogenous-input (NARMAX) model of the FLM on-line. It can be noted that the model parameters of the FLM can be identified online and offline. However, the main limitation of system identification is that some of the phenomena of the original plant cannot be deduced from the input-output relationship [132].

Input shaping is one of the traditional and effective vibration control techniques for flexible mechanical systems with known dynamic characteristics. However, it is an open-loop strategy. Therefore, the input shaping method is combined with other feedback controllers to overcome its problem of open-loop nature. Newman and Vaughan [133] presented a concurrent design of linear feedback control with input shaping for the energy-efficient point-to-point motion of a two-link flexible manipulator while minimizing command-induced vibration. Mehria and Foruzantabarb [91] proposed a closed-loop input-shaping control technique based on the linear matrix inequality method to solve the problem of open-loop input shaping control. Tahir et al. [62] designed output based filter and incorporated it with linear quadratic regulator and PID controller separately for the position and residual vibration control of single-link flexible manipulator and highlighted the superior performance of linear quadratic regulator over PID controller in tracking, vibration suppression, and robustness to payload variation. Ju et al. [134] combined the state feedback control with the input shaping technique for vibration control of translational flexible manipulator under variable load conditions. Giorgio and Del Vescovo [24] studied trajectory tracking and vibration control of the highly flexible planar multi-link flexible manipulator using an optimal input pre-shaping approach and feedback from the joint angles to make the system less sensitive to external disturbances.

Many classical feedback control techniques have been explored for the active vibration suppression of FLMs. Lou et al. [130] presented experimental identification and multi-mode vibration suppression of a flexible manipulator with piezoelectric actuators and strain sensors using optimal multi-poles placement control technique. Badfar and Abdollahi [46] used a linear matrix inequality approach to address trajectory tracking control of two-link rigid-flexible manipulator based on linear state-space model and linear quadratic regulator. Singh and Rajendran [88] proposed an integral fast output sampling control for FLMs with the LMI approach and compared the performance of the proposed method with an observer-based discrete-time state feedback strategy.

Ghasemi [135] proposed a filtered feedback linearization controller for the simultaneous positioning and vibration suppression of a single-link flexible manipulator that requires limited model information, specifically, knowledge of the vector re-

lative degree, and knowledge of the dynamic-inversion matrix. Additionally, the filtered feedback linearization controller was combined with a high-gain adaptive law for robust control and addressed the problem of model uncertainty. Cambera and Feliu-Batlle [29] and Cambera and Feliu-Batlle [31] studied the input state feedback linearization controller for the tip positioning and vibration suppression of a single-link flexible link arm with and without gravity compensation, respectively. They implemented the controller into a double loop cascade control scheme, in which the inner loop is for joint position control in the presence of friction disturbances, and the outer loop is for trajectory tracking and vibration suppression of the end-effector.

Njeri et al. [132] proposed a filtered inverse controller for the suppression of link vibration in a multi-link flexible manipulator. Saeed et al. [45] presented model-based nonlinear control of the planar two-link rigid-flexible manipulator based on the full state model of the system. Abe [16] proposed an optimal trajectory planning technique based on particle swarm optimization algorithm for suppressing residual vibrations in two-link rigid-flexible manipulators. Zhang and Liu [112] proposed the optimal trajectory boundary control of the two-link flexible manipulator based on the PDE model. Cao and Liu [136] studied the optimal trajectory control problem for the trajectory tracking and vibration suppression of a two-link rigid-flexible manipulator based on the ODE-PDE model of the system.

Some control strategies, like input-output control, need all of the states' feedback. But, in FLMs, measuring all the flexural states is practically impossible. To overcome this problem, Mosayebi et al. [137] proposed input-output control of FLM based on a nonlinear high gain observer to estimate the elastic degrees of freedom and their time derivatives. Reddy and Jacob [48] proposed the Kalman filter based state-dependent Riccati equation controller for accurate positioning and vibration suppression of the FLM. Ripamonti et al. [131] presented model-based sliding mode control for vibration suppression of a three-link flexible manipulator using the linear and nonlinear sliding surface. They used a nonlinear state-space observer from the identified modal model of the FLM for sliding mode control.

Zhang and Liu [107] proposed observer-based boundary control for end-effector regulation, vibration suppression, and trajectory tracking of a two-link flexible manipulator in task space. The proposed method relies on the accurate dynamic model of the FLM. Liu and He [138] presented boundary control for the one-link flexible manipulator using singular perturbation techniques that includes a position controller and a direct feedback controller to suppress the vibration. Cao and Liu [117] proposed a controller with input quantization based on the PDE model of a two-link rigid-flexible manipulator for joint angle control and vibration suppression.

Li et al. [118] studied unknown control direction problem of the FLMs based on the PDE model and proposed boundary control for angle tracing and vibration elimination

of the single-link flexible manipulator and adopted the Nussbaum technique in the controller design to circumvent the problem of uncertain control directions. To deal with the parametric uncertainties, varying payloads, and disturbances, adaptive and robust boundary control techniques are proposed [139, 140]. Jiang et al. [141] proposed a boundary controller for the FLM based on the PDE robust observer to achieve the stability control, regulate the joint position, and suppress elastic vibration. He et al. [142] designed the boundary controller with input backlash and the output feedback controller based on the PDE model to drive the FLM to the desired position, suppress its vibrations, eliminate the effects of the backlash nonlinearity and the time-varying disturbance. They further illustrated that the FLM system was better stable under the controller with output feedback. Cao and Liu [108] designed a boundary controller for a two-link rigid-flexible manipulator with full state constraints via Barrier Lyapunov Function.

The combination of input shaping and feedback control was used to formulate a new control approach called wave-based control, where the launch wave being a simple, shaped input, and the absorb part the feedback contribution [143]. Yanan et al. [19] proposed the wave-based control method to solve the problem of residual vibration in the point-to-point movement of a two-link flexible space manipulator. They claimed that the wave-based control has many advantages, such as not dependent on an accurate physical model, simple and easy to implement, and strong robustness. Comi et al. [4] combined the wave-based control technique to the P/PI scheme (a cascade joint controller with an inner loop on the motor velocity and an outer loop on the load position) for vibration suppression of flexible manipulator and highlighted the superior performance of the velocity-based implementation of the wave-based controller with respect to the position-based one. Bian and Gao [101] and Bian et al. [100] proposed vibration control of FLMs based on internal resonance.

- Advantages

  (a) Using robot dynamic models, better motion control (faster settling time and better trajectory following) can be achieved.

  (b) In some cases (using feed-forward control), model-based control eliminates the need for the feedback sensors (e.g., force sensor), thereby reducing cost and simplifying system design.

  (c) Robot paths are optimized using dynamic modeling.

  (d) Enhanced robot behavior and drive performance are achieved because the paths are highly optimized by calculating the torque required to reach different positions using model-based algorithms.

(e) The mathematical model of the FLMs may be used for the model-based safety systems, for example, fast collision detection. Hence, the use of the model in more than control applications makes it advantageous from a product point of view to use model-based control methods instead of completely model-free methods.

- Disadvantages

(a) They rely on the accurate model of the FLM system to be controlled, which is difficult and challenging to obtain. However, the model of the FLM system may be needed for design, identification, and collision detection.

(b) The control input (designed for open-loop model-based control) does not account for changes in the system, like varying payload. However, it could be possible to change parameters accurately, for example, payload and load inertia to obtain a seamless motion after gripping an object. The payload parameters are known or can be identified by the robot. This functionality is implemented in industrial robots for several years.

(c) Open-loop model-based control is not robust to parameter uncertainties and disturbances. However, it could be handled by online servos and model parameter control, which is used for industrial robots today.

(d) They require the solution of a numerical optimization problem, which can be a daunting task, especially when nonlinear models are needed that lead to non-convex problems. However, this problem is less significant if the calculations can be performed offline [144].

A.3.2 Model-free control techniques

Model-free control is a technique to control complex systems by using a simplified representation of the system and subsequent algebraic estimation techniques to design a simple, but effective, controller [145]. The controller does not rely on the precise mathematical model of the system but solely based on the measurements obtained from the system. Recently, there is a trend of using the combination of different control techniques to achieve better control performances than using individual control methods. Model-free control techniques (see figure A.1) include, but are not limited to, robust control, adaptive control, sliding mode control, intelligent control methods, composite control (inner/outer loop control, two-time scale control), PID control, singular perturbations technique, integral resonant control, generalized proportional integrator control, fractional order control, direct strain feedback control, repetitive control, passivity-based control, positive/negative position feedback control, end-point acceleration feedback control, and linear velocity feedback control [1].

Mohamed et al. [119] proposed a robust PD controller based on linear matrix inequality for joint position control of the two-link flexible manipulator under various payload conditions. They claimed that the proposed control provided better robustness and system performance compared to Ziegler-Nichols tuned PD controller. Cao and Liu [146] studied the actuator fault problem for a two-link rigid-flexible manipulator system and designed a novel controller that included a PD feedback structure, a disturbance observer, and a fault-tolerant algorithm for joint position regulation and vibration suppression in the presence of disturbance and actuator fault. Abd Latip et al. [147] designed an adaptive PID controller for the joint position and tracking control of a single-link flexible manipulator, which may automatically online tune the control gains to accommodate the actuator fault. Boucetta et al. [87] compared PD, fuzzy PD, and fractional order fuzzy PD controllers in terms of trajectory tracking, vibration suppression, robustness against disturbances, and energy consumption to control the rigid-flexible two-link manipulator. They highlighted that the fractional order fuzzy PD controller performed better than other controllers. Agrawal et al. [92] compared a modified optimal PIDD^2 (proportional, integral, derivative, and second-order derivative) controller with the PID controller for controlling the position and trajectory of the single-link flexible manipulator with minimum tip oscillation. They reported the superior performance of the PIDD^2 controller through simulation. Singh and Ohri [121] presented a comparative study of different nature-inspired soft computing based PID control tuning strategies, including genetic algorithm, ant colony optimization, and particle swarm optimization for the position and vibration control of a single-link flexible manipulator. Pradhan and Subudhi [86] proposed a nonlinear self-tuning PID controller to control the joint position and link deflection of the FLM subjected to varying payloads.

Fareh et al. [148] presented robust active disturbance rejection control for FLM to solve joint trajectories tracking control problem and minimize the link's vibrations. Xu et al. [149] proposed a second order non-singular terminal sliding mode optimal control technique for a two-link flexible manipulator with uncertain model parameters. Lochan et al. [27] and Lochan and Roy [51] used the sliding mode control technique with the PID sliding surface and the second-order sliding surface respectively, to control a two-link flexible manipulator. Yang and Tan [75] designed a sliding mode control for joint position control and vibration suppression of a single-link flexible manipulator by using an adaptive neural approximator to compensate for the modeling uncertainties and external disturbances. Si et al. [89] proposed a fast non-singular terminal sliding mode control for trajectory tracking of the two-link flexible manipulators with payload and external disturbances. Backstepping control based on a continuous-time extended state observer and a sampled-data extended state observer was proposed by Sahu and Patra [61] and Sahu et al. [150], respectively,

to solve tip tracking control problem of two-link flexible manipulator. Wang et al. [151] proposed an adaptive fault-tolerant controller using the backstepping technique for a flexible manipulator with bounded disturbance, actuator partial failure, and output constraints.

Huan and Xian [123] presented a backstepping control method for trajectory tracking of the two-link flexible manipulator based on extended state observer, which estimates the uncertainties as well as the system state vector. Zhao et al. [152] studied the disturbance observer-based boundary control to achieve the vibration control, disturbance attenuation, and desired angular positioning of the FLM. Liu and Liu [153] proposed boundary control of the FLM with input disturbances and output constraints using disturbance observer to regulate the angular position and suppress elastic vibration simultaneously. Liu et al. [110] proposed disturbance observer-based boundary control for trajectory tracking and vibration suppression of a single-link flexible manipulator with the input saturation and external input disturbances. They used smooth hyperbolic function for handling input saturation. Liu et al. [115] proposed boundary control with disturbance observers to solve the trajectory tracking and the vibration suppression control problems of the FLMs in $3D$ space. Yang et al. [74] proposed infinite dimensional disturbance observer-based control to solve the problems of distributed disturbances and output constraints while achieving the joint position regulation and vibration suppression.

He et al. [154] studied the problems of input and output constraints and designed a robust adaptive boundary controller with the disturbance observer for the control of single-link flexible manipulator with unknown system parameters and time-varying disturbances. Cao and Liu [5] studied joint angle control and vibration suppression control of a two-link rigid-flexible manipulator in $3D$ space under input saturation using the hyperbolic tangent function.

Neural network models can be used to approximate the underlying dynamics of the FLMs to overcome the difficulty of obtaining the accurate dynamic formulation of the manipulator[125]. Gao et al. [44] investigated full-state and output feedback neural network controllers for a two-link flexible manipulator based on a radial basis function neural network to achieve trajectory tracking and vibration suppression. They claimed that the proposed adaptive neural network controller had better performance than the PD controller. Ouyang et al. [47] proposed a reinforcement learning control to suppress the vibration of a single-link flexible manipulator by using two radial basis function neural networks: actor neural network to design proper control input and critic neural network to approximate the cost function of the system. Sun et al. [28] used adaptive neural networks for control design using full-state feedback and output feedback separately to suppress the vibration of single-link flexible manipulator and highlighted better control performance than the PD control

strategy. However, input nonlinearities were not considered in the control design. Sun et al. [83] investigated fuzzy neural network control for trajectory tracking and vibration suppression of single-link flexible manipulator and compared the control performance of the proposed technique with the PD control. He et al. [30] designed the adaptive full state feedback neural network controller and the adaptive output feedback neural network controller to suppress the vibration of a single-link flexible manipulator with input deadzone. Radial basis function neural networks are used to approximate the effect of input deadzone and unknown dynamics of the FLM. Qiu and Zhang [85] proposed a diagonal recurrent neural network control technique for the vibration control of the single-link flexible manipulator using non-contact vibration measurement based on structure light sensor. They also proposed a trajectory optimization technique to obtain optimal vibration suppression trajectory using the particle swarm optimization algorithm. Qiu et al. [52] presented experimental studies on active vibration control of a two-link flexible manipulator by employing three control algorithms: generalized minimum variance self-tuning control, Takagi-Sugeno model-based fuzzy neural network control, and PD control. Furthermore, they evaluated the effectiveness of the first two controllers as compared to that of the PD control in terms of vibration suppression. Zhang et al. [116] designed a weighted multiple neural network boundary controller for joint position tracking and vibration suppression of a single-link flexible manipulator with uncertain parameters. Njeri et al. [120] presented a self-tuning strain feedback gain controller for high-speed vibration control of a $3D$ two-link flexible manipulator using the artificial neural network and highlighted that the tuned gains achieved better performance than that achieved by using fixed gain in terms of link strain and joint trajectories.

Cao and Liu [155] proposed an adaptive boundary iterative learning control scheme with a PD feedback structure for the joint trajectory tracking and vibration suppression of a two-link rigid-flexible manipulator with parametric uncertainties and external disturbances. Liu and Liu [156] investigated the adaptive iterative learning control scheme for joint position tracking and vibration suppression of a single-link flexible manipulator in the presence of external disturbance and output constraints. Dong et al. [90] proposed iterative learning control combined with an open-closed-loop PD scheme for trajectory tracking of a single-link flexible manipulator even in the presence of disturbances and uncertainties. In the proposed method, an angular correction term was introduced to achieve self-adjustment of the iterative learning control law by using angular relationships of the system output vectors. Yang et al. [76] proposed adaptive distributed iterative learning control by combining a PD feedback structure and an iterative term for simultaneous trajectory tracking and vibration suppression of a single-link flexible manipulator subjected to system parameters uncertainties and spatio-temporal distributed disturbances. Chen et al.

[157] presented iterative learning control for simultaneous trajectory tracking and vibration suppression of a single-link flexible manipulator with uncertain parameters and unknown repetitive disturbances. Meng and He [77] addressed the problem of the trajectory tracking control of rigid hub and vibration suppression of the flexible link simultaneously for a single-link flexible manipulator by using iterative learning control law.

Meng et al. [49] designed a fast, stable control technique based on system energy for a planar single-link flexible manipulator for joint position control and vibration suppression. Moreover, they proposed an online optimization method based on fuzzy-genetic algorithm to optimize the controller design parameter and improve the performance of the system. Zhang et al. [50] designed a nonlinear controller based on energy analysis for joint position control and vibration suppression control of the single-link flexible manipulator.

Yang et al. [158] studied the problems of tip position regulation and vibration suppression of FLM using model-free composite control based on adaptive dynamic programming. Jia et al. [99] proposed a composite control strategy for a flexible space manipulator as a combination of an adaptive sliding mode controller for the slow subsystem and an adaptive controller for the fast subsystem. Lochan et al. [84] designed a composite controller using contraction theory, which consists of two separate controllers designed for the slow-subsystem and fast subsystem for fast trajectory tracking and quick vibration suppression of a two-link flexible manipulator. Xu [159] investigated the singular perturbation theory based composite learning control of FLM using neural networks and disturbance observer. Sliding mode control was used for the fast dynamics and intelligent control based on neural network, and disturbance observer was used for the slow dynamics.

- Advantages

  (a) An accurate mathematical model of the system is not required, which is complex and difficult to obtain.

  (b) Simpler and easier to implement than model-based approaches.

  (c) Adaptive controllers deal with the correct adjustment of the control parameters online in order to incorporate the effect of disturbances and model uncertainties [140].

  (d) Active disturbance rejection control technique has an excellent disturbance rejection capability [148].

- Disadvantages

  (a) There is a problem of input delay in the feedback loop because the estimations of the system states are calculated based on the sensor reading.

(b) Pure sensor-based approaches will not be able to act in advance, which is potentially possible with a model-based approach and feed-forward control.

A.4 Conclusion

This paper presented a survey of different modeling and control techniques for flexible manipulators. In recent years, the PDE models have gained increasing popularity because of the underlying advantages of infinite dimensional models that avoid spillover and model truncation errors. The review of the recent literature shows that limited research has been carried out in the modeling and control of FLMs undergoing large deflection. Because of the difficulty in obtaining the accurate dynamic model of the FLMs, model-free control methods are used more often than the model-based controllers. Moreover, model-free controllers are popular because of their robustness to parameter uncertainty and disturbances in FLMs. On the contrary, only a few model-free methods (for example, PID control and iterative learning control) are used to control industrial robots. Other model-free methods may need additional attention to solve the problem of low dynamic accuracy and/or unstable control because of the non-collocated system.

In order to solve the problem of individual controllers, there is a trend of combining two or more control techniques to achieve better control performance than using individual control techniques. A recent boost in computing power and the emergence of machine learning algorithms has enabled scientists to apply intelligent control techniques or combine learning-based control approaches with other methods to control FLMs. It is visible that a lot of recent control techniques proposed in the literature are based on neural networks and other learning-based algorithms. This literature review on the state-of-the-art modeling and control techniques of FLMs reveals that most of the studies are limited to planar single-link and two-link flexible manipulators. More research studies are required for the modeling and control of multi-link flexible manipulators undergoing general $3D$ motion. Benchmarking and understanding the merits and limitations of the recent modeling and control methods is required to use them in the FLM (product) development. This is challenging without the development of suitable benchmark tests.

In spite of the fact that significant advancements have been made in many aspects of FLMs over the last few decades, there are many issues yet to be resolved, and simple, robust, reliable, and effective controls of FLMs still remain a challenge. Undoubtedly, further research efforts in this area would contribute significantly to the development of lightweight flexible manipulators for space research and long reach manipulators for offshore industries to perform different robotic operations safely. The mooring

operation could be executed autonomously by mounting long-reach arm/s on a floating vessel/ship. Cleaning, repair, and maintenance operations in offshore wind farms and sea farms could be carried out autonomously or semi-autonomously with the reduction of oscillations in the long-reach arm. Furthermore, the construction industry can utilize the long-reach manipulator for material handling and assembly tasks. Application-oriented studies on FLMs could be one of the possible future directions of research.

Acknowledgments

The work was partially funded by the Research Council of Norway through the centre SFI Offshore Mechatronics, project 237896.

References – Paper A

[1] Chang Tai Kiang, Andrew Spowage, and Chan Kuan Yoong. Review of Control and Sensor System of Flexible Manipulator. *Journal of Intelligent and Robotic Systems: Theory and Applications*, 77(1):187–213, 2015. ISSN 15730409. doi: 10.1007/s10846-014-0071-4.

[2] Marco Sabatini, Paolo Gasbarri, Riccardo Monti, and Giovanni Battista Palmerini. Vibration control of a flexible space manipulator during on orbit operations. *Acta Astronautica*, 73:109–121, 2012. ISSN 00945765. doi: 10.1016/j.actaastro.2011.11.012.

[3] Zhongliang Jing, Qimin Xu, and Jianzhe Huang. A review on kinematic analysis and dynamic stable control of space flexible manipulators. *Aerospace Systems*, 2 (1):1–14, 2019. ISSN 2523-3947. doi: 10.1007/s42401-018-00024-4.

[4] Fabio Comi, Aitor Orive Miguel, Francesco Cavenago, Gianni Ferretti, Gianantonio Magnani, and Andrea Rusconi. Modelling, validation and control of DELIAN flexible manipulator. *IFAC-PapersOnLine*, 52(15):364–369, 2019. ISSN 24058963. doi: 10.1016/j.ifacol.2019.11.702.

[5] Fangfei Cao and Jinkun Liu. Three-dimensional modeling and input saturation control for a two-link flexible manipulator based on infinite dimensional model. *Journal of the Franklin Institute*, 357(2):1026–1042, 2020. ISSN 00160032. doi: 10.1016/j.jfranklin.2019.10.018.

[6] Zheng Li, Jan Feiling, Hongliang Ren, and Haoyong Yu. A Novel Tele-Operated Flexible Robot Targeted for Minimally Invasive Robotic Surgery. *Engineering*, 1(1):073–078, 2015. ISSN 20958099. doi: 10.15302/J-ENG-2015011.

[7] Mark Runciman, Ara Darzi, and George P Mylonas. Soft Robotics in Minimally Invasive Surgery. *Soft Robotics*, 6(4):423–443, 2019. doi: 10.1089/soro.2018.0136.

[8] A Suarez, A M Giordano, K Kondak, G Heredia, and A Ollero. Flexible link long reach manipulator with lightweight dual arm: Soft-collision detection, reaction, and obstacle localization. In *2018 IEEE International*

Conference on Soft Robotics (RoboSoft), pages 406–411, apr 2018. doi: 10.1109/ROBOSOFT.2018.8404953.

[9] K. Lochan, B. K. Roy, and B. Subudhi. A review on two-link flexible manipulators. *Annual Reviews in Control*, 42:346–367, 2016. ISSN 13675788. doi: 10.1016/j.arcontrol.2016.09.019.

[10] Mostafa Sayahkarajy, Z. Mohamed, and Ahmad Athif Mohd Faudzi. Review of modelling and control of flexible-link manipulators. *Proceedings of the Institution of Mechanical Engineers. Part I: Journal of Systems and Control Engineering*, 230(8):861–873, 2016. ISSN 20413041. doi: 10.1177/0959651816642099.

[11] Esmail Ali Alandoli, Marizan Sulaiman, M. Z.A. Rashid, H. N.M. Shah, and Z. Ismail. A review study on flexible link manipulators. *Journal of Telecommunication, Electronic and Computer Engineering*, 8(2):93–97, 2016. ISSN 22898131.

[12] M. T. Hussein. A review on vision-based control of flexible manipulators. *Advanced Robotics*, 29(24):1575–1585, 2015. ISSN 15685535. doi: 10.1080/01691864.2015.1078743.

[13] H. N. Rahimi and M. Nazemizadeh. Dynamic analysis and intelligent control techniques for flexible manipulators: A review. *Advanced Robotics*, 28(2):63–76, 2014. ISSN 01691864. doi: 10.1080/01691864.2013.839079.

[14] Santosha Kumar Dwivedy and Peter Eberhard. Dynamic analysis of flexible manipulators, a literature review. *Mechanism and Machine Theory*, 41(7): 749–777, 2006. ISSN 0094114X. doi: 10.1016/j.mechmachtheory.2006.01.014.

[15] M. Benosman and G. Le Vey. Control of flexible manipulators: A survey. *Robotica*, 22(5):533–545, 2004. ISSN 02635747. doi: 10.1017/S0263574703005642.

[16] Akira Abe. Trajectory planning for residual vibration suppression of a two-link rigid-flexible manipulator considering large deformation. *Mechanism and Machine Theory*, 44(9):1627–1639, 2009. ISSN 0094114X. doi: 10.1016/j.mechmachtheory.2009.01.009.

[17] S. Esmaeilzadeh Khadem and Ali Akbar Pirmohammadi. Analytical development of dynamic equations of motion for a three-dimensional flexible link manipulator with revolute and prismatic joints. *IEEE Transactions on Systems, Man, and Cybernetics, Part B: Cybernetics*, 33(2):237–249, 2003. ISSN 10834419. doi: 10.1109/TSMCB.2003.810439.

[18] J. B. Jonker and R. G.K.M. Aarts. A Perturbation Method for Dynamic Analysis and Simulation of Flexible Manipulators. *Multibody System Dynamics*, 6(3): 245–266, 2001. ISSN 13845640. doi: 10.1023/A:1012070525137.

[19] Li Yanan, Meng Deshan, Liu Houde, W. Xueqian, and Liang Bin. Modeling and control of a two-link flexible space manipulator using the wave-based method. *Proceedings of the 29th Chinese Control and Decision Conference, CCDC 2017*, 0:512–519, 2017. doi: 10.1109/CCDC.2017.7978148.

[20] Jin Wei, Dengqing Cao, Lun Liu, and Wenhu Huang. Global mode method for dynamic modeling of a flexible-link flexible-joint manipulator with tip mass. *Applied Mathematical Modelling*, 48:787–805, 2017. ISSN 0307904X. doi: 10.1016/j.apm.2017.02.025.

[21] R. G.K.M. Aarts and J. B. Jonker. Dynamic simulation of planar flexible link manipulators using adaptive modal integration. *Multibody System Dynamics*, 7 (1):31–50, 2002. ISSN 13845640. doi: 10.1023/A:1015271000518.

[22] Dipendra Subedi, Ilya Tyapin, and Geir Hovland. Modeling and Analysis of Flexible Bodies Using Lumped Parameter Method. *2020 IEEE 11th International Conference on Mechanical and Intelligent Manufacturing Technologies (ICMIMT)*, pages 161–166, 2020. doi: 10.1109/icmimt49010.2020.9041188.

[23] Jin Soo Kim and Masaru Uchiyama. Vibration mechanism of constrained spatial flexible manipulators. *JSME International Journal, Series C: Mechanical Systems, Machine Elements and Manufacturing*, 46(1):123–128, 2003. ISSN 13447653. doi: 10.1299/jsmec.46.123.

[24] Ivan Giorgio and Dionisio D. Del Vescovo. Non-linear lumped-parameter modeling of planar multi-link manipulators with highly flexible arms. *Robotics*, 7(4): 1–13, 2018. ISSN 22186581. doi: 10.3390/robotics7040060.

[25] Julian Wanner and Oliver Sawodny. A lumped parameter model of the boom of a mobile concrete pump. *2019 18th European Control Conference, ECC 2019*, pages 2808–2813, 2019. doi: 10.23919/ECC.2019.8796004.

[26] Carmine Maria Pappalardo and Domenico Guida. Development of a new inertial-based vibration absorber for the active vibration control of flexible structures. *Engineering Letters*, 26(3):372–385, 2018. ISSN 18160948.

[27] K. Lochan, B. K. Roy, and B. Subudhi. SMC controlled chaotic trajectory tracking of two-link flexible manipulator with PID sliding surface. *IFAC-PapersOnLine*, 49(1):219–224, 2016. ISSN 24058963. doi: 10.1016/j.ifacol.2016.03.056.

[28] Changyin Sun, Wei He, and Jie Hong. Neural Network Control of a Flexible Robotic Manipulator Using the Lumped Spring-Mass Model. *IEEE Transactions on Systems, Man, and Cybernetics: Systems*, 47(8):1863–1874, 2016. ISSN 21682232. doi: 10.1109/TSMC.2016.2562506.

[29] Juan Carlos Cambera and Vicente Feliu-Batlle. Input-state feedback linearization control of a single-link flexible robot arm moving under gravity and joint friction. *Robotics and Autonomous Systems*, 88:24–36, 2017. ISSN 09218890. doi: 10.1016/j.robot.2016.11.019.

[30] Wei He, Xiuyu He, and Changyin Sun. Vibration Control of an Industrial Moving Strip in the Presence of Input Deadzone. *IEEE Transactions on Industrial Electronics*, 64(6):4680–4689, 2017. ISSN 02780046. doi: 10.1109/TIE.2017.2674592.

[31] Juan Carlos Cambera and Vicente Feliu-Batlle. Feedback Linearizing Controller for a Single Link Flexible Arm with a Passive Gravity Compensation Mechanism. *IEEE International Conference on Intelligent Robots and Systems*, pages 6404–6410, 2018. ISSN 21530866. doi: 10.1109/IROS.2018.8594409.

[32] Florian Pucher, Hubert Gattringer, and Andreas Müller. Collision detection for flexible link robots using accelerometers. *IFAC-PapersOnLine*, 52(16):514–519, 2019. ISSN 24058963. doi: 10.1016/j.ifacol.2019.12.013.

[33] Florian Pucher, Hubert Gattringer, and Andreas Müller. Investigation of the Behavior of Vibration-Damped Flexible Link Robots in End-Effector Contact: Simulation and Experiment. In *Multibody Dynamics 2019*, pages 139–146, Cham, 2020. Springer International Publishing. ISBN 978-3-030-23132-3.

[34] Rex J. Theodore and Ashitava Ghosal. Comparison of the Assumed Modes and Finite Element Models for Flexible Multilink Manipulators. *The International Journal of Robotics Research*, 14(2):91–111, 1995. ISSN 17413176. doi: 10.1177/027836499501400201.

[35] M Osman Tokhi and Abul K M Azad. *Flexible robot manipulators: modelling, simulation and control*, volume 68. Iet, 2008.

[36] Atef A. Ata, Waleed F. Fares, and Mohamed Y. Sa'Adeh. Dynamic analysis of a two-link flexible manipulator subject to different sets of conditions. *Procedia Engineering*, 41(Iris):1253–1260, 2012. ISSN 18777058. doi: 10.1016/j.proeng.2012.07.308.

[37] E Barbieri and U Ozguner. Unconstrained and Constrained Mode Expansions for a Flexible Slewing Link. In *1988 American Control Conference*, pages 83–88, jun 1988. doi: 10.23919/ACC.1988.4789697.

[38] Alessandro De Luca and Bruno Siciliano. Closed-Form Dynamic Model of Planar Multilink Lightweight Robots. *IEEE Transactions on Systems, Man and Cybernetics*, 21(4):826–839, 1991. ISSN 21682909. doi: 10.1109/21.108300.

[39] W J Book. Modeling, design, and control of flexible manipulator arms: a tutorial review. In *29th IEEE Conference on Decision and Control*, pages 500–506 vol.2, dec 1990. doi: 10.1109/CDC.1990.203648.

[40] Thomas R Kurfess. *Robotics and automation handbook*. CRC press, 2018.

[41] M. A. Ahmad, Z. Mohamed, and N. Hambali. Dynamic modelling of a two-link flexible manipulator system incorporating payload. *2008 3rd IEEE Conference on Industrial Electronics and Applications, ICIEA 2008*, pages 96–101, 2008. doi: 10.1109/ICIEA.2008.4582487.

[42] Moh. Khairudin Moh. Khairudin. Dynamic Modelling of a Flexible Link Manipulator Robot Using Amm. *TELKOMNIKA (Telecommunication Computing Electronics and Control)*, 6(3):185, 2008. ISSN 1693-6930. doi: 10.12928/telkomnika.v6i3.566.

[43] Laura Celentano and Alessandro Coppola. A computationally efficient method for modeling flexible robots based on the assumed modes method. *Applied Mathematics and Computation*, 218(8):4483–4493, 2011. ISSN 00963003. doi: 10.1016/j.amc.2011.10.029.

[44] Hejia Gao, Wei He, Chen Zhou, and Changyin Sun. Neural Network Control of a Two-Link Flexible Robotic Manipulator Using Assumed Mode Method. *IEEE Transactions on Industrial Informatics*, 15(2):755–765, 2018. ISSN 15513203. doi: 10.1109/TII.2018.2818120.

[45] Anjum Saeed, Fahad Mumtaz Malik, Hameed Ullah, Zeeshan Ali Akbar, and Naveed Mazhar. Model-Based Control of Planar Rigid-Flexible Manipulator. In *2019 IEEE 7th Conference on Systems, Process and Control (ICSPC)*, number December, pages 122–126. IEEE, 2019. ISBN 9781728118260.

[46] Ehsan Badfar and Rohollah Abdollahi. Trajectory tracking of rigid-flexible manipulator based on LMI optimization approach. *EEA - Electrotehnica, Electronica, Automatica*, 67(2):62–67, 2019. ISSN 2392828X.

[47] Yuncheng Ouyang, Wei He, and Xiajing Li. Reinforcement learning control of a singlelink flexible robotic manipulator. *IET Control Theory and Applications*, 11(9):1426–1433, 2017. ISSN 17518652. doi: 10.1049/iet-cta.2016.1540.

[48] Mule Pala Prasad Reddy and Jeevamma Jacob. Vibration control of flexible link manipulator using SDRE controller and Kalman filtering. *Studies in Informatics and Control*, 26(2):143–150, 2017. ISSN 1841429X. doi: 10.24846/v26i2y201702.

[49] Qing Xin Meng, Xu Zhi Lai, Ya Wu Wang, and Min Wu. A fast stable control strategy based on system energy for a planar single-link flexible manipulator. *Nonlinear Dynamics*, 94(1):615–626, 2018. ISSN 1573269X. doi: 10.1007/s11071-018-4380-1.

[50] Chenglin Zhang, Tong Yang, Ning Sun, and Jianyi Zhang. A Simple Control Method of Single-Link Flexible Manipulators. *3rd International Symposium on Autonomous Systems, ISAS 2019*, pages 300–304, 2019. doi: 10.1109/ISASS.2019.8757711.

[51] Kshetrimayum Lochan and Binoy Krishna Roy. Second-order SMC for tip trajectory tracking and tip deflection suppression of an AMM modelled nonlinear TLFM. *International Journal of Dynamics and Control*, 6(3):1310–1318, 2018. ISSN 21952698. doi: 10.1007/s40435-017-0371-1.

[52] Zhi-cheng Qiu, Cheng Li, and Xian min Zhang. Experimental study on active vibration control for a kind of two-link flexible manipulator. *Mechanical Systems and Signal Processing*, 118:623–644, 2019. ISSN 10961216. doi: 10.1016/j.ymssp.2018.09.001.

[53] Kshetrimayum Lochan, Jay Prakash Singh, and Binoy Krishna Roy. *Tracking control and deflection suppression of an AMM modelled TLFM using backstepping based adaptive SMC technique*, volume 581. Springer Singapore, 2020. ISBN 9789811394188. doi: 10.1007/978-981-13-9419-5_4.

[54] Moharam Habibnejad Korayem, H. N. Rahimi, and A. Nikoobin. Mathematical modeling and trajectory planning of mobile manipulators with flexible links and joints. *Applied Mathematical Modelling*, 36(7):3229–3244, 2012. ISSN 0307904X. doi: 10.1016/j.apm.2011.10.002.

[55] W. Beres, J. Z. Sasiadek, and G. Vukovich. Control and dynamic analysis of multilink flexible manipulator. *Proceedings - IEEE International Conference on Robotics and Automation*, 3:478–483, 1993. ISSN 10504729. doi: 10.1109/robot.1993.292218.

[56] F.M.L. Amirouche and M. Xie. An explicit matrix formulation of the dynamical equations for flexible multibody systems: A recursive approach. *Computers & Structures*, 46(2):311–321, jan 1993. ISSN 0045-7949. doi: 10.1016/0045-7949(93)90195-J.

[57] Xuping Zhang and Yue Qing Yu. Motion control of flexible robot manipulators via optimizing redundant configurations. *Mechanism and Machine Theory*, 36 (7):883–892, 2001. ISSN 0094114X. doi: 10.1016/S0094-114X(01)00020-9.

[58] M. H. Korayem, M. Haghpanahi, H. N. Rahimi, and A. Nikoobin. Finite element method and optimal control theory for path planning of elastic manipulators. *Studies in Computational Intelligence*, 199:117–126, 2009. ISSN 1860949X. doi: 10.1007/978-3-642-00909-9_12.

[59] H R Heidari, M H Korayem, M Haghpanahi, and V Feliu Batlle. A new nonlinear finite element model for the dynamic modeling of flexible link manipulators undergoing large deflections. In *2011 IEEE International Conference on Mechatronics*, pages 375–380, apr 2011. doi: 10.1109/ICMECH.2011.5971314.

[60] Ashish Singla and Amardeep Singh. Dynamic Modeling of Flexible Robotic Manipulators. In *Harmony Search and Nature Inspired Optimization Algorithms*, pages 819–834, Singapore, 2019. Springer Singapore. ISBN 978-981-13-0761-4.

[61] U K Sahu and D Patra. Observer based backstepping method for tip tracking control of 2-DOF Serial Flexible Link Manipulator. In *2016 IEEE Region 10 Conference (TENCON)*, pages 3563–3568, nov 2016. doi: 10.1109/TENCON.2016.7848721.

[62] Nura Musa Tahir, Sabo Miya Hassan, Zaharuddin Mohamed, and Ahmed Garba Ibrahim. Output based input shaping for optimal control of single link flexible manipulator. *International Journal on Smart Sensing and Intelligent Systems*, 10(2):367–386, 2017. ISSN 11785608. doi: 10.21307/ijssis-2017-216.

[63] O. A. Garcia-Perez, G. Silva-Navarro, and J. F. Peza-Solis. Flexible-link robots with combined trajectory tracking and vibration control. *Applied Mathematical Modelling*, 70:285–298, 2019. ISSN 0307904X. doi: 10.1016/j.apm.2019.01.035.

[64] R W Krauss and W J Book. A Python Module for Modeling and Control Design of Flexible Robots. *Computing in Science Engineering*, 9(3):41–45, may 2007. ISSN 1558-366X. doi: 10.1109/MCSE.2007.44.

[65] Alessandro De Luca and Wayne J Book. *Robots with Flexible Elements*, pages 243–282. Springer International Publishing, Cham, 2016. ISBN 978-3-319-32552-1. doi: 10.1007/978-3-319-32552-1_11.

[66] Ryan Krauss and Mohamed Okasha. Discrete-time transfer matrix modeling of flexible robots under feedback control. *Proceedings of the American Control Conference*, pages 4104–4109, 2013. ISSN 07431619. doi: 10.1109/acc.2013.6580469.

[67] Haijie Li and Xuping Zhang. A Method for Modeling Flexible Manipulators: Transfer Matrix Method with Finite Segments. *International Journal of Computer and Information Engineering*, 10(6):1086–1093, 2016.

[68] Arto Kivila, Wayne Book, and William Singhose. Exact Modeling of n-Link Spatial Serial Structures Using Transfer Matrices. *Journal of Dynamic Systems, Measurement, and Control*, 139(11), jun 2017. ISSN 0022-0434. doi: 10.1115/1.4036555.

[69] R Krauss. An Improved Approach for Spatial Discretization of Transfer Matrix Models of Flexible Structures. In *2019 American Control Conference (ACC)*, pages 3123–3128, jul 2019. doi: 10.23919/ACC.2019.8814650.

[70] Ryan W. Krauss. Computationally efficient modeling of flexible robots using the transfer matrix method. *JVC/Journal of Vibration and Control*, 18(5):596–608, 2012. ISSN 10775463. doi: 10.1177/1077546311408466.

[71] Thomas R Kane and David A Levinson. Formulation of Equations of Motion for Complex Spacecraft. *Journal of Guidance and Control*, 3(2):99–112, 1980. doi: 10.2514/3.55956.

[72] X Ding, T J Tarn, and A K Bejczy. A general dynamic model of flexible robot arms for control. In *Proceedings, 1989 International Conference on Robotics and Automation*, pages 1678–1683 vol.3, may 1989. doi: 10.1109/ROBOT.1989.100217.

[73] Mustafa Dogan and Ömer Morgül. On the control of two-link flexible robot arm with nonuniform cross section. *JVC/Journal of Vibration and Control*, 16(5): 619–646, 2010. ISSN 10775463. doi: 10.1177/1077546309340994.

[74] Hong Jun Yang, Jin Kun Liu, and Wei He. Distributed disturbance-observer-based vibration control for a flexible-link manipulator with output constraints. *Science China Technological Sciences*, 61(10):1528–1536, 2018. ISSN 1862281X. doi: 10.1007/s11431-017-9280-1.

[75] Hong-Jun Yang and Min Tan. Sliding Mode Control for Flexible-link Manipulators Based on Adaptive Neural Networks. *International Journal of Automation and Computing*, 15(2):239–248, 2018. ISSN 1751-8520. doi: 10.1007/s11633-018-1122-2.

[76] Y Yang, Z Liu, and G Ma. Adaptive Distributed Control of a Flexible Manipulator Using an Iterative Learning Scheme. *IEEE Access*, 7:145934–145943, 2019. ISSN 2169-3536. doi: 10.1109/ACCESS.2019.2946018.

[77] Tingting Meng and Wei He. *ILC for a Flexible Single-Link Manipulator*, pages 109–128. Springer Singapore, Singapore, 2020. ISBN 978-981-15-2784-5. doi: 10.1007/978-981-15-2784-5_5.

[78] M H Korayem and A M Shafei. Inverse dynamic equation of motion for flexible link manipulators using recursive gibbs-appell formulation. In *2007 IEEE International Conference on Robotics and Biomimetics (ROBIO)*, pages 2160–2165, dec 2007. doi: 10.1109/ROBIO.2007.4522504.

[79] F Boyer and N Glandais. Simulation of flexible manipulators with elastic nonlinearities. In *Proceedings 1999 IEEE International Conference on Robotics and Automation (Cat. No.99CH36288C)*, volume 1, pages 759–766 vol.1, may 1999. doi: 10.1109/ROBOT.1999.770066.

[80] L Bascetta, G Ferretti, and B Scaglioni. Closed form Newton-Euler dynamic model of flexible manipulators. *Robotica*, 35(5):1006–1030, 2017. doi: 10.1017/S0263574715000934.

[81] Bruno Scaglioni, Luca Bascetta, Marco Baur, and Gianni Ferretti. Closed-form control oriented model of highly flexible manipulators. *Applied Mathematical Modelling*, 52:174–185, 2017. ISSN 0307904X. doi: 10.1016/j.apm.2017.07.034.

[82] Fernando Malvezzi, Renato M M Orsino, and Tarcisio Antonio Hess Coelho. Lagrange's, Maggi's and Kane's Equations Applied to the Dynamic Modelling of Serial Manipulator. In *Proceedings of DINAME 2017*, pages 291–304, Cham, 2019. Springer International Publishing. ISBN 978-3-319-91217-2.

[83] C Sun, H Gao, W He, and Y Yu. Fuzzy Neural Network Control of a Flexible Robotic Manipulator Using Assumed Mode Method. *IEEE Transactions on Neural Networks and Learning Systems*, 29(11):5214–5227, nov 2018. ISSN 2162-2388. doi: 10.1109/TNNLS.2017.2743103.

[84] Kshetrimayum Lochan, Binoy Krishna Roy, and Bidyadhar Subudhi. Use of memristive chaotic signal as a desired trajectory for a two-link flexible manipulator using contraction theory based on a composite control technique. *European Physical Journal: Special Topics*, 228(10):2215–2231, 2019. ISSN 19516401. doi: 10.1140/epjst/e2019-900038-5.

[85] Zhi-cheng Qiu and Wen-zheng Zhang. Trajectory planning and diagonal recurrent neural network vibration control of a flexible manipulator using structural light sensor. *Mechanical Systems and Signal Processing*, 132:563–594, 2019. ISSN 10961216. doi: 10.1016/j.ymssp.2019.07.014.

[86] Santanu Kumar Pradhan and Bidyadhar Subudhi. Position control of a flexible manipulator using a new nonlinear self-Tuning PID controller. *IEEE/CAA Journal of Automatica Sinica*, 7(1):136–149, 2020. ISSN 23299274. doi: 10.1109/JAS.2017.7510871.

[87] R Boucetta, S Hamdi, and S Bel Hadj Ali. *Flexible-Link Manipulators: Dynamic Analysis and Advanced Control Strategies*, pages 19–46. Springer Singapore, Singapore, 2020. ISBN 978-981-15-1819-5. doi: 10.1007/978-981-15-1819-5_2.

[88] N Singh and S Rajendran. Integral Fast Output Sampling control for Flexible Link Manipulators with LMI approach. In *2016 IEEE 1st International Conference on Power Electronics, Intelligent Control and Energy Systems (ICPEICES)*, pages 1–6, jul 2016. doi: 10.1109/ICPEICES.2016.7853698.

[89] Y Si, J Pu, and L Sun. A fast terminal sliding mode control of two-link flexible manipulators for trajectory tracking. In *2017 Chinese Automation Congress (CAC)*, pages 6387–6391, oct 2017. doi: 10.1109/CAC.2017.8243928.

[90] J Dong, B He, M Ma, C Zhang, and G Li. Open-Closed-Loop PD Iterative Learning Control Corrected With the Angular Relationship of Output Vectors for a Flexible Manipulator. *IEEE Access*, 7:167815–167822, 2019. ISSN 2169-3536. doi: 10.1109/ACCESS.2019.2930559.

[91] Foruzan Mehria and Ahmad Foruzantabarb. Control of Flexible Link Robot using a Closed Loop Input-Shaping Approach. *Journal of Artificial Intelligence in Electrical Engineering*, 8(29):41–52, 2019. ISSN 2345-4652.

[92] Komal Agrawal, Richa Negi, and Nitin Singh. Dynamically Tuned PIDD2 Controller for Single-Link Flexible Manipulator. In *Advances in VLSI, Communication, and Signal Processing*, pages 907–924, Singapore, 2020. Springer Singapore. ISBN 978-981-32-9775-3.

[93] C . Li and T S Sankar. Systematic methods for efficient modeling and dynamics computation of flexible robot manipulators. *IEEE Transactions on Systems, Man, and Cybernetics*, 23(1):77–95, jan 1993. ISSN 2168-2909. doi: 10.1109/21.214769.

[94] Thomas R Kane and David A Levinson. *Dynamics, theory and applications*. McGraw Hill, 1985.

[95] K W Buffinton. Dynamics of Elastic Manipulators With Prismatic Joints. *Journal of Dynamic Systems, Measurement, and Control*, 114(1):41–49, mar 1992. ISSN 0022-0434. doi: 10.1115/1.2896506.

[96] Ali Meghdari and Farbod Fahimi. On the First-Order Decoupling of Dynamical Equations of Motion for Elastic Multibody Systems as Applied to a Two-Link Flexible Manipulator. *Multibody System Dynamics*, 5(1):1–20, 2001. ISSN 13845640. doi: 10.1023/A:1026576603498.

[97] Ding-guo Zhang and Sheng-feng Zhou. Dynamic analysis of flexible-link and flexible-joint robots. *Applied Mathematics and Mechanics*, 27(5):695–704, 2006. ISSN 1573-2754. doi: 10.1007/s10483-006-0516-1.

[98] Shanshan Ren, Ming Chu, and Qingxuan Jia. Position inner loop impedance control of flexible link and flexible joint. In *2016 4th International Conference on Sensors, Mechatronics and Automation (ICSMA 2016)*, pages 454–459. Atlantis Press, 2016. ISBN 978-94-6252-274-9. doi: 10.2991/icsma-16.2016.81.

[99] Shiyuan Jia, Yinghong Jia, Shijie Xu, and Quan Hu. Maneuver and Active Vibration Suppression of Free-Flying Space Robot. *IEEE Transactions on Aerospace and Electronic Systems*, 54(3):1115–1134, 2017. ISSN 00189251. doi: 10.1109/TAES.2017.2775780.

[100] Yushu Bian, Zhihui Gao, Xin Lv, and Ming Fan. Theoretical and experimental study on vibration control of flexible manipulator based on internal resonance. *JVC/Journal of Vibration and Control*, 24(15):3321–3337, 2018. ISSN 17412986. doi: 10.1177/1077546317704792.

[101] Yushu Bian and Zhihui Gao. Nonlinear vibration control for flexible manipulator using 1: 1 internal resonance absorber. *Journal of Low Frequency Noise Vibration and Active Control*, 37(4):1053–1066, 2018. ISSN 20484046. doi: 10.1177/1461348418765951.

[102] Ma Xiang-feng and Xu Xiang-rong. A further study on kane's equations approach of robots dynamics. In *Proceedings of the 1988 IEEE International Conference on Systems, Man, and Cybernetics*, volume 1, pages 107–112, aug 1988. doi: 10.1109/ICSMC.1988.754252.

[103] Laura Celentano. Modeling of Flexible Robots with Varying Cross Section and Large Link Deformations. *Journal of Dynamic Systems, Measurement and Control, Transactions of the ASME*, 138(2):1–12, 2016. ISSN 15289028. doi: 10.1115/1.4032133.

[104] Habib Esfandiar, Moharam H Korayem, and Mohammad Haghpanahi. Large deformation modeling of flexible manipulators to determine allowable load. *Structural Engineering and Mechanics*, 62(5):619–629, 2017.

[105] Hongjun Yang, Jinkun Liu, and Xu Lan. Observer design for a flexible-link manipulator with PDE model. *Journal of Sound and Vibration*, 341:237–245, 2015. ISSN 10958568. doi: 10.1016/j.jsv.2014.12.033.

[106] X. Zhang, W. Xu, and S. S. Nair. Comparison of some modeling and control issues for a flexible two link manipulator. *ISA Transactions*, 43(4):509–525, 2004. ISSN 00190578. doi: 10.1016/s0019-0578(07)60165-7.

[107] L Zhang and J Liu. Observer-based partial differential equation boundary control for a flexible two-link manipulator in task space. *IET Control Theory Applications*, 6(13):2120–2133, 2012. ISSN 1751-8652. doi: 10.1049/iet-cta.2011.0545.

[108] Fangfei Cao and Jinkun Liu. Vibration control for a rigid-flexible manipulator with full state constraints via Barrier Lyapunov Function. *Journal of Sound and Vibration*, 406:237–252, 2017. ISSN 10958568. doi: 10.1016/j.jsv.2017.05.050.

[109] Xiaoping Zhang, Wenwei Xu, Satish S. Nair, and Vijay Sekhar Chellaboina. PDE Modeling and Control of a Flexible Two-Link Manipulator. *IEEE Transactions on Control Systems Technology*, 13(2):301–312, 2005. ISSN 15580865. doi: 10.1109/TCST.2004.842446.

[110] Zhijie Liu, Jinkun Liu, and Wei He. Partial differential equation boundary control of a flexible manipulator with input saturation. *International Journal of Systems Science*, 48(1):53–62, 2017. doi: 10.1080/00207721.2016.1152416.

[111] L Zhang and J Liu. Nonlinear PDE observer design for a flexible two-link manipulator. In *2012 American Control Conference (ACC)*, pages 5336–5341, jun 2012. doi: 10.1109/ACC.2012.6314625.

[112] Linjun Zhang and Jinkun Liu. Optimal trajectory control of flexible two-link manipulator based on PDE model. *Proceedings of the IEEE Conference on Decision and Control*, pages 4406–4411, 2012. ISSN 01912216. doi: 10.1109/CDC.2012.6427070.

[113] Linjun Zhang and Jinkun Liu. Adaptive boundary control for flexible two-link manipulator based on partial differential equation dynamic model. *IET Control Theory and Applications*, 7(1):43–51, 2013. ISSN 17518644. doi: 10.1049/iet-cta.2011.0593.

[114] Tingting Jiang, Jinkun Liu, and Wei He. A robust observer design for a flexible manipulator based on a PDE model. *Journal of Vibration and Control*, 23(6): 871–882, 2017. doi: 10.1177/1077546315587443.

[115] Zhijie Liu, Jinkun Liu, and Wei He. Dynamic modeling and vibration control for a nonlinear 3-dimensional flexible manipulator. *International Journal of Robust and Nonlinear Control*, 28(13):3927–3945, 2018. ISSN 10991239. doi: 10.1002/rnc.4113.

[116] Y Zhang, Q Li, W Zhang, Y Liu, and Z Xue. Weighted Multiple Neural Network Boundary Control for a Flexible Manipulator With Uncertain Parameters. *IEEE Access*, 7:57633–57641, 2019. ISSN 2169-3536. doi: 10.1109/ACCESS.2019.2914077.

[117] Fangfei Cao and Jinkun Liu. Boundary vibration control for a two-link rigid–flexible manipulator with quantized input. *JVC/Journal of Vibration and Control*, 25(23-24):2935–2945, 2019. ISSN 17412986. doi: 10.1177/1077546319873507.

[118] Le Li, Fangfei Cao, and Jinkun Liu. Vibration control of flexible manipulator with unknown control direction. *International Journal of Control*, 0(0):1–13, 2020. doi: 10.1080/00207179.2020.1731609.

[119] Z. Mohamed, M. Khairudin, A. R. Husain, and B. Subudhi. Linear matrix inequality-based robust proportional derivative control of a two-link flexible manipulator. *JVC/Journal of Vibration and Control*, 22(5):1244–1256, 2016. ISSN 17412986. doi: 10.1177/1077546314536427.

[120] Waweru Njeri, Minoru Sasaki, and Kojiro Matsushita. Gain Tuning for High-Speed Vibration Control of a Multilink Flexible Manipulator Using Artificial Neural Network. *Journal of Vibration and Acoustics*, 141(4), apr 2019. ISSN 1048-9002. doi: 10.1115/1.4043241.

[121] V K Singh and J Ohri. Simultaneous control of position and vibration of flexible link manipulator by nature-inspired algorithms. In *2018 IEEE 8th Power India International Conference (PIICON)*, pages 1–6, dec 2018. doi: 10.1109/POWERI.2018.8704403.

[122] Umesh Kumar Sahu, Arun Mishra, Biswajeet Sahu, Prateek Priyaranjan Pradhan, Dipti Patra, and Bidyadhar Subudhi. Vision-Based Tip Position Control of a Single-Link Robot Manipulator. *SSRN Electronic Journal*, pages 1416–1422, 2019. doi: 10.2139/ssrn.3356203.

[123] G Huan and W Q Xian. Observer based tracking control of flexible manipulator. In *2017 2nd International Conference on Advanced Robotics and Mechatronics (ICARM)*, pages 662–666, aug 2017. doi: 10.1109/ICARM.2017.8273241.

[124] Ji Wang, Yangjun Pi, Yumei Hu, Zhencai Zhu, and Lingbin Zeng. Adaptive simultaneous motion and vibration control for a multi flexible-link mechanism with uncertain general harmonic disturbance. *Journal of Sound and Vibration*, 408:60–72, 2017. ISSN 10958568. doi: 10.1016/j.jsv.2017.07.024.

[125] Lianfang Tian, Jun Wang, and Zongyuan Mao. Constrained motion control of flexible manipulators based on a dynamic neural network. *Proceedings of the IEEE International Conference on Industrial Technology*, 2(3):678–683, 2002. doi: 10.1109/ICIT.2002.1189246.

[126] Gerasimos Rigatos and Krishna Busawon. *Flexible-Link Robots*, pages 271–300. Springer International Publishing, Cham, 2018. ISBN 978-3-319-77851-8. doi: 10.1007/978-3-319-77851-8_5.

[127] Ali Bazaei and Mehrdad Moallem. Improving force control bandwidth of flexible-link arms through output redefinition. *IEEE/ASME Transactions on Mechatronics*, 16(2):380–386, 2010. ISSN 10834435. doi: 10.1109/TMECH.2010.2046332.

[128] F Matsuno and K Yamamoto. Dynamic hybrid position/force control of a flexible manipulator. In *[1993] Proceedings IEEE International Conference on Robotics and Automation*, pages 462–467 vol.2, may 1993. doi: 10.1109/ROBOT.1993.291914.

[129] Baigeng Wang, Shurong Li, and Zhe Liu. Robust Adaptive Position/Force Control for Flexible-Link with Flexible-Joint Manipulator. In *Proceedings of the 11th International Conference on Modelling, Identification and Control (ICMIC2019)*, pages 1215–1227, Singapore, 2020. Springer Singapore. ISBN 978-981-15-0474-7.

[130] Junqiang Lou, Jiangjiang Liao, Yanding Wei, Yiling Yang, and Guoping Li. Experimental identification and vibration control of a piezoelectric flexible manipulator using optimal multi-poles placement control. *Applied Sciences*, 7 (3), 2017. ISSN 20763417. doi: 10.3390/APP7030309.

[131] Francesco Ripamonti, Lorenzo Orsini, and Ferruccio Resta. A Nonlinear Sliding Surface in Sliding Mode Control to Reduce Vibrations of a Three-Link Flexible Manipulator. *Journal of Vibration and Acoustics*, 139(5), jun 2017. ISSN 1048-9002. doi: 10.1115/1.4036502.

[132] Waweru Njeri, Minoru Sasaki, and Kojiro Matsushita. Enhanced vibration control of a multilink flexible manipulator using filtered inverse controller. *ROBOMECH Journal*, 5(1):1–19, dec 2018. ISSN 21974225. doi: 10.1186/s40648-018-0125-7.

[133] Daniel Newman and Joshua Vaughan. Concurrent Design of Linear Control with Input Shaping for a Two-Link Flexible Manipulator Arm. *IFAC-PapersOnLine*, 51(14):66–71, 2018. ISSN 24058963. doi: 10.1016/j.ifacol.2018.07.200.

[134] Jin Yong Ju, Wei Li, Yufei Liu, and Chunrui Zhang. Master-slave integrated control for the transverse vibration of a translational flexible manipulator based on input shaping and state feedback. *Shock and Vibration*, 2019, 2019. ISSN 10709622. doi: 10.1155/2019/8419591.

[135] Amir H. Ghasemi. Slewing and vibration control of a single-link flexible manipulator using filtered feedback linearization. *Journal of Intelligent Material Systems and Structures*, 28(20):2887–2895, 2017. ISSN 15308138. doi: 10.1177/1045389X17704067.

[136] Fangfei Cao and Jinkun Liu. Optimal trajectory control for a two-link rigid-flexible manipulator with ODE-PDE model. *Optimal Control Applications and Methods*, 39(4):1515–1529, 2018. ISSN 10991514. doi: 10.1002/oca.2423.

[137] Masoud Mosayebi, Mostafa Ghayour, and Mohammad Jafar Sadigh. A nonlinear high gain observer based input-output control of flexible link manipulator. *Mechanics Research Communications*, 45:34–41, 2012. ISSN 00936413. doi: 10.1016/j.mechrescom.2012.06.004.

[138] Jinkun Liu and Wei He. Boundary Control for Flexible Manipulator Using Singular Perturbation. In *Distributed Parameter Modeling and Boundary Control of Flexible Manipulators*, pages 27–43. Springer Singapore, Singapore, 2018. ISBN 978-981-10-8300-6. doi: 10.1007/978-981-10-8300-6_4.

[139] Zhijie Liu, Jinkun Liu, and Wei He. Adaptive boundary control of a flexible-manipulator with input saturation. *International Journal of Control*, 89(6): 1191–1202, 2016. ISSN 13665820. doi: 10.1080/00207179.2015.1125022.

[140] Fabian Schnelle and Peter Eberhard. Adaptive nonlinear model predictive control design of a flexible-link manipulator with uncertain parameters. *Acta Mechanica Sinica*, 33(3):529–542, 2017. ISSN 1614-3116. doi: 10.1007/s10409-017-0669-4.

[141] Tingting Jiang, Jinkun Liu, and Wei He. Boundary control for a flexible manipulator with a robust state observer. *JVC/Journal of Vibration and Control*, 24(2):260–271, 2018. ISSN 17412986. doi: 10.1177/1077546316635343.

[142] Wei He, Xiuyu He, Mingfo Zou, and Hongyi Li. PDE Model-Based Boundary Control Design for a Flexible Robotic Manipulator with Input Backlash.

IEEE Transactions on Control Systems Technology, 27(2):790–797, 2018. ISSN 15580865. doi: 10.1109/TCST.2017.2780055.

[143] William J O'Connor. *Wave-based Control of Flexible Mechanical Systems*, pages 25–34. Springer Berlin Heidelberg, Berlin, Heidelberg, 2008. ISBN 978-3-540-79142-3. doi: 10.1007/978-3-540-79142-3_3.

[144] B. Depraetere, M. Liu, G. Pinte, I. Grondman, and R. Babuška. Comparison of model-free and model-based methods for time optimal hit control of a badminton robot. *Mechatronics*, 24(8):1021–1030, 2014. ISSN 09574158. doi: 10.1016/j.mechatronics.2014.08.001.

[145] Hebertt Sira-Ramírez, Alberto Luviano-Juárez, Mario Ramírez-Neria, and Eric William Zurita-Bustamante. Chapter 4 - Extensions of ADRC. In *Active Disturbance Rejection Control of Dynamic Systems*, pages 109–172. Butterworth-Heinemann, 2017. ISBN 978-0-12-849868-2. doi: 10.1016/B978-0-12-849868-2.00004-6.

[146] Fangfei Cao and Jinkun Liu. Adaptive actuator fault compensation control for a rigid-flexible manipulator with ODEs-PDEs model. *International Journal of Systems Science*, 49(8):1748–1759, 2018. ISSN 14645319. doi: 10.1080/00207721.2018.1479002.

[147] Siti Fadilah Abd Latip, Abdul Rashid Husain, Zaharuddin Mohamed, and Mohd Ariffanan Mohd Basri. Adaptive PID actuator fault tolerant control of single-link flexible manipulator. *Transactions of the Institute of Measurement and Control*, 41(4):1019–1031, 2019. ISSN 01423312. doi: 10.1177/0142331218776720.

[148] Raouf Fareh, Mohammad Al-Shabi, Maamar Bettayeb, and Jawhar Ghommam. Robust Active Disturbance Rejection Control for Flexible Link Manipulator. *Robotica*, 38(1):118–135, 2020. ISSN 14698668. doi: 10.1017/S026357471900050X.

[149] Q Xu, W Wang, H Xia, Y Wang, and Y Feng. Second-Order Non-Singular Terminal Sliding Mode Optimal Control of Uncertain Flexible Manipulator. In *2018 IEEE 8th Annual International Conference on CYBER Technology in Automation, Control, and Intelligent Systems (CYBER)*, pages 1376–1381, jul 2018. doi: 10.1109/CYBER.2018.8688134.

[150] Umesh Kumar Sahu, Bidyadhar Subudhi, and Dipti Patra. Sampled-data extended state observer-based backstepping control of two-link flexible manipulator. *Transactions of the Institute of Measurement and Control*, 41(13):3581–3599, 2019. ISSN 01423312. doi: 10.1177/0142331219832954.

[151] Lijun Wang, Dan Zhang, Jinkun Liu, Haifeng Huang, and Qiuyue Shi. Adaptive Fault-Tolerant Control for a Flexible Manipulator of Output-Constrained. In *2018 IEEE 8th Annual International Conference on CYBER Technology in Automation, Control, and Intelligent Systems (CYBER)*, pages 1048–1052, 2018.

[152] Z Zhao, X He, and C K Ahn. Boundary Disturbance Observer-Based Control of a Vibrating Single-Link Flexible Manipulator. *IEEE Transactions on Systems, Man, and Cybernetics: Systems*, pages 1–9, 2019. ISSN 2168-2232. doi: 10.1109/TSMC.2019.2912900.

[153] Zhijie Liu and Jinkun Liu. Boundary Control of a Flexible Robotic Manipulator With Output Constraints. *Asian Journal of Control*, 19(1):332–345, 2017. ISSN 19346093. doi: 10.1002/asjc.1342.

[154] Xiuyu He, Wei He, and Changyin Sun. Robust adaptive vibration control for an uncertain flexible Timoshenko robotic manipulator with input and output constraints. *International Journal of Systems Science*, 48(13):2860–2870, 2017. ISSN 14645319. doi: 10.1080/00207721.2017.1360963.

[155] Fangfei Cao and Jinkun Liu. An adaptive iterative learning algorithm for boundary control of a coupled ODE–PDE two-link rigid–flexible manipulator. *Journal of the Franklin Institute*, 354(1):277–297, 2017. ISSN 00160032. doi: 10.1016/j.jfranklin.2016.10.013.

[156] Zhijie Liu and Jinkun Liu. Adaptive Iterative Learning Boundary Control of a Flexible Manipulator with Guaranteed Transient Performance. *Asian Journal of Control*, 20(3):1027–1038, 2018. ISSN 19346093. doi: 10.1002/asjc.1379.

[157] T Chen, M Li, and J Shan. Iterative learning control of a flexible manipulator considering uncertain parameters and unknown repetitive disturbance. In *2019 American Control Conference (ACC)*, pages 2209–2214, jul 2019. doi: 10.23919/ACC.2019.8815014.

[158] Chunyu Yang, Yiming Xu, Linna Zhou, and Yongzheng Sun. Model-free composite control of flexible manipulators based on adaptive dynamic programming. *Complexity*, 2018, 2018. ISSN 10990526. doi: 10.1155/2018/9720309.

[159] Bin Xu. Composite learning control of flexible-link manipulator using NN and DOB. *IEEE Transactions on Systems, Man, and Cybernetics: Systems*, 48(11): 1979–1985, nov 2017. ISSN 21682232. doi: 10.1109/TSMC.2017.2700433.

Paper B

Modeling and Analysis of Flexible Bodies Using Lumped Parameter Method

Dipendra Subedi, Ilya Tyapin and Geir Hovland

This paper has been published as:

Dipendra Subedi, Ilya Tyapin and Geir Hovland. Modeling and Analysis of Flexible Bodies Using Lumped Parameter Method. *2020 IEEE 11th International Conference on Mechanical and Intelligent Manufacturing Technologies (ICMIMT)*, pages 161–166, 2020. doi: 10.1109/ICMIMT49010.2020.9041188.

Modeling and Analysis of Flexible Bodies Using Lumped Parameter Method

Dipendra Subedi, Ilya Tyapin and Geir Hovland

Department of Engineering Sciences
University of Agder
4879 Grimstad, Norway

Abstract **The modeling, identification and analysis of a flexible beam is presented. The lumped parameter method is used to model a flexible beam. The use of camera measurements to identify lumped parameters, namely spring stiffness and damping coefficient, is described. The measurements of the tip oscillations using a high-speed camera and high-precision laser tracker are compared. The static and dynamic behavior of the flexible beam model is compared to the experimental results to show the validity of the model.**

B.1 Introduction

Development of flexible manipulators is of on-going interest for researchers worldwide. The use of light flexible manipulators has many advantages over conventional industrial robots such as low cost, reduced energy consumption, high payload-to-robot-weight ratio, high operational speed, better transportability, safe operation due to reduced inertia and so on [1]. However, link flexibility causes unwanted oscillations and problems in the precise position control of the end-effector which may even lead to an unstable system. For achieving minimum oscillations and good position accuracy, the industrial robots are designed with highly stiff materials (like heavy steel with bulky design) which consequently require expensive high-power drives.

The vibration of end-effector at high speed and high load is still present due to industrial robot elasticity. In this context, lightweight flexible manipulators are better alternatives if the control architecture is designed to reduce the vibration of the end-effector to an acceptable range. The non-linear dynamics of the system with an infinite number of degrees of freedom make the control of flexible manipulator more complicated than the rigid robots. In order to develop efficient control algorithm for the flexible manipulator, it is necessary to construct a mathematical model of the system incorporating flexibility of the links. Due to impracticability to model the flexible link with infinite degree of freedom for dynamic analysis and simulations, it is necessary to describe the system with finite degree of freedom and still being able

to represent all the dynamically relevant flexibility effects. A dynamically accurate and computationally affordable simulation model is required to represent the actual system behavior to design suitable control algorithm.

The goal of flexible beam modeling is to achieve an accurate model of a flexible manipulator system formed by the combination of multiple flexible links connected together by revolute joints represented by a spring and damper system. This paper represents a part of the work done for modeling a long reach $3R$ planar manipulator constructed using flexible links.

Different models of flexible bodies are available in the literature depending upon the assumptions and required complexity. Accuracy of the models depends on the assumptions made to simplify the complexity of the flexible link manipulator system. There are three main approaches that are used traditionally in the literature: lumped parameter method, assumed mode method and finite element method [2]. In assumed mode method, it is difficult to calculate modes of the link with varying cross-sections [3]. Finite element method is computationally very expensive. Recently, researchers have used lumped parameter method to model flexible arms of multi-link manipulators [4], boom of a mobile concrete pump [5], and other flexible mechanical structures [6].

Lumped parameter method is explored further in this paper because it is a good compromise between the complexity of continuous non-linear dynamical system and the simplicity of neglecting the elasticity with a rigid body model [7]. The computational cost and the accuracy of lumped parameter method can be controlled by changing the number of lumped elements.

Different modeling techniques, control approaches and sensor systems for flexible manipulator are explored in literature [1, 2]. However, there is very limited work done in the experimental identification of model parameters of flexible manipulator. This paper describes a simple approach of identification of lumped parameters of a flexible link using a camera sensor.

In this paper, the lumped parameter method is used to model a flexible beam. High-speed RGB-camera is used to measure the tip oscillations and the high-precision laser tracker to validate the results. The parameters of the flexible beam are identified using camera measurements. The results obtained from the simulation model are compared to the experimental data.

The paper is organized into five sections as follows. The modeling of flexible cantilever beam is described in section B.2. The simulation model is verified with experiments in section B.3. The results obtained from the simulation model are compared to the experimental values in section B.4. Conclusions and discussions follow in section B.5.

B.2 Modeling

The flexible beam is modeled as a set of mass, rotational spring and damper system [2, 7, 8]. The reasons behind using this method for modeling flexibility are simplicity of the method and possibility of extending the model for varying cross-section of the links. Lumped parameter models of a flexible beam with one and two flexible elements are shown in Fig. B.1 and Fig. B.2 respectively. In Fig. B.1, the center of mass is located at the origin of coordinate frame S_1, and k, c, F, M, δ_v, δ_θ represent stiffness, damping coefficient, end load, moment, vertical deflection and angular deflection respectively. In Fig. B.2, two flexible elements are connected in such a way that the spring and damper are in series between two segments. The modeling parameters k and c depend on the dimension and material used in the beam and can be identified/approximated via experiments. The bending of the flexible beam is modeled about one axis, i.e. rotational degree of freedom about the Z-axis.

Considering L, F, E, I as the length of the beam, load attached to the end of the beam,Young's modulus, and area moment of inertia, the vertical tip deflection (δ^u_{vA})

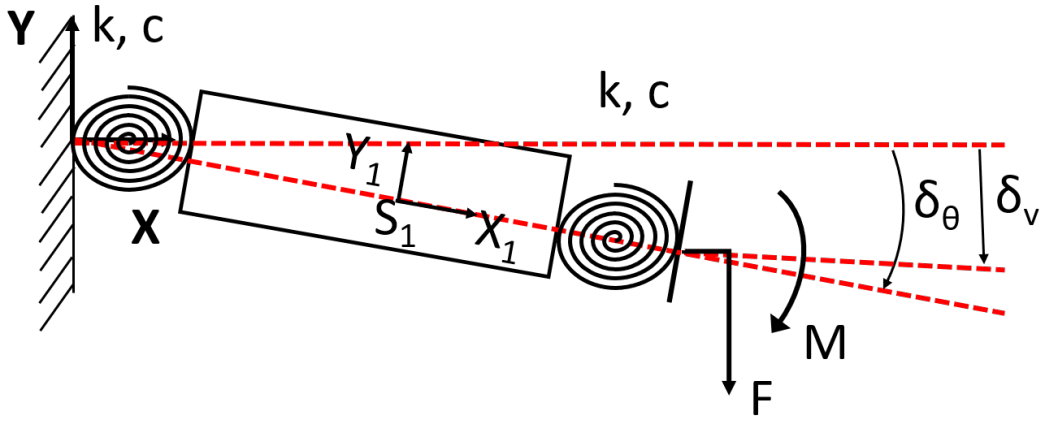

Figure B.1: Lumped parameter model of an end-loaded cantilever flexible beam with one flexible element

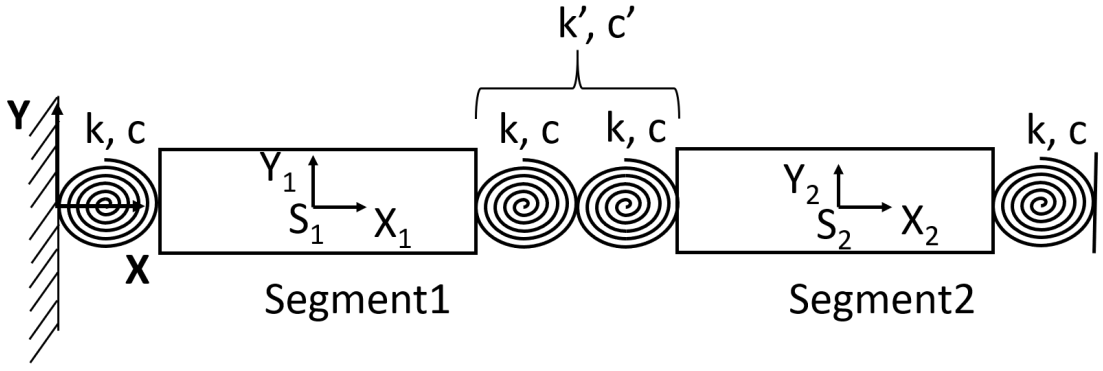

Figure B.2: Lumped parameter model of a flexible beam with two flexible elements

and the angular deflection ($\delta^u_{\theta A}$) of the beam under a uniform load ($q = a\rho g$) is given by (B.1) and (B.2) respectively, where a, ρ, and g are cross-section area, density, and gravity respectively and indices A and u represent analytical solution and uniform load condition respectively [9]. The vertical tip deflection (δ^e_{vA}) of the beam due to end load (F) shown in Fig. B.1 is given by (B.3), where index e represents end load condition. The angular tip deflection ($\delta^e_{\theta A}$) of the cantilever beam due to end load is given by (B.4). The total vertical tip deflection (δ_{vA}) and angular tip deflection ($\delta_{\theta A}$) of the beam are given by a sum of deflection under uniform load and deflection due to end load as given by (B.5).

$$\delta^u_{vA} = \frac{qL^4}{8EI} \tag{B.1}$$

$$\delta^u_{\theta A} = \frac{qL^3}{6EI} \tag{B.2}$$

$$\delta^e_{vA} = \frac{FL^3}{3EI} \tag{B.3}$$

$$\delta^e_{\theta A} = \frac{FL^2}{2EI} \tag{B.4}$$

$$\delta_{\theta A} = \delta^u_{\theta A} + \delta^e_{\theta A}; \quad \delta_{vA} = \delta^u_{vA} + \delta^e_{vA} \tag{B.5}$$

The *equivalent stiffness* of the beam under end-loaded condition is given by (B.6). The *equivalent stiffness* of the beam is used in the lumped parameter model. Both angular and vertical deflections of the beam in lumped parameter model can be approximated using (B.7) and (B.8) respectively, where index L represents lumped parameter approximation.

$$k_A = \frac{FL}{\delta^e_{\theta A}} = \frac{2EI}{L} \tag{B.6}$$

$$\delta^e_{\theta L} = \frac{FL}{k_A} = \frac{FL^2}{2EI} \tag{B.7}$$

$$\delta^e_{vL} = L\delta^e_{\theta_L} = \frac{FL^3}{2EI} \tag{B.8}$$

The angular deflection obtained analytically in (B.4) and using the lumped parameter model in (B.7) are equal. However, the vertical deflection obtained analytically in (B.3) and using the lumped parameter model in (B.8) are not equal.

To improve the approximation in lumped parameter model, the total length of the beam is divided into n_s smaller segments, each segment has a length $L_s = L/n_s$, and the lumped segments are connected together to form the model of the beam.

The stiffness of a single beam segment is given by (B.9). The equivalent stiffness k' of two springs, each of stiffness k, connected in series between two beam segments is given by (B.10). Similarly, the equivalent damping coefficient c' of two dampers c connected in series between two beam segments is given by (B.11) and shown in Fig. B.2.

$$k = \frac{2EI}{L_s} \tag{B.9}$$

$$k' = \frac{k^2}{2k} \tag{B.10}$$

$$c' = \frac{c^2}{2c} \tag{B.11}$$

Considering uniform beam cross-section, the total *equivalent stiffness* (k_{tE}) of the beam can be approximated experimentally, where index E represents experimentally identified value. Using known tip load (F_E), the deflection (δ_{vE}) can be measured to calculate the *equivalent stiffness* by using (B.12). Thus obtained total *equivalent stiffness* of the beam is multiplied by the number of beam segments to obtain individual segment stiffness k_E as given in (B.13).

$$k_{tE} = \frac{F_E L}{\delta^e_{\theta E}} = \frac{2F_E L^2}{3\delta^e_{vE}} \tag{B.12}$$

$$k_E = n_s k_{tE} \tag{B.13}$$

Equations of motion

The model of a flexible beam in Fig. B.3 consists of n_s rigid elements with mass m_i connected together by rotational joints P_i, rotational spring stiffness k_i and damper with damping coefficient c_i, where $i = 1, 2, \ldots, n_s$. The first segment spring stiffness is $k_1 = k$ and damping coefficient is $c_1 = c$. All other segment stiffnesses and dampers are $k_i = k'$ and $c_i = c'$ respectively. The rotation of each element is described by angle φ_i. A Newtonian frame O_I is located at the first rotational joint P_1 of the cantilever beam. Body fixed frame S_i of each element is located at the center of gravity.

Equations of motion are derived using Newton-Euler formulation. Considering J_{Ti} as Jacobian matrix for translational motion, J_{Ri} as Jacobian matrix for rotational motion, p_i as linear momentum, l_i as angular momentum, F_i as applied forces, M_i as applied moments for body i, the principles of linear and angular momentum are

applied to get (B.14).

$$\sum_{i=1}^{n_s}[J_{Ti}^T(\dot{p}_i - F_i) + J_{Ri}^T(\dot{l}_i - M_i)] = 0 \tag{B.14}$$

Considering r_{s_i} as the position vector from Newtonian frame O_I to body fixed frame S_i, r_{p_i} as the position vector from Newtonian frame O_I to joint P_i, R_i as the rotation matrix representing rotation of frame S_i with respect to frame O_I about the Z axis, I_i as the inertia tensor, v_{s_i} as the linear velocity, ω_i as the angular velocity, and calculating the translational parts in frame O_I and rotational parts in body reference frame S_i, (B.14) can be written to (B.16) using (B.15) where the cross product $\omega \times r$ is replaced by matrix operation $\tilde{\omega}r$. The mass of tip load is added to m_{n_s} for the last segment.

$$\dot{p}_i = m_i\ddot{r}_{s_i}; \quad \dot{l}_i = I_i\dot{\omega}_i + \tilde{\omega}_i I_i\omega_i \tag{B.15}$$

$$\sum_{i=1}^{n_s} J_{Ti}^T[m_i\ddot{r}_{s_i} - F_i] + J_{Ri}^T[I_i\dot{\omega}_i + \tilde{\omega}_i I_i\omega_i - M_i] = 0 \tag{B.16}$$

Kinematics of the bodies in generalized coordinates $q = (\varphi_1, \varphi_2, \cdots, \varphi_{n_s})^T$ is given by (B.17).

$$\left.\begin{aligned}
R_i &= \begin{bmatrix} cos\varphi_i & -sin\varphi_i & 0 \\ sin\varphi_i & cos\varphi_i & 0 \\ 0 & 0 & 1 \end{bmatrix} \\
r_{p_i} &= r_{p_{i-1}} + R_{i-1}[L_s; 0; 0], \quad r_{p_1} = [0; 0; 0] \\
r_{s_i} &= r_{p_i} + R_i[L_s/2; 0; 0] \\
J_{Ti} &= \frac{\partial r_{s_i}}{\partial q} \\
v_{s_i} &= J_{Ti}\dot{q} \\
\omega_i &= [0; 0; \dot{\varphi}_i] \\
J_{Ri} &= \frac{\partial \omega_i}{\partial \dot{q}} \\
\ddot{r}_{s_i} &= J_{Ti}\ddot{q} + \frac{\partial v_{s_i}}{\partial q}\dot{q} \\
\dot{\omega}_i &= J_{Ri}\ddot{q} + \frac{\partial \omega_i}{\partial q}\dot{q}
\end{aligned}\right\} \tag{B.17}$$

Using the kinematic equations, (B.16) can be rearranged to (B.18). The applied forces are given by the weight of the beam segments and the applied moments by the rotational springs and dampers. In addition, the applied force and moment by

the end-load is considered for the last segment of the beam.

$$\sum_{i=1}^{n_s}\left\{-J_{Ti}^T[m_i\frac{\partial v_i}{\partial q}\dot{q}-F_i]-J_{Ri}^T[I_i\frac{\partial \omega_i}{\partial q}\dot{q}+\tilde{\omega}_i I_i\omega_i-M_i]\right\}- \\ -\sum_{i=1}^{n_s}\left\{m_i J_{Ti}^T J_{Ti}+J_{Ri}^T I_i J_{Ri}\right\}\ddot{q}=0 \tag{B.18}$$

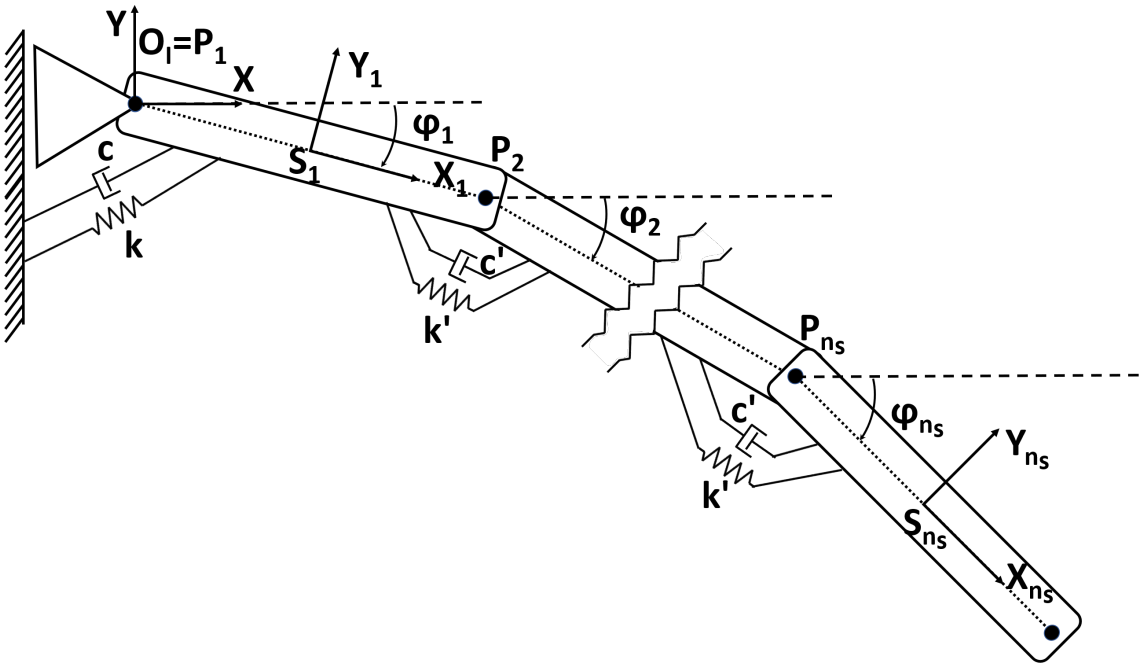

Figure B.3: Model of a flexible beam with n_s dofs

B.3 Simulations and Experiments

A hollow rectangular aluminium beam of length $L = 2.32\ m$, width $W = 0.04\ m$, height $H = 0.04\ m$, thickness $T = 2 \times 10^{-3}\ m$, density $\rho = 2700\ kg/m^3$, Young's modulus $E = 69 \times 10^9\ Pa$ is used in the simulation and experimental studies. The area moment of inertia I of the hollow rectangular beam is calculated using (B.19).

$$I = \frac{1}{12}WH^3 - \frac{1}{12}(W-2T)(H-2T)^3 \tag{B.19}$$

A load of $m_l = 4.5\ kg$ is applied at the tip of the beam and the corresponding deflection at the tip is recorded in the simulation and compared to the experimental data. The analytical vertical tip deflection obtained from (B.3) is $\delta_{vA}^e = 0.0363\ m$.

B.3.1 Simulation of analytical lumped parameter model

The stiffness of each flexible element/segment of the beam is calculated using (B.9) and (B.10). The deflection of the tip of the beam due to uniform load (δ^u_{vL}), end-load (δ^e_{vL}) and total deflection (δ_{vL}) for different values of n_s is shown in table B.1 (using *MATLAB ode23* for time integration with fixed step size of 0.01 s).

Dynamic response

To show the dynamic response of the tip of the beam, tip load of 4.5 kg is dropped after ensuring that the tip is stationary before dropping. To reduce the frequency of vibration a body ($m_d = 2.5\ kg$) is mounted at the tip. Moreover, the weight of the camera mounted at the tip is also considered in the simulation. The damping coefficient $c = \beta k$ is used in the simulation, where $\beta = 2.2 \times 10^{-4}$ is the tuning factor. To simulate the oscillation produced only due to the drop, the initial tuning factor is increased 5 times to ensure quick damping (before dropping). The position of the tip of the beam is shown in Fig. B.4. The frequency of vibration of the model ($n_s = 10$) is $f = 3.42\ Hz$.

B.3.2 Experimental identification of stiffness and damping ratio

A 7×9 checkerboard is mounted on the wall in such a way that it is completely visible from the camera when the beam is oscillating. The camera is calibrated intrinsically before mounting on the beam. The position of the checkerboard with

Table B.1: Tip deflection taking different number of flexible elements using analytically obtained lumped parameters

$\mathbf{n_s}$	$\delta^{\mathbf{u}}_{\mathbf{vL}}(\mathbf{m})$ $(m_l = 0kg)$	$\delta_{\mathbf{vL}}(\mathbf{m})$ $(m_l = 4.5kg)$	$\delta^{\mathbf{e}}_{\mathbf{vL}} = \delta_{\mathbf{vL}}$ - $\delta^{\mathbf{u}}_{\mathbf{vL}}(\mathbf{m})$
1	0.0115	0.0387	0.0272
2	0.0072	0.0480	0.0408
3	0.0064	0.0447	0.0383
4	0.0060	0.0435	0.0375
5	0.0060	0.0430	0.0370
6	0.0059	0.0427	0.0368
7	0.0059	0.0425	0.0366
8	0.0059	0.0424	0.0365
9	0.0058	0.0424	0.0366
10	0.0058	0.0423	0.0365

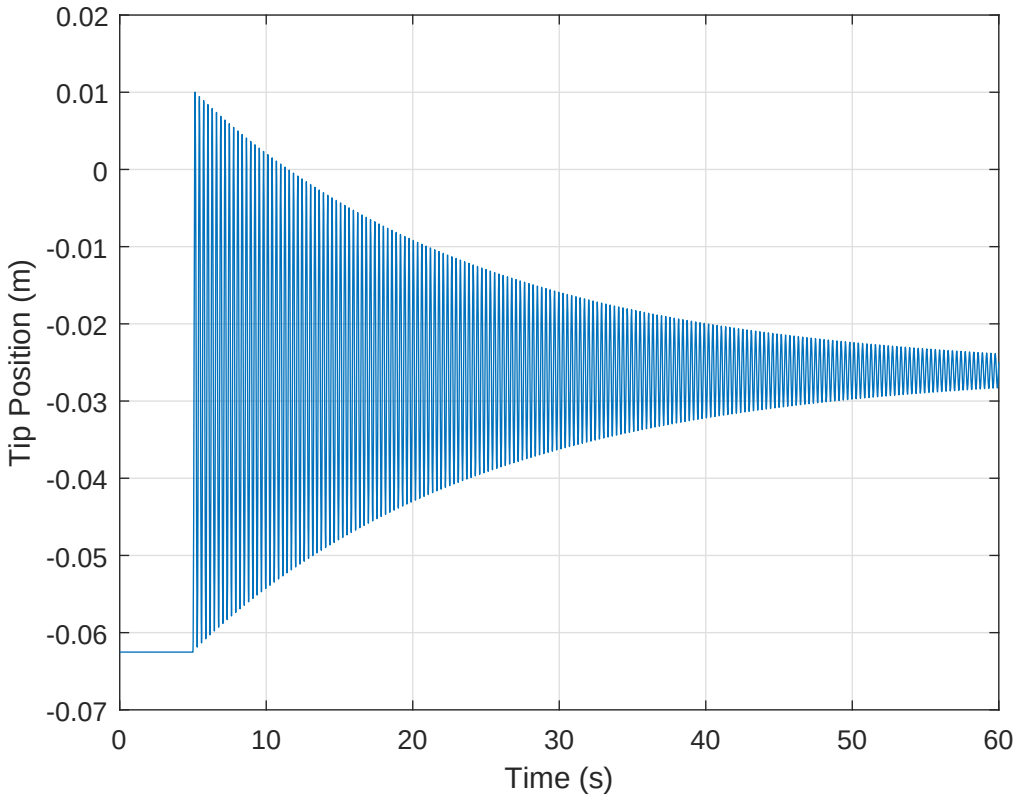

Figure B.4: Tip oscillations using analytical parameters

respect to a camera is determined using *OpenCV*.

In Fig. B.5, an experimental setup consisting of flexible beam (2) mounted on the wall (1) is shown. A spherically mounted retroreflector (3) is mounted at the tip of the beam to track the position of the tip using Leica AT960 laser tracker. Basler ace (acA2040-180kc) color camera (4) is mounted at the tip of the wall mounted cantilever beam and is connected to the computer via a connector (7). Object (6) to be dropped is hanging in the rope (8) at the tip of the beam. Additional object (5) is mounted at the tip to reduce the frequency of oscillation. The initial tip position of the beam is recorded before applying any load at the tip. Then a load of $m_l = 4.5\ kg$ is applied to the tip of the beam and the corresponding deflection of the tip is recorded. The difference gives the deflection (δ^e_{vE}) caused due to the load at the tip. Using (B.12), the total *equivalent stiffness* k_{tE} of the beam is determined. From (B.10) and (B.13), the stiffnesses (k_{1E} and k_{2E}) of each flexible element of the beam are approximated for n_s segments. Experimentally approximated parameters are $\delta^e_{vE} = 0.0403\ m$ and $k_{tE} = 3.8991 \times 10^3\ Nm/rad$.

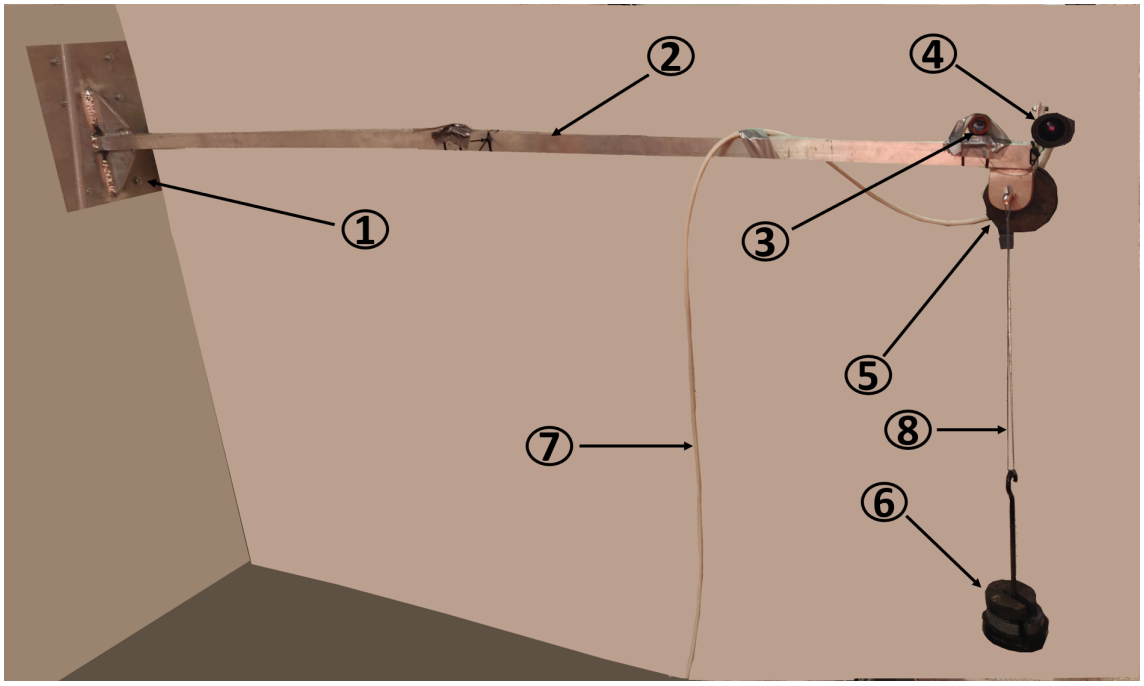

Figure B.5: Experimental setup (1. Wall mount, 2. Flexible beam, 3. Leica spherically mounted retroreflector ball probe, 4. Camera, 5. Tip load, 6. Tip load to be dropped, 7. Camera connector,8. Rope)

Dynamic response

The position of the tip of the beam recorded experimentally using camera is shown in Fig. B.6. The frequency of vibration (eigen frequency) of the beam is $f_E = 3.24\ Hz$. The damping ratio ζ is approximated by calculating logarithmic decrement δ using (B.20) and (B.21) where A_1 and A_n are two successive amplitudes n periods apart [10].

$$\delta = \frac{1}{n} ln \frac{A_1}{A_n} \tag{B.20}$$

$$\zeta = \frac{1}{\sqrt{1 + (2\pi/\delta)^2}} \tag{B.21}$$

The damping coefficient c_{te} is approximated using (B.22) where $\omega_d = 2\pi f_E$ is the frequency of vibration.

$$c_{tE} = 2\zeta\omega_d \tag{B.22}$$

For simulation purposes, the damping coefficient c_E for each flexible element of the flexible beam is approximated using (B.23) where β is the tuning parameter to match simulation model with the experiment. Experimentally approximated parameters are $c_{tE} = 0.08\ Nms/rad$, $\beta = 12$.

$$c_E = \beta n_s c_{tE} \tag{B.23}$$

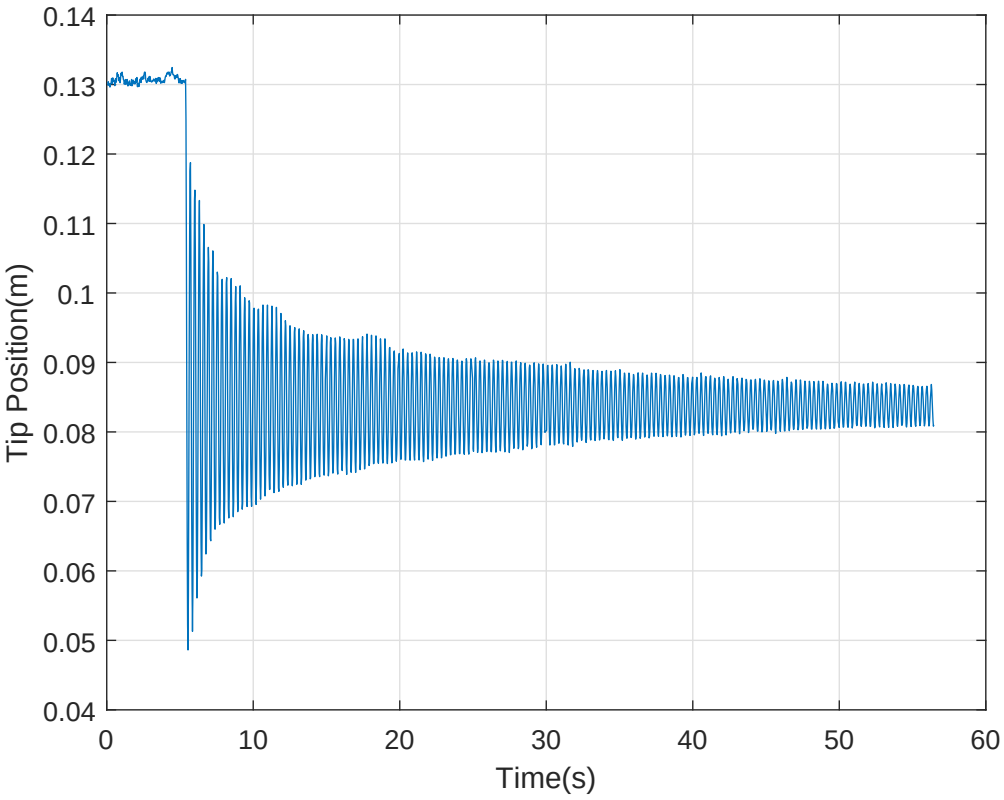

Figure B.6: Tip oscillations recorded using camera

B.3.3 Simulation of experimentally identified lumped parameter model

The stiffness of each flexible elements/segments of the beam approximated experimentally is used in the lumped model of the beam and the corresponding deflection of the tip due to uniform load (δ^u_{vL}), end-load (δ^e_{vL}) and total deflection (δ_{vL}) for different values of n_s is shown in table B.2 (using *MATLAB ode23* for time integration with fixed step size of 0.01 s).

Dynamic response

The position of the tip of the beam using experimentally identified parameters in the model($n_s = 10$) is shown in Fig. B.7. To ensure quick damping in the beginning (before dropping), the tuning parameter β is increased by 5 times. The frequency of vibration of the beam is $f_{Em} = 3.24\ Hz$.

Table B.2: Tip deflection taking different number of flexible elements using experimentally identified lumped parameters

$\mathbf{n_s}$	$\delta^{\mathbf{u}}_{\mathbf{vL}}(\mathbf{m})$ $(m_l = 0kg)$	$\delta_{\mathbf{vL}}(\mathbf{m})$ $(m_l = 4.5kg)$	$\delta^{\mathbf{e}}_{\mathbf{vL}} = \delta_{\mathbf{vL}}$ - $\delta^{\mathbf{u}}_{\mathbf{vL}}(\mathbf{m})$
1	0.0129	0.0434	0.0305
2	0.0081	0.0537	0.0456
3	0.0072	0.0500	0.0428
4	0.0068	0.0487	0.0419
5	0.0067	0.0481	0.0414
6	0.0066	0.0478	0.0412
7	0.0066	0.0477	0411
8	0.0065	0.0475	0.0410
9	0.0065	0.0475	0.0410
10	0.0065	0.0474	0.0409

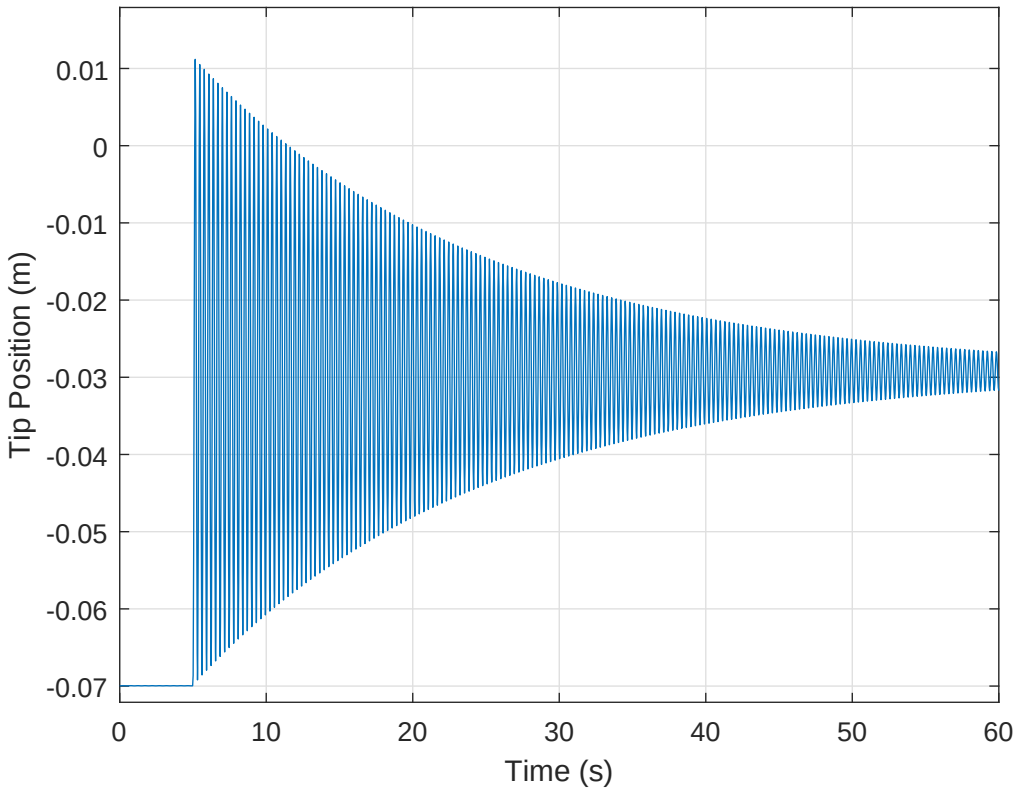

Figure B.7: Tip oscillations using experimentally identified parameters

B.4 Results

The position of the tip of the beam recorded by a camera and laser tracker is shown in Fig. B.8. The possibility of using camera for detecting the oscillations in a flexible structure seems promising. The static deflection due to 6.5 kg load at the end obtained from the experiments using a camera and static deflection approximated from the model ($n_s = 10$) are 0.0583 m and 0.0590 m respectively. Analytically computed static deflection due to 6.5 kg end load from (B.3) is 0.0524 m which is less accurate than the one approximated from the simulation model. It can be seen that the simulation model, where experimentally identified parameters are used, is accurate enough to approximate the static deflection of the real system.

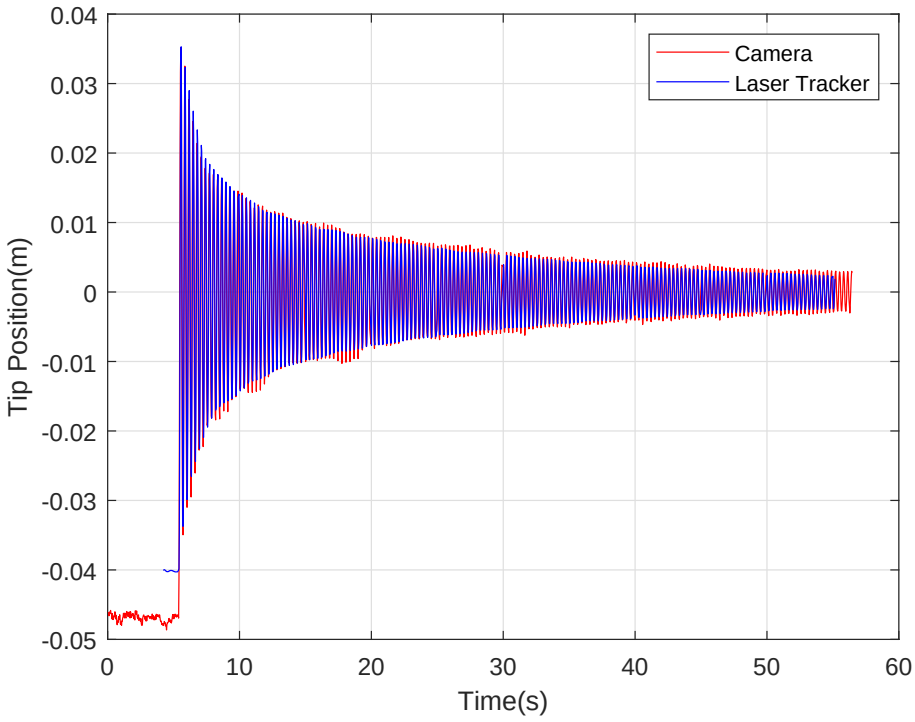

Figure B.8: Tip oscillations using camera and laser tracker

To show the validity of the model, damping load $m_d = 4.5\ kg$ is mounted at the end including the mass of the camera and the end load of $m_l = 4.5\ kg$ is dropped. The corresponding oscillations of the tip recorded by a camera are shown in Fig. B.9. The frequency of the beam vibration obtained from the experimental data collected by a camera is $f_{Ev} = 2.42\ Hz$. The oscillations of the tip obtained from the simulation model ($n_s = 10$) are shown in Fig. B.10. The frequency of vibration of the beam obtained from the simulation model is $f_{mv} = 2.51\ Hz$. The error in frequency of oscillation in the model is approximately 5 %.The tuning parameter β used in simulations is 12.

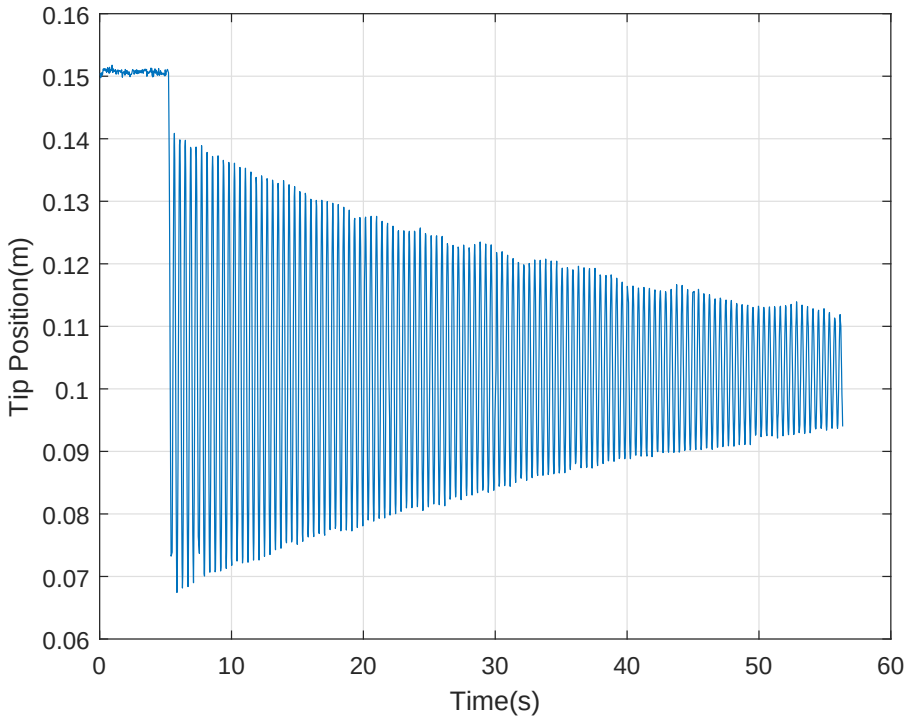

Figure B.9: Tip oscillations recorded using camera for validation

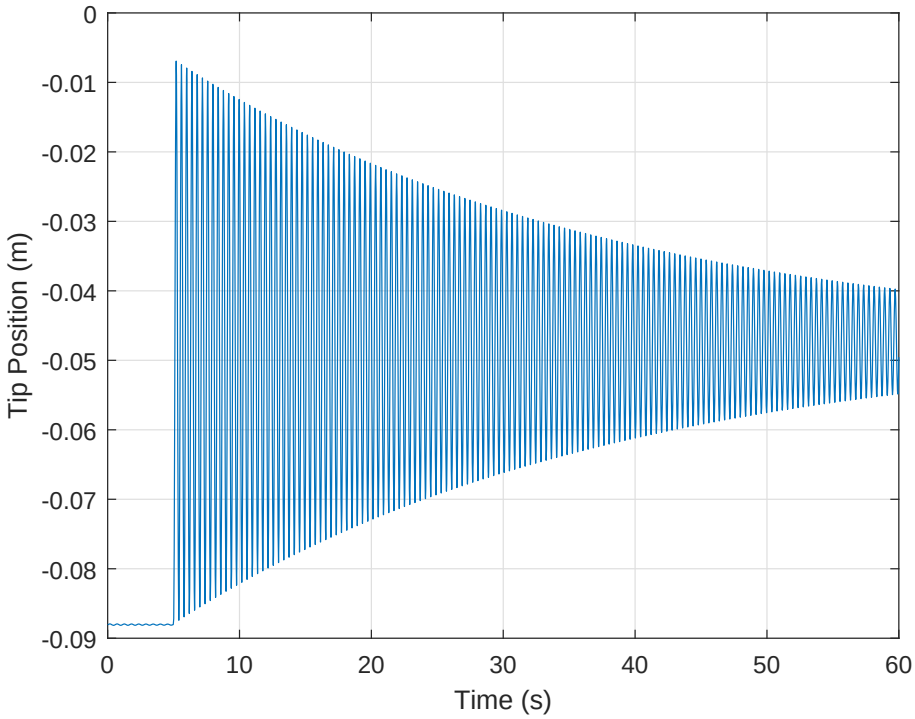

Figure B.10: Tip oscillations using experimentally identified parameters for validation

B.5 Conclusions and Discussions

The accuracy of the static deflection and computational cost increase with the increase in the number of flexible segments. A simulation model of flexible cantilever beam is developed using lumped parameter method. The static and dynamic behavior of the model are compared with the experimental results. The use of camera to identify the lumped parameters of a flexible structure experimentally is presented. The proposed method can be used to model a beam of composite/custom material whose modulus of elasticity is unknown. Although the experimental identification of the lumped parameters gives better approximation of the actual system, the analytically determined parameters could be used with reduced accuracy whenever the experiments are not feasible.

In the next step of the project, the work will be extended to the modeling of flexible beam with varying cross-section and to the development of simulation model for multi-link flexible manipulator. Furthermore, development of a procedure to tune β and ways of reducing error in the oscillation frequency will be explored.

Acknowledgment

The work was funded by the Norwegian Research Council, project number 261647/$O$20. The authors thank lab engineers at the University of Agder for helping to build the experimental setup.

References – Paper B

[1] Chang Tai Kiang, Andrew Spowage, and Chan Kuan Yoong. Review of control and sensor system of flexible manipulator. *Journal of Intelligent & Robotic Systems*, 77(1):187–213, 2015.

[2] Santosha Kumar Dwivedy and Peter Eberhard. Dynamic analysis of flexible manipulators, a literature review. *Mechanism and machine theory*, 41(7): 749–777, 2006.

[3] Rex J Theodore and Ashitava Ghosal. Comparison of the assumed modes and finite element models for flexible multilink manipulators. *The International journal of robotics research*, 14(2):91–111, 1995.

[4] Ivan Giorgio and Dionisio Del Vescovo. Non-linear lumped-parameter modeling of planar multi-link manipulators with highly flexible arms. *Robotics*, 7(4):60, 2018.

[5] Julian Wanner and Oliver Sawodny. A lumped parameter model of the boom of a mobile concrete pump. In *2019 18th European Control Conference (ECC)*, pages 2808–2813. IEEE, 2019.

[6] Carmine Maria Pappalardo and Domenico Guida. Development of a new inertial-based vibration absorber for the active vibration control of flexible structures. *Engineering Letters*, 26(3), 2018.

[7] Wisama Khalil and Maxime Gautier. Modeling of mechanical systems with lumped elasticity. In *Proceedings 2000 ICRA. Millennium Conference. IEEE International Conference on Robotics and Automation. Symposia Proceedings (Cat. No. 00CH37065)*, volume 4, pages 3964–3969. IEEE, 2000.

[8] G Zhu, Shuzhi Sam Ge, and Tong Heng Lee. Simulation studies of tip tracking control of a single-link flexible robot based on a lumped model. *Robotica*, 17 (1):71–78, 1999.

[9] Dr James Gere and Barry J Goodno. *Mechanics of Materials, SI Edition*. Cengage Learning, 2017.

[10] Daniel J Inman and Ramesh Chandra Singh. *Engineering vibration*, volume 3. Prentice Hall Englewood Cliffs, NJ, 1994.

Paper C

Dynamic Modeling of Planar Multi-Link Flexible Manipulators

Dipendra Subedi, Ilya Tyapin and Geir Hovland

This paper has been published as:

Dipendra Subedi, Ilya Tyapin and Geir Hovland. Dynamic Modeling of Planar Multi-Link Flexible Manipulators. *Robotics*, 10(2):70, 2021. doi: 10.3390/robotics10020070.

Dynamic Modeling of Planar Multi-Link Flexible Manipulators

Dipendra Subedi, Ilya Tyapin and Geir Hovland
Department of Engineering Sciences
University of Agder
4879 Grimstad, Norway

Abstract **A closed-form dynamic model of the planar multi-link flexible manipulator is presented. The assumed modes method is used with the Lagrangian formulation to obtain the dynamic equations of motion. Explicit equations of motion are derived for a three-link case assuming two modes of vibration for each link. The eigenvalue problem associated with the mass boundary conditions, which changes with the robot configuration and payload, is discussed. The time-domain simulation results and frequency-domain analysis of the dynamic model are presented to show the validity of the theoretical derivation.**

C.1 Introduction

The use of lightweight materials and the long or slender design of manipulators introduce link flexibility. Neglecting this during the modeling and control design of flexible link manipulators (FLMs) causes static steady-state and dynamic tracking and vibration errors. Lightweight flexible arms have many advantages over rigid body robots such as high payload-to-weight ratio, smaller actuators, and safer operation (due to reduced inertia) because of which they can be used in many engineering applications such as construction automation, robotic surgery, aerospace industry, and space research [1]. Some applications require the design of long and slender mechanical structures which possess some degrees of in-built flexibility because of the material used and the length of the link. Moreover, the use of lighter arms and cheaper gears by robot manufacturers is justifiable in order to compete with lower prices of the manipulators in recent years. However, the link flexibility causes deflection of the links and unwanted oscillations leading to problems in precise position control of the end-effector. To fully use the lightweight flexible manipulators, the problem of oscillations must be properly addressed by designing a suitable control algorithm to reduce the vibration of the end-effector to an acceptable range depending on the application.

The highly nonlinear dynamics of the FLMs with an infinite number of degrees of freedom (DoFs) make their control more complicated compared to the conventional

industrial robot. An accurate model of the system aids in the development of efficient and optimal model-based control algorithms for the FLMs. In this context, it is desirable to build a mathematical model of the system incorporating flexible link dynamics in an accurate and computationally affordable way. The complexity associated with the modeling of link flexibility in FLMs with infinite DoFs must be addressed by describing the system with finite DoFs and still being able to represent all the dynamically relevant properties of the actual system such as flexibility effects, dynamic interactions, and coupling effects. There are different models of the flexible bodies available in the literature depending upon the assumptions, model complexity, and accuracy. The accuracy of the models depends on the assumptions made to simplify the complexity of the FLM system. The major approaches of modeling flexible bodies include lumped parameter method (LPM), finite element method (FEM), transfer matrix method (TMM), and assumed modes method (AMM). Apart from these methods, there are many other methods that are used for obtaining the dynamic model of the FLMs which include, but are not limited to, perturbation method, pseudo-rigid body method, global mode method, and modal integration method [1].

In LPM, the link flexibility is modeled by a set of mass, spring, and damper connected in series. Although LPM is simple and easy to implement, there is difficulty in determining the spring constant accurately. In FEM, the flexible link is modeled as a combination of a finite number of elements interconnected at nodes, and the displacement at any point of the continuous element is expressed in terms of the finite number of displacements at the nodal points multiplied by the polynomial interpolation functions [2]. The FEM is applicable for complex structures and can handle nonlinear and mixed boundary conditions, but it is computationally expensive because of a large number of state-space equations. In TMM, each element of the system is represented by a transfer matrix that transfers a state vector from one end of the element to the other, and the individual element matrices are multiplied together to obtain the system transfer matrix [3]. The TMM is a frequency-domain technique but it is difficult to include the interaction between the gross motion and the flexible dynamics of the manipulator [4].

Among different modeling methods, AMM is more widely used in the literature. AMM has been used by many researchers to develop a dynamic model of flexible mechanical systems and verified experimentally [5–8]. In this method, the link flexibility is represented by a combination of spatial mode shapes and time-varying generalized coordinates. The modal series is truncated to a finite dimension based on the fact that the dynamics and overall motion of the links are dominantly governed by the first few low-frequency modes [4]. The choice of proper boundary conditions is important while using AMM for modeling FLMs. It is also equally important

to select compatible joint variables, deflection variables, and their corresponding mode shapes functions [9, 10]. Four applicable boundary conditions according to the general beam vibration theories, pinned-pinned, clamped-pinned, clamped-free, and clamped-clamped, are detailed in [11, 12].

The finite element discretization of the flexible bodies introduces a large number of DoFs which causes the simulation of the multibody system computationally expensive. Therefore, model reduction is a necessary procedure for reducing the elastic DoFs to allow an efficient simulation of the multibody system while keeping an accurate description of the predominant dynamic behavior. Model reduction involves a trade-off between the model order and the accuracy of representing the real plant dynamics by the model. In other words, the order of the dynamic model should such that it is suitable to be used for real-time control and at the same time should not lead to a spill-over effect (the problem of un-modeled residual modes) that destabilizes the system. Various model reduction techniques have been developed in the literature which can be divided into three main categories: 1. Static condensation, substructuring, and modal truncation (Guyan reduction, dynamic reduction, component mode synthesis, improved reduction system method, and system equivalent expansion reduction process), 2. Padé and Padé-type approximations (Krylov subspace method), and 3. Balancing-related truncation techniques [13, 14]. The Craig-Bampton method (component mode synthesis technique) is one of the most often applied methods for the reduction of mechanical systems [15]. The quality of the reduced models depends on the selection of the right modes in complex systems, which needs an experienced user.

In the AMM, the reduced-order dynamic model is obtained by omitting the higher frequency system dynamics from the model. It is based on the assumptions that the modes of higher frequency, omitted from the reduced-order model, have little effect on the performance of the manipulator system, as they contain little energy compared with the retained modes [8]. In this way, it is reasonable to reduce the number of vibration modes to a small finite number for obtaining the reduced-order model suitable for real-time control. Other justifications for retaining fewer modes in the model are based on the low amplitudes of high-frequency terms that are dropped and the fact that the actuators and sensors cannot operate in the high-frequency range. However, the higher modes should be included in the model if it is likely that these modes may excite the servo-loop frequencies [2]. Although FEM with more DoFs yields more precise results than AMM, AMM is preferred to FEM for real-time control purposes [16].

Accurate dynamic modeling of FLMs is of ongoing interest for researchers world-wide. The Equivalent Rigid-Link System (ERLS) approach for 3-D FLM has been developed in [17] through FEM and component mode synthesis techniques. Hamilton's

principle is applied in [16] to obtain the dynamic model of a single-link flexible manipulator stiffened with cables. In [18], AMM is used in conjunction with recursive Gibbs-Appell formulation to obtain the dynamic model of flexible cooperative mobile manipulators that are kinematically and dynamically constrained. Explicit dynamic models of the one-link flexible arm [19–27] and the two-link flexible arm [6, 28–33] have been derived and methods to obtain the mathematical model of a general n-link flexible arm [6] have been formulated based on AMM.

The research in the field of FLMs is more concentrated with the one-link, and two-link flexible manipulators than with the FLMs with more than two links. Although various formulations have been proposed for general dynamic modeling of multi-link flexible manipulators, an explicit model of manipulators with more than two links has not been well-studied in the literature. The issue about the mode shapes and eigenfrequencies variation with the robot configuration becomes more prominent for the arm with more than one link. In most of the studies that are based on the AMM, the effects of robot configurations on the mode shapes and eigenfrequencies have been ignored.

The aim of this work is to derive a dynamic model of the planar multi-link flexible manipulator using the AMM and discuss the eigenvalue problem associated with the mass boundary conditions, which changes with the robot configuration and payload. The Lagrangian method is used to derive the equations of motion, where the links are modeled as Euler-Bernoulli beams satisfying clamped-mass boundary conditions. The authors in [6] have discussed the problem of time-varying mass boundary conditions for the first link in the two-link arm. This paper further explores this problem for a three-link case. The effects of robot configurations on the mode shapes and frequencies are discussed in detail. The time-domain simulation results and frequency-domain analysis of the dynamic model of the planar three-link flexible manipulator are presented. The benefits of including passive structural damping in the simulation model are discussed.

The paper is organized into five sections as follows. Section C.2 describes the kinematic relationships and the dynamic model for a multi-link planar manipulator using the AMM and Lagrangian formulation. Section C.3 presents a dynamic model of a three-link planar flexible manipulator assuming two mode shapes for each link. The simulation results are reported in Section C.4. Conclusions and discussions follow in Section C.5.

C.2 Modeling

C.2.1 Kinematics

Consider a planar n-link flexible serial manipulator with n revolute joints. The following assumptions are made for the development of the dynamic model of the manipulator.

1. Each link of the manipulator can undergo bending deformations (transversal deflection) in the plane of motion.

2. The torsional effects and shear deformations are neglected.

3. All joints are rigid and revolute. This assumption is considered because of higher joint stiffness compared to link stiffness.

4. Link deflections are small.

Figure C.1 shows a model of a planar three-link flexible manipulator. The direct kinematic model of the planar manipulator can be formulated in terms of displacement vectors and rotation matrices. The coordinate frames for the manipulator are assigned following a methodology similar to the Denavit-Hartenberg convention: the inertial frame $(\widehat{X}_0, \widehat{Y}_0)$, the rigid body moving frame associated to link i (X_i, Y_i) located at joint i, and the flexible body moving frame associated to link i $(\widehat{X}_i, \widehat{Y}_i)$ located at the tip of link i. The rigid motion of link i is represented by the joint i position q_{ri}, and the deflection at any point x_i along the link i is described by $w_i(x_i)$, where $0 \leq x_i \leq \ell_i$, and ℓ_i is the length of the link i.

The position of a point along the link i and its endpoint referred to frame (X_i, Y_i) are given by Equations (C.1) and (C.2) respectively. Here, ${}^i\boldsymbol{r}_{i+1}$ also denotes the position of the origin of frame (X_{i+1}, Y_{i+1}) with respect to frame (X_i, Y_i). The absolute positions of the aforementioned points referred to frame $(\widehat{X}_0, \widehat{Y}_0)$ are given by Equations (C.3) and (C.4) respectively, where $\boldsymbol{W}_i$ is the cumulative transformation from inertial frame $(\widehat{X}_0, \widehat{Y}_0)$ to frame (X_i, Y_i). $\boldsymbol{W}_i$ can be calculated recursively using Equations (C.5)–(C.7), where $\boldsymbol{A}_i$ represents the joint rotation matrix, and $\boldsymbol{E}_{i-1}$ represents the influence of the elastic deformation of the previous link $i-1$ in the orientation of link i. The orientations of frames (X_i, Y_i) and $(\widehat{X}_{i-1}, \widehat{Y}_{i-1})$ with respect to frame $(\widehat{X}_0, \widehat{Y}_0)$ are given by Equations (C.8) and (C.9) respectively.

$$ {}^i\boldsymbol{p}_i = \begin{bmatrix} x_i & w_i(x_i) \end{bmatrix}^T \tag{C.1} $$

$$ {}^i\boldsymbol{r}_{i+1} = {}^i\boldsymbol{p}_i\big|_{x_i=\ell_i} = \begin{bmatrix} \ell_i & w_{ie} \end{bmatrix}^T \tag{C.2} $$

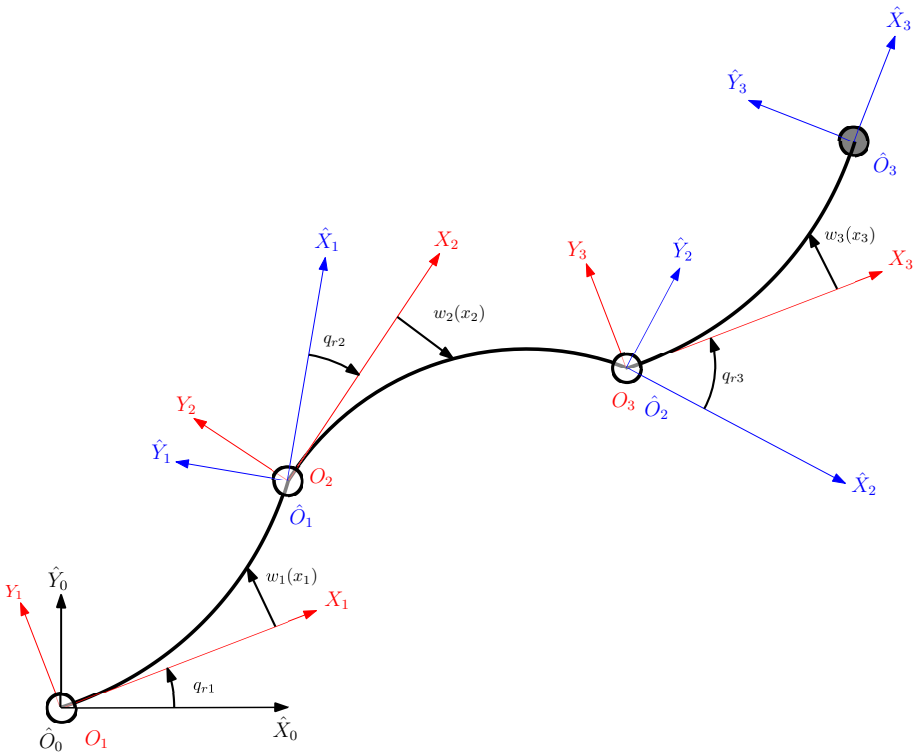

Figure C.1: Planar three-link flexible manipulator.

$$\boldsymbol{p}_i = \boldsymbol{r}_i + \boldsymbol{W}_i^i \boldsymbol{p}_i \tag{C.3}$$

$$\boldsymbol{r}_{i+1} = \boldsymbol{r}_i + \boldsymbol{W}_i^i \boldsymbol{r}_{i+1} \tag{C.4}$$

$$\boldsymbol{W}_i = \boldsymbol{W}_{i-1}\boldsymbol{E}_{i-1}\boldsymbol{A}_i = \widehat{\boldsymbol{W}}_{i-1}\boldsymbol{A}_i, \quad \boldsymbol{W}_0 = \widehat{\boldsymbol{W}}_0 = \boldsymbol{I} \tag{C.5}$$

$$\boldsymbol{A}_i = \begin{bmatrix} cos(q_i) & -sin(q_i) \\ sin(q_i) & cos(q_i) \end{bmatrix} \tag{C.6}$$

$$\boldsymbol{E}_i = \begin{bmatrix} 1 & -w'_{ie} \\ w'_{ie} & 1 \end{bmatrix}, \quad w'_{ie} = \left.\frac{\partial w_i(x_i)}{\partial x_i}\right|_{x_i=\ell_i}, \quad \boldsymbol{E}_0 = \boldsymbol{I} \tag{C.7}$$

$$\alpha_i = \sum_{j=1}^{i} q_{rj} + \sum_{k=1}^{i-1} w'_{ke}, \quad i \leq n \tag{C.8}$$

$$\widehat{\alpha}_i = \sum_{j=1}^{i-1} q_{rj} + \sum_{k=1}^{i-1} w'_{ke}, \quad i \leq n+1 \tag{C.9}$$

The differential kinematics can be obtained using the time derivatives of the

displacement and rotation as shown in Equations (C.10)–(C.19).

$$ {}^{i}\dot{\boldsymbol{p}}_i = \begin{bmatrix} 0 & \dot{w}_i \end{bmatrix}^T \tag{C.10} $$

$$ {}^{i}\dot{\boldsymbol{r}}_{i+1} = {}^{i}\dot{\boldsymbol{p}}_i\big|_{x_i=\ell_i} = \begin{bmatrix} 0 & \dot{w}_{ie} \end{bmatrix}^T \tag{C.11} $$

$$ \dot{\boldsymbol{p}}_i = \dot{\boldsymbol{r}}_i + \dot{\boldsymbol{W}}_i^i p_i + \boldsymbol{W}_i^i \dot{\boldsymbol{p}}_i \tag{C.12} $$

$$ \dot{\boldsymbol{r}}_{i+1} = \dot{\boldsymbol{r}}_i + \dot{\boldsymbol{W}}_i^i r_{i+1} + \boldsymbol{W}_i^i \dot{\boldsymbol{r}}_{i+1} \tag{C.13} $$

$$ \dot{\alpha}_i = \sum_{j=1}^{i} \dot{q}_j + \sum_{k=1}^{i-1} \dot{w}'_{ke} \tag{C.14} $$

$$ \dot{\hat{\alpha}}_i = \sum_{j=1}^{i-1} \dot{q}_j + \sum_{k=1}^{i-1} \dot{w}'_{ke} \tag{C.15} $$

$$ \dot{\boldsymbol{A}}_i = \boldsymbol{S}\boldsymbol{A}_i \dot{q}_i, \quad \boldsymbol{S} = \begin{bmatrix} 0 & -1 \\ 1 & 0 \end{bmatrix} \tag{C.16} $$

$$ \dot{\boldsymbol{E}}_i = \boldsymbol{S}\dot{w}'_{ie} \tag{C.17} $$

$$ \dot{\boldsymbol{W}}_i = \dot{\widehat{\boldsymbol{W}}}_{i-1}\boldsymbol{A}_i + \widehat{\boldsymbol{W}}_{i-1}\dot{\boldsymbol{A}}_i \tag{C.18} $$

$$ \dot{\widehat{\boldsymbol{W}}}_{i-1} = \dot{\boldsymbol{W}}_{i-1}\boldsymbol{E}_{i-1} + \boldsymbol{W}_{i-1}\dot{\boldsymbol{E}}_{i-1} \tag{C.19} $$

C.2.2 Assumed Modes Method

Flexible Links of the manipulator are modeled as Euler-Bernoulli beams of uniform density (mass per unit length) ρ_i and constant flexural rigidity $(EI)_i$. The elastic deformation $w_i(x_i, t)$ of Euler-Bernoulli beam at time t satisfies the partial differential equation given by Equation (C.20), where $c_i = \sqrt{\frac{EI}{\rho_i}}$ [6].

$$ c_i^2 \frac{\partial^4 w_i(x_i,t)}{\partial x_i^4} + \frac{\partial^2 w_i(x_i,t)}{\partial t^2} = 0, \quad i = 1, \cdots, n \tag{C.20} $$

Equation (C.20) can be solved by imposing proper boundary conditions at the base and the end of each link. Clamped boundary condition at the base of each link (assuming that the closed feedback control loop around the joint enforces the clamped assumptions [6]) is given by Equations (C.21) and (C.22).

$$ w_i(x_i,t)\big|_{x_i=0} = 0, \quad i = 1, \cdots, n \tag{C.21} $$

$$ \left.\frac{\partial w_i(x_i,t)}{\partial x_i}\right|_{x_i=0} = 0, \quad i = 1, \cdots, n \tag{C.22} $$

Assuming that the tip of each link is free of the dynamic constraints, the mass boundary conditions presented in [6, 28] are used in this paper which are given by Equations (C.23) and (C.24), where J_{Di} is the moment of inertia at the end of the

link i, m_{Di} is the actual mass at the end of the link i, and M_{Di} accounts for the contributions of the masses of the distal links, hubs, and payloads non-collocated at the end of the link i, weighted by the relative distance from the axis Y_i (shearing axis at the end of link i) [6]. The contribution of M_{Di} is not included in the mode shape analysis in [6, 28]. In this paper, the contribution of M_{Di} is considered along with the effect of robot configurations while calculating J_{Di}. The values of M_{Di} and J_{Di} are evaluated in correspondence to the unreformed configuration.

$$(EI)_i \left.\frac{\partial^2 w_i(x_i,t)}{\partial x_i^2}\right|_{x_i=\ell_i} = -J_{Di}\frac{d^2}{dt^2}\left(\left.\frac{\partial w_i(x_i,t)}{\partial x_i}\right|_{x_i=\ell_i}\right) - M_{Di}\frac{d^2}{dt^2}\left(w_i(x_i,t)|_{x_i=\ell_i}\right), \quad i = 1,\cdots,n \tag{C.23}$$

$$(EI)_i \left.\frac{\partial^3 w_i(x_i,t)}{\partial x_i^3}\right|_{x_i=\ell_i} = m_{Di}\frac{d^2}{dt^2}\left(w_i(x_i,t)|_{x_i=\ell_i}\right) + M_{Di}\frac{d^2}{dt^2}\left(\left.\frac{\partial w_i(x_i,t)}{\partial x_i}\right|_{x_i=\ell_i}\right), \quad i = 1,\cdots,n \tag{C.24}$$

Using AMM, the link deflection is expressed using a finite-dimensional model of order n_f as shown in Equation (C.25), where $q_{fij}(t)$ is the time-varying variable related to the spatial assumed mode shape $\phi_{ij}(x_i)$ of link i and mode of vibration j [6].

$$w_i(x_i,t) = \sum_{j=1}^{n_f} \phi_{ij}(x_i) q_{fij}(t) \tag{C.25}$$

Using separation of variables, shown in Equation (C.25), the solution of Equation (C.20) can be written as Equation (C.26), where $a_{ij} = \omega_{ij}^2$ is a positive constant, and ω_{ij} is the j^{th} natural angular frequency of link i.

$$\frac{c_i^2}{\phi_{ij}(x_i)}\frac{d^4\phi_{ij}(x_i)}{dx_i^4} = -\frac{1}{q_{fij}(t)}\frac{d^2 q_{fij}(t)}{dt^2} = a_{ij} = \omega_{ij}^2 \tag{C.26}$$

From Equation (C.26), the time harmonic function $q_{fij}(t)$ and the spatial assumed mode shapes $\phi_{ij}(x_i)$ are given by Equations (C.27) and (C.28) respectively, where β_{ij} is given by Equation (C.29).

$$q_{fij}(t) = e^{\sqrt{-1}\omega_{ij}^2 t} \tag{C.27}$$

$$\phi_{ij}(x_i) = c_{1ij}sin(\beta_{ij}x_i) + c_{2ij}cos(\beta_{ij}x_i) + c_{3ij}sinh(\beta_{ij}x_i) + c_{4ij}cosh(\beta_{ij}x_i) \tag{C.28}$$

$$\beta_{ij}^4 = \frac{\omega_{ij}^2}{c_i^2} = \frac{\rho_i \omega_{ij}^2}{EI} \tag{C.29}$$

Additionally, Equation (C.26) is rearranged to obtain Equation (C.30).

$$\frac{\ddot{q}_{fij}(t)}{q_{fij}(t)} = -\frac{\beta_{ij}^4 (EI)_i}{\rho_i} \tag{C.30}$$

The values of c_{1ij}, c_{2ij}, c_{3ij}, c_{4ij}, and the natural frequencies ω_{ij} are calculated from the boundary conditions. The boundary conditions given by Equations (C.21) and (C.22) are modified according to the AMM as

$$q_{fij}(t)\phi_{ij}(x_i)\big|_{x_i=0} = 0 \implies \phi_{ij}(x_i)\big|_{x_i=0} = 0, \tag{C.31}$$

$$q_{fij}(t)\frac{\partial \phi_{ij}(x_i)}{\partial x_i}\bigg|_{x_i=0} = 0 \implies \phi'_{ij}(x_i)\big|_{x_i=0} = 0. \tag{C.32}$$

Similarly, the boundary conditions given by Equations (C.23) and (C.24) are modified according to the AMM as

$$(EI)_i\, \phi''_{ij}(x_i)\big|_{x_i=\ell_i} q_{fij}(t) = -J_{Di}\, \phi'_{ij}(x_i)\big|_{x_i=\ell_i} \ddot{q}_{fij}(t) - M_{Di}\, \phi_{ij}(x_i)|_{x_i=\ell_i} \ddot{q}_{fij}(t), \tag{C.33}$$

$$(EI)_i\, \phi'''_{ij}(x_i)\big|_{x_i=\ell_i} q_{fij}(t) = m_{Di}\, \phi_{ij}(x_i)|_{x_i=\ell_i} \ddot{q}_{fij}(t) + M_{Di}\, \phi'_{ij}(x_i)\big|_{x_i=\ell_i} \ddot{q}_{fij}(t). \tag{C.34}$$

Substituting Equation (C.30) in Equations (C.33) and (C.34), we get

$$\phi''_{ij}(x_i)\big|_{x_i=\ell_i} - \frac{\beta_{ij}^4}{\rho_i}\left[J_{Di}\, \phi'_{ij}(x_i)\big|_{x_i=\ell_i} + M_{Di}\, \phi_{ij}(x_i)|_{x_i=\ell_i}\right] = 0, \tag{C.35}$$

$$\phi'''_{ij}(x_i)\big|_{x_i=\ell_i} + \frac{\beta_{ij}^4}{\rho_i}\left[m_{Di}\, \phi_{ij}(x_i)|_{x_i=\ell_i} + M_{Di}\, \phi'_{ij}(x_i)\big|_{x_i=\ell_i}\right] = 0. \tag{C.36}$$

Substituting Equation (C.28) in Equations (C.31) and (C.32), we get

$$c_{3ij} = -c_{1ij}, \quad \text{and} \quad c_{4ij} = -c_{2ij}. \tag{C.37}$$

Similarly, substituting Equation (C.28) in Equations (C.35) and (C.36), we get a homogeneous system of equations of the form

$$\boldsymbol{F}(\beta_{ij}) \begin{bmatrix} c_{1ij} \\ c_{2ij} \end{bmatrix} = \mathbf{0}, \quad \boldsymbol{F}(\beta_{ij}) = \begin{bmatrix} F_{11} & F_{12} \\ F_{21} & F_{22} \end{bmatrix}, \tag{C.38}$$

$$\begin{aligned} F_{11} = \quad & \rho_i[\sin(\beta_{ij}\ell_i) + \sinh(\beta_{ij}\ell_i)] + \beta_{ij}^2[M_{Di}(\sin(\beta_{ij}\ell_i) - \sinh(\beta_{ij}\ell_i)) + \\ & + J_{Di}\beta_{ij}(\cos(\beta_{ij}\ell_i) - \cosh(\beta_{ij}\ell_i))], \\ F_{12} = \quad & \rho_i[\cos(\beta_{ij}\ell_i) + \cosh(\beta_{ij}\ell_i)] + \beta_{ij}^2[M_{Di}(\cos(\beta_{ij}\ell_i) - \cosh(\beta_{ij}\ell_i)) - \end{aligned}$$

$$
\begin{aligned}
& - J_{Di}\beta_{ij}(\sin(\beta_{ij}\ell_i) + \sinh(\beta_{ij}\ell_i))], \\
F_{21} = \quad & \rho_i[\cos(\beta_{ij}\ell_i) + \cosh(\beta_{ij}\ell_i)] - \beta_{ij}[m_{Di}(\sin(\beta_{ij}\ell_i) - \sinh(\beta_{ij}\ell_i)) + \\
& + M_{Di}\beta_{ij}(\cos(\beta_{ij}\ell_i) - \cosh(\beta_{ij}\ell_i))], \\
F_{22} = \quad & - \beta_{ij}[m_{Di}[\cos(\beta_{ij}\ell_i) - \cosh(\beta_{ij}\ell_i)] - M_{Di}\beta_{ij}[\sin(\beta_{ij}\ell_i) + \sinh(\beta_{ij}\ell_i)]] - \\
& - \rho_i[\sin(\beta_{ij}\ell_i) - \sinh(\beta_{ij}\ell_i)],
\end{aligned}
$$

where β_{ij} for each link i and mode of vibration j is obtained from the nontrivial solution of Equation (C.38), i.e. $det(\boldsymbol{F}(\beta_{ij})) = 0$, which results into the transcendental equation given by Equation (C.39). The solutions (n_f positive roots) of Equation (C.39) ($\beta_{ij} \in [\beta_{i1} \cdots \beta_{in_f}]$) are obtained numerically and the natural frequencies ω_{ij} are obtained using Equation (C.29). It can be noted that the values of β_{ij} depends explicitly on m_{Di}, J_{Di}, and M_{Di}.

$$
\begin{aligned}
& \rho_i^2 + \rho_i^2 \cos(\beta_{ij}\ell_i)\cosh(\beta_{ij}\ell_i) + J_{Di}\beta_{ij}^4 m_{Di} + M_{Di}^2\beta_{ij}^4 \cos(\beta_{ij}\ell_i)\cosh(\beta_{ij}\ell_i) + \\
& + \beta_{ij} m_{Di}\rho_i \cos(\beta_{ij}\ell_i)\sinh(\beta_{ij}\ell_i) = M_{Di}^2\beta_{ij}^4 + \beta_{ij} m_{Di}\rho_i \cosh(\beta_{ij}\ell_i)\sin(\beta_{ij}\ell_i) + \\
& + J_{Di}\beta_{ij}^4 m_{Di}\cos(\beta_{ij}\ell_i)\cosh(\beta_{ij}\ell_i) + J_{Di}\beta_{ij}^3\rho_i \cos(\beta_{ij}\ell_i)\sinh(\beta_{ij}\ell_i) + \\
& + J_{Di}\beta_{ij}^3\rho_i \cosh(\beta_{ij}\ell_i)\sin(\beta_{ij}\ell_i) + 2M_{Di}\beta_{ij}^2\rho_i \sin(\beta_{ij}\ell_i)\sinh(\beta_{ij}\ell_i)
\end{aligned} \tag{C.39}
$$

The constants c_{1ij} and c_{2ij} are calculated by substituting the corresponding values of β_{ij} in Equation (C.38) and scaled using the orthonormalization condition of the modes of vibration represented by Equation (C.40), where δ_{jk} is the Kronecker delta symbol, and $m_{\ell i}$ is the mass of link i.

$$
\int_0^{\ell_i} \left\{ \begin{array}{l} \rho_i\phi_{ij}(x_i)\,\phi_{ik}(x_i)\,dx_i + m_{Di}\phi_{ij}(\ell_i)\,\phi_{ik}(\ell_i) + M_{Di}\phi_{ij}(\ell_i)\,\phi'_{ik}(\ell_i) + \\ + J_{Di}\phi'_{ij}(\ell_i)\,\phi'_{ik}(\ell_i) + M_{Di}\phi'_{ij}(\ell_i)\,\phi_{ik}(\ell_i) \end{array} \right\} = m_{\ell i}\delta_{jk} \tag{C.40}
$$

C.2.3 Equations of Motion

Consider m_{hi} is the mass of hub i, m_p is the mass of payload, $J_{\ell i}$ is the inertia of link i about the axis at its center of mass, J_{hi} is the inertia of hub i about the joint i axis, J_p is the inertia of the payload about the axis at its center of mass, $d_{\ell ij}$ is the distance of the center of mass of link i from joint j axis, d_{hij} is the distance of the center of mass of hub i from joint j axis, and d_{pj} is the distance of the center of mass of the payload from the joint j axis.

The equations of motion of a planar n-link manipulator can be derived using the Lagrangian method. The total kinetic energy of the manipulator system (T) is given by the sum of the kinetic energy of links (T_l), hubs (T_h), and the payload (T_p) as

shown in Equation (C.41).

$$T = \sum_{i=1}^{n} T_{hi} + \sum_{i=1}^{n} T_{\ell i} + T_p \tag{C.41}$$

$$T_{hi} = \frac{1}{2} m_{hi} \dot{\boldsymbol{r}}_i^{\mathrm{T}} \dot{\boldsymbol{r}}_i + \frac{1}{2} J_{hi} \dot{\alpha}_i^2 \tag{C.42}$$

$$T_{\ell i} = \frac{1}{2} \rho_i \int_0^{\ell_i} \dot{\boldsymbol{p}}_i^{\mathrm{T}}(x_i)\, \dot{\boldsymbol{p}}_i(x_i)\, dx_i \tag{C.43}$$

$$T_p = \frac{1}{2} m_p \dot{\boldsymbol{r}}_{n+1}^{\mathrm{T}} \dot{\boldsymbol{r}}_{n+1} + \frac{1}{2} J_p \dot{\hat{\alpha}}_{n+1}^2 \tag{C.44}$$

The potential energy of the robot is due to gravity and link flexibility (elasticity). The total potential energy of the robot is given by the sum of elastic energy stored in n-links ($U_{e\ell}$), gravitational potential energy stored in n-links ($U_{g\ell}$), n-hubs (U_{gh}), and the payload (U_{gp}), as shown in Equation (C.45), where $\boldsymbol{g}_v$ is the gravity acceleration vector.

$$U = \sum_{i=1}^{n} U_{e\ell i} + \sum_{i=1}^{n} U_{ghi} + \sum_{i=1}^{n} U_{g\ell i} + U_{gp} \tag{C.45}$$

$$U_{e\ell i} = \frac{1}{2} (EI)_i \int_0^{\ell_i} \left(\frac{\partial^2 w_i(x_i, t)}{\partial x_i^2} \right)^2 dx_i \tag{C.46}$$

$$U_{ghi} = -m_{hi} \boldsymbol{g}_v^T \boldsymbol{r}_i \tag{C.47}$$

$$U_{g\ell i} = -\boldsymbol{g}_v^T \rho_i \int_0^{\ell_i} \boldsymbol{p}_i(x_i) dx_i \tag{C.48}$$

$$U_{gp} = -m_p \boldsymbol{g}_v^T \boldsymbol{r}_{n+1} \tag{C.49}$$

The spatial dependence present in the energy terms (Equations (C.41)–(C.45)) can be resolved and simplified by introducing the following constant parameters [6]:

$$v_{ij} = \int_0^{\ell_i} \rho_i \phi_{ij}(x_i) dx_i \tag{C.50}$$

$$w_{ij} = \int_0^{\ell_i} \rho_i \phi_{ij}(x_i) x_i dx_i \tag{C.51}$$

$$z_{ijk} = \int_0^{\ell_i} \rho_i \phi_{ij}(x) \phi_{ik}(x) dx \tag{C.52}$$

$$k_{ijk} = \int_0^{\ell_i} (EI)_i \phi_{ij}''(x) \phi_{ik}''(x) dx = m_{\ell_i} \omega_{ij}^2 \delta_{jk} \tag{C.53}$$

Here, v_{ij} and w_{ij} are deformation moments of order zero and one of mode j of link i; z_{ijk} is the cross moment of modes j and k of link i; and k_{ijk} is the cross elasticity coefficient of modes j and k of link i.

The Lagrangian in terms of $N = n + \sum_{i=1}^{n} n_f$ generalized coordinates is given by Equation (C.54).

$$L = T - U \tag{C.54}$$

The Euler-Lagrange equation can be written as Equation (C.55), where $q_i(t)$ are the generalized coordinates, τ_i are the generalized forces acting on q_i, q_r are the generalized coordinates associated with rigid dynamics, and q_f are the generalized coordinates associated with flexible dynamics.

$$\frac{d}{dt}\left(\frac{\partial L}{\partial \dot{q}_i}\right) - \frac{\partial L}{\partial q_i} = \tau_i, \qquad i = 1, \ldots, N, \tag{C.55}$$

where

$$\boldsymbol{q} = \begin{bmatrix} q_1 & q_2 & \cdots & q_N \end{bmatrix}^T = \begin{bmatrix} \boldsymbol{q}_r & \boldsymbol{q}_f \end{bmatrix}^T, \tag{C.56}$$

$$\boldsymbol{q}_r = \begin{bmatrix} q_{r1} & q_{r2} & \cdots & q_{rn} \end{bmatrix}^T, \tag{C.57}$$

$$\boldsymbol{q}_f = \begin{bmatrix} q_{f11} & q_{f12} & \cdots & q_{f1n_f} \cdots & q_{fn1} & q_{fn2} & \cdots & q_{fnn_f} \end{bmatrix}^T. \tag{C.58}$$

Equation (C.55) can be written in a standard form

$$\boldsymbol{M}(\boldsymbol{q})\ddot{\boldsymbol{q}} + \boldsymbol{c}(\boldsymbol{q}, \dot{\boldsymbol{q}}) + \boldsymbol{g}(\boldsymbol{q}) + \boldsymbol{K}\boldsymbol{q} = \boldsymbol{\tau}, \tag{C.59}$$

where $\boldsymbol{M}(\boldsymbol{q})$ is the inertia matrix, $\boldsymbol{c}(\boldsymbol{q}, \dot{\boldsymbol{q}})$ is the vector of Coriolis and centripetal effects, $\boldsymbol{g}(\boldsymbol{q})$ is the gravity term, and $\boldsymbol{K}$ is the rigidity modal matrix. Joint viscous friction and link structural damping can be included by adding a damping matrix $\boldsymbol{D}$ as

$$\boldsymbol{M}(\boldsymbol{q})\ddot{\boldsymbol{q}} + \boldsymbol{c}(\boldsymbol{q}, \dot{\boldsymbol{q}}) + \boldsymbol{g}(\boldsymbol{q}) + \boldsymbol{K}\boldsymbol{q} + \boldsymbol{D}\dot{\boldsymbol{q}} = \boldsymbol{\tau}. \tag{C.60}$$

Equation (C.60) is transformed to obtain the direct dynamic model of the robot as

$$\ddot{\boldsymbol{q}} = \boldsymbol{M}(\boldsymbol{q})^{-1}(\boldsymbol{\tau} - \boldsymbol{c}(\boldsymbol{q}, \dot{\boldsymbol{q}}) - \boldsymbol{g}(\boldsymbol{q}) - \boldsymbol{K}\boldsymbol{q} - \boldsymbol{D}\dot{q}). \tag{C.61}$$

The components of vector $\boldsymbol{c}(\boldsymbol{q}, \dot{\boldsymbol{q}})$ can be evaluated through the Christoffel symbols as shown in Equation (C.62).

$$c_i = \sum_{j=1}^{N}\sum_{k=1}^{N}\left(\frac{\delta M_{ij}}{\delta q_k} - \frac{1}{2}\frac{\delta M_{jk}}{\delta q_i}\right)\dot{q}_j\dot{q}_k, \qquad i = 1 \cdots N \tag{C.62}$$

The components of vector $\boldsymbol{g}(\boldsymbol{q})$ can be determined using Equation (C.63), where $U_g = \sum_{i=1}^{n} U_{ghi} + \sum_{i=1}^{n} U_{g\ell i} + U_{gp}$ is the total gravitational potential energy of the system.

$$g_i = \frac{\delta U_g}{\delta q_i}, \qquad i = 1 \cdots N \tag{C.63}$$

The components of matrix $\boldsymbol{K}$ can be determined using Equation (C.64), where $U_{e\ell} = \sum_{i=1}^{n} U_{\ell i}$ is the total elastic potential energy of the system.

$$\boldsymbol{K}\boldsymbol{q} = \frac{\delta U_{e\ell}}{\delta \boldsymbol{q}} \tag{C.64}$$

Because of the orthonormalization of mode shapes, it can be noted that the stiffness matrix $\boldsymbol{K}$ reduces to a diagonal matrix as in Equation (C.65), where k_i is the stiffness coefficient given by Equation (C.66). In Equation (C.66), $k_i = 0$ for $1 \leq i \leq n$ is based on the assumption that all joints are considered rigid. If joint flexibility is to be taken into account, then $k_i \neq 0$ for $1 \leq i \leq n$.

$$\boldsymbol{K} = \begin{bmatrix} k_1 & & \\ & \ddots & \\ & & k_N \end{bmatrix} \tag{C.65}$$

$$k_i = \begin{cases} 0 & \text{if} \quad 1 \leq i \leq n, \\ m_{\ell_u}\omega_{uv}^2 & \text{if} \quad n + (u-1)n_f < i \leq n + un_f; \quad u = 1, \cdots, n; \quad v = 1 \cdots n_f. \end{cases} \tag{C.66}$$

The damping matrix $\boldsymbol{D}$ is calculated using Equation (C.67), where d_i is the damping coefficient given by Equation (C.68), ζ_{uv} represents damping ratio corresponding to mode v of link u, and b_i represents viscus damping constant corresponding to joint i [7, 34].

$$\boldsymbol{D} = \begin{bmatrix} d_1 & & \\ & \ddots & \\ & & d_N \end{bmatrix}, \tag{C.67}$$

$$d_i = \begin{cases} b_i & \text{if} \quad 1 \leq i \leq n, \\ 2\zeta_{uv}\sqrt{k_i/m_{\ell_u}} & \text{if} \quad n + (u-1)n_f < i \leq n + un_f; u = 1, \cdots, n; v = 1 \cdots n_f. \end{cases} \tag{C.68}$$

C.3 Explicit Dynamic Model of a Three-Link Flexible Manipulator

Consider a planar manipulator with three links ($n = 3$) with two assumed mode shapes for each link ($n_f = 2$). The vector of generalized coordinates becomes $\boldsymbol{q} = \begin{bmatrix} q_{r1} & q_{r2} & q_{r3} & q_{f11} & q_{f12} & q_{f21} & q_{f22} & q_{f31} & q_{f32} \end{bmatrix}^T$. The values of m_{Di}, J_{Di}, and M_{Di} are calculated considering the undeformed configuration of the manipulator as follows:

Link 1:

$$\left.\begin{aligned} J_{D1} &= J_{h2} + J_{\ell 2} + m_{\ell 2} d_{l22}^2 + J_{h3} + m_{h3} d_{h32}^2 + J_{\ell 3} + m_{\ell 3} d_{\ell 32}^2 + J_p + m_p d_{p2}^2, \\ m_{D1} &= m_{h2} + m_{\ell 2} + m_{h3} + m_{\ell 3} + m_p, \\ M_{D1} &= m_{\ell 2} d_{\ell 22} \cos q_2 + m_{h3} d_{h32} \cos q_2 + m_{\ell 3} \left[d_{h32} \cos q_2 + d_{\ell 33} \cos (q_2 + q_3) \right] + \\ &\quad + m_p \left[d_{h32} \cos q_2 + d_{p3} \cos (q_2 + q_3) \right], \end{aligned}\right\} \tag{C.69}$$

where

$$\left.\begin{aligned} d_{\ell 22} &= \tfrac{\ell_2}{2}, \\ d_{h32} &= \ell_2, \\ d_{\ell 32} &= \ell_2 + \tfrac{\ell_3}{2} \cos q_3, \\ d_{p2} &= \ell_2 + \ell_3 \cos q_3, \\ d_{\ell 33} &= \tfrac{\ell_3}{2}, \\ d_{p3} &= \ell_3. \end{aligned}\right\} \tag{C.70}$$

Link 2:

$$\left.\begin{aligned} J_{D2} &= J_{h3} + J_{\ell 3} + m_{\ell 3} d_{\ell 33}^2 + J_p + m_p d_{p3}^2, \\ m_{D2} &= m_{h3} + m_{\ell 3} + m_p, \\ M_{D2} &= m_{\ell 3} d_{\ell 33} \cos q_3 + m_p d_{p3} \cos q_3, \end{aligned}\right\} \tag{C.71}$$

where

$$\left.\begin{aligned} d_{\ell 33} &= \tfrac{\ell_3}{2}, \\ d_{p3} &= \ell_3. \end{aligned}\right\} \tag{C.72}$$

Link 3:

$$\left.\begin{aligned} J_{D3} &= J_p, \\ m_{D3} &= m_p, \\ M_{D3} &= 0. \end{aligned}\right\} \tag{C.73}$$

From Equations (C.69)–(C.71), it is evident that J_{D1}, M_{D1}, and M_{D2} depend on the manipulator configuration. In particular, M_{D1} depends on the position of both joint 2 (q_{r2}) and joint 3 (q_{r3}), whereas J_{D1} and M_{D2} depend only on the position of joint 3 (q_{r3}). Therefore, for the mode shapes computations, J_{D1}, M_{D1}, and M_{D2} should be updated as functions of the manipulator configurations. However, this increases the computational complexity of the model.

To solve this problem, a lookup table is created after offline calculation of J_{D1}, M_{D1}, and M_{D2} and the corresponding mode shapes for different robot configurations that are divided uniformly within the joint limits of the manipulator. If the robot configuration is different than the one available in the lookup table, the offline calculated values are interpolated. In this way, the online computation complexity is reduced for updating different parameters (such as $\phi_{ije} = \phi_{ij}(x_i)|_{x_i=\ell_i}$, $\phi'_{ie} = \left.\frac{\delta\phi_{ij}(x_i)}{\delta x_i}\right|_{x_i=\ell_i}$, ω_{ij}, v_{ij}, w_{ij}, and z_{ijk}), which are dependent on J_{D1}, M_{D1}, and M_{D2}, as a function of manipulator configurations.

For each flexible link i, the transcendental equation (Equation (C.39)) is solved numerically to obtain its first $n_f = 2$ positive roots $\beta_{ij} \in \begin{bmatrix}\beta_{i1} & \beta_{i2}\end{bmatrix}$ for $i = 1, 2, 3$ and $j = 1, 2$. Using the corresponding values of β_{ij} in Equation (C.38), the constants c_{1ij} and c_{2ij} are determined and scaled using Equation (C.40). Thus, obtained values of β_{ij}, c_{1ij}, c_{2ij}, c_{3ij} and c_{4ij} (c_{3ij} and c_{4ij} are calculated from Equation (C.37)) are used to obtain the spatial assumed mode shapes $\phi_{ij}(x)$ using Equation (C.28).

The inertia matrix $\boldsymbol{M}(\boldsymbol{q})$, vector of Coriolis and centripetal effects $\boldsymbol{c}(\boldsymbol{q}, \dot{\boldsymbol{q}})$ and gravity term $\boldsymbol{g}(\boldsymbol{q})$ in Equation (C.60) for the three-link planar robot are obtained symbolically using Maple (Because of limited space, the expressions are not included in this paper but can be obtained from authors). The stiffness matrix $\boldsymbol{K}$ and the

damping matrix $\boldsymbol{D}$ are given by Equations (C.74) and (C.75) respectively,

$$\boldsymbol{K} = \begin{bmatrix} k_1 & 0 & 0 & 0 & 0 & 0 & 0 & 0 & 0 \\ 0 & k_2 & 0 & 0 & 0 & 0 & 0 & 0 & 0 \\ 0 & 0 & k_3 & 0 & 0 & 0 & 0 & 0 & 0 \\ 0 & 0 & 0 & k_4 & 0 & 0 & 0 & 0 & 0 \\ 0 & 0 & 0 & 0 & k_5 & 0 & 0 & 0 & 0 \\ 0 & 0 & 0 & 0 & 0 & k_6 & 0 & 0 & 0 \\ 0 & 0 & 0 & 0 & 0 & 0 & k_7 & 0 & 0 \\ 0 & 0 & 0 & 0 & 0 & 0 & 0 & k_8 & 0 \\ 0 & 0 & 0 & 0 & 0 & 0 & 0 & 0 & k_9 \end{bmatrix} \tag{C.74}$$

$$\boldsymbol{D} = \begin{bmatrix} d_1 & 0 & 0 & 0 & 0 & 0 & 0 & 0 & 0 \\ 0 & d_2 & 0 & 0 & 0 & 0 & 0 & 0 & 0 \\ 0 & 0 & d_3 & 0 & 0 & 0 & 0 & 0 & 0 \\ 0 & 0 & 0 & d_4 & 0 & 0 & 0 & 0 & 0 \\ 0 & 0 & 0 & 0 & d_5 & 0 & 0 & 0 & 0 \\ 0 & 0 & 0 & 0 & 0 & d_6 & 0 & 0 & 0 \\ 0 & 0 & 0 & 0 & 0 & 0 & d_7 & 0 & 0 \\ 0 & 0 & 0 & 0 & 0 & 0 & 0 & d_8 & 0 \\ 0 & 0 & 0 & 0 & 0 & 0 & 0 & 0 & d_9 \end{bmatrix} \tag{C.75}$$

where $k_1 = k_2 = k_3 = 0$, $k_4 = m_{\ell_1}\omega_{11}^2$, $k_5 = m_{\ell_1}\omega_{12}^2$, $k_6 = m_{\ell_2}\omega_{21}^2$, $k_7 = m_{\ell_2}\omega_{22}^2$, $k_8 = m_{\ell_3}\omega_{31}^2$, $k_9 = m_{\ell_3}\omega_{32}^2$, $d_1 = b_1$, $d_2 = b_2$, $d_3 = b_3$, $d_4 = 2\zeta_{11}\sqrt{k_4/m_{\ell_1}}$, $d_5 = 2\zeta_{12}\sqrt{k_5/m_{\ell_1}}$, $d_6 = 2\zeta_{21}\sqrt{k_6/m_{\ell_2}}$, $d_7 = 2\zeta_{22}\sqrt{k_7/m_{\ell_2}}$, $d_8 = 2\zeta_{31}\sqrt{k_8/m_{\ell_3}}$, and $d_9 = 2\zeta_{32}\sqrt{k_9/m_{\ell_3}}$.

C.4 Simulation Results

The planar flexible manipulator used in this study has three links of dimensions as shown in Table C.1, where each link is a hollow rectangular aluminium beam. The parameters of the manipulator used in the simulation studies are listed in Table C.2.

Table C.1: Link dimensions.

	Length (m)	**Width (m)**	**Height (m)**	**Thickness (m)**
Link 1	1.5	50×10^{-3}	50×10^{-3}	4×10^{-3}
Link 2	1.5	40×10^{-3}	40×10^{-3}	3×10^{-3}
Link 3	1.5	30×10^{-3}	30×10^{-3}	2.5×10^{-3}

Table C.2: Simulation Parameters.

Parameters	**Values**
ℓ_1	1.5 m
ℓ_2	1.5 m
ℓ_3	1.5 m
ρ_1	1.9872 kgm^{-1}
ρ_2	1.1988 kgm^{-1}
ρ_3	0.7425 kgm^{-1}
$m_{\ell 1}$	2.9808 kg
$m_{\ell 2}$	1.7982 kg
$m_{\ell 3}$	1.1138 kg
$(EI)_1$	1.8045×10^4 Nm^2
$(EI)_2$	7.0361×10^3 Nm^2
$(EI)_3$	2.4114×10^3 Nm^2
$J_{\ell 1}$	0.5589 kgm^2
$J_{\ell 2}$	0.3372 kgm^2
$J_{\ell 3}$	0.2088 kgm^2
J_{h1}	0.0022 kgm^2
J_{h2}	6.631×10^{-4} kgm^2
J_{h3}	7.0100×10^{-5} kgm^2
J_p	3.2×10^{-4} kgm^2
$\boldsymbol{g}_v$	$\begin{bmatrix}0 & -9.81\end{bmatrix}^T$ ms^{-2}

C.4.1 Effect of Payload on Mode Shapes and Eigenfrequencies

The effect of payload on the mode shapes and eigenfrequencies is studied with fixed robot configuration ($q_{r2} = 0°$ and $q_{r3} = 0°$). The mode shapes are calculated with the step of 0.01 m. The mode shapes under no payload ($m_p = 0$ kg) and nominal payload ($m_p = 2$ kg) conditions are shown in Figure C.2a,b respectively. The effect of payload on the mode shapes of link 3 is more evident compared to its effect on the other two links. The eigenfrequencies for links 1, 2, and 3 under no payload and nominal payload conditions are tabulated in Table C.3. The results show that the eigenfrequencies decrease with the increase in payload.

Table C.3: Effect of payload on eigenfrequencies.

	Eigenfrequencies (Hz) $\boldsymbol{f_i} = \begin{bmatrix}\boldsymbol{f_{i1}} & \boldsymbol{f_{i2}}\end{bmatrix}$	
	$\boldsymbol{m_p = 0}$ **kg**	$\boldsymbol{m_p = 2}$ **kg**
Link 1	$\begin{bmatrix}2.56 & 17.38\end{bmatrix}$	$\begin{bmatrix}2.02 & 15.03\end{bmatrix}$
Link 2	$\begin{bmatrix}4.34 & 28.74\end{bmatrix}$	$\begin{bmatrix}2.67 & 18.82\end{bmatrix}$
Link 3	$\begin{bmatrix}14.17 & 88.82\end{bmatrix}$	$\begin{bmatrix}4.90 & 63.97\end{bmatrix}$

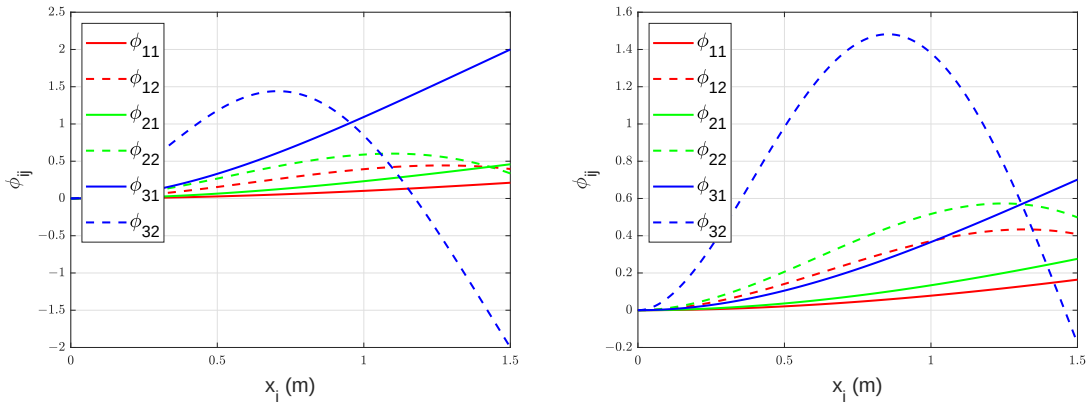

(**a**) (**b**)

Figure C.2: (**a**) Mode shapes for link 1, 2, and 3 with no payload ($m_p = 0$ kg), $q_{r2} = 0°$, and $q_{r3} = 0°$, (**b**) Mode shapes for link 1, 2, and 3 with nominal payload ($m_p = 2$ kg), $q_{r2} = 0°$, and $q_{r3} = 0°$.

C.4.2 Effect of Arm Configuration on Mode Shapes and Eigenfrequencies

The effect of arm configuration on mode shapes and eigenfrequencies is studied by dividing the arm configuration (q_{r1}, q_{r1}, and q_{r1}) uniformly from $-180°$ to $180°$ with a step of $30°$. It can be noticed (see Equations (C.69) and (C.71)) that the changes in the manipulator configuration, change the boundary values J_{D1}, M_{D1}, and M_{D2}, which are shown in Figure C.3. This in turn modifies the mode shapes and eigenfrequencies of link 1 and link 2. To study the effect of change in manipulator configuration, the mode shapes and eigenfrequencies are calculated with nominal payload ($m_p = 2$ kg) for different arm positions.

The change in q_{r1} does not alter the mode shapes (and eigenfrequencies) of any of the links. The variation in mode shapes of link 1 with the change in q_{r2} keeping q_{r3} ($= 0$) constant is shown in Figure C.4a. Similarly, Figure C.4b shows the change in mode shapes of link 1 with the change in q_{r3} keeping $q_{r2}(= 0°)$ constant. For link 2, the change in q_{r1} and q_{r2} does not affect its mode shapes (and eigenfrequencies). The change in mode shapes of link 2 occurs with the change in q_{r3} which is shown in Figure C.4c. The mode shapes (and eigenfrequencies) of link 3 remain unaffected with any changes in manipulator configuration. The constant mode shapes of link 3 for all manipulator configurations with nominal payload are given in Figure C.2b.

The overall effect of arm configuration on mode shapes is visualized in Figure C.5, where only a few manipulator configurations are shown along with the corresponding mode shapes of each link. The links are represented by thick dashed lines (link 1: red, link 2: green, and link 3: blue), and the mode shapes are represented by thinner lines with a color corresponding to the links. The thinner solid lines represent mode shapes

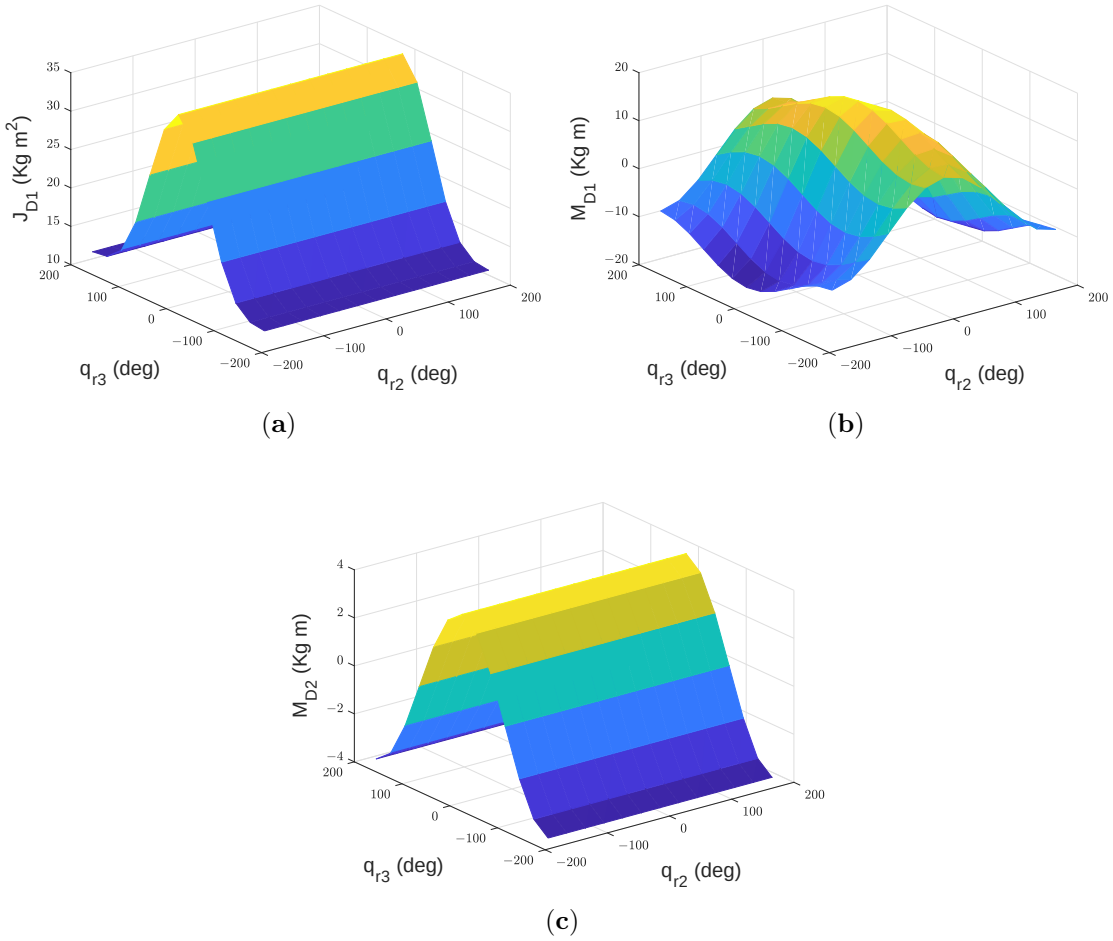

Figure C.3: (**a**) J_{D1} with nominal payload, (**b**) M_{D1} with nominal payload, (**c**) M_{D2} with nominal payload.

corresponding to the first modes and the thinner dashed lines represent the mode shapes corresponding to the second modes of the links. The joint coordinate frame (X_i, Y_i) of link i is represented by black arrowed lines, where the new positions of the frames are marked with [I], [II] and [III] for 0°, 90°, and 180° rotations respectively.

In Figure C.5a, link 3 is rotated about joint 3 (i.e., q_{r3} is varied) by 0° (I), 90° (II), and 180° (III) keeping $q_{r1} = 0°$ and $q_{r2} = 0°$ constant. It is observable that the mode shapes of both links 1 and 2 changed with the change in q_{r3}. In Figure C.5b, link 2 is rotated about joint 2 (i.e., q_{r2} is varied) by 0° (I), 90° (II), and 180° (III) keeping $q_{r1} = 0°$ and $q_{r3} = 0°$ constant. It can be noticed that the mode shapes of link 1 alter with the change in q_{r3} but that of links 2 and 3 remain unaltered.

The effect of q_{r3} on the eigenfrequencies of link 1 and link 2 is shown in Figure C.6a,c,e, with the constant q_{r2} at 0°, 90°, and 180° respectively. Similarly, the effect of q_{r2} on the eigenfrequencies of link 1 and link 2 is shown in Figure C.6b,d,f, with the constant q_{r3} at 0°, 90°, and 180° respectively. The eigenfrequencies of link 2 remains unchanged with the change in q_{r1} and q_{r2}. The eigenfrequencies of link 3

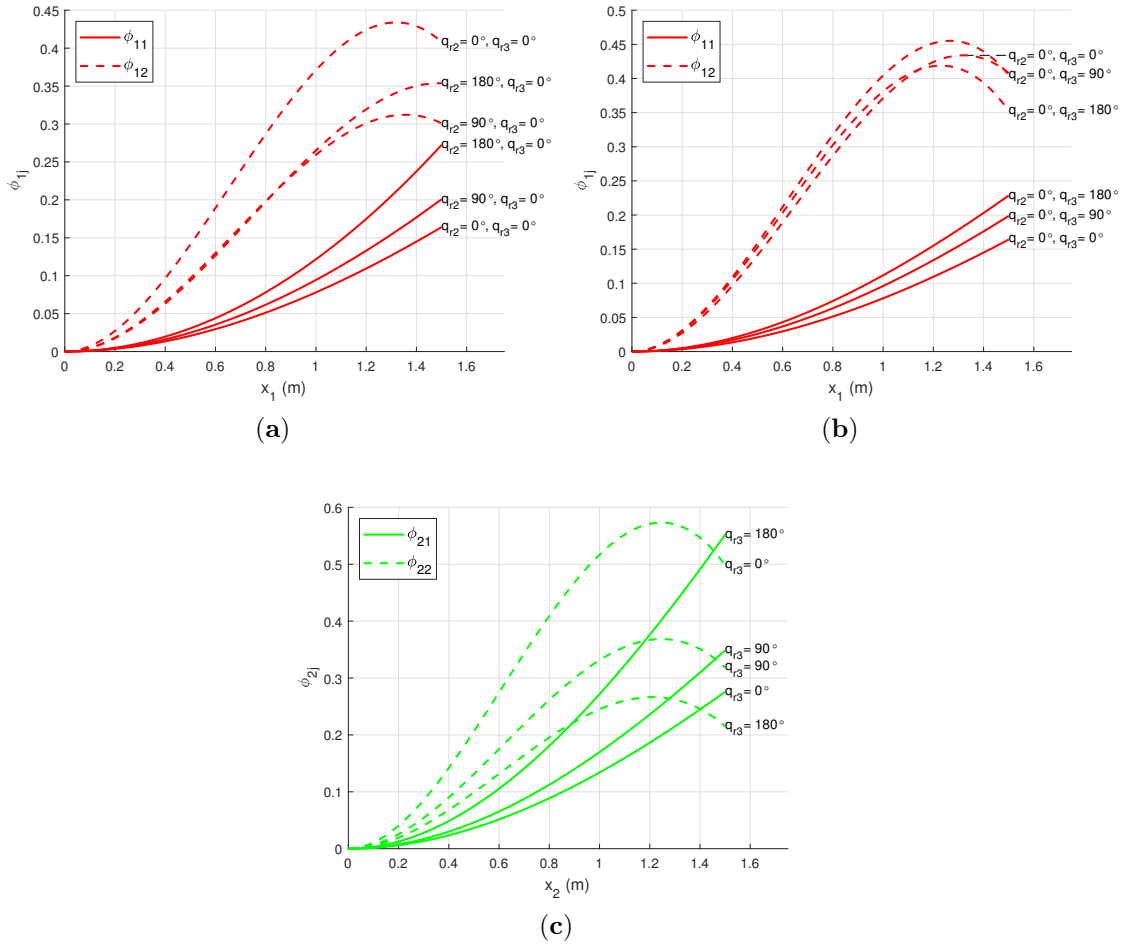

Figure C.4: (**a**) Mode shapes for link 1 with nominal payload and $q_{r3} = 0°$, (**b**) Mode shapes for link 1 with nominal payload and $q_{r2} = 0°$, (**c**) Mode shapes for link 2 with nominal payload.

remain unaffected by any change in q_{r1}, q_{r2}, and q_{r3}. The constant eigenfrequencies of link 3 for all manipulator configurations with nominal payload are given in Table C.3. Similarly, the eigenfrequencies of link 1, link 2, and link 3 are not altered by any variation in q_{r1}.

The overall effect of arm configuration on the eigenfrequencies of link 1 and link 2 is shown in Figure C.7.

C.4.3 Time-Domain Simulation

A set of numerical simulations have been performed to validate the theoretical model. The equations of motion are integrated using a fourth-order Runge-Kutta method with a fixed step size of 1 ms. The free and forced vibration responses of the dynamic model have been simulated. The nominal payload ($m_p = 2$ kg) condition is used for all time-domain simulations.

Firstly, free vibration response of the system is simulated without structural (and

viscus) damping under gravity starting with initial deformation in link 3 ($q_{r1}(0) = q_{r2}(0) = q_{r3}(0) = 0°$, $q_{f11}(0) = q_{f12}(0) = q_{f21}(0) = q_{f22}(0) = 0$ m, $q_{f31}(0) = 0.1$ m, and $q_{f32}(0) = 0.002$ m). The associated joint positions, link deflections, and tip motion are shown in Figure C.8. Then, the passive structural damping ($\zeta_{11} = \zeta_{12} = \zeta_{21} = \zeta_{22} = \zeta_{31} = \zeta_{32} = 0.005$, $b_1 = b_2 = b_3 = 0$) is added into the system. The free vibration response of the system with passive structural damping under gravity starting with initial deformation ($q_{f31}(0) = 0.1$ m and $q_{f32}(0) = 0.002$ m) is shown in Figure C.9. The benefits of adding passive structural damping are evident from Figures C.8 and C.9. The overall manipulator motion is improved because of the addition of the passive damping in the arm structure.

For empirical validation of the model, energies of the system under free vibration are considered. The elastic potential energy (U_{el}) of the system without damping is shown in Figure C.10a. Similarly, the potential energy due to gravity (U_g), kinetic energy (T) and the total mechanical energy of the system without damping are shown in Figure C.10b. The corresponding energies of the system when the damping is introduced into the system are shown in Figure C.11. In Figure C.11a, the elastic energy is high in the beginning (because of the initial deformation ($q_{f31}(0) = 0.1$ m and $q_{f32}(0) = 0.002$ m) introduced into the system) and it gradually decreases due to structural damping. It is evident from Figure C.11a,b that the total energy of the system is decreasing due to damping.

The forced vibration response of the system is studied by applying a symmetric bang-bang input torque with an amplitude of 50 Nm and acceleration (and deceleration) period of 0.1 s at joint 3 starting from $q_{r1}(0) = q_{r2}(0) = q_{r3}(0) = 0°$, and $q_{f11}(0) = q_{f12}(0) = q_{f21}(0) = q_{f22}(0) = q_{f31}(0) = q_{f32}(0) = 0$ m (undeformed configuration). The effect of gravity is ignored in this study (i.e., $\boldsymbol{g}_v = \begin{bmatrix} 0 & 0 \end{bmatrix}^T$ ms^{-2}) to show the coupled vibrations induced only due to bang-bang input torque. The forced vibration of all links at the joints and the tip level without damping are shown in Figure C.12. The forced vibration response of the system after the passive structural damping ($\zeta_{11} = \zeta_{12} = \zeta_{21} = \zeta_{22} = \zeta_{31} = \zeta_{32} = 0.005$, $b_1 = b_2 = b_3 = 0$) is introduced into the system without gravity starting with undeformed configuration is shown in Figure C.13. The slow relative drifting phenomenon is observable in the joint trajectories shown in Figure C.12a,b [6]. The coupled vibrations induced in all links are smoothed down with the introduction of damping. The potential energy due to gravity ($U_g = 0$), elastic potential energy (U_{el}), kinetic energy (T) and the total mechanical energy of the system without damping are shown in Figure C.12f and corresponding energies with damping are shown in Figure C.13f.

C.4.4 Frequency-Domain Analysis

The deflection of the tip of each link $w_{ie} = w_i|_{x_i=\ell_i}$ of the manipulator with damping under gravity starting with initial deformation in link 3 ($q_{r1}(0) = q_{r2}(0) = q_{r3}(0) = 0°$, $q_{f11}(0) = q_{f12}(0) = q_{f21}(0) = q_{f22}(0) = 0$ m, $q_{f31}(0) = 0.1$ m, and $q_{f32}(0) = 0.002$ m) is considered for the frequency-domain analysis. The nominal payload is used and the deflection values are recorded for 2 s with a fixed step size of 1 ms for this study.

A fast Fourier transform algorithm is used to compute the Fourier transform of the deflection signal which contains $N_s = 2000$ number of samples. The power spectrum of the discrete Fourier transform $W_{ie}(f)$ of the deflection w_{ie} of link i is computed for all links using the uniformly sampled (at 1 ms) time-domain deflection signal of the tip of each link. The deflection of the tip of each link and its corresponding frequency response (power spectrum) is shown in Figure C.14a–f, where $|W_{ie}(f)|$ is the amplitude of the discrete Fourier transform of w_{ie} corresponding to link i and f is the frequency of the signal in Hz. From Figure C.14a–f, the frequency components of the deflection signal of each link are revealed by the spikes in the power as follows: Link 1: 0.4883 Hz, 1.465 Hz; Link 2: 0.883 Hz, 42.48 Hz; and Link 3: 0.9766 Hz, 42.48 Hz.

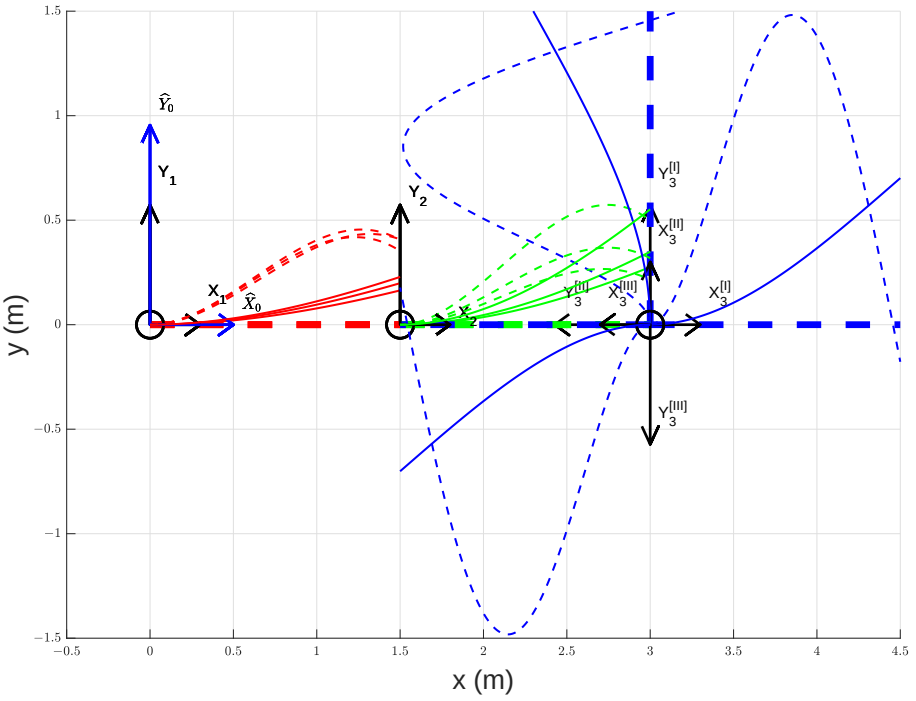

(**a**)

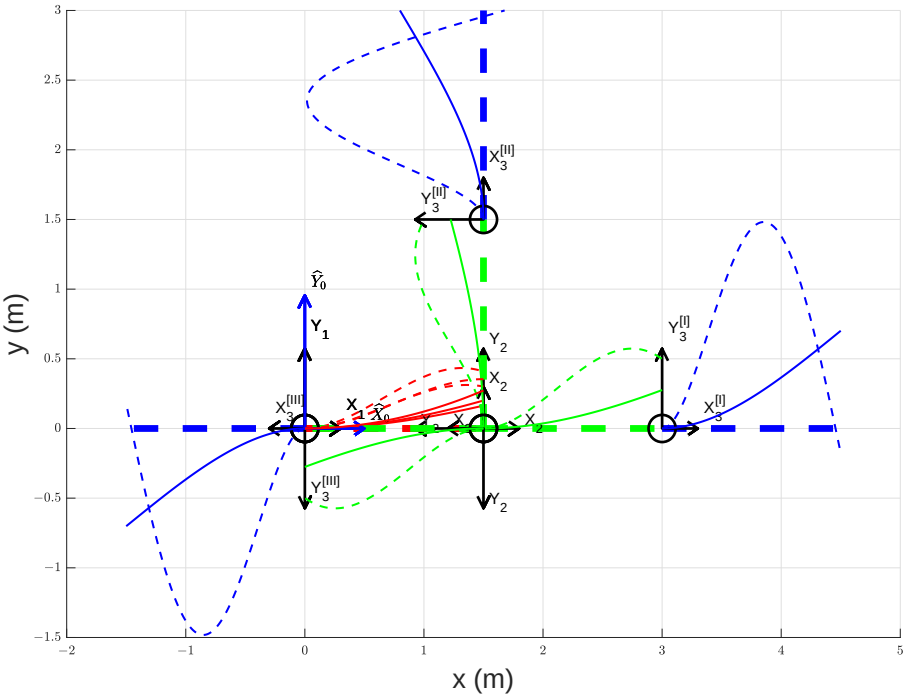

(**b**)

Figure C.5: (**a**) Mode shapes for link 1 (red), 2 (green), and 3 (blue) with nominal payload, $q_{r1} = 0°$, $q_{r2} = 0°$, and $q_{r3} = 0°$ (I), 90° (II), 180° (III) (**b**) Mode shapes for link 1 (red), 2 (green), and 3 (blue) with nominal payload, $q_{r1} = 0°$, $q_{r3} = 0°$, and $q_{r2} = 0°$ (I), 90° (II), 180° (III).

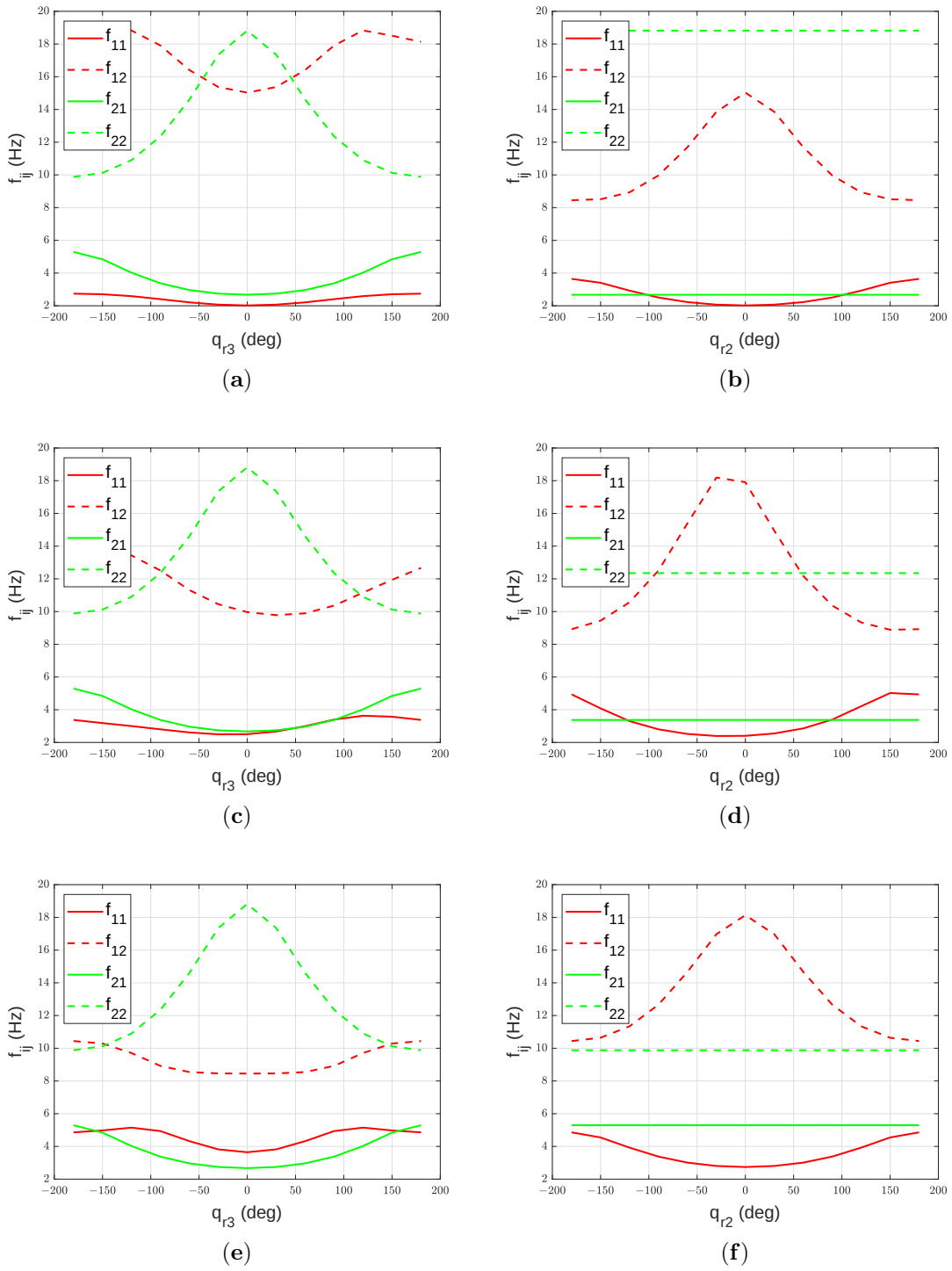

Figure C.6: (**a**) Eigenfrequencies for link 1 and 2 with nominal payload and $q_{r2} = 0°$, (**b**) Eigenfrequencies for link 1 and 2 with nominal payload and $q_{r3} = 0°$, (**c**) Eigenfrequencies for link 1 and 2 with nominal payload and $q_{r2} = 90°$, (**d**) Eigenfrequencies for link 1 and 2 with nominal payload and $q_{r3} = 90°$, (**e**) Eigenfrequencies for link 1 and 2 with nominal payload and $q_{r2} = 180°$, (**f**) Eigenfrequencies for link 1 and 2 with nominal payload and $q_{r3} = 180°$.

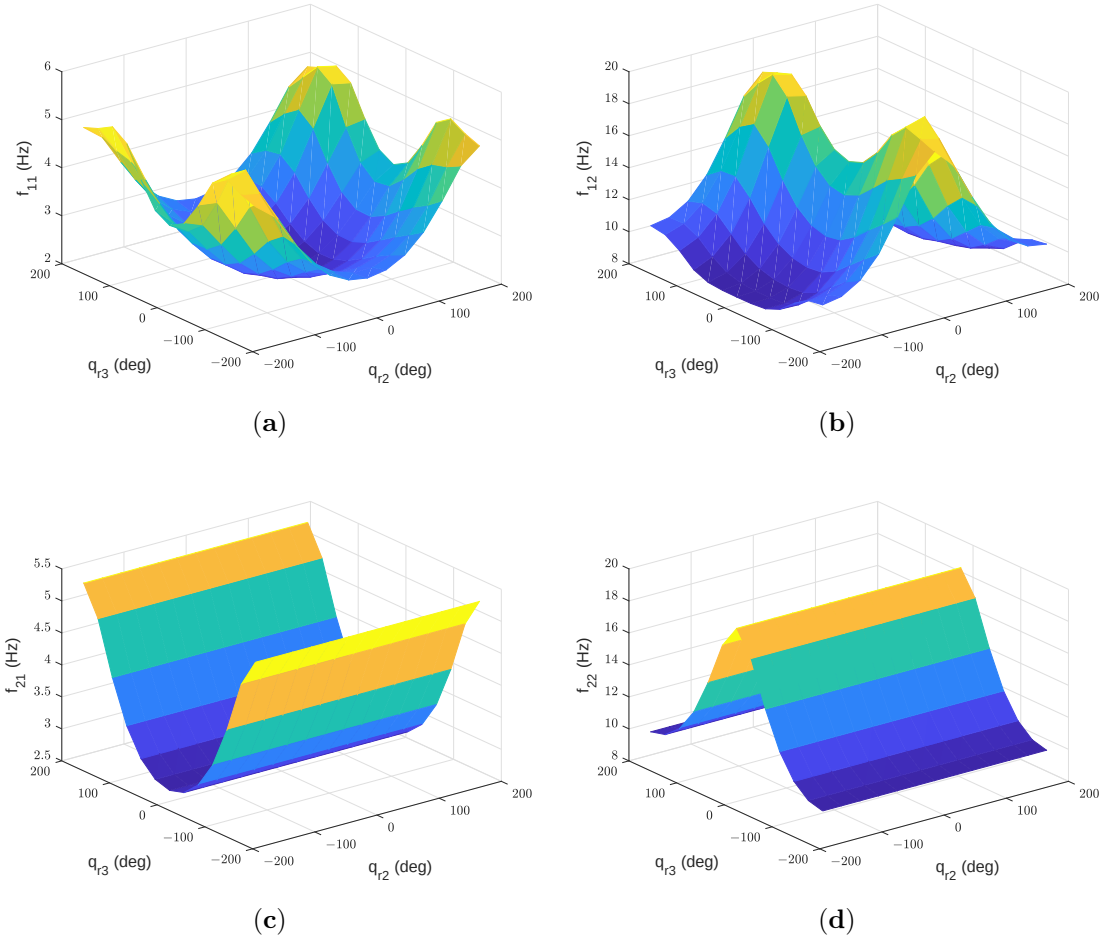

Figure C.7: (**a**) Eigenfrequency f_{11} for link 1 with nominal payload, (**b**) Eigenfrequency f_{12} for link 1 with nominal payload, (**c**) Eigenfrequency f_{21} for link 2 with nominal payload, (**d**) Eigenfrequencies f_{22} for link 2 with nominal payload.

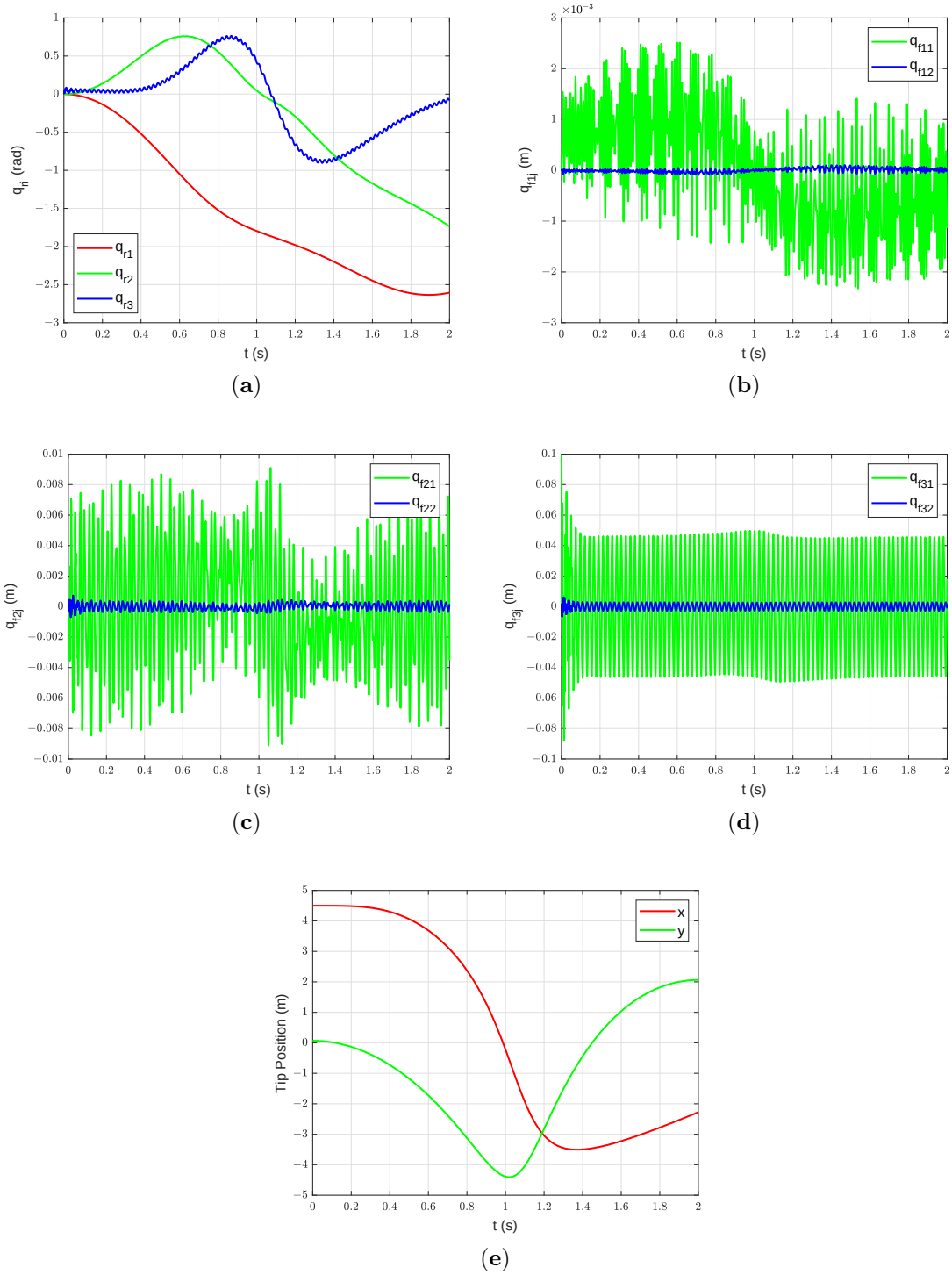

Figure C.8: Free vibration response without damping under gravity starting with initial deformation ($q_{f31}(0) = 0.1$ m and $q_{f32}(0) = 0.002$ m): (**a**) Joint Position, (**b**) Deflections of link 1, (**c**) Deflections of link 2, (**d**) Deflections of link 3, (**e**) Manipulator tip position.

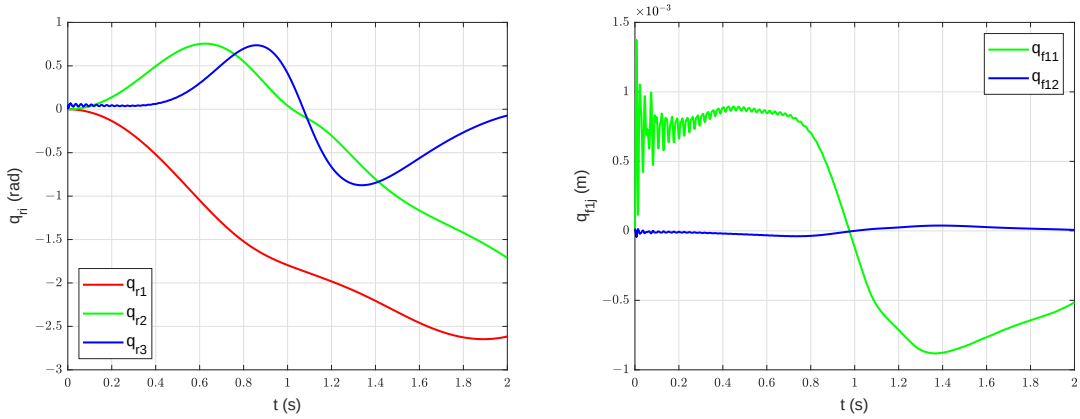

(**a**)

(**b**)

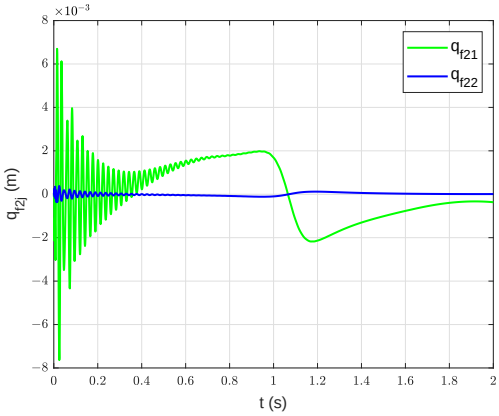

(**c**)

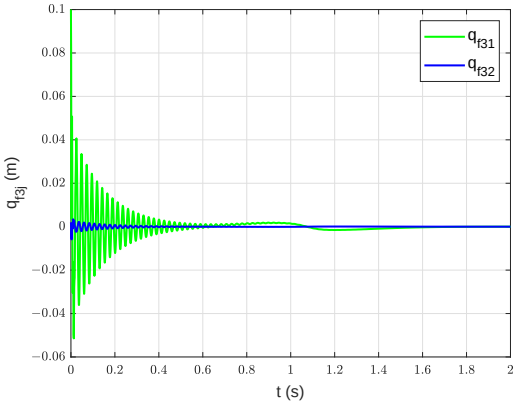

(**d**)

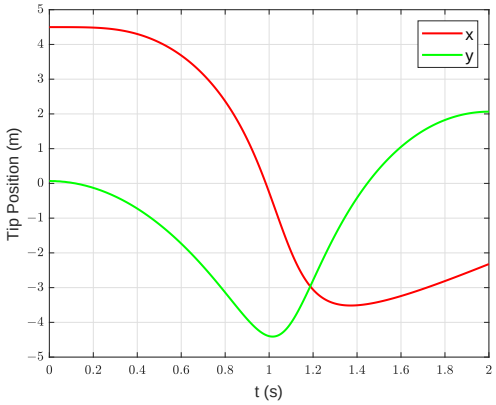

(**e**)

Figure C.9: Free vibration response with damping under gravity starting with initial deformation ($q_{f31}(0) = 0.1$ m and $q_{f32}(0) = 0.002$ m): (**a**) Joint Position, (**b**) Deflections of link 1, (**c**) Deflections of link 2, (**d**) Deflections of link 3, (**e**) Manipulator tip position.

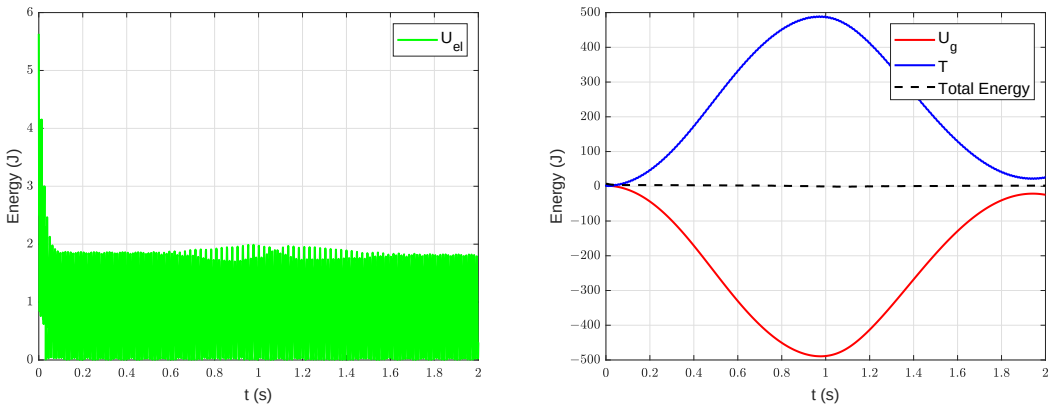

(**a**) (**b**)

Figure C.10: Energy of the manipulator system under free vibration without damping under gravity starting with initial deformation ($q_{f31}(0) = 0.1$ m and $q_{f32}(0) = 0.002$ m): (**a**) Elastic energy, (**b**) Potential energy due to gravity, kinetic and total energy.

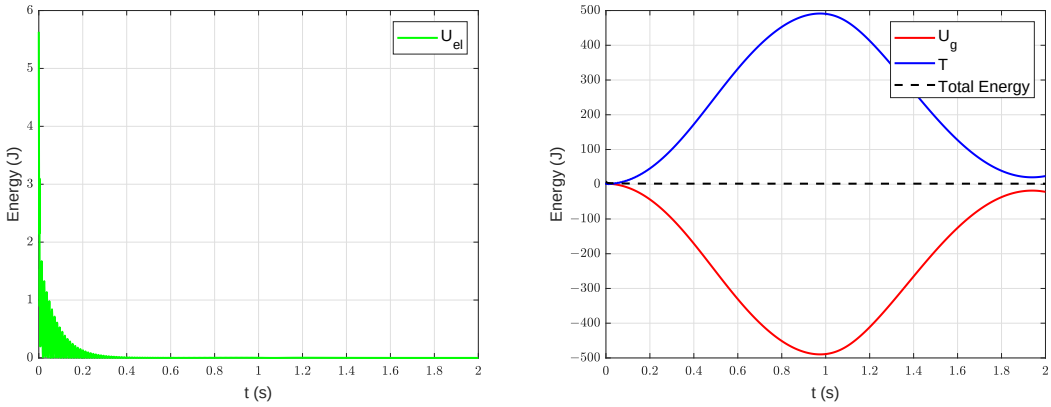

(**a**) (**b**)

Figure C.11: Energy of the manipulator system under free vibration with damping under gravity starting with initial deformation ($q_{f31}(0) = 0.1$ m and $q_{f32}(0) = 0.002$ m): (**a**) Elastic energy, (**b**) Potential energy due to gravity, kinetic and total energy.

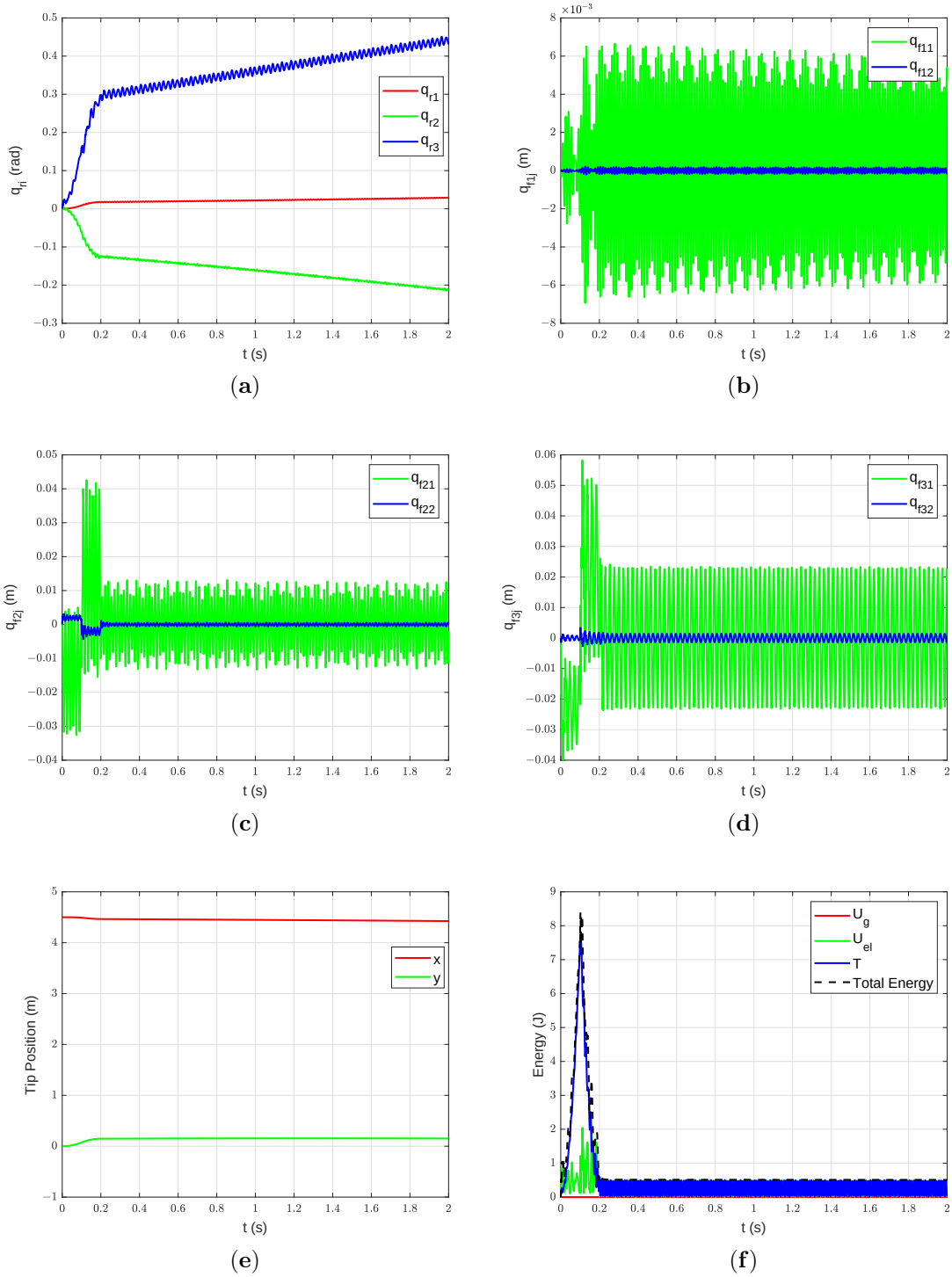

Figure C.12: Forced vibration response without damping without gravity starting with undeformed configuration: (**a**) Joint Position, (**b**) Deflections of link 1, (**c**) Deflections of link 2, (**d**) Deflections of link 3, (**e**) Manipulator tip position, (**f**) Energy of the manipulator system.

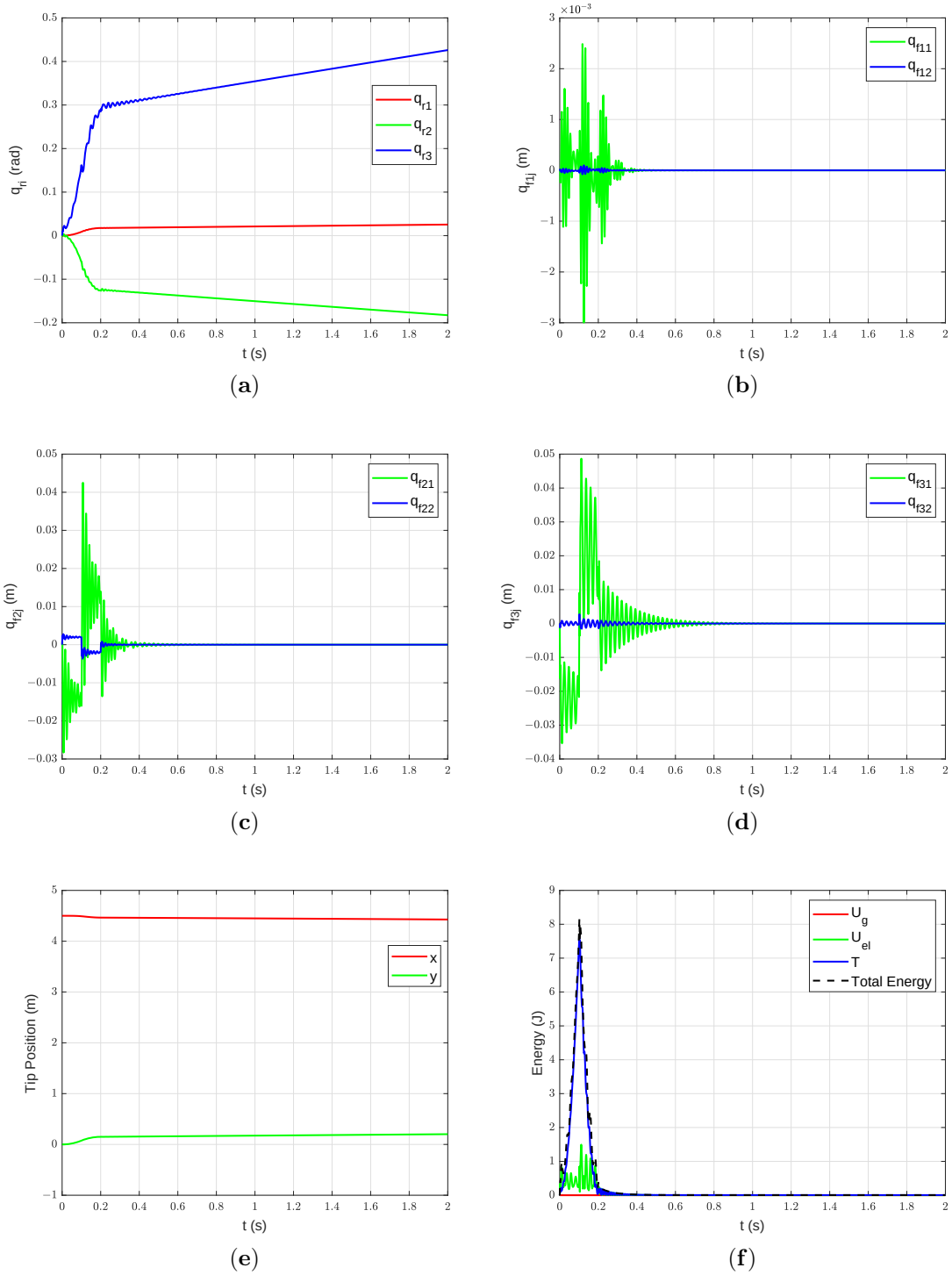

Figure C.13: Forced vibration response with damping without gravity starting with undeformed configuration: (**a**) Joint Position, (**b**) Deflections of link 1, (**c**) Deflections of link 2, (**d**) Deflections of link 3, (**e**) Manipulator tip position, (**f**) Energy of the manipulator system.

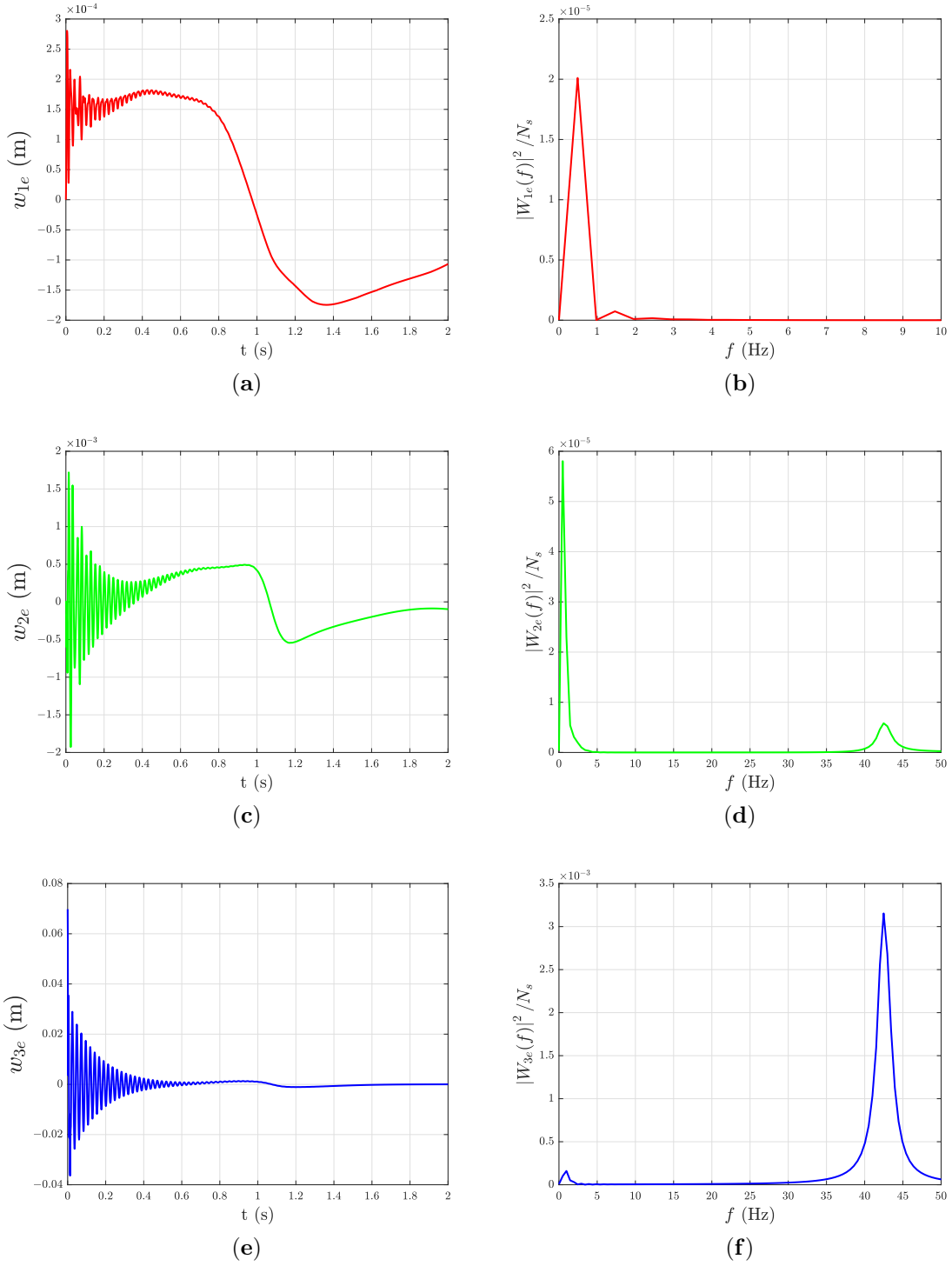

Figure C.14: Time-domain and frequency-domain representation of tip deflection of the links with damping under gravity starting with initial deformation ($q_{f31}(0) = 0.1$ m and $q_{f32}(0) = 0.002$ m): (**a**) Tip deflection of link 1, (**b**) Frequency response of the tip deflection of link 1, (**c**) Tip deflection of link 2, (**d**) Frequency response of the tip deflection of link 2, (**e**) Tip deflection of link 3, (**f**) Frequency response of the tip deflection of link 3.

C.5 Conclusions and Discussions

The closed-form dynamic model of the planar multi-link flexible manipulator is derived and the results of the time-domain and frequency-domain simulation of a three-link manipulator are reported. The effect of robot configuration and payload on the mode shapes and eigenfrequencies of the flexible links are discussed.

The mathematical model of the planar three-link flexible manipulator developed in this work will be experimentally validated in the future. The dynamic model developed in this work will be used for developing and testing (model-based) controllers and for simulation-based trajectory optimization.

Author Contributions: Conceptualization, D.S.; methodology, D.S.; software, D.S.; validation, D.S.; formal analysis, D.S.; investigation, D.S.; resources, D.S.; data curation, D.S.; writing—original draft preparation, D.S.; writing—review and editing, D.S., I.T. and G.H.; visualization, D.S.; supervision, I.T. and G.H.; project administration, I.T. and G.H.; funding acquisition, I.T. and G.H. All authors have read and agreed to the published version of the manuscript.

Funding: The work was funded by the Norwegian Research Council, project number 261647/$O$20, and SFI Offshore Mechatronics, project number 237896.

Institutional Review Board Statement: Not applicable.

Informed Consent Statement: Not applicable.

Data Availability Statement: Not applicable.

Conflicts of Interest: The authors declare no conflict of interest.

References – Paper C

[1] Dipendra Subedi, Ilya Tyapin, and Geir Hovland. Review on Modeling and Control of Flexible Link Manipulators. *Modeling, Identification and Control*, 41 (3):141–163, 2020. doi: 10.4173/mic.2020.3.2.

[2] Rex J. Theodore and Ashitava Ghosal. Comparison of the Assumed Modes and Finite Element Models for Flexible Multilink Manipulators. *The International Journal of Robotics Research*, 14(2):91–111, 1995. ISSN 17413176. doi: 10.1177/027836499501400201.

[3] R Krauss. An Improved Approach for Spatial Discretization of Transfer Matrix Models of Flexible Structures. In *2019 American Control Conference (ACC)*, pages 3123–3128, jul 2019. doi: 10.23919/ACC.2019.8814650.

[4] M Osman Tokhi and Abul K M Azad. *Flexible robot manipulators: modelling, simulation and control*, volume 68. Iet, 2008.

[5] A De Luca, L Lanari, P Lucibello, S Panzieri, and G Ulivi. Control experiments on a two-link robot with a flexible forearm. In *29th IEEE Conference on Decision and Control*, pages 520–527 vol.2, 1990. doi: 10.1109/CDC.1990.203651.

[6] Alessandro De Luca and Bruno Siciliano. Closed-Form Dynamic Model of Planar Multilink Lightweight Robots. *IEEE Transactions on Systems, Man and Cybernetics*, 21(4):826–839, 1991. ISSN 21682909. doi: 10.1109/21.108300.

[7] Franklyn Gerardo Duarte Vera. *Modeling and sliding-mode control of flexible-link robotic structures for vibration suppression.* Technische Universität Clausthal, 2016.

[8] Xuping Zhang, James K Mills, and William L Cleghorn. Dynamic Modeling and Experimental Validation of a 3-PRR Parallel Manipulator with Flexible Intermediate Links. *Journal of Intelligent and Robotic Systems*, 50(4):323–340, 2007. ISSN 1573-0409. doi: 10.1007/s10846-007-9167-4. URL `https://doi.org/10.1007/s10846-007-9167-4`.

[9] W J Book. Modeling, design, and control of flexible manipulator arms: a tutorial review. In *29th IEEE Conference on Decision and Control*, pages 500–506 vol.2, dec 1990. doi: 10.1109/CDC.1990.203648.

[10] Thomas R Kurfess. *Robotics and automation handbook*. CRC press, 2018.

[11] H. N. Rahimi and M. Nazemizadeh. Dynamic analysis and intelligent control techniques for flexible manipulators: A review. *Advanced Robotics*, 28(2):63–76, 2014. ISSN 01691864. doi: 10.1080/01691864.2013.839079.

[12] K. Lochan, B. K. Roy, and B. Subudhi. A review on two-link flexible manipulators. *Annual Reviews in Control*, 42:346–367, 2016. ISSN 13675788. doi: 10.1016/j.arcontrol.2016.09.019.

[13] P Koutsovasilis and M Beitelschmidt. Comparison of model reduction techniques for large mechanical systems. *Multibody System Dynamics*, 20(2):111–128, 2008.

[14] Renato Vidoni, Lorenzo Scalera, Alessandro Gasparetto, and Marco Giovagnoni. Comparison of model order reduction techniques for flexible multibody dynamics using an equivalent rigid-link system approach. In *Proceedings of the 8th EC-COMAS Thematic Conference on Multibody Dynamics, Prague, Czech Republic*, pages 19–22, 2017.

[15] L Wu, Paolo Tiso, and F van Keulen. A modal derivatives enhanced Craig-Bampton method for geometrically nonlinear structural dynamics. In *Proceedings of ISMA*, pages 3524–3615, 2016.

[16] Lewei Tang, Marc Gouttefarde, Haining Sun, Lairong Yin, and Changjiang Zhou. Dynamic modelling and vibration suppression of a single-link flexible manipulator with two cables. *Mechanism and Machine Theory*, 162:104347, 2021. ISSN 0094-114X. doi: https://doi.org/10.1016/j.mechmachtheory.2021.104347. URL `https://www.sciencedirect.com/science/article/pii/S0094114X21001051`.

[17] Renato Vidoni, Lorenzo Scalera, and Alessandro Gasparetto. 3-D ERLS based dynamic formulation for flexible-link robots: theoretical and numerical comparison between the finite element method and the component mode synthesis approaches. *Int. J. Mech. Control*, 19:39–50, 2018.

[18] M H Korayem and S F Dehkordi. Dynamic modeling of flexible cooperative mobile manipulator with revolute-prismatic joints for the purpose of moving common object with closed kinematic chain using the recursive Gibbs-Appell formulation. *Mechanism and Machine Theory*, 137:254–279, 2019. ISSN 0094-114X. doi: https://doi.org/10.1016/j.mechmachtheory.2019.03.026. URL `https://www.sciencedirect.com/science/article/pii/S0094114X18306529`.

[19] Chenglin Zhang, Tong Yang, Ning Sun, and Jianyi Zhang. A Simple Control Method of Single-Link Flexible Manipulators. *3rd International Symposium on Autonomous Systems, ISAS 2019*, pages 300–304, 2019. doi: 10.1109/ISASS.2019.8757711.

[20] Zhijie Liu, Jinkun Liu, and Wei He. Dynamic modeling and vibration control for a nonlinear 3-dimensional flexible manipulator. *International Journal of Robust and Nonlinear Control*, 28(13):3927–3945, 2018. ISSN 10991239. doi: 10.1002/rnc.4113.

[21] Qing Xin Meng, Xu Zhi Lai, Ya Wu Wang, and Min Wu. A fast stable control strategy based on system energy for a planar single-link flexible manipulator. *Nonlinear Dynamics*, 94(1):615–626, 2018. ISSN 1573269X. doi: 10.1007/s11071-018-4380-1.

[22] Wei He, Xiuyu He, Mingfo Zou, and Hongyi Li. PDE Model-Based Boundary Control Design for a Flexible Robotic Manipulator with Input Backlash. *IEEE Transactions on Control Systems Technology*, 27(2):790–797, 2018. ISSN 15580865. doi: 10.1109/TCST.2017.2780055.

[23] C Sun, H Gao, W He, and Y Yu. Fuzzy Neural Network Control of a Flexible Robotic Manipulator Using Assumed Mode Method. *IEEE Transactions on Neural Networks and Learning Systems*, 29(11):5214–5227, nov 2018. ISSN 2162-2388. doi: 10.1109/TNNLS.2017.2743103.

[24] Mule Pala Prasad Reddy and Jeevamma Jacob. Vibration control of flexible link manipulator using SDRE controller and Kalman filtering. *Studies in Informatics and Control*, 26(2):143–150, 2017. ISSN 1841429X. doi: 10.24846/v26i2y201702.

[25] Amir H. Ghasemi. Slewing and vibration control of a single-link flexible manipulator using filtered feedback linearization. *Journal of Intelligent Material Systems and Structures*, 28(20):2887–2895, 2017. ISSN 15308138. doi: 10.1177/1045389X17704067.

[26] Yuncheng Ouyang, Wei He, Xiajing Li, Jin Kun Liu, and Guang Li. Vibration Control Based on Reinforcement Learning for a Single-link Flexible Robotic Manipulator. *IFAC-PapersOnLine*, 50(1):3476–3481, 2017. ISSN 24058963. doi: 10.1016/j.ifacol.2017.08.932.

[27] Yuncheng Ouyang, Wei He, and Xiajing Li. Reinforcement learning control of a singlelink flexible robotic manipulator. *IET Control Theory and Applications*, 11(9):1426–1433, 2017. ISSN 17518652. doi: 10.1049/iet-cta.2016.1540.

[28] Kshetrimayum Lochan and Binoy Krishna Roy. Second-order SMC for tip trajectory tracking and tip deflection suppression of an AMM modelled nonlinear TLFM. *International Journal of Dynamics and Control*, 6(3):1310–1318, 2018. ISSN 21952698. doi: 10.1007/s40435-017-0371-1.

[29] Ashish Singla and Amardeep Singh. Dynamic Modeling of Flexible Robotic Manipulators. In *Harmony Search and Nature Inspired Optimization Algorithms*, pages 819–834, Singapore, 2019. Springer Singapore. ISBN 978-981-13-0761-4.

[30] Zhi-cheng Qiu, Cheng Li, and Xian min Zhang. Experimental study on active vibration control for a kind of two-link flexible manipulator. *Mechanical Systems and Signal Processing*, 118:623–644, 2019. ISSN 10961216. doi: 10.1016/j.ymssp.2018.09.001.

[31] Hejia Gao, Wei He, Chen Zhou, and Changyin Sun. Neural Network Control of a Two-Link Flexible Robotic Manipulator Using Assumed Mode Method. *IEEE Transactions on Industrial Informatics*, 15(2):755–765, 2018. ISSN 15513203. doi: 10.1109/TII.2018.2818120.

[32] Santanu Kumar Pradhan and Bidyadhar Subudhi. Position control of a flexible manipulator using a new nonlinear self-Tuning PID controller. *IEEE/CAA Journal of Automatica Sinica*, 7(1):136–149, 2020. ISSN 23299274. doi: 10.1109/JAS.2017.7510871.

[33] Ivan Giorgio and Dionisio D. Del Vescovo. Non-linear lumped-parameter modeling of planar multi-link manipulators with highly flexible arms. *Robotics*, 7(4): 1–13, 2018. ISSN 22186581. doi: 10.3390/robotics7040060.

[34] Dipendra Subedi, Ilya Tyapin, and Geir Hovland. Modeling and Analysis of Flexible Bodies Using Lumped Parameter Method. *2020 IEEE 11th International Conference on Mechanical and Intelligent Manufacturing Technologies (ICMIMT)*, pages 161–166, 2020. doi: 10.1109/icmimt49010.2020.9041188.

Paper D

Static Deflection Compensation of Multi-Link Flexible Manipulators Under Gravity

Dipendra Subedi, Teodor Nilsen Aune, Ilya Tyapin and Geir Hovland

This paper has been published as:

Dipendra Subedi, Teodor Nilsen Aune, Ilya Tyapin and Geir Hovland. Static Deflection Compensation of Multi-Link Flexible Manipulators Under Gravity. *IEEE Access*, 10:9658-9667, 2022. doi: 10.1109/ACCESS.2022.3144404.

Static Deflection Compensation of Multi-Link Flexible Manipulators Under Gravity

Dipendra Subedi, Teodor Nilsen Aune, Ilya Tyapin and Geir Hovland
Department of Engineering Sciences
University of Agder
4879 Grimstad, Norway

Abstract **The static deflection compensation method of a planar multi-link flexible manipulator is proposed using the feedback from inertial sensors mounted at the tip of each link. The proposed compensation technique is validated experimentally using a high-precision laser tracker. The proposed strategy is experimentally verified using a three-link flexible manipulator. A strategy to compensate for the centripetal and tangential acceleration induced on the accelerometer mounted on the rotating link is proposed for correct inclination estimation. The improvement in the inclination estimation using the proposed compensation technique is verified both in simulation and experimental studies.**

D.1 Introduction

The interest in using long-reach manipulators for different applications has increased significantly in recent years [1]. Because of the use of elastic material and slender design of the arm, link flexibility is introduced in the manipulator system. This causes static (due to gravity) and dynamic (oscillations) deflections of the end-effector.

The end-effector control of the flexible link manipulator (FLM) is more difficult than the rigid link manipulator because of the presence of unwanted deflections and vibrations in the FLM. The rigid body kinematics and joint position feedback are not enough for the precise position and orientation control of the FLMs. Additional sensors (e.g. inertial sensors and vision sensors) are therefore required to be integrated into the FLM control architecture to sense deflections and oscillations. For correct end-effector positioning in the FLM, the deflection should be estimated by using a suitable sensor system and should be compensated using a feedback control strategy of adjusting joint variables.

There are many methods to estimate flexible deformation, including strain gauges, inertial measurement units (IMUs), optical/vision systems, position sensitive devices, piezoelectric materials, ultrasonic sensors, and range sensors [2]. Each of these sensor systems has associated merits and limitations. A vision system that can capture the

deformed shape of the flexible link may take a long processing time which makes it unsuitable for real-time applications [3]. Additionally, the optical sensor systems are obstructed when an object comes in between the camera and the FLM [4]. The strain gauges are versatile and accurate but are difficult to install properly as they must be perfectly bonded to the material across the entire face to strain with the link. Moreover, the electronics necessary to amplify the signal and acquire the data are costly. Strain gauges are susceptible to temperature drift and have a drawback of excess wiring when many of them are used. The IMU (accelerometer and gyroscope) allows the system to know the true course of motion and can be used to obtain the position, velocity, and acceleration estimations (considering the joint encoder readings are available).

The static deformation-compensation method based on inclination-sensor feedback is presented in [5]. The accelerometers are used for the estimation of flexural states of a macro-micro manipulator in [3]. Although the inertial sensors, placed typically at the tip of the flexible link, are used for measuring oscillations; they have not been used for measuring static deflections [4]. Several optical sensing systems have been used for measuring the link deflections [6–10]. The strain gauges that are strategically placed along a link are the sensor systems used to estimate the deflections indirectly [4, 11, 12].

The use of an IMU mounted at the tip of each flexible link is highlighted in this paper for measuring the deflection of the flexible link. The static deflection compensation using the tip-mounted inertial sensor is validated using a high-precision laser tracker. The proposed strategy is experimentally verified in a planar three-link flexible manipulator.

Inclination estimation using an accelerometer uses the gravity vector and its projection on the axes of the accelerometer to determine the tilt angle [13]. Rotating an accelerometer through gravity changes the projection of gravity on the axes of interest due to centripetal acceleration induced on the accelerometer. This results in the incorrect calculation of the inclination. A strategy is proposed in this paper to compensate for the centripetal and tangential acceleration induced on the accelerometer mounted on the rotating link for correct inclination estimation. Furthermore, the improvement in the inclination estimation using the proposed compensation technique is verified both in simulation and experimental studies.

The paper is organized into five sections as follows. The kinematic model of the three-link flexible manipulator is described in section D.2. The independent joint control of FLM with static deflection compensation using link-mounted IMU is elaborated in section D.3. The results obtained from the simulation and experimental studies are presented in section D.4. Conclusions and discussions follow in section D.5.

Table D.1: DH PARAMETERS.

Axis	TranZ	RotZ	TranX	RotX
1	0.0	q_1	ℓ_1	0.0
2	0.0	q_2	ℓ_2	0.0
3	0.0	q_3	ℓ_3	0.0

D.2 Kinematic Modeling

Fig. D.1 shows a planar three-link flexible manipulator with coordinate frames assigned as in [14] and Fig. D.2 shows its rigid body schematic with Denavit-Hartenberg (DH) parameters given in Table D.1. The kinematic model of the planar multi-link flexible manipulator is presented in [14].

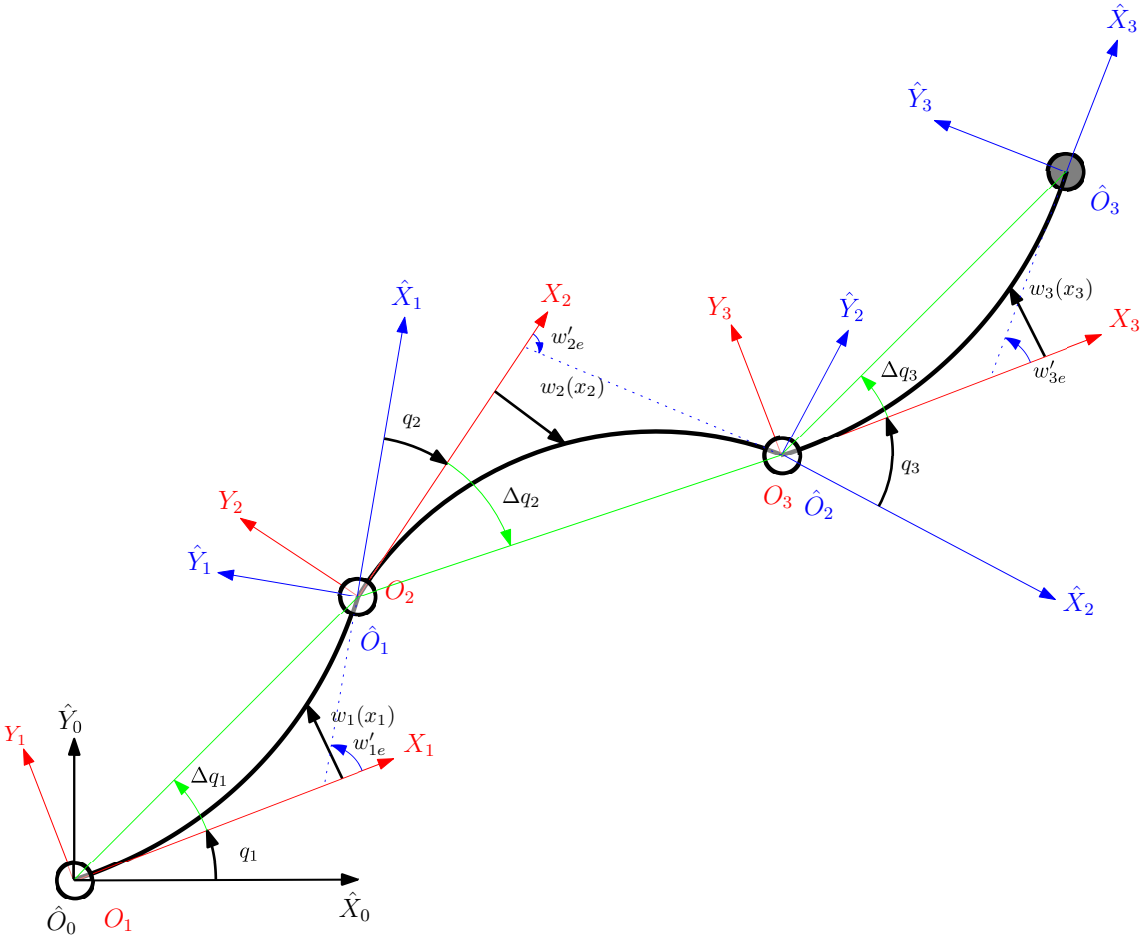

Figure D.1: Planar three-link flexible manipulator.

The rigid motion of link i is represented by the joint i position q_i, and the deflection at any point x_i along the link i is described by $w_i(x_i)$, where $0 \leq x_i \leq \ell_i$, and ℓ_i is the length of the link i. The slope of the deflection curve at any point x_i along the link i and at its endpoint is given by (D.1) and (D.2) respectively. The angular deflection estimated (by an inertial sensor) at the tip of link i corresponds to $arctan(w'_{ie}) \approx w'_{ie}$ considering small link deflection. Moreover, when ℓ_i is not large

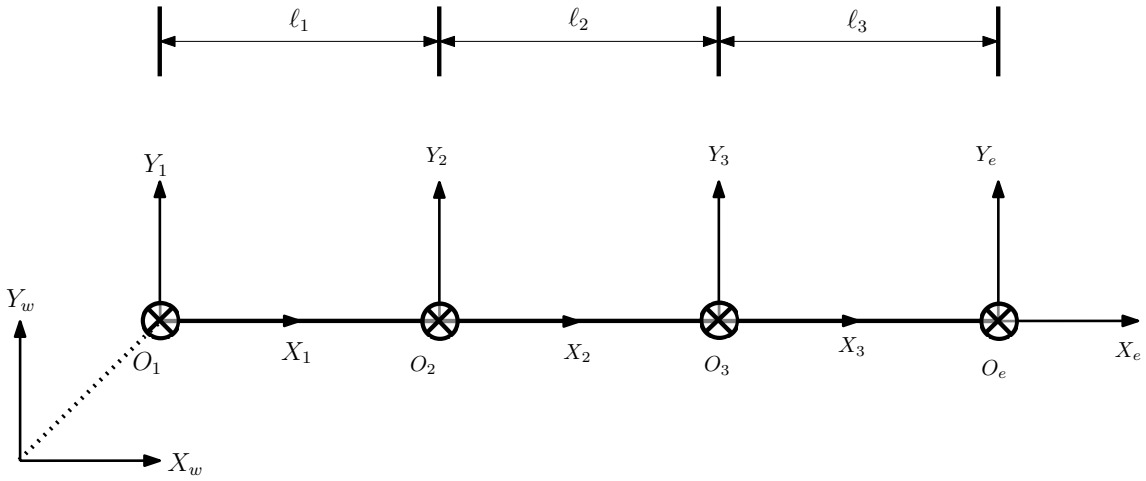

Figure D.2: Equivalent rigid body kinematics.

and deformation is small then $w'_{ie} \approx \Delta q_i$, where Δq_i is the static compensation angle [5].

$$w'_i = \frac{\partial w_i(x_i)}{\partial x_i} \tag{D.1}$$

$$w'_{ie} = \left.\frac{\partial w_i(x_i)}{\partial x_i}\right|_{x_i=\ell_i} \tag{D.2}$$

From Fig. D.1, it is visible that there is some error introduced when using $w'_{ie} \approx \Delta q_i$ for static deflection compensation, as $w'_{ie} > \Delta q_i$ in reality. It results in the overcompensation of the static deflection. However, this method is a good trade-off between accuracy and cost. Moreover, it is a good compromise between the complexity (and cost) of determining accurate deflection and the simplicity of neglecting the static deflection.

D.3 Control

D.3.1 Trajectory Generation

Apart from knowing the initial and final joint configuration of the robot, it is desirable for the motion of each joint to be smooth from the initial to the final configuration. Jerky and rough motions cause unwanted vibrations and may excite resonances in the manipulator. There are many methods of generating smooth joint trajectories as discussed in [15]. One of the methods is by defining the function that is continuous and has continuous first and higher-order derivatives. In this paper, a quintic polynomial $q_{i_d}(t)$ is used to generate the desired trajectory of joint i from the initial joint position q_{i_0} to final joint position q_{i_f} as given in (D.3). Here, $\dot{q}_{i_0}$, $\dot{q}_{i_f}$, $\ddot{q}_{i_0}$, and $\ddot{q}_{i_f}$ are the initial ($t = t_0 = 0$) and final ($t = t_f$) joint velocities and accelerations.

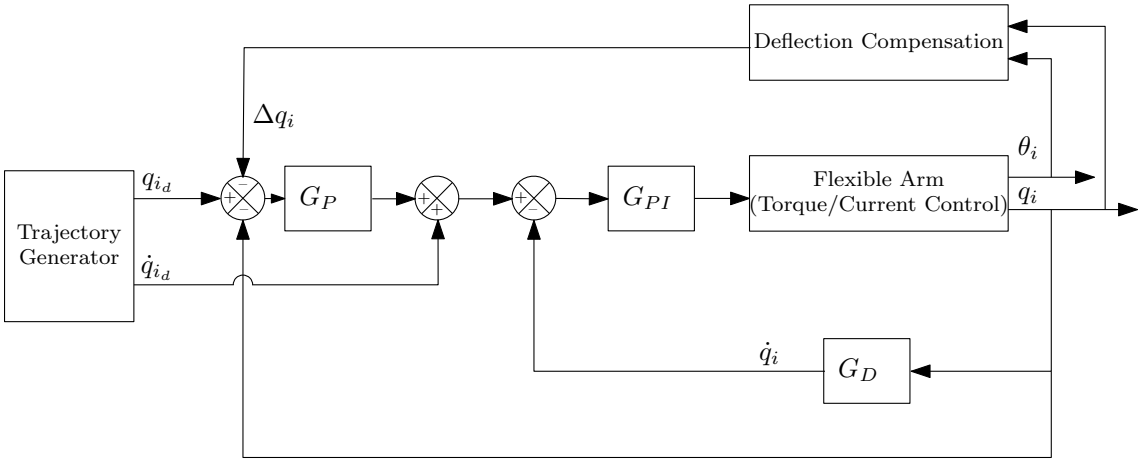

Figure D.3: A general architecture for independent joint control with deflection compensation.

For generating a trajectory for rest to rest motion, zero velocity and acceleration boundary conditions are used, i.e., $\dot{q}_{i_0} = \dot{q}_{i_f} = \ddot{q}_{i_0} = \ddot{q}_{i_f} = 0$.

$$q_{i_d}(t) = a_0 + a_1 t + a_2 t^2 + a_3 t^3 + a_4 t^4 + a_5 t^5, \tag{D.3}$$

where,

$$\begin{aligned}
a_0 &= q_{i_0}, a_1 = \dot{q}_0, a_2 = \frac{\ddot{q}_0}{2}, \\
a_3 &= \frac{20(q_{i_f} - q_{i_0}) - (8\dot{q}_{i_f} + 12\dot{q}_{i_0})t_f - (3\ddot{q}_{i_0} - \ddot{q}_{i_f})t_f^2}{2t_f^3}, \\
a_4 &= \frac{\begin{array}{r}30(q_{i_0} - q_{i_f}) + (14\dot{q}_{i_f} + 16\dot{q}_{i_0})t_f \\ + (3\ddot{q}_{i_0} - 2\ddot{q}_{i_f})t_f^2\end{array}}{2t_f^4}, \quad \text{and} \\
a_5 &= \frac{12(q_{i_f} - q_{i_0}) - (6\dot{q}_{i_f} + 6\dot{q}_{i_0})t_f - (\ddot{q}_{i_0} - \ddot{q}_{i_f})t_f^2}{2t_f^5}.
\end{aligned}$$

D.3.2 Independent Joint Control

An independent joint control strategy based on a cascaded architecture is presented in [16] for rigid link manipulators and in [17] for flexible link manipulators. However, the joint position feedback used in the current paper is augmented by compensating for the slow varying static deflection caused by gravity as shown in Fig. D.3. The innermost loop is a proportional-integral (PI) current controller. The next cascade level is a PI velocity control loop and the outermost cascade level is a proportional (P) position controller. The static deflection compensation action enters into the position cascade level.

The design guidelines for selecting suitable gains for the cascaded joint control topology are described in [16] and [17] for the rigid link and flexible link manip-

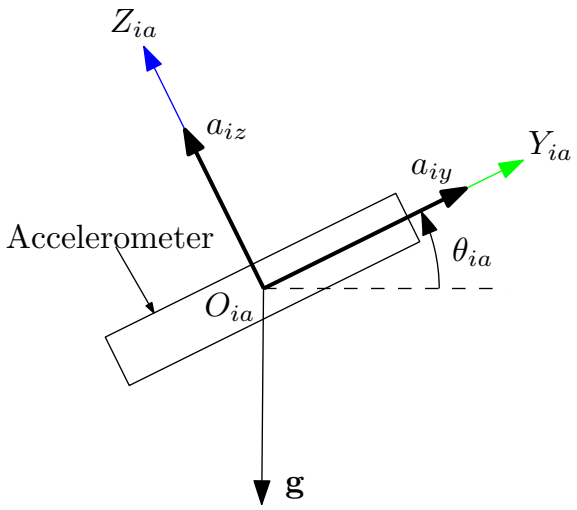

Figure D.4: Dual-axis inclination sensing.

ulators respectively using root locus analysis. Although the design requirements imposing large values of feedback gains may not be verified in practice because of the links' flexibilities, the smaller gain in the position feedback loop will be enough for compensating for the slow varying static deflection.

D.3.3 Deflection Compensation

The deflection angle must be estimated first for compensating it. The IMU mounted at the tip of each link is used for sensing the deflection.

Considering θ_i as the inclination angle estimated using IMU i, then the angular deflection $w'_{ie} \approx \Delta q_i$ of link i at the tip (or at the place where IMU is mounted on the link) is given by (D.4).

$$\Delta q_i = \theta_i - (q_i + \theta_{i-1}), \quad \theta_0 = 0 \tag{D.4}$$

The inclination angle $\theta_{ia} = arctan2(a_{iy}, a_{iz})$ estimated using the accelerometer in the range $(-\pi, \pi]$ is given by (D.5), where a_{iy} and a_{iz} represent accelerations measured by the accelerometer on link i along its Y-axis and Z-axis respectively. Here, the gravity vector ($\boldsymbol{g}$) and its projection on the axes of the accelerometer are used to determine the inclination angle (see Fig. D.4). The accelerometers suffer from external accelerations (joint motion) that add to gravity and make the inclination estimation inaccurate. The data from the accelerometer is in general noisy and susceptible to external acceleration interference but is stable and without drift in the long term.

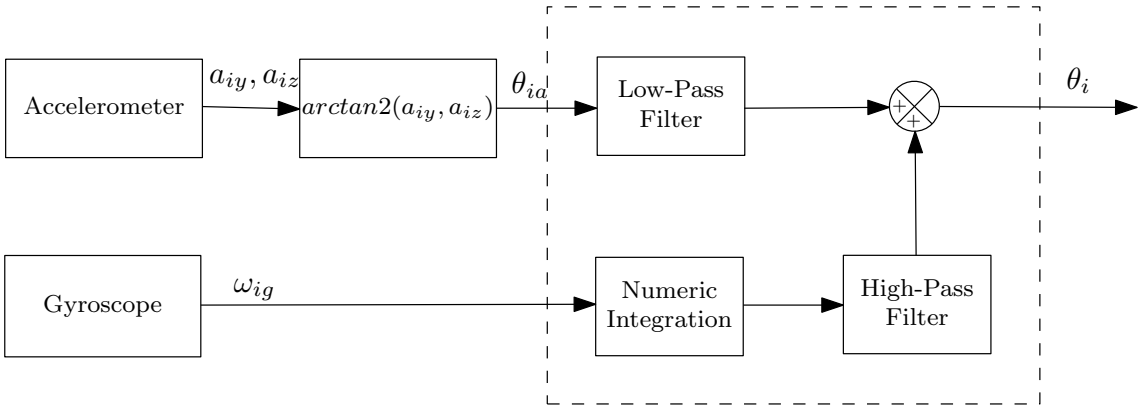

Figure D.5: Complementary filter.

$$\theta_{ia} = \begin{cases} 2\arctan\left(\frac{a_{iy}}{\sqrt{a_{iz}^2+a_{iy}^2}+a_{iz}}\right) & \text{if } a_{iz} > 0, \\ 2\arctan\left(\frac{\sqrt{a_{iz}^2+a_{iy}^2}-a_{iz}}{a_{iy}}\right) & \text{if } a_{iz} \leq 0 \text{ and } a_{iy} \neq 0, \\ \pi & \text{if } a_{iz} < 0 \text{ and } a_{iy} = 0, \\ \text{undefined} & \text{if } a_{iz} = 0 \text{ and } a_{iy} = 0. \end{cases} \tag{D.5}$$

Another method to estimate the inclination angle is to integrate the output of a gyroscope. Although the gyroscope data is not susceptible to external acceleration interference like accelerometer, it drifts because of the angular velocity data bias accumulation over time. This causes an apparent rotation even when the device is stationary as the integration period is increased. So, to use the advantages of both accelerometer and gyroscope, IMU data fusion is essential for reliable and real-time inclination sensing.

The Kalman filter and the complementary filter are the most widely used IMU data fusion techniques and the latter is used in this paper. The complementary filter can be represented diagrammatically by Fig. D.5 and mathematically by (D.6), where θ_i is the inclination angle, α_i is the filter coefficient in the range $[0, 1]$, ω_{ig} is the angular velocity obtained from the gyroscope, T_s is the sample period, and θ_{ia} is the inclination angle obtained from the accelerometer data [18]. Here, $\alpha = \tau/(\tau + T_s)$ can be calculated using the desired time constant τ and sample period.

$$\theta_i = \alpha_i(\theta_i + \omega_{ig}T_s) + (1 - \alpha_i)\theta_{ia} \tag{D.6}$$

Centripetal and Tangential Acceleration

The inclination estimation from accelerometer data can be improved by removing the external acceleration (other than gravity acceleration) measured by the accelerometer. The external acceleration induced in the accelerometer mounted on the link is mainly

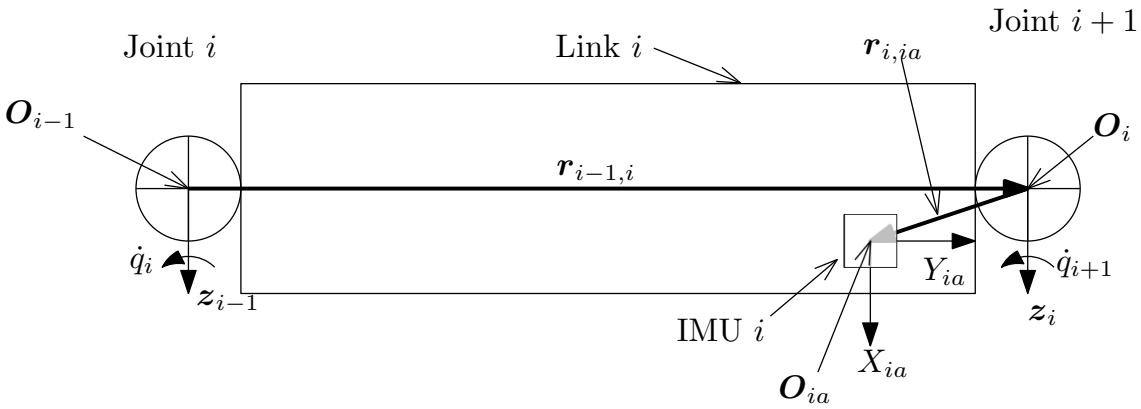

Figure D.6: Joint i, link i, IMU i, and related definitions.

due to the rotational joint motion. Considering the planar motion of the arm, there are two main components of the externally induced linear acceleration measured by the accelerometer mounted on the link, namely tangential acceleration (directed perpendicular to the length of the link) and centripetal acceleration (directed parallel to the length of the link).

With reference to the generic link i, shown in Fig. D.6, $\boldsymbol{z}_{i-1}$ represents the unit vector along the axis of joint i, $\boldsymbol{r}_{i-1,i} = \boldsymbol{O}_i - \boldsymbol{O}_{i-1}$, $\boldsymbol{r}_{i,ia} = \boldsymbol{O}_{ia} - \boldsymbol{O}_i$, where $\boldsymbol{O}_i$ and $\boldsymbol{O}_{ia}$ are respectively the origin of the i-th reference frame, and reference frame of the accelerometer mounted on link i. Considering ${}^{i-1}\boldsymbol{R}_i$ be the rotation of frame i (represented by subscript) with respect to frame $i-1$ (represented by superscript), the forward recursions on the angular velocity (${}^i\boldsymbol{\omega}_i$), angular acceleration (${}^i\dot{\boldsymbol{\omega}}_i$), and linear acceleration (${}^i\boldsymbol{a}_i$) of the frame origin of each link i are given by (D.7)–(D.9) respectively [19]. Note that the superscript represents the reference frame with respect to which the quantities (vectors and rotations) are expressed. The linear acceleration of the frame origin of the accelerometer reference frame expressed with respect to i-th reference frame and accelerometer reference frame of link i are given by (D.10) and (D.11) respectively.

$$ {}^i\boldsymbol{\omega}_i = {}^{i-1}\boldsymbol{R}_i^T[{}^{i-1}\boldsymbol{\omega}_{i-1} + \dot{q}_i \boldsymbol{z}_{i-1}] \tag{D.7} $$

$$ {}^i\dot{\boldsymbol{\omega}}_i = {}^{i-1}\boldsymbol{R}_i^T[{}^{i-1}\dot{\boldsymbol{\omega}}_{i-1} + \ddot{q}_i \boldsymbol{z}_{i-1} + {}^{i-1}\boldsymbol{\omega}_{i-1} \times \dot{q}_i \boldsymbol{z}_{i-1}] \tag{D.8} $$

$$ {}^i\boldsymbol{a}_i = {}^{i-1}\boldsymbol{R}_i^{Ti-1}\boldsymbol{a}_{i-1} + {}^i\dot{\boldsymbol{\omega}}_i \times {}^i\boldsymbol{r}_{i-1,i} + {}^i\boldsymbol{\omega}_i \times ({}^i\boldsymbol{\omega}_i \times {}^i\boldsymbol{r}_{i-1,i}) \tag{D.9} $$

$$ {}^i\boldsymbol{a}_{ia} = {}^i\boldsymbol{a}_i + {}^i\dot{\boldsymbol{\omega}}_i \times {}^i\boldsymbol{r}_{i,ia} + {}^i\boldsymbol{\omega}_i \times ({}^i\boldsymbol{\omega}_i \times {}^i\boldsymbol{r}_{i,ia}) \tag{D.10} $$

$$ {}^{ia}\boldsymbol{a}_{ia} = {}^{ia}\boldsymbol{R}_i {}^i\boldsymbol{a}_{ia} \tag{D.11} $$

where,

$$ i = 1, 2, 3 $$

$$\boldsymbol{z}_{i-1} = \begin{bmatrix} 0 & 0 & 1 \end{bmatrix}^T$$
$${}^{i}\boldsymbol{r}_{i-1,i} = \begin{bmatrix} \ell_i & 0 & 0 \end{bmatrix}^T$$
$${}^{ia}\boldsymbol{R}_i = \begin{bmatrix} 0 & 0 & 1 \\ 1 & 0 & 0 \\ 0 & 1 & 0 \end{bmatrix}$$
$${}^{0}\boldsymbol{a}_0 = \begin{bmatrix} 0 & 9.81 & 0 \end{bmatrix}^T$$
$${}^{0}\boldsymbol{\omega}_0 = {}^{0}\dot{\boldsymbol{\omega}}_0 = 0$$

Ideally, the accelerometer readings should be equal to ${}^{ia}\boldsymbol{a}_{ia}$ assuming that the link on which it is mounted is rigid. To compensate for the centripetal and tangential acceleration induced in the accelerometer due to joint motion, we calculate ${}^{ia}\boldsymbol{a}_{ia}$ from (D.7)–(D.11) assuming zero gravity (i.e., ${}^{0}\boldsymbol{a}_0 = \begin{bmatrix} 0 & 0 & 0 \end{bmatrix}^T$) and subtract this value from the actual accelerometer readings before using them for computing the inclination. In this way, the inclination estimations from the accelerometer measurement and inclination obtained from the complementary filter after compensating for the joint-induced accelerations are more accurate compared to the estimations done without the compensation.

D.4 Experimental Setup and Results

The experimental setup used in this study is shown in Fig. D.7. It consists of a planar three-link flexible manipulator with three revolute joints. Each link of the flexible arm is made of a hollow aluminium profile of length $\ell_1 = \ell_2 = \ell_3 = 1.5$ m. Each joint consists of a hub, motor, and planetary gearbox. The STIM300 IMU sensor is mounted closer to the tip of each link (${}^{1}\boldsymbol{r}_{1,1a} = \begin{bmatrix} -0.185 & 0.035 & 0.0198 \end{bmatrix}^T$ m, ${}^{2}\boldsymbol{r}_{2,2a} = \begin{bmatrix} -0.160 & 0.030 & 0.0198 \end{bmatrix}^T$ m, ${}^{3}\boldsymbol{r}_{3,3a} = \begin{bmatrix} -0.063 & 0.025 & 0.0198 \end{bmatrix}^T$ m) and the Leica spherical reflector is mounted closer to the tip of the last link (${}^{3}\boldsymbol{r}_{3,3L} = \begin{bmatrix} -0.175 & 0.0430 & 0 \end{bmatrix}^T$ m) so that Leica AT960 laser tracker can track the precise position of the reflector. The Leica tracker is used for validating the deflection compensation method proposed in this paper. The Leica tracker is calibrated with respect to the inertial frame $(\widehat{X}_0, \widehat{Y}_0)$ so that the reflector position with respect to the inertial frame could be measured using the tracker.

To validate the inclination estimation using the accelerometer mounted on each link, all three links are considered rigid. The joint position, velocity, and acceleration trajectories used in the simulation are shown in Figs. D.8, D.9, D.10 respectively. The joint trajectories are obtained using (D.3), where the joints are moved from rest

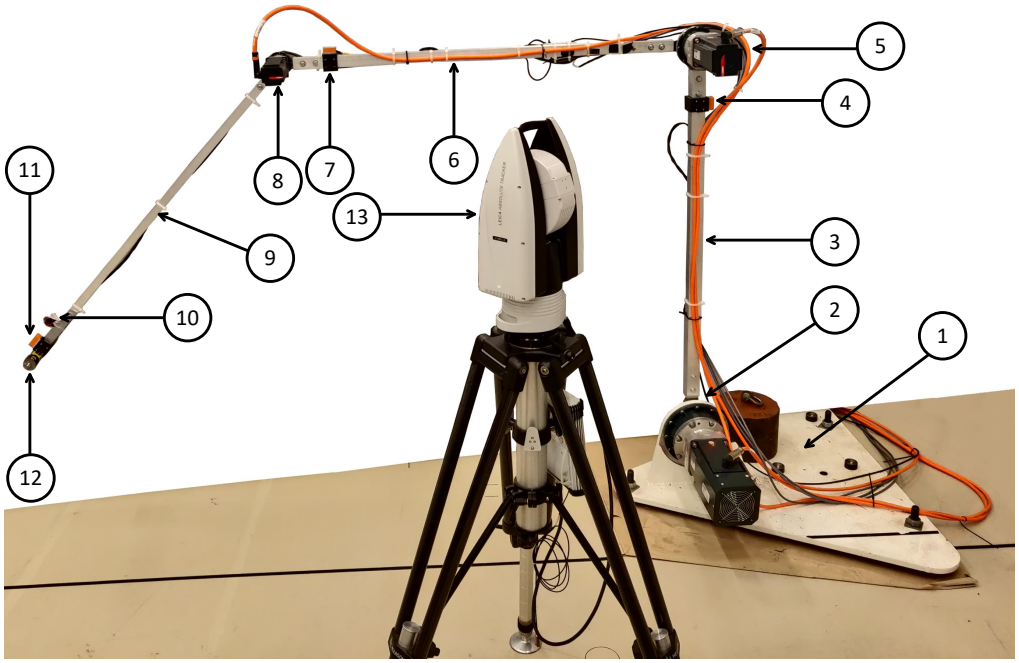

(**a**)

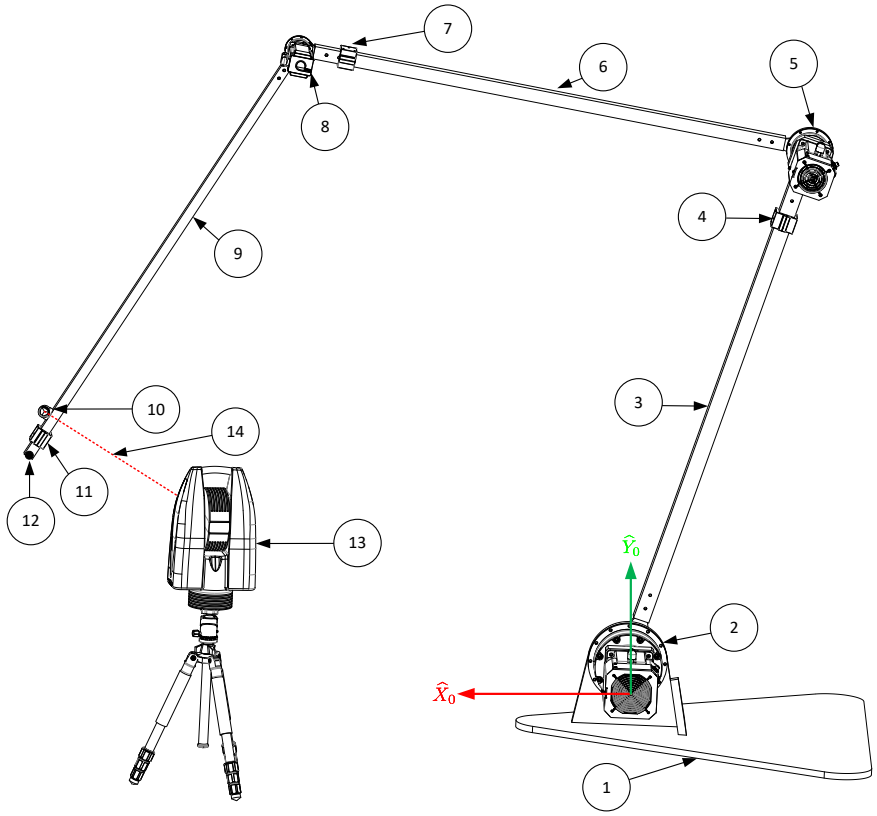

(**b**)

Figure D.7: Experimental setup (1. Robot base, 2. Joint 1, 3. Link 1, 4. IMU 1, 5. Joint 2, 6. Link 2, 7. IMU 2, 8. Joint 3, 9. Link 3, 10. Leica spherical reflector, 11. IMU 3, 12. Payload, 13. Leica AT960 laser tracker, 14. Laser beam): (**a**) actual, (**b**) the schematic.

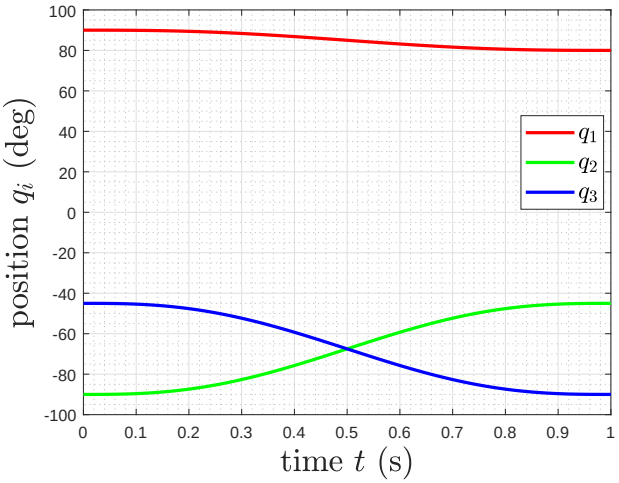

Figure D.8: Joint position trajectory used for evaluating the performance of inclination angle estimation with joint-induced acceleration compensation in simulation.

to rest ($\dot{\boldsymbol{q}}_0 = \dot{\boldsymbol{q}}_f = \begin{bmatrix} 0 & 0 & 0 \end{bmatrix}^T$ deg/s, $\ddot{\boldsymbol{q}}_0 = \ddot{\boldsymbol{q}}_f = \begin{bmatrix} 0 & 0 & 0 \end{bmatrix}^T$ deg/s^2) from initial joint positions $\boldsymbol{q}_0 = \begin{bmatrix} 90 & -90 & -45 \end{bmatrix}^T$ deg to final joint positions $\boldsymbol{q}_f = \begin{bmatrix} 80 & -45 & -90 \end{bmatrix}^T$ deg in $t_f = 1$ s.

The linear acceleration of the origin of the accelerometer reference frame with respect to the same frame is calculated using (D.7)–(D.11), which is shown in Figs. D.11–D.13. Then the inclination angle of each link is calculated using (D.5).

For compensating for the acceleration induced due to joint motion, the linear acceleration of the origin of the accelerometer reference frame with respect to the same frame is calculated again using (D.7)–(D.11) by assuming zero gravity to obtain the acceleration caused due to joint motion alone, which is shown in Figs. D.14–D.16. Thus obtained acceleration is subtracted from the total acceleration (along with gravity) to compensate for the acceleration induced due to joint motion. This compensated acceleration is used to obtain the inclination angle more accurately compared to the inclination calculated without compensation.

The inclination estimation using the proposed centripetal and tangential acceleration compensation method, as shown in Fig. D.18, is validated with the inclination estimated using the joint position values as shown in Fig. D.19. The inclination angle calculated without compensation as shown in Fig. D.17 is inaccurate (see Fig. D.19 as reference inclination for comparison) due to external acceleration interference (caused by joint motion).

In the experimental studies of static deflection compensation, the joints are moved from rest to rest ($\dot{\boldsymbol{q}}_0 = \dot{\boldsymbol{q}}_f = \begin{bmatrix} 0 & 0 & 0 \end{bmatrix}^T$ deg/s, $\ddot{\boldsymbol{q}}_0 = \ddot{\boldsymbol{q}}_f = \begin{bmatrix} 0 & 0 & 0 \end{bmatrix}^T$ deg/s^2) from initial joint positions $\boldsymbol{q}_0 = \begin{bmatrix} 90 & -90 & -45 \end{bmatrix}^T$ deg to final joint positions

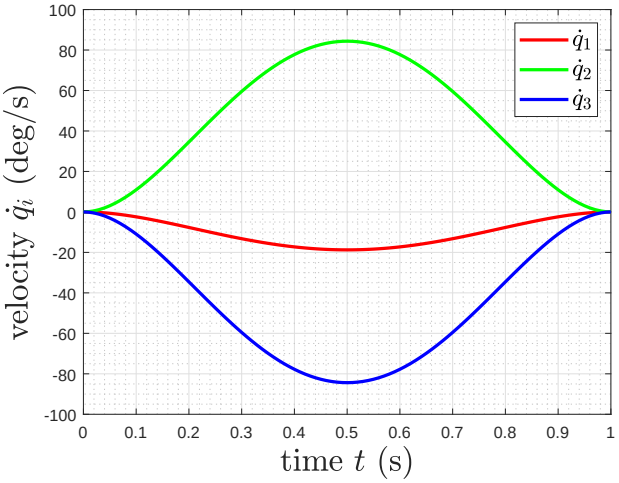

Figure D.9: Joint velocity trajectory used for evaluating the performance of inclination angle estimation with joint-induced acceleration compensation in simulation.

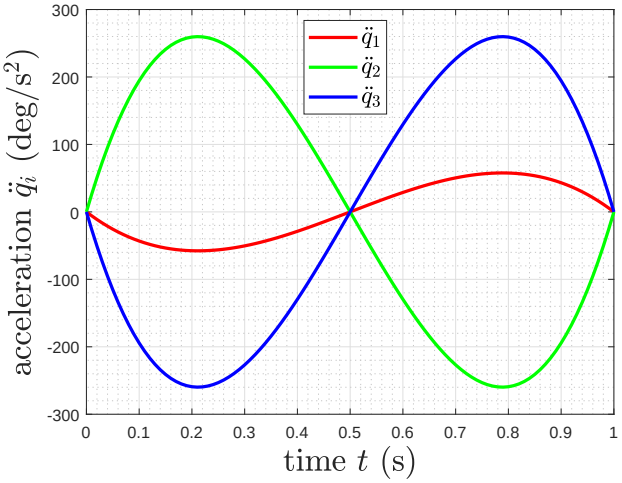

Figure D.10: Joint acceleration trajectory used for evaluating the performance of inclination angle estimation with joint-induced acceleration compensation in simulation.

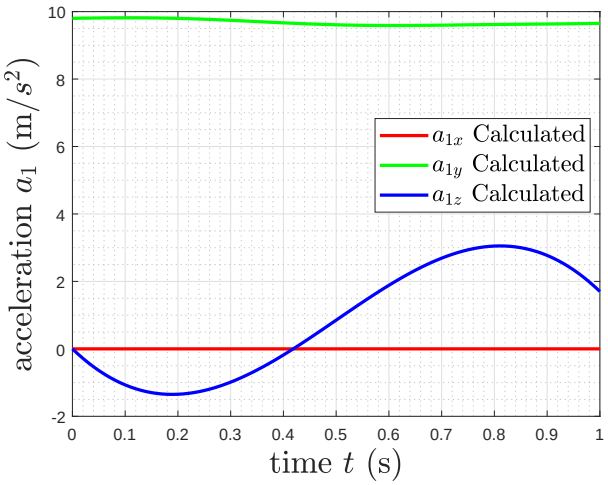

Figure D.11: Link 1 accelerometer readings calculated with gravity in simulation.

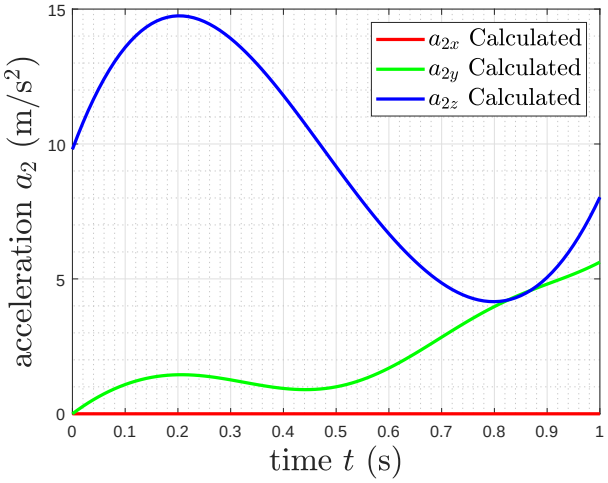

Figure D.12: Link 2 accelerometer readings calculated with gravity in simulation.

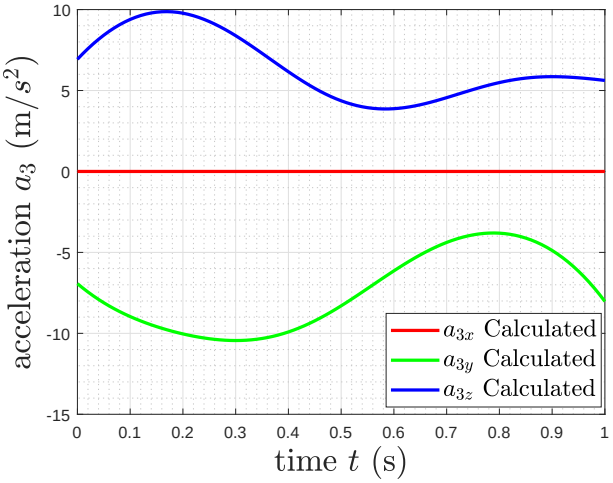

Figure D.13: Link 3 accelerometer readings calculated with gravity in simulation.

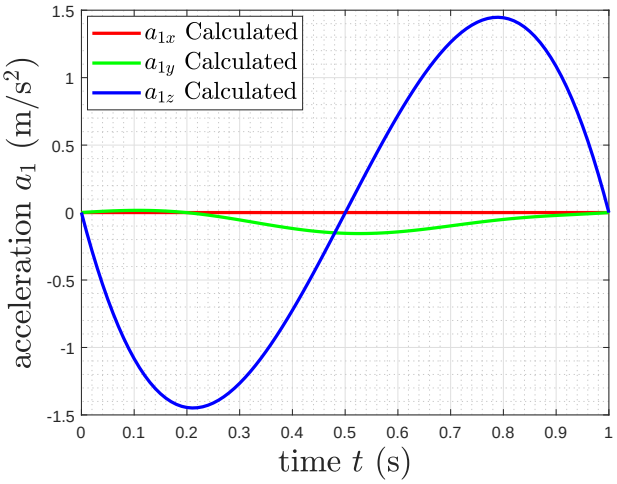

Figure D.14: Link 1 accelerometer readings calculated assuming zero gravity in simulation.

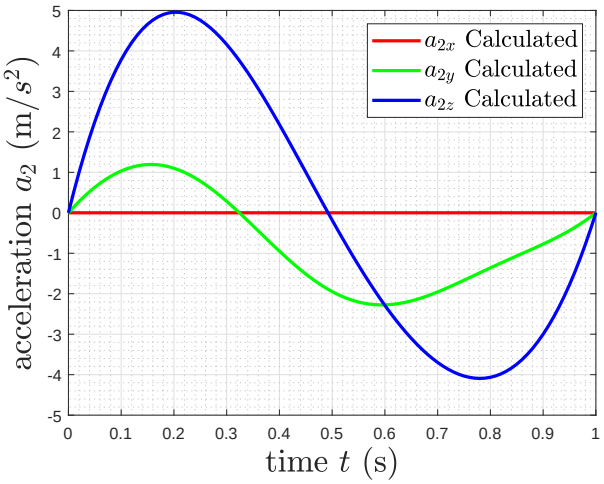

Figure D.15: Link 2 accelerometer readings calculated assuming zero gravity in simulation.

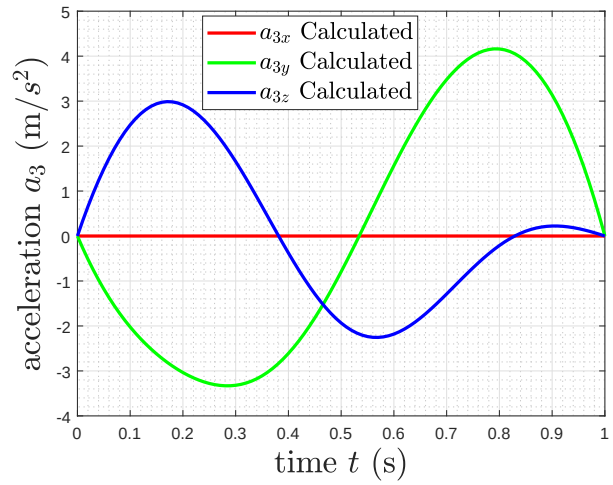

Figure D.16: Link 3 accelerometer readings calculated assuming zero gravity in simulation.

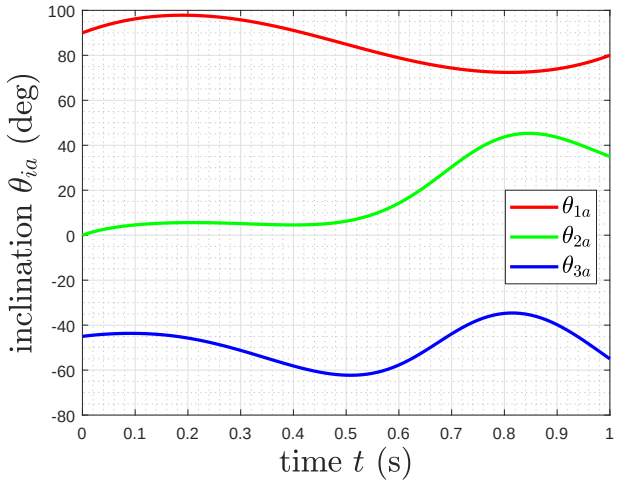

Figure D.17: Uncompensated inclination angle from the accelerometer in simulation.

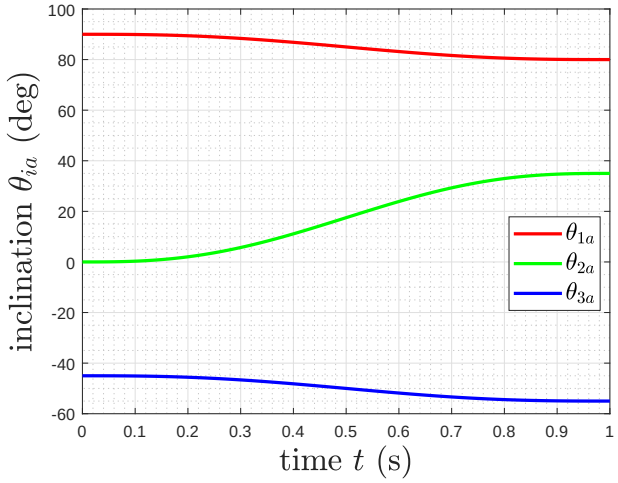

Figure D.18: Compensated inclination angle from the accelerometer in simulation.

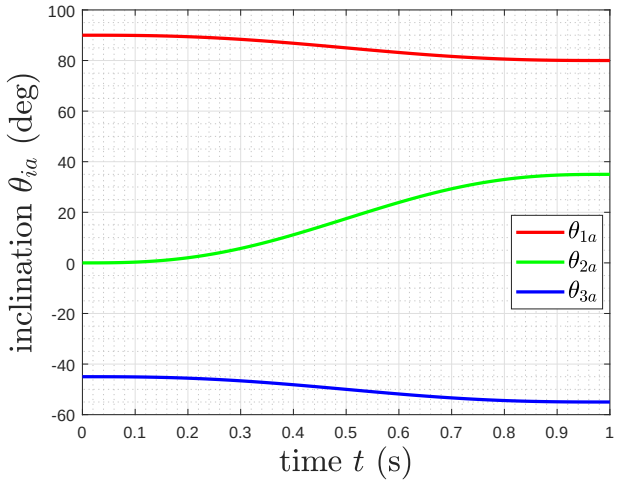

Figure D.19: Inclination angle calculated using joint position in simulation.

$\boldsymbol{q}_f = \begin{bmatrix} 80 & -45 & -90 \end{bmatrix}^T$ deg in $t_f = 5$ s, as shown in Fig. D.20.

The static deflection estimated after joint-induced acceleration compensation is shown in Fig. D.21. A first-order low pass filter is used with a cut-off frequency at 0.1 Hz in the estimated static deflection to obtain a smooth signal that is then used for compensation. To validate the effect of static deflection compensation, the reflector position is measured using the Leica AT960 laser tracker. The reflector positions measured using Leica tracker with respect to the robot reference frame $(\widehat{X}_0, \widehat{Y}_0)$ with and without static deflection compensation are shown in Figs. D.22 and D.23. Moreover, the reference reflector position calculated using forward kinematics with reference joint position is also shown to verify the effectiveness of the static compensation. Figs. D.24 and D.25 show the error in x and y position of the reflector with and without static deflection compensation obtained by calculating the difference between the reference position and the actual position of the reflector. The error in Fig. D.25 is the result of overcompensation of the static deflection by using $w'_{ie} \approx \Delta q_i$ for static deflection compensation, as $w'_{ie} > \Delta q_i$ in reality (see Fig. D.1). Since the error in Fig. D.25 is marginal, the proposed method is proved to be a good compromise between the complexity (and cost) of determining accurate deflection and the simplicity of neglecting the static deflection.

The joint-induced acceleration compensation in the link mounted accelerometer readings is verified experimentally by moving joints 3 from -90 deg to 0 deg in 2 s and keeping the other two joints stationary as shown in Fig. D.26. Fig. D.27 shows the linear acceleration measured by the accelerometer mounted on link 3 and the acceleration computed using (D.7)–(D.11). The measured and calculated acceleration values at the origin of the accelerometer, shown in Fig. D.27, are almost overlapping apart from the error introduced due to the rigid link assumption while calculating the acceleration.

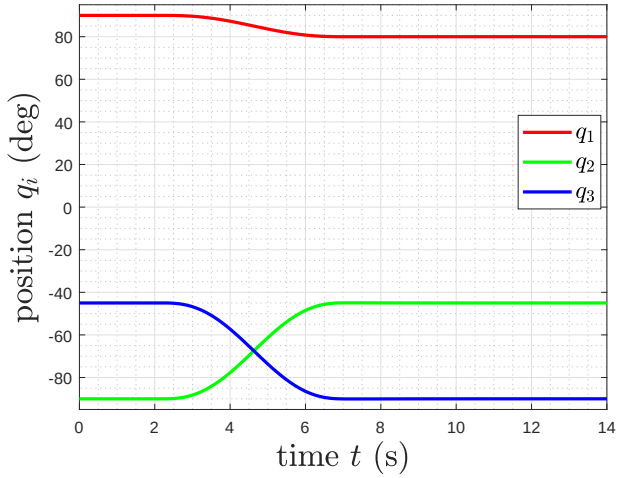

Figure D.20: Joint position trajectory used for evaluating the performance of static deflection compensation.

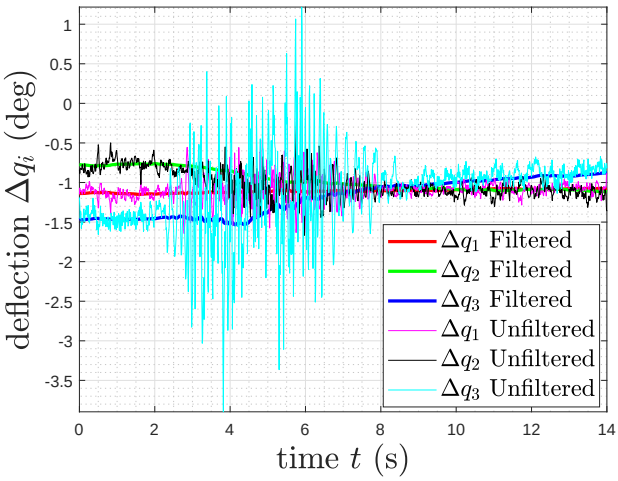

Figure D.21: Link deflections.

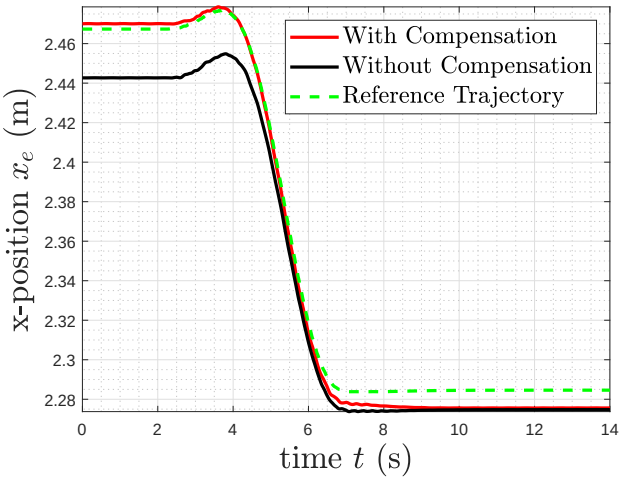

Figure D.22: Reflector x-position measured using laser tracker with and without static deflection compensation.

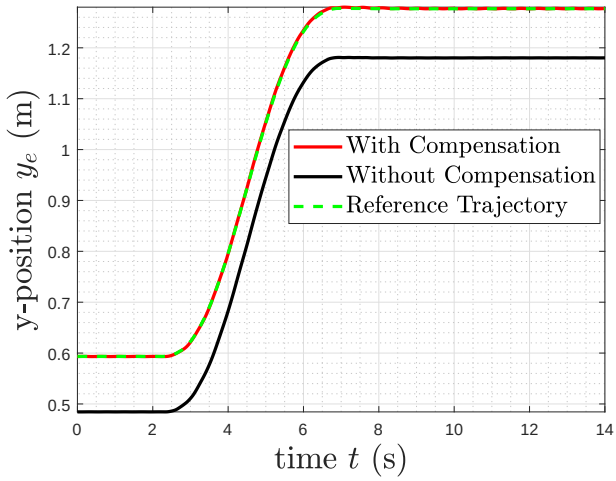

Figure D.23: Reflector y-position measured using laser tracker with and without static deflection compensation.

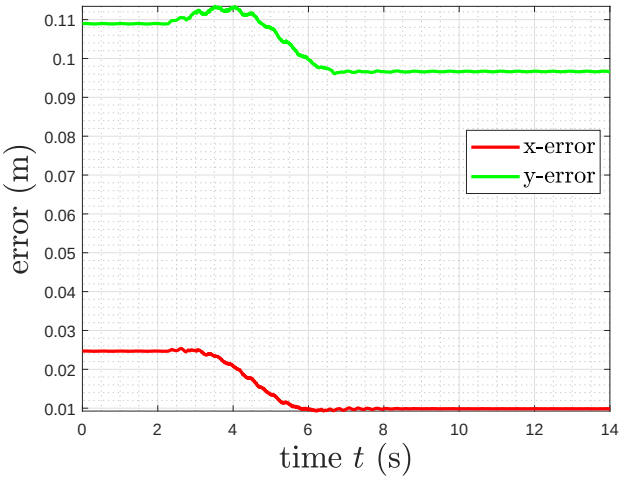

Figure D.24: Reflector position error without static deflection compensation.

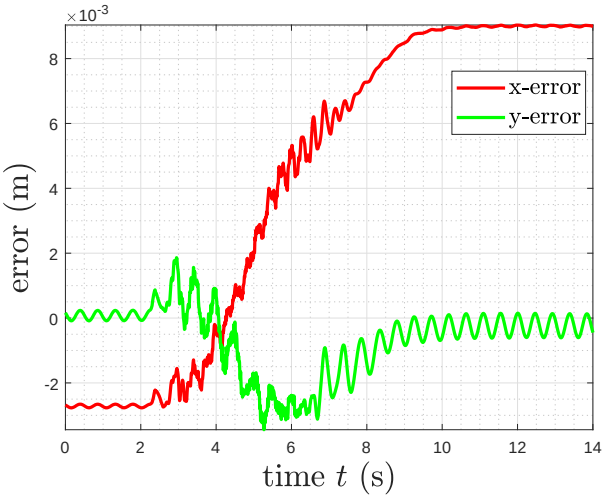

Figure D.25: Reflector position error with static deflection compensation.

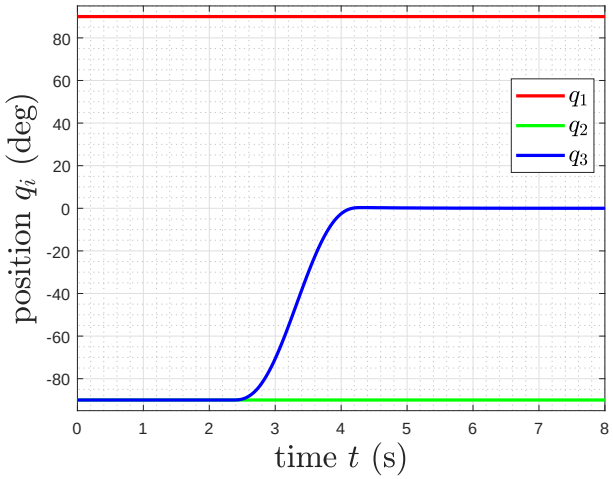

Figure D.26: Joint position trajectory used for evaluating the performance of deflection estimation with joint-induced acceleration compensation.

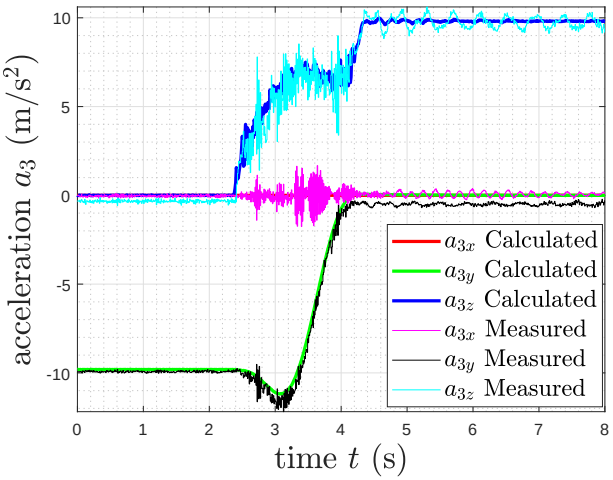

Figure D.27: Link 3 accelerometer readings calculated vs measured.

The linear acceleration of the origin of the accelerometer reference frame with respect to the same frame induced due to joint 3 motion only (assuming no gravity acceleration) is shown in Fig. D.28. The joint-induced acceleration calculated assuming no gravity is compensated (subtracted) from the IMU readings to estimate the link deflection. Figs. D.29 and D.30 show the deflection of link 3 calculated without and with joint-induced acceleration compensation. A first-order low pass filter is used with a cut-off frequency at 0.1 Hz in the estimated static deflection to obtain a smooth deflection signal. The negative influence of joint motion in static deflection estimation without the joint-induced acceleration compensation is clearly visible in Fig. D.29. The static deflection estimation is improved by compensating for the joint-induced acceleration as shown in Fig. D.30.

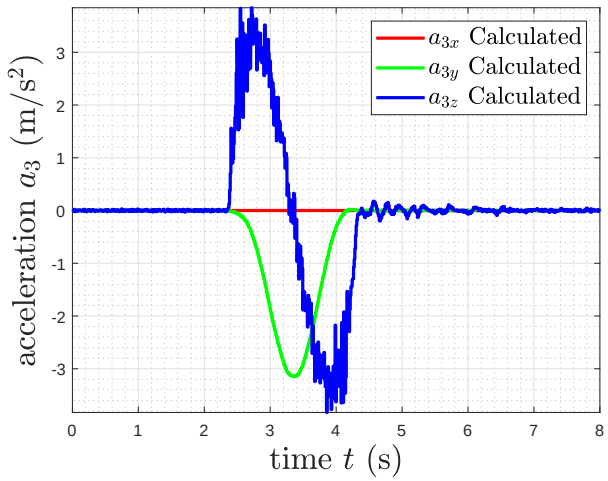

Figure D.28: Link 3 accelerometer readings calculated assuming zero gravity.

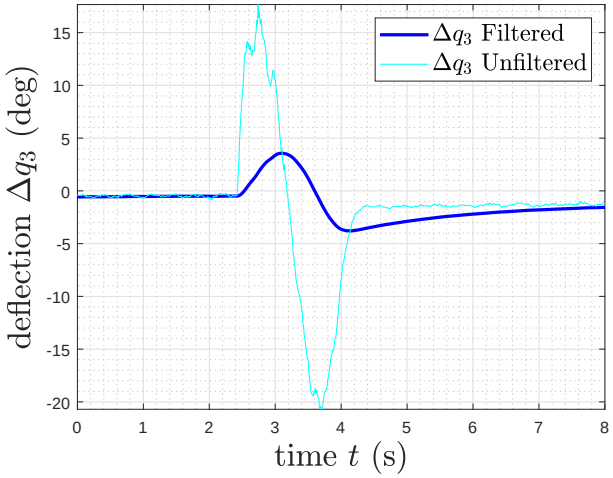

Figure D.29: Link 3 deflection estimated without joint-induced acceleration compensation.

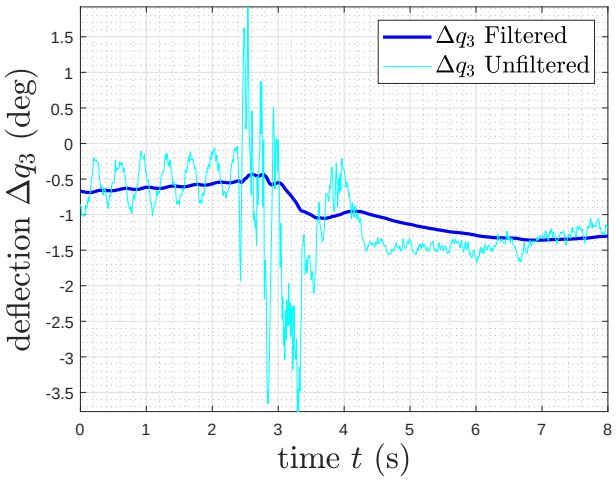

Figure D.30: Link 3 deflection estimated with joint-induced acceleration compensation.

D.5 Conclusions and Discussions

The static deflection compensation technique of planar multi-link flexible manipulators under gravity is proposed and experimentally validated. The performance of the IMU-based deflection estimation is validated using the high-precision laser tracker.

The cut-off frequency of the low pass filter used in smoothing the deflection signal should be smaller than the smallest resonance frequency of the arm while manipulating the maximum payload. This is done to avoid resonance that may occur during the compensation. It should be noted that the resonance frequencies depend on the robot configuration and the payload [14].

In the next step, the work will be extended to the implementation of oscillation damping control using the deflection signal from the IMU mounted on each link of the multi-link manipulator. Moreover, the use of the redundant degree of freedom of the planar three-link flexible arm will be explored for suppressing the elastic vibrations.

Acknowledgment

This work was partially funded by the Research Council of Norway through the centre SFI Offshore Mechatronics, project 237896.

References – Paper D

[1] Dipendra Subedi, Ilya Tyapin, and Geir Hovland. Review on Modeling and Control of Flexible Link Manipulators. *Modeling, Identification and Control*, 41 (3):141–163, 2020. doi: 10.4173/mic.2020.3.2.

[2] Chang Tai Kiang, Andrew Spowage, and Chan Kuan Yoong. Review of control and sensor system of flexible manipulator. *Journal of Intelligent & Robotic Systems*, 77(1):187–213, 2015.

[3] K. Parsa, J. Angeles, and A.K. Misra. Estimation of the flexural states of a macro-micro manipulator using point-acceleration data. *IEEE Transactions on Robotics*, 21(4):565–573, 2005. doi: 10.1109/TRO.2005.844677.

[4] Ismael Payo and Vicente Feliu. Strain gauges based sensor system for measuring 3-d deflections of flexible beams. *Sensors and Actuators A: Physical*, 217:81–94, sep 2014. doi: 10.1016/j.sna.2014.06.014.

[5] Jianyong Qian, Qi Su, Fu Zhang, Yun Ma, Zifan Fang, and Bing Xu. Static deformation-compensation method based on inclination-sensor feedback for large-scale manipulators with hydraulic actuation. *Processes*, 8(1):81, jan 2020. doi: 10.3390/pr8010081.

[6] Klaus Obergfell and Wayne J. Book. End-point position measurements of long-reach flexible manipulators. *IFAC Proceedings Volumes*, 27(14):669–674, sep 1994. doi: 10.1016/s1474-6670(17)47382-4.

[7] W.L. Xu, S.K. Tso, and X.S. Wang. Sensor-based deflection modeling and compensation control of flexible robotic manipulator. *Mechanism and Machine Theory*, 33(7):909–924, oct 1998. doi: 10.1016/s0094-114x(98)00009-3.

[8] S.K. Tso, T.W. Yang, W.L. Xu, and Z.Q. Sun. Vibration control for a flexible-link robot arm with deflection feedback. *International Journal of Non-Linear Mechanics*, 38(1):51–62, jan 2003. doi: 10.1016/s0020-7462(01)00040-3.

[9] Zhao-Hui Jiang and A. Goto. Visual sensor based vibration control and end-effector control for flexible robot arms. In *2005 IEEE International Conference on Industrial Technology*, pages 383–388, 2005. doi: 10.1109/ICIT.2005.1600668.

[10] I Weerasekera, G Balyasin, W-H Zhu, and G Liu. Lens-less PSD measurement of flexible link deflection. *Measurement Science and Technology*, 30(1):015003, dec 2018. doi: 10.1088/1361-6501/aaed01.

[11] C. Mavroidis, P. Rowe, and S. Dubowsky. Inferred end-point control of long reach manipulators. In *Proceedings 1995 IEEE/RSJ International Conference on Intelligent Robots and Systems. Human Robot Interaction and Cooperative Robots*, volume 2, pages 71–76 vol.2, 1995. doi: 10.1109/IROS.1995.526141.

[12] M. H. Korayem, A. M. Shafei, and F. Absalan. Estimate a flexible link's shape by the use of strain gauge sensors. *ISRN Robotics*, 2013:1–9, oct 2013. doi: 10.5402/2013/212805.

[13] Christopher J Fisher. Using an accelerometer for inclination sensing. *AN-1057, Application note, Analog Devices*, pages 1–8, 2010.

[14] Dipendra Subedi, Ilya Tyapin, and Geir Hovland. Dynamic modeling of planar multi-link flexible manipulators. *Robotics*, 10(2):70, may 2021. doi: 10.3390/robotics10020070.

[15] John J Craig. *Introduction to robotics: mechanics and control, 3/E*. Pearson Education India, 2009.

[16] Lorenzo Sciavicco and Bruno Siciliano. *Modelling and control of robot manipulators*. Springer Science & Business Media, 2001.

[17] Jörn Malzahn. *Modeling and control of multi-elastic-link robots under gravity: from oscillation damping and position control to physical interaction*. PhD thesis, Faculty of Electrical Engineering and Information Technology, TU Dortmund University, Dortmund, Germany, 2014. URL `http://hdl.handle.net/2003/33694`.

[18] Pengfei Gui, Liqiong Tang, and Subhas Mukhopadhyay. Mems based imu for tilting measurement: Comparison of complementary and kalman filter based data fusion. In *2015 IEEE 10th Conference on Industrial Electronics and Applications (ICIEA)*, pages 2004–2009, 2015. doi: 10.1109/ICIEA.2015.7334442.

[19] Alessandro De Luca and Lorenzo Ferrajoli. A modified newton-euler method for dynamic computations in robot fault detection and control. In *2009 IEEE*

International Conference on Robotics and Automation, pages 3359–3364, 2009. doi: 10.1109/ROBOT.2009.5152618.

Paper E

Control of Redundant Flexible Manipulators with Redundancy Resolution

Dipendra Subedi, Ilya Tyapin and Geir Hovland

This paper has been published as:

Dipendra Subedi, Ilya Tyapin and Geir Hovland. Control of Redundant Flexible Manipulators with Redundancy Resolution. *2022 8th International Conference on Mechatronics and Robotics Engineering (ICMRE)*, pages 116–121, 2022. doi: 10.1109/ICMRE54455.2022.9734097.

Control of Redundant Flexible Manipulators with Redundancy Resolution

Dipendra Subedi, Ilya Tyapin and Geir Hovland
Department of Engineering Sciences
University of Agder
4879 Grimstad, Norway

Abstract **This paper deals with the online control of a redundant flexible link manipulator to achieve minimum oscillations using the redundancy resolution technique. Different redundancy resolution techniques proposed and used for rigid link manipulators are tested for their use in the case of flexible link manipulators. The simulation model of a planar three-link flexible manipulator is used in this study. The redundancy resolution using kinetic energy minimization techniques is compared with the local joint acceleration minimization method to show the advantage of achieving minimum vibrations.**

E.1 Introduction

In most robotic applications the tasks are specified in the Cartesian space. However, the robot commands are executed in the joint space. Therefore, it is necessary to solve the inverse kinematics problem to find the corresponding joint positions for achieving the desired end-effector position and orientation. A redundant manipulator has more degrees of freedom (DoFs) than required to achieve the desired end-effector position and orientation. The redundant DoFs can be exploited to achieve different criteria for improving the performance of the redundant manipulator without affecting the primary goal of reaching task space configurations (i.e., end-effector position and orientation). Different redundancy resolution methods are available in the literature for rigid link manipulators. Manipulator redundancy has been exploited in the literature to achieve different criteria like joint limits avoidance [1, 2], minimization of kinetic energy [3], obstacles avoidance [4], singularity avoidance [5, 6], and minimization of joint torques [7]. However, their application in redundant flexible link manipulators (FLMs) has not been explored. This work's aim is to explore different redundancy resolution methods and utilize them to control redundant FLMs for achieving minimum vibrations.

Different optimal planning methods have been studied in the literature for the rest-to-rest motion of the FLM to achieve minimum end-effector vibration when approaching a desired final position in the desired traveling time [8, 9]. Particle

swarm optimization algorithms and genetic algorithms have been applied to trajectory planning of flexible redundant manipulators to minimize vibration in [10] and [11] respectively. Although these optimization methods are offline, they require a dynamic model of the FLM which is computationally expensive. Therefore, it is time-consuming and impractical to run the optimization procedure whenever there is a change in the initial position, goal position, or traveling time. The configurations of the FLMs affect the end-effector vibration as highlighted in [12] and [13]. However, there has been little reported work on online control of the FLMs exploiting the redundant configuration of the manipulators for reducing vibrations.

The redundancy resolution methods based on minimum kinetic energy are used in this work for the online control of the FLMs for achieving minimum vibration and compared to the minimum norm joint acceleration solution.

The paper is organized into six sections as follows. Section E.2 describes the kinematics of manipulators. The dynamic model of the planar FLM is presented in section E.3. Different redundancy resolution methods are presented in section E.4. The results obtained from three different redundancy resolution methods when applied to control FLMs are presented in section E.5. Conclusions and discussions follow in section E.6.

E.2 Rigid Body Kinematics

The forward kinematics of a manipulator describing the pose of the end-effector as a function of the joint angles is given by (E.1), where $\boldsymbol{x} \in \mathbb{R}^m$ is the vector representing the pose of the end-effector, and $\boldsymbol{q}_r \in \mathbb{R}^n$ is the vector of joint positions.

$$\boldsymbol{x} = f(\boldsymbol{q}_r) \tag{E.1}$$

For the planar three-link manipulator, $n = 3$ represents three joints and $m = 2$ represents the 2D position of the end-effector. Differentiating (E.1) with respect to time, the relation between joint velocity and end-effector velocity is obtained as shown in (E.2), which is called differential kinematics of the manipulator, where $\boldsymbol{J}(\boldsymbol{q}_r) \in \mathbb{R}^{m \times n}$ is the $m \times n$ Jacobian matrix.

$$\dot{\boldsymbol{x}} = \boldsymbol{J}(\boldsymbol{q}_r)\dot{\boldsymbol{q}}_r \tag{E.2}$$

Similarly, the relation between the joint acceleration and end-effector acceleration is obtained by differentiating (E.2) with respect to time as shown in (E.3).

$$\ddot{\boldsymbol{x}} = \boldsymbol{J}(\boldsymbol{q}_r)\ddot{\boldsymbol{q}}_r + \dot{\boldsymbol{J}}(\boldsymbol{q}_r, \dot{\boldsymbol{q}}_r)\dot{\boldsymbol{q}}_r \tag{E.3}$$

Hereafter, $\boldsymbol{J}$ and $\dot{\boldsymbol{J}}$ are used instead of $\boldsymbol{J}(\boldsymbol{q}_r)$ and $\dot{\boldsymbol{J}}(\boldsymbol{q}_r, \dot{\boldsymbol{q}}_r)$ respectively.

E.3 Manipulator Dynamics

The dynamic model of the planar multi-link flexible manipulator derived using the assumed modes method is given by (E.4), where $\boldsymbol{q} = \begin{bmatrix} \boldsymbol{q}_r & \boldsymbol{q}_f \end{bmatrix}^T$, $\boldsymbol{q}_r = \begin{bmatrix} q_{r1} & q_{r2} & \cdots & q_{rn} \end{bmatrix}^T$, $\boldsymbol{q}_f = \begin{bmatrix} q_{f11} & q_{f12} & \cdots & q_{f1n_f} \cdots & q_{fn1} & q_{fn2} & \cdots & q_{fnn_f} \end{bmatrix}^T$, q_{ri} represents the i^{th} joint position, q_{fij} represents the time-varying variable related to the spatial assumed mode shape of link i and mode of vibration j, n_f represents the total number of assumed modes of vibration, $\boldsymbol{M}(\boldsymbol{q})$ is the inertia matrix, $\boldsymbol{c}(\boldsymbol{q}, \dot{\boldsymbol{q}})$ is the vector of Coriolis and centripetal effects, $\boldsymbol{g}(\boldsymbol{q})$ is the gravity term, and $\boldsymbol{K}$ is the rigidity modal matrix [13].

$$\boldsymbol{M}(\boldsymbol{q})\ddot{\boldsymbol{q}} + \boldsymbol{c}(\boldsymbol{q}, \dot{\boldsymbol{q}}) + \boldsymbol{g}(\boldsymbol{q}) + \boldsymbol{K}\boldsymbol{q} = \boldsymbol{\tau} \tag{E.4}$$

Joint viscous friction and link structural damping can be included by adding a damping matrix $\boldsymbol{D}$ as

$$\boldsymbol{M}(\boldsymbol{q})\ddot{\boldsymbol{q}} + \boldsymbol{c}(\boldsymbol{q}, \dot{\boldsymbol{q}}) + \boldsymbol{g}(\boldsymbol{q}) + \boldsymbol{K}\boldsymbol{q} + \boldsymbol{D}\dot{\boldsymbol{q}} = \boldsymbol{\tau}. \tag{E.5}$$

The dynamic equation can be written in another form separating rigid and flexible parts as in (E.6)–(E.8).

$$\begin{bmatrix} \boldsymbol{M}_{rr} & \boldsymbol{M}_{rf} \\ \boldsymbol{M}_{rf}^T & \boldsymbol{M}_{ff} \end{bmatrix} \begin{bmatrix} \ddot{\boldsymbol{q}}_r \\ \ddot{\boldsymbol{q}}_f \end{bmatrix} + \begin{bmatrix} \boldsymbol{c}_r \\ \boldsymbol{c}_f \end{bmatrix} + \begin{bmatrix} \boldsymbol{g}_r \\ \boldsymbol{g}_f \end{bmatrix} + \begin{bmatrix} \boldsymbol{0} & \boldsymbol{0} \\ \boldsymbol{0} & \boldsymbol{K}_{ff} \end{bmatrix} \begin{bmatrix} \boldsymbol{q}_r \\ \boldsymbol{q}_f \end{bmatrix} + \begin{bmatrix} \boldsymbol{D}_{rr} & \boldsymbol{0} \\ \boldsymbol{0} & \boldsymbol{D}_{ff} \end{bmatrix} \begin{bmatrix} \dot{\boldsymbol{q}}_r \\ \dot{\boldsymbol{q}}_f \end{bmatrix} = \begin{bmatrix} \boldsymbol{\tau}_r \\ \boldsymbol{0} \end{bmatrix} \tag{E.6}$$

$$\boldsymbol{M}_{rr}\ddot{\boldsymbol{q}}_r + \boldsymbol{M}_{rf}\ddot{\boldsymbol{q}}_f + \boldsymbol{c}_r + \boldsymbol{g}_r + \boldsymbol{D}_{rr}\dot{\boldsymbol{q}}_r = \boldsymbol{\tau}_r \tag{E.7}$$

$$\boldsymbol{M}_{rf}^T\ddot{\boldsymbol{q}}_r + \boldsymbol{M}_{ff}\ddot{\boldsymbol{q}}_f + \boldsymbol{c}_f + \boldsymbol{g}_f + \boldsymbol{K}_{ff}\boldsymbol{q}_f + \boldsymbol{D}_{ff}\dot{\boldsymbol{q}}_f = \boldsymbol{0} \tag{E.8}$$

E.4 Redundancy Resolution

A redundant manipulator has more DoFs than required to achieve the desired end-effector position and orientation. That is, the number of DoFs n of a redundant manipulator is greater than the number of controlled end-effector DoFs m. There is an infinite number of robot configurations possible to achieve any given pose of the end-effector.

For redundant manipulators i.e., $n > m$, the general solutions for (E.2) and (E.3)

are given by (E.9) and (E.10) respectively, where $\boldsymbol{J}^+$ represents the pseudoinverse of $\boldsymbol{J}$, $(\boldsymbol{I} - \boldsymbol{J}^+\boldsymbol{J})$ is a projector of arbitrary vectors $\boldsymbol{z}_1 \in \mathbb{R}^n$ and $\boldsymbol{z}_2 \in \mathbb{R}^n$ onto the null space of $\boldsymbol{J}$.

$$\dot{\boldsymbol{q}}_r = \boldsymbol{J}^+\dot{\boldsymbol{x}} + (\boldsymbol{I} - \boldsymbol{J}^+\boldsymbol{J})\boldsymbol{z}_1 \tag{E.9}$$

$$\ddot{\boldsymbol{q}}_r = \boldsymbol{J}^+(\ddot{\boldsymbol{x}} - \dot{\boldsymbol{J}}\dot{\boldsymbol{q}}_r) + (\boldsymbol{I} - \boldsymbol{J}^+\boldsymbol{J})\boldsymbol{z}_2 \tag{E.10}$$

By considering $\boldsymbol{z}_1 = \boldsymbol{0}$ and $\boldsymbol{z}_2 = \boldsymbol{0}$ in (E.9) and (E.10), the pseudoinverse solutions (exact solution) at the velocity and acceleration levels are obtained, which result in the minimum norm joint velocity and minimum norm joint acceleration solutions respectively.

The joint velocity and acceleration solutions given by (E.9) and (E.10) are the solutions of the constrained linear-quadratic optimization problems given by (E.11) and (E.12) respectively.

$$\begin{aligned} \underset{\dot{\boldsymbol{q}}_r}{\text{minimize}} \quad & \boldsymbol{H}(\dot{\boldsymbol{q}}_r) = \frac{1}{2}(\dot{\boldsymbol{q}}_r - \boldsymbol{z}_1)^T(\dot{\boldsymbol{q}}_r - \boldsymbol{z}_1) \\ \text{subject to} \quad & \boldsymbol{J}\dot{\boldsymbol{q}}_r - \dot{\boldsymbol{x}} = \boldsymbol{0} \end{aligned} \tag{E.11}$$

$$\begin{aligned} \underset{\ddot{\boldsymbol{q}}_r}{\text{minimize}} \quad & \boldsymbol{H}(\ddot{\boldsymbol{q}}_r) = \frac{1}{2}(\ddot{\boldsymbol{q}}_r - \boldsymbol{z}_2)^T(\ddot{\boldsymbol{q}}_r - \boldsymbol{z}_2) \\ \text{subject to} \quad & \boldsymbol{J}\ddot{\boldsymbol{q}}_r + \dot{\boldsymbol{J}}\dot{\boldsymbol{q}}_r - \ddot{\boldsymbol{x}} = \boldsymbol{0} \end{aligned} \tag{E.12}$$

The tasks defined by $\boldsymbol{z}_1$ and $\boldsymbol{z}_2$ have no effect on the end-effector motion. Therefore, by choosing suitable vectors $\boldsymbol{z}_1$ and $\boldsymbol{z}_2$, the redundant DoFs could be exploited to optimize certain performance measures (secondary task) without altering the task space configurations (primary goal). Other methods to achieve desired performance characteristics include task augmentation [14] and weighted pseudoinverse technique [3, 7, 15–18].

The general redundancy resolution at velocity and acceleration levels for finding the local optimal motions can be formulated as the constrained linear-quadratic optimization problems given by (E.13) and (E.14) respectively, where $\boldsymbol{W} \in \mathbb{R}^{n\times n}$ is an arbitrary positive-definite symmetric weight matrix.

$$\begin{aligned} \underset{\dot{\boldsymbol{q}}_r}{\text{minimize}} \quad & \boldsymbol{H}(\dot{\boldsymbol{q}}_r) = \frac{1}{2}(\dot{\boldsymbol{q}}_r - \boldsymbol{z}_1)^T\boldsymbol{W}(\dot{\boldsymbol{q}}_r - \boldsymbol{z}_1) \\ \text{subject to} \quad & \boldsymbol{J}\dot{\boldsymbol{q}}_r - \dot{\boldsymbol{x}} = \boldsymbol{0} \end{aligned} \tag{E.13}$$

$$\begin{aligned} \underset{\ddot{\boldsymbol{q}}_r}{\text{minimize}} \quad & \boldsymbol{H}(\ddot{\boldsymbol{q}}_r) = \frac{1}{2}(\ddot{\boldsymbol{q}}_r - \boldsymbol{z}_2)^T\boldsymbol{W}(\ddot{\boldsymbol{q}}_r - \boldsymbol{z}_2) \\ \text{subject to} \quad & \boldsymbol{J}\ddot{\boldsymbol{q}}_r + \dot{\boldsymbol{J}}\dot{\boldsymbol{q}}_r - \ddot{\boldsymbol{x}} = \boldsymbol{0} \end{aligned} \tag{E.14}$$

The solutions of (E.13) and (E.14), which can be derived using Lagrange multipliers, are given by (E.15) and (E.16) respectively, where $\boldsymbol{J}_W^+$ is the weighted pseudoinverse of $\boldsymbol{J}$ given by (E.17).

$$\dot{\boldsymbol{q}}_r = \boldsymbol{J}_W^+ \dot{\boldsymbol{x}} + (\boldsymbol{I} - \boldsymbol{J}_W^+ \boldsymbol{J})\boldsymbol{z}_1 \tag{E.15}$$

$$\ddot{\boldsymbol{q}}_r = \boldsymbol{J}_W^+ (\ddot{\boldsymbol{x}} - \dot{\boldsymbol{J}}\dot{\boldsymbol{q}}_r) + (\boldsymbol{I} - \boldsymbol{J}_W^+ \boldsymbol{J})\boldsymbol{z}_2 \tag{E.16}$$

$$\boldsymbol{J}_W^+ = \boldsymbol{W}^{-1}\boldsymbol{J}^T(\boldsymbol{J}\boldsymbol{W}^{-1}\boldsymbol{J}^T)^{-1} \tag{E.17}$$

In (E.17), the $\boldsymbol{J}_W^+$ becomes ill-conditioned when $\boldsymbol{J}$ is not full (row) rank or when the manipulator reaches a singularity. The singularity problem can be solved by using the Damped-Least-Squares approach which can be formulated as an unconstrained minimization problem of the forms given by (E.18) (at velocity level) and (E.19) (at acceleration level), where a scalar damping or singularity robustness factor λ is used to specify the relative importance of the norms of joint rates/accelerations and the tracking accuracy.

$$\begin{aligned} \underset{\dot{\boldsymbol{q}}_r}{\text{minimize}} \quad \boldsymbol{H}(\dot{\boldsymbol{q}}_r) = \frac{\lambda^2}{2}(\dot{\boldsymbol{q}}_r - \boldsymbol{z}_1)^T \boldsymbol{W}(\dot{\boldsymbol{q}}_r - \boldsymbol{z}_1) \\ + (\boldsymbol{J}\dot{\boldsymbol{q}}_r - \dot{\boldsymbol{x}})^T(\boldsymbol{J}\dot{\boldsymbol{q}}_r - \dot{\boldsymbol{x}}) \end{aligned} \tag{E.18}$$

$$\begin{aligned} \underset{\ddot{\boldsymbol{q}}_r}{\text{minimize}} \quad \boldsymbol{H}(\ddot{\boldsymbol{q}}_r) = \frac{\lambda^2}{2}(\ddot{\boldsymbol{q}}_r - \boldsymbol{z}_2)^T \boldsymbol{W}(\ddot{\boldsymbol{q}}_r - \boldsymbol{z}_2) \\ + (\boldsymbol{J}\ddot{\boldsymbol{q}}_r + \dot{\boldsymbol{J}}\dot{\boldsymbol{q}}_r - \ddot{\boldsymbol{x}})^T(\boldsymbol{J}\ddot{\boldsymbol{q}}_r + \dot{\boldsymbol{J}}\dot{\boldsymbol{q}}_r - \ddot{\boldsymbol{x}}) \end{aligned} \tag{E.19}$$

The solutions of (E.18) and (E.19), which can be derived using Lagrange multipliers, are given by (E.20) and (E.21) respectively, where $\boldsymbol{J}_{W,DLS}^+$ is the damped weighted pseudoinverse of $\boldsymbol{J}$ given by (E.22).

$$\dot{\boldsymbol{q}}_r = \boldsymbol{J}_{W,DLS}^+ \dot{\boldsymbol{x}} + (\boldsymbol{I} - \boldsymbol{J}_{W,DLS}^+ \boldsymbol{J})\boldsymbol{z}_1 \tag{E.20}$$

$$\ddot{\boldsymbol{q}}_r = \boldsymbol{J}_{W,DLS}^+ (\ddot{\boldsymbol{x}} - \dot{\boldsymbol{J}}\dot{\boldsymbol{q}}_r) + (\boldsymbol{I} - \boldsymbol{J}_{W,DLS}^+ \boldsymbol{J})\boldsymbol{z}_2 \tag{E.21}$$

$$\boldsymbol{J}_{W,DLS}^+ = \boldsymbol{W}^{-1}\boldsymbol{J}^T(\boldsymbol{J}\boldsymbol{W}^{-1}\boldsymbol{J}^T + \lambda^2\boldsymbol{I})^{-1} \tag{E.22}$$

It can only be presumed that the sum of squares of joint velocities minimized by the generalized pseudoinverse ((using (E.9)) approximately minimizes the kinetic energy. The inertia-weighted pseudoinverse can be used to realize the true minimization of

kinetic energy [3, 7, 19]. The kinetic energy T of the system is given by (E.23).

$$T = \frac{1}{2}\dot{\boldsymbol{q}}_r^T \boldsymbol{M}_{rr} \dot{\boldsymbol{q}}_r \tag{E.23}$$

The joint acceleration solution of the constrained linear-quadratic optimization problem given by (E.24) that minimizes the manipulator's instantaneous kinetic energy is given by (E.25), where the inertia-weighted pseudoinverse $\boldsymbol{J}_M^+$ used to realize local minimization of kinetic energy is given by (E.26). The inertia-weighted pseudoinverse $\boldsymbol{J}_M^+$ in (E.26) is same as the weighted pseudoinverse in (E.17) with the weighting matrix $\boldsymbol{W} = \boldsymbol{M}_{rr}$.

$$\begin{aligned} \underset{\ddot{\boldsymbol{q}}_r}{\text{minimize}} \quad & \boldsymbol{H}(\ddot{\boldsymbol{q}}_r) = \frac{1}{2}\dot{\boldsymbol{q}}_r^T \boldsymbol{M}_{rr} \dot{\boldsymbol{q}}_r \\ \text{subject to} \quad & \boldsymbol{J}\ddot{\boldsymbol{q}}_r + \dot{\boldsymbol{J}}\dot{\boldsymbol{q}}_r - \ddot{\boldsymbol{x}} = \boldsymbol{0} \end{aligned} \tag{E.24}$$

$$\ddot{\boldsymbol{q}}_r = \boldsymbol{J}_M^+(\ddot{\boldsymbol{x}} - \dot{\boldsymbol{J}}\dot{\boldsymbol{q}}_r) \tag{E.25}$$

$$\boldsymbol{J}_M^+ = \boldsymbol{M}_{rr}^{-1}\boldsymbol{J}^T(\boldsymbol{J}\boldsymbol{M}_{rr}^{-1}\boldsymbol{J}^T)^{-1} \tag{E.26}$$

Similarly, the sum of squares of joint accelerations minimized by the generalized pseudoinverse (using (E.10)) is presumed to approximately minimize the joint torques. Since the manipulators are actually controlled by specifying joint torques to achieve the desired accelerations, it is desirable to optimize joint torques rather than joint velocities or accelerations. Torque minimization methods for redundancy resolution have been thoroughly studied in the literature [3, 6, 7, 16, 18, 20].

In [3], it is shown that the local optimization of the inertia inverse weighted dynamic torque given by (E.27) corresponds to the global kinetic energy minimization problem.

$$\begin{aligned} \underset{\ddot{\boldsymbol{q}}_r}{\text{minimize}} \quad & \boldsymbol{H}(\ddot{\boldsymbol{q}}_r) = \frac{1}{2}\boldsymbol{\tau}_r^T \boldsymbol{M}_{rr}^{-1} \boldsymbol{\tau}_r \\ \text{subject to} \quad & \boldsymbol{J}\ddot{\boldsymbol{q}}_r + \dot{\boldsymbol{J}}\dot{\boldsymbol{q}}_r - \ddot{\boldsymbol{x}} = \boldsymbol{0} \end{aligned} \tag{E.27}$$

The joint acceleration solution of the constrained linear-quadratic minimization problem given by (E.27) derived using Lagrange multipliers is given by (E.28).

$$\ddot{\boldsymbol{q}}_r = \boldsymbol{J}_M^+(\ddot{\boldsymbol{x}} - \dot{\boldsymbol{J}}\dot{\boldsymbol{q}}_r) - (\boldsymbol{I} - \boldsymbol{J}_M^+\boldsymbol{J})\boldsymbol{M}_{rr}^{-1}\boldsymbol{c}_r \tag{E.28}$$

In (E.28), the gravity-related terms are neglected in order to only consider the dynamic effects and to prevent the manipulator configuration from drooping as it attempts to reduce the gravitational potential energy of the system [3, 18]. Moreover, (E.28) is equivalent to (E.16) with the weighting matrix $\boldsymbol{W} = \boldsymbol{M}_{rr}$ and

$\boldsymbol{z}_2 = -\boldsymbol{M}_{rr}^{-1}\boldsymbol{c}_r$.

The joint acceleration solutions using (E.28) leave the joint velocities in the null-space untouched causing the joints that do not contribute to the end-effector motion to move freely. This can make the system unstable. The null space damping method can be used to ensure stability by appending a damping term to the redundant task as given by (E.29), where β is a positive scalar [18, 20].

$$\ddot{\boldsymbol{q}}_r = \boldsymbol{J}_M^{+}(\ddot{\boldsymbol{x}} - \dot{\boldsymbol{J}}\dot{\boldsymbol{q}}_r) - (\boldsymbol{I} - \boldsymbol{J}_M^{+}\boldsymbol{J})(\boldsymbol{M}_{rr}^{-1}\boldsymbol{c}_r + \beta\dot{\boldsymbol{q}}_r) \tag{E.29}$$

The open-loop solutions of joint variables obtained by numerical integration lead to solutions drift and then to task space errors. The Closed-Loop Inverse Kinematics (CLIK) algorithm can be used to overcome the joint drift problem which is based on the task space error between the desired and the actual end-effector positions or the task space velocity error [1]. The CLIK algorithm with redundancy resolution at the acceleration level is shown in Fig. E.1, where $\boldsymbol{K}_p$ and $\boldsymbol{K}_v$ are symmetric positive definite matrices and their choices guarantee that the task-space position error ($\boldsymbol{e}_p = \boldsymbol{x}_d - \boldsymbol{x}$) and velocity error ($\boldsymbol{e}_v = \dot{\boldsymbol{x}}_d - \boldsymbol{J}\dot{\boldsymbol{q}}_r$) uniformly converge to zero. The joint trajectories generated using the redundancy resolution techniques are used for the online control of the FLM as shown in Fig. E.1.

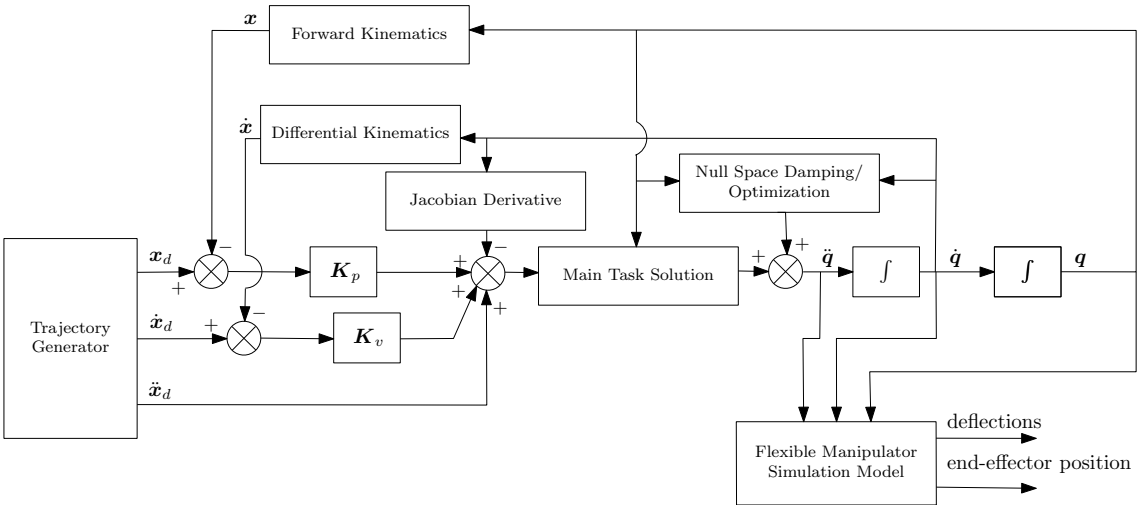

Figure E.1: CLIK algorithm with redundancy resolution at the acceleration level.

E.5 Simulation Results

A planar three-link flexible manipulator with three revolute joints ($n = 3$) is used in the simulation for the end-effector position control in the 2D Cartesian space ($m = 2$). Each link of the flexible arm is made of a hollow aluminium profile of length $\ell_1 = \ell_2 = \ell_3 = 1.5$ m. Each joint consists of a hub, motor, and planetary gearbox.

The simulation parameters of the FLM are detailed in [13].

Fig. E.2 shows the equivalent rigid body schematic of a three-link manipulator with Denavit-Hartenberg (DH) parameters given in Table E.1.

The quintic trajectory generator is used to generate a smooth Cartesian trajectory to move the end-effector from the initial position ($x_0 = \begin{bmatrix} 3 & 1.5 \end{bmatrix}^T$) to goal position ($x_f = \begin{bmatrix} 2 & 2 \end{bmatrix}^T$) in 0.5 s. The end-effector position, velocity, and acceleration trajectories used in this paper are shown in Fig. E.3. Since the flexible dynamics of the FLM is simulated for 2 s (to study about the residual oscillations) the trajectories are shown for the whole simulation time. The method proposed in [12] is used to estimate the optimal initial configuration of the redundant arm representing weak-vibration configuration.

The flexible dynamics of the FLM is simulated for 2 s using (E.8), where the joint trajectories are generated using different redundancy resolution techniques (see Fig. E.1). *MATLAB ode45* is used for time integration of dynamic equation given by (E.8). The joint trajectories generated using the redundancy resolution techniques are fed to the simulation model of the FLM to study the effects in the flexible dynamics of the FLM as shown in Fig. E.1. Following three cases of redundancy resolution methods are compared for their use in FLMs:

1. Case A: Local minimization of the joint acceleration (LMJA).

$$\begin{aligned} \ddot{\boldsymbol{q}}_r = \boldsymbol{J}^+((\ddot{\boldsymbol{x}}_d + \boldsymbol{K}_p(\boldsymbol{x}_d - \boldsymbol{x}) + \boldsymbol{K}_v(\dot{\boldsymbol{x}}_d - \boldsymbol{J}\dot{\boldsymbol{q}}) \\ - \dot{\boldsymbol{J}}\dot{\boldsymbol{q}}_r) + (\boldsymbol{I} - \boldsymbol{J}^+\boldsymbol{J})(-\beta\dot{\boldsymbol{q}}_r) \end{aligned} \tag{E.30}$$

   Here, $\boldsymbol{K}_p$ and $\boldsymbol{K}_v$ are symmetric positive definite matrices and their choices guarantee that the task-space position and velocity errors uniformly converge to zero.

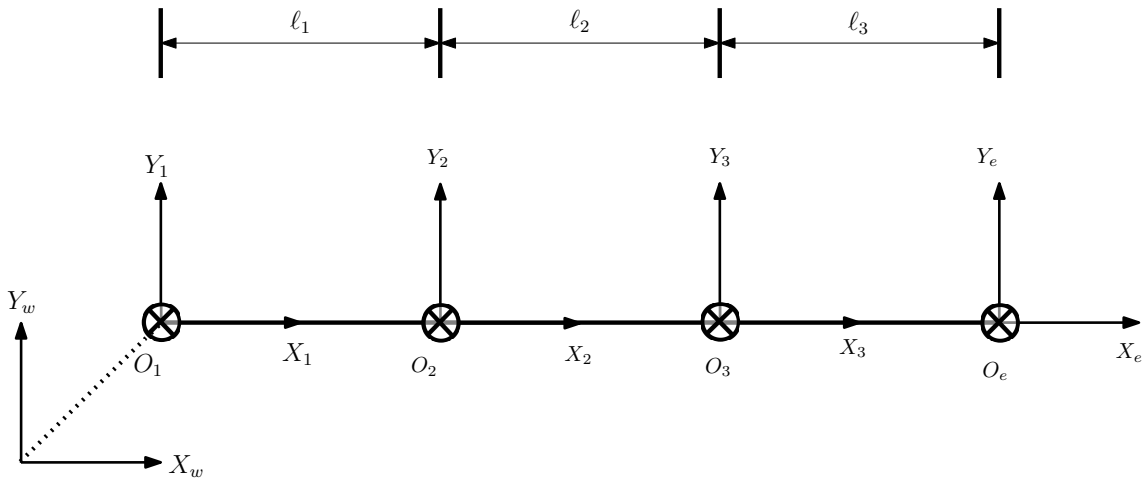

Figure E.2: Equivalent rigid body kinematics.

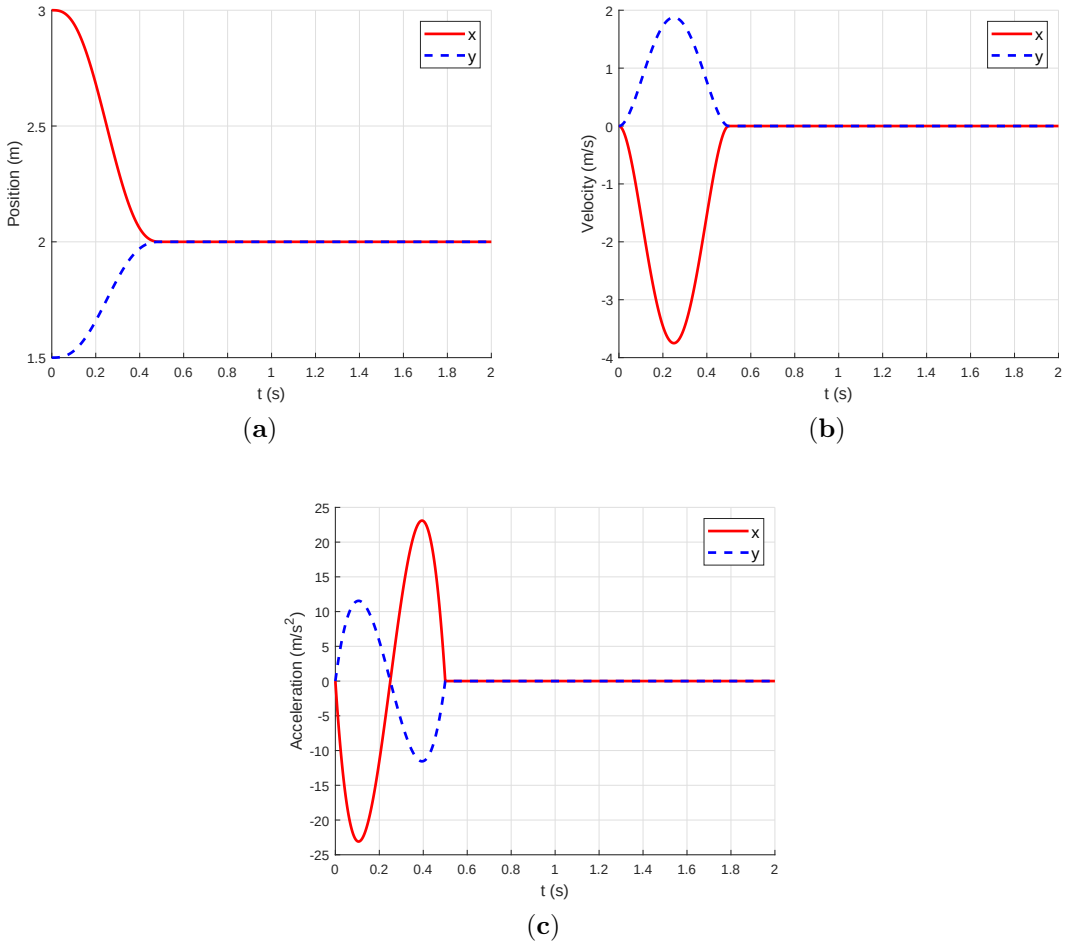

Figure E.3: End-effector trajectories (**a**) position, (**b**) velocity, and (**c**) acceleration.

2. Case B: Local minimization of the kinetic energy (LMKE).

$$\begin{aligned}\ddot{\boldsymbol{q}}_r = \boldsymbol{J}_M^+((\ddot{\boldsymbol{x}}_d + \boldsymbol{K}_p(\boldsymbol{x}_d - \boldsymbol{x}) + \boldsymbol{K}_v(\dot{\boldsymbol{x}}_d - \boldsymbol{J}\dot{\boldsymbol{q}}) \\ - \dot{\boldsymbol{J}}\dot{\boldsymbol{q}}_r) + (\boldsymbol{I} - \boldsymbol{J}^+\boldsymbol{J})(-\beta\dot{\boldsymbol{q}}_r)\end{aligned} \tag{E.31}$$

3. Case C: Local minimization of the inertia inverse weighted dynamic driving force or global minimization of the kinetic energy (GMKE).

$$\begin{aligned}\ddot{\boldsymbol{q}}_r = \boldsymbol{J}_M^+((\ddot{\boldsymbol{x}}_d + \boldsymbol{K}_p(\boldsymbol{x}_d - \boldsymbol{x}) + \boldsymbol{K}_v(\dot{\boldsymbol{x}}_d - \boldsymbol{J}\dot{\boldsymbol{q}}) \\ - \dot{\boldsymbol{J}}\dot{\boldsymbol{q}}_r) - (\boldsymbol{I} - \boldsymbol{J}_M^+\boldsymbol{J})(\boldsymbol{M}_{rr}^{-1}\boldsymbol{c}_r + \beta\dot{\boldsymbol{q}}_r)\end{aligned} \tag{E.32}$$

Table E.1: DH PARAMETERS

Axis	**TranZ**	**RotZ**	**TranX**	**RotX**
1	0.0	q_{r1}	ℓ_1	0.0
2	0.0	q_{r2}	ℓ_2	0.0
3	0.0	q_{r3}	ℓ_3	0.0

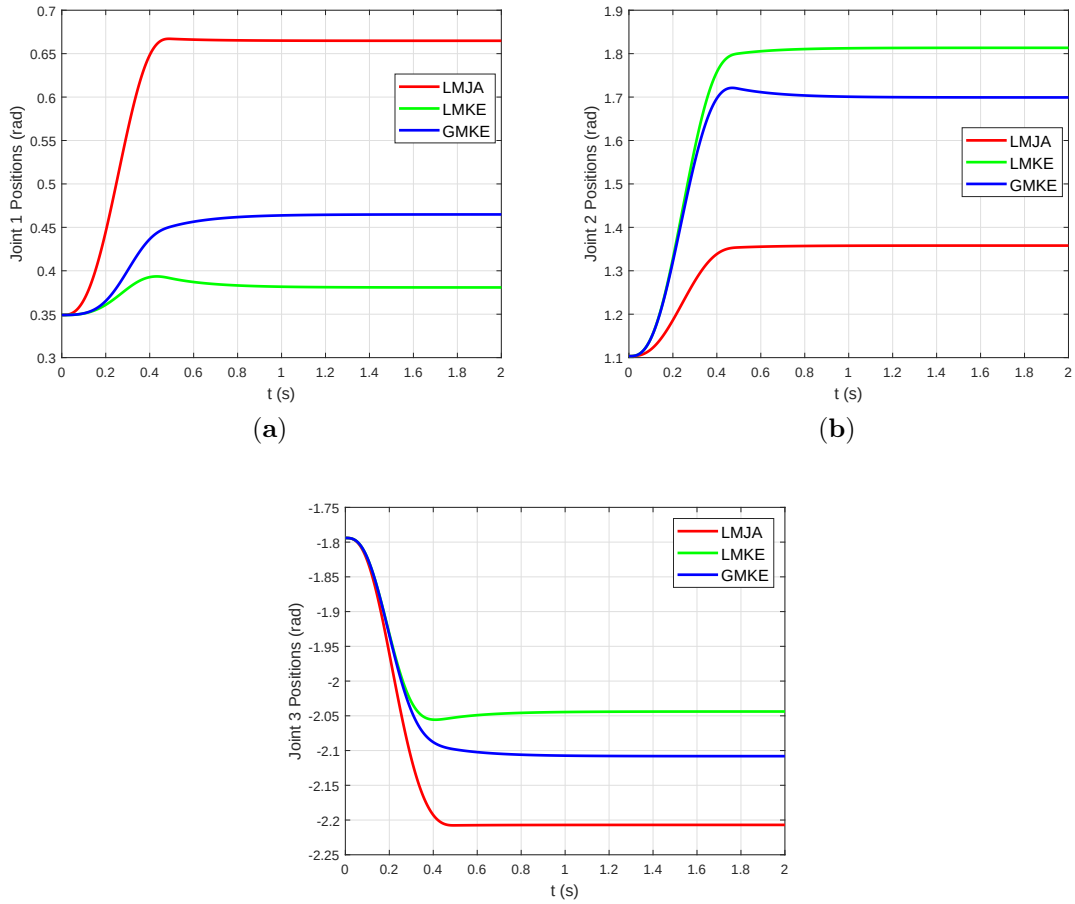

Figure E.4: Joint trajectories when using different redundancy resolution methods (**a**) joint 1 position, (**b**) joint 2 position, and (**c**) joint 3 position.

All the above cases have been implemented with $\beta = 5$, $\boldsymbol{K}_p = \begin{bmatrix} 1 & 0 \\ 0 & 1 \end{bmatrix}$, and $\boldsymbol{K}_v = \begin{bmatrix} 1 & 0 \\ 0 & 1 \end{bmatrix}$. The forward Euler method is used with a step size of 1×10^{-4} s to integrate the joint accelerations to obtain joint velocities and positions. The joint position trajectories obtained by integrating joint acceleration solutions given by (E.30)–(E.32) are shown in Fig. E.4. Although the manipulator starts with the same initial configuration in all three cases, the final joint configurations are different. The final joint configuration has an effect on the residual vibration of the end-effector [12, 13].

The link deflections and end-effector position, shown in Fig. E.5, are estimated using the assumed modes method as presented in [13]. The simulation model of the FLM (given by (E.7) and (E.8)) is used only to show the flexible dynamics of the FLM when applying different redundancy resolution techniques. The online control method with redundancy resolution used in this paper is not based on the dynamic

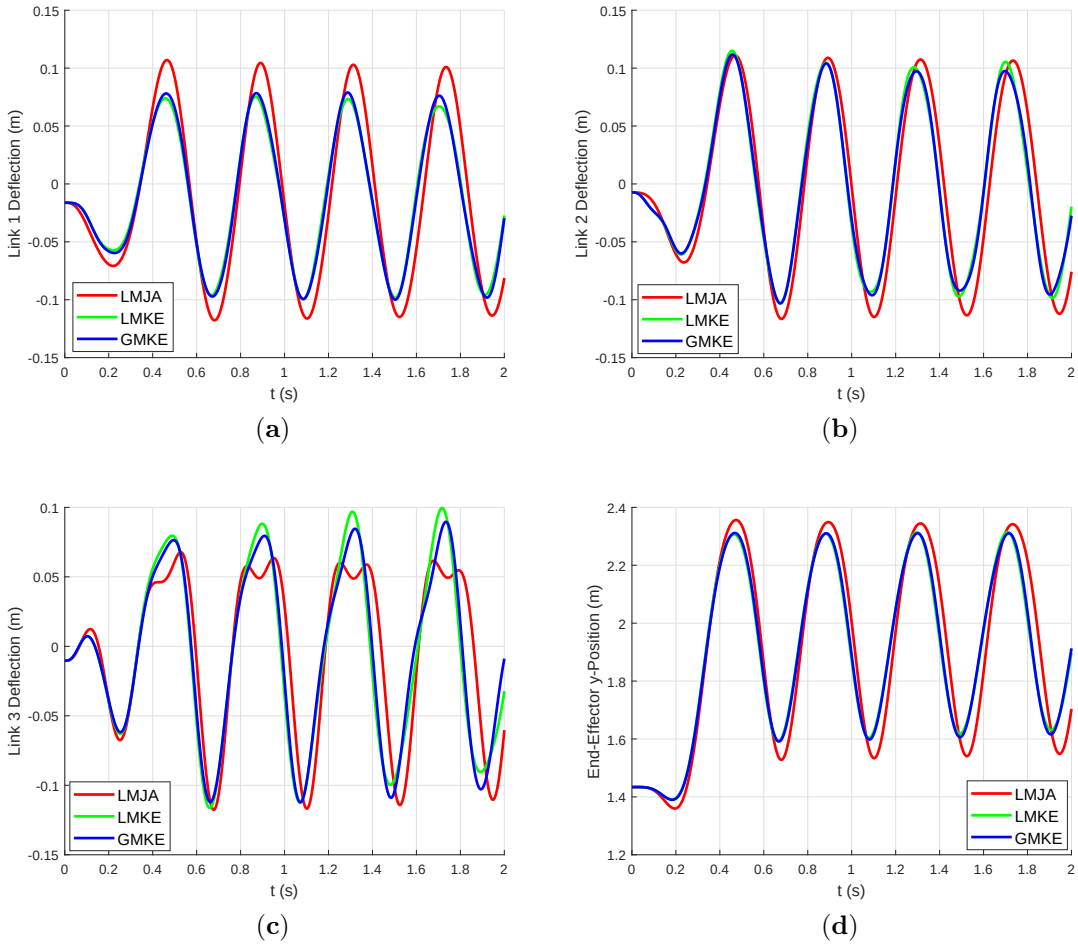

Figure E.5: Link deflections and end-effector y-position when using different redundancy resolution methods (**a**) Link 1 deflection, (**b**) Link 2 deflection, (**c**) Link 3 deflection, and (**d**) End-effector y-position.

model of the FLM. However, the inertia matrix ($\boldsymbol{M}_{rr}$) and the vector of Coriolis and centripetal effects ($\boldsymbol{c}_r$) equivalent to the rigid model of the FLM are used in case of kinetic energy minimization approaches of redundancy resolution.

Fig. E.5 shows that the link-tip deflections with respect to its base and the end-effector vibration when using the kinetic energy minimization methods of redundancy resolution are lower compared to the minimum joint acceleration method. Moreover, there is not much difference visible (see Fig. E.5) in the vibration minimization when using the global kinetic energy minimization method compared to the local kinetic energy minimization method.

E.6 Conclusion

Different methods to control redundant manipulators using redundancy resolution techniques are presented. The redundancy resolution by minimizing kinetic energy

is compared to the solution obtained from local minimization of joint acceleration concerning elastic vibration in the FLM. The results proved that the kinetic energy minimization approaches reduce the elastic vibrations compared to the local joint acceleration minimization method. Although, the kinetic energy minimization approaches of redundancy resolution use the inertia matrix ($\boldsymbol{M}_{rr}$) and the vector of Coriolis and centripetal effects ($\boldsymbol{c}_r$) equivalent to the rigid model of the FLM, these methods can still be used for the online control of the FLM. This is because only the rigid parts of the inertia matrix $\boldsymbol{M}$ and the vector of Coriolis and centripetal effects $\boldsymbol{c}$ are used in the online control of the FLM.

In the next step, it is worth testing the redundancy resolution methods, aimed at reducing elastic vibrations, in the actual experimental setup of the FLM.

Acknowledgment

The work was partially funded by the Research Council of Norway through the centre SFI Offshore Mechatronics, project 237896.

References – Paper E

[1] Jingguo Wang, Yangmin Li, and Xinhua Zhao. Inverse kinematics and control of a 7-DOF redundant manipulator based on the closed-loop Algorithm. *International Journal of Advanced Robotic Systems*, 7(4):1–9, 2010. ISSN 17298814. doi: 10.5772/10495.

[2] Fabrizio Flacco, Alessandro De Luca, and Oussama Khatib. Control of Redundant Robots under Hard Joint Constraints: Saturation in the Null Space. *IEEE Transactions on Robotics*, 31(3):637–654, 2015. ISSN 15523098. doi: 10.1109/TRO.2015.2418582.

[3] A. Nedungadi and K. Kazerouinian. A Local Solution with Global Characteristics for the Joint Torque Optimization of a Redundant Manipulator. *Advanced Robotics: 1989*, 6(5):559–591, 1989. doi: 10.1007/978-3-642-83957-3_39.

[4] M Kirćanski and M Vukobratović. *Trajectory Planning for Redundant Manipulators in the Presence of Obstacles*, pages 57–63. Springer US, Boston, MA, 1985. ISBN 978-1-4615-9882-4. doi: 10.1007/978-1-4615-9882-4_6.

[5] Charles W Wampler. Manipulator Inverse Kinematic Solutions Based on Vector Formulations and Damped Least-Squares Methods. *IEEE Transactions on Systems, Man, and Cybernetics*, 16(1):93–101, 1986. doi: 10.1109/TSMC.1986.289285.

[6] C. Y. Chung, B. H. Lee, M. S. Kim, and C. W. Lee. Torque optimizing control with singularity-robustness for kinematically redundant robots. *Journal of Intelligent and Robotic Systems: Theory and Applications*, 28(3):231–258, 2000. ISSN 09210296. doi: 10.1023/A:1008152705719.

[7] John M. Hollerbach and Ki C. Suh. Redundancy resolution of manipulators through torque optimization. In *Proceedings - IEEE International Conference on Robotics and Automation*, pages 1016–1021, 1985. ISBN 0818606150. doi: 10.1109/ROBOT.1985.1087285.

[8] M Benosman, G Le Vey, L Lanari, and A De Luca. Rest-to-Rest Motion for Planar Multi-Link Flexible Manipulator Through Backward Recursion. *Journal*

of Dynamic Systems, Measurement, and Control, 126(1):115–123, apr 2004. ISSN 0022-0434. doi: 10.1115/1.1649976.

[9] M. H. Korayem, A. Nikoobin, and V. Azimirad. Trajectory optimization of flexible link manipulators in point-to-point motion. *Robotica*, 27(6):825–840, 2009. ISSN 02635747. doi: 10.1017/S0263574708005183.

[10] Pengfei Xin, Jili Rong, Yongtai Yang, Dalin Xiang, and Yang Xiang. Trajectory planning with residual vibration suppression for space manipulator based on particle swarm optimization algorithm. *Advances in Mechanical Engineering*, 9 (4):1–16, 2017. ISSN 16878140. doi: 10.1177/1687814017692694.

[11] Shigang Yue, Dominik Henrich, W. L. Xu, and S. K. Tso. Point-to-point trajectory planning of flexible redundant robot manipulators using genetic algorithms. *Robotica*, 20(3):269–280, 2002. ISSN 02635747. doi: 10.1017/S0263574701003861.

[12] Yue Shigang. Weak-vibration configurations for flexible robot manipulators with kinematic redundancy. *Mechanism and Machine Theory*, 35(2):165–178, 2000. ISSN 0094114X. doi: 10.1016/S0094-114X(98)00071-8.

[13] Dipendra Subedi, Ilya Tyapin, and Geir Hovland. Dynamic Modeling of Planar Multi-Link Flexible Manipulators. *Robotics*, 10(2), 2021. ISSN 2218-6581. doi: 10.3390/robotics10020070.

[14] Pyung Chang. A closed-form solution for inverse kinematics of robot manipulators with redundancy. *IEEE Journal on Robotics and Automation*, 3(5):393–403, 1987. doi: 10.1109/JRA.1987.1087114.

[15] Daniel E. Whitney. Resolved Motion Rate Control of Manipulators and Human Prostheses. *IEEE Transactions on Man-Machine Systems*, 10(2):47–53, 1969. ISSN 21682860. doi: 10.1109/TMMS.1969.299896.

[16] B. Hu, C. L. Teo, and H. P. Lee. Local Optimization of Weighted Joint Torques for Redundant Robotic Manipulators. *IEEE Transactions on Robotics and Automation*, 11(3):422–425, 1995. ISSN 1042296X. doi: 10.1109/70.388785.

[17] Yunong Zhang, Shuzhi Sam Ge, and Tong Heng Lee. A unified quadratic-programming-based dynamical system approach to joint torque optimization of physically constrained redundant manipulators. *IEEE Transactions on Systems, Man, and Cybernetics, Part B: Cybernetics*, 34(5):2126–2132, 2004. ISSN 10834419. doi: 10.1109/TSMCB.2004.830347.

[18] Jon Woolfrey, Wenjie Lu, and Dikai Liu. A Control Method for Joint Torque Minimization of Redundant Manipulators Handling Large External Forces.

Journal of Intelligent and Robotic Systems: Theory and Applications, 96(1): 3–16, 2019. ISSN 15730409. doi: 10.1007/s10846-018-0964-8.

[19] O Khatib. A unified approach for motion and force control of robot manipulators: The operational space formulation. *IEEE Journal on Robotics and Automation*, 3(1):43–53, 1987. doi: 10.1109/JRA.1987.1087068.

[20] H.-J. Kang and R A Freeman. Joint torque optimization of redundant manipulators via the null space damping method. In *Proceedings 1992 IEEE International Conference on Robotics and Automation*, pages 520–525 vol.1, 1992. doi: 10.1109/ROBOT.1992.220239.

Paper F

Camera-LiDAR Data Fusion for Autonomous Mooring Operation

Dipendra Subedi, Ajit Jha, Ilya Tyapin and Geir Hovland

This paper has been published as:

Dipendra Subedi, Ajit Jha, Ilya Tyapin and Geir Hovland. Camera-LiDAR Data Fusion for Autonomous Mooring Operation. *2020 15th IEEE Conference on Industrial Electronics and Applications (ICIEA)*, pages 1176-1181, 2020. doi: 10.1109/ICIEA48937.2020.9248089.

Camera-LiDAR Data Fusion for Autonomous Mooring Operation

Dipendra Subedi, Ajit Jha, Ilya Tyapin and Geir Hovland
Department of Engineering Sciences
University of Agder
4879 Grimstad, Norway

Abstract **The use of camera and LiDAR sensors to sense the environment has gained increasing popularity in robotics. Individual sensors, such as cameras and LiDARs, fail to meet the growing challenges in complex autonomous systems. One such scenario is autonomous mooring, where the ship has to be tied to a fixed rigid structure (bollard) to keep it stationary safely. The detection and pose estimation of the bollard based on data fusion from the camera and LiDAR are presented here. Firstly, a single shot extrinsic calibration of LiDAR with the camera is presented. Secondly, the camera-LiDAR data fusion method using camera intrinsic parameters and camera to LiDAR extrinsic parameters is proposed. Finally, the use of an image-based segmentation method to segment the corresponding point cloud from the fused camera-LiDAR data is developed and tailored for its application in autonomous mooring operation.**

F.1 Introduction

When thinking of autonomous shipping operations, it is also necessary to consider the autonomous mooring system. One possible solution to this problem is to incorporate a long-reach robot on the ship/vessel (shown in Fig. F.1), which requires feedback from different sensors. To undertake the mooring operations without human intervention using the robotic arm would require the arm to take the mooring rope with a loop and wrap around the bollard on the dock. Autonomous operations rely on an accurate perception of the environment with several complementary sensory modalities.

With the rapid development of range sensor technology and the advancement of machine learning algorithms using data from a camera, the use of camera-LiDAR combination for perception has gained popularity in recent years. The rich and complementary information provided by a camera and LiDAR can be used to sense the environment for autonomous operations. The camera offers better information about the color and features of the surroundings, and LiDAR provides range information. Machine learning algorithms for object detection, identification, and segmentation

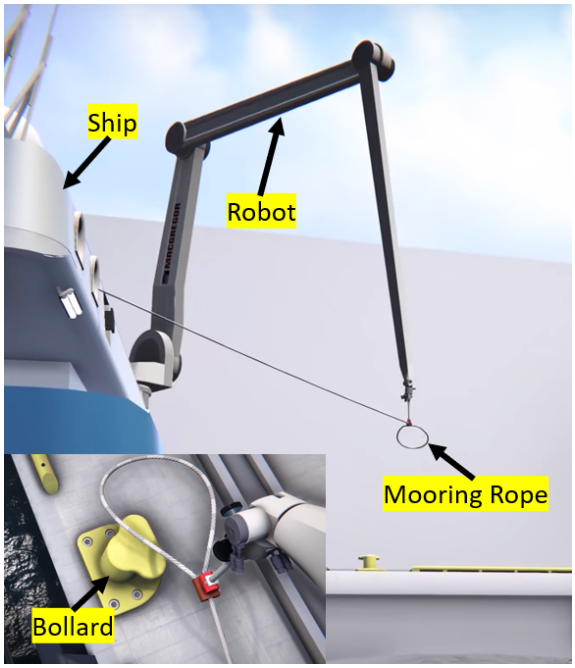

Figure F.1: Autonomous mooring operation (with permission from MacGregor Norway AS)[1]

using the camera data are matured in the literature. In contrary to the stereo camera-based vision system, the LiDAR range measurements have high accuracy for long-range depth measurements [1]. Therefore, the object pose estimation using the LiDAR range measurements is a better alternative to image-based pose estimation.

In order to utilize the information obtained from both the sensors, data from them have to be fused together so that the correspondences between image data and LiDAR point cloud could be made. The environment can be sensed better by using the fused image and point cloud data than by using individual data from each sensor. For fusing camera and LiDAR data, it is necessary to know the relative pose of sensors with respect to each other.

In recent years, the problem of determining the relative pose of the camera and LiDAR has been addressed by many researchers [1–7]. When calibrating LiDAR-LiDAR pair or LiDAR-stereo camera pair, both generating point clouds, the target-based calibration method is widely used for finding corresponding features in both point clouds and using Iterative Closest Point (ICP) to find the transform between two sensors [1]. However, in [2], a markerless online calibration method is proposed for real-time estimation of the camera to LiDAR pose. Another technique to calibrate LiDAR and camera without a need for a specific target is detailed in [5], which is based on finding maximum mutual information between the sensor-measured surface intensities in the LiDAR and the camera data. In [3], ArUco tags are used on the calibration target, and $3D - 3D$ point correspondences are used to determine

[1] `https://youtu.be/Co211gU_J5w`

the transformation between camera and LiDAR. Calibration of RGB camera with Velodyne LiDAR using a 3D marker is presented in [4]. Another method of calibrating multiple RGB cameras with a LiDAR using a spherical object is proposed in [6].

In this work, a single shot calibration method to determine the relative pose of LiDAR with respect to a camera is presented. The proposed calibration method is relatively fast compared to the existing methods.

In order to carry out the mooring operation autonomously, it is necessary to detect the bollard and estimate the pose of the bollard with respect to the robot coordinate frame. With the rapid development in machine learning methods, deep learning methods, and the boost in computing power, learning-based approaches for object classification, detection, and segmentation have attracted much research attention in recent years. In [8], deep learning-based object detection frameworks are reviewed. In this work, Mask R-CNN is used for bollard detection and segmentation because of its simplicity with promising instance segmentation and object detection results [9].

The presented work in this paper deals with the fusion of camera-LiDAR data in order to use an image-based segmentation method to segment the object of interest (bollard) and corresponding point cloud for pose estimation.

The paper is organized into five sections as follows. Section F.2 describes the intrinsic and extrinsic calibration of the camera and LiDAR. The camera-LiDAR data fusion method is elaborated in section F.3. The results obtained from the data fusion method are presented in section F.4. Conclusions and discussions follow in section F.5.

F.2 Camera and LiDAR Calibration

In computer vision, a generic camera model provides a mapping between the $3D$ world and $2D$ image given by eq. (F.1), where $x = (U, V, W)^T$ is $2D$ image point in the homogeneous form (3×1), $X = (X_w, Y_w, Z_w, 1)^T$ is $3D$ world point in the homogeneous form (4×1), and P is the camera matrix (3×4). Considering the pinhole camera model, the camera matrix P can be written as in eq. (F.2), where K is the intrinsic camera matrix given by eq. (F.3) , R is the $3D$ rotation of camera frame $\{\mathbf{C}\}$ with respect to world frame $\{\mathbf{W}\}$, t is the $3D$ translation of camera frame $\{\mathbf{C}\}$ with respect to world frame $\{\mathbf{W}\}$, (c_x, c_y) is the optical center (the principal point) in pixels, and (f_x, f_y) is the focal length in pixels. Assuming that the camera and world share the same coordinate system (i.e., $R = I_{3\times3}$ and $t = (0, 0, 0)^T$), the camera matrix can be written as in eq. (F.4). The pixel position $x' = (u, v)^T$ can be obtained from the homogeneous representation of image point x using eq. (F.5). The

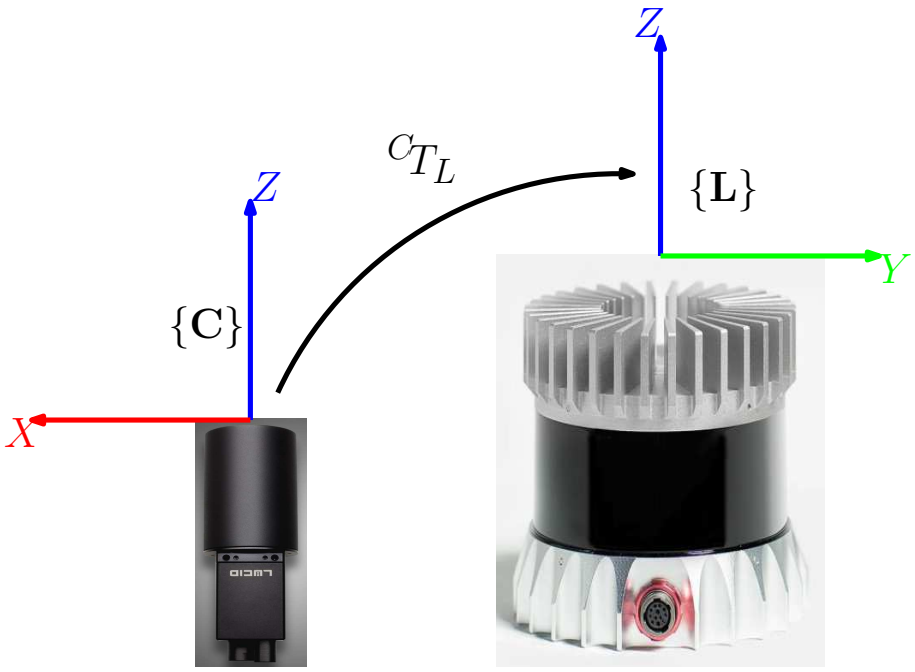

Figure F.2: Camera to LiDAR transformation

intrinsic camera matrix K is obtained from the intrinsic calibration of the camera.

$$x = PX \tag{F.1}$$

$$P = K[R|t] \tag{F.2}$$

$$K = \begin{bmatrix} f_x & 0 & c_x \\ 0 & f_y & c_y \\ 0 & 0 & 1 \end{bmatrix} \tag{F.3}$$

$$P = \begin{bmatrix} f_x & 0 & c_x & 0 \\ 0 & f_y & c_y & 0 \\ 0 & 0 & 1 & 0 \end{bmatrix} \tag{F.4}$$

$$x' = \begin{pmatrix} u \\ v \end{pmatrix} = \frac{1}{W} \begin{pmatrix} U \\ V \end{pmatrix} \tag{F.5}$$

To estimate the rigid body transformation (${}^{C}T_{L}$) of LiDAR coordinate frame {**L**} with respect to camera coordinate frame {**C**}, as shown in Fig. F.2, a calibration target with known dimensions, as shown in Fig. F.3, is used.

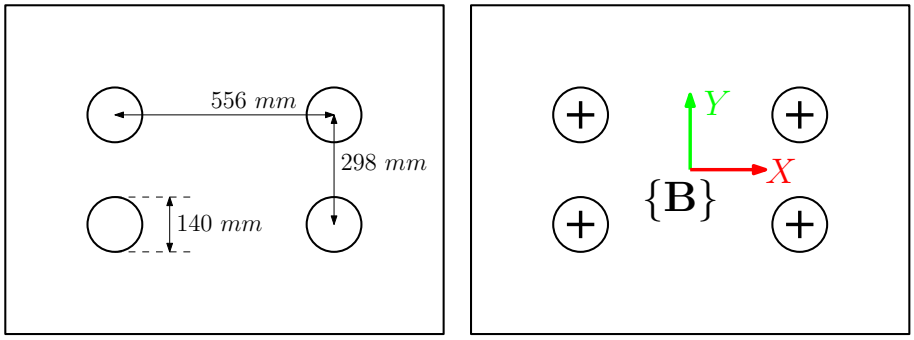

Figure F.3: Calibration target with the target coordinate frame {**B**}

F.2.1 Camera Pose Estimation

To estimate the position of the camera with respect to the calibration target, it is necessary to locate the exact position of the four circular blobs on the calibration target by using the information from the camera only. The Circle Hough Transform (CHT) is used to detect blobs on the calibration target. In order to avoid inaccurate circle detection using CHT, the calibration target should be placed parallel to the camera. The centers of the detected blobs are sorted anticlockwise, starting from the lower left center. The pose of the calibration target with respect to the camera is found using $3D - 2D$ point correspondences (OpenCV SolvePnP algorithm) [10].

F.2.2 LiDAR Pose Estimation

The point cloud obtained from the LiDAR is processed to find the calibration target plane using *PCL RANSAC parallel plane model* [11]. The edges of the planar cloud are detected based on the discontinuities in the range data of the points [2]. From the point cloud containing the planar edges, the circles are detected using the method proposed in [1]. The centers of the detected blobs are sorted anticlockwise, starting from the lower left center. The pose of the calibration target with respect to the LiDAR is found by the least-square rigid motion using the Singular Value Decomposition (SVD) technique [3, 12, 13].

Considering ${}^{L}P$ and ${}^{B}P$ are two sets of corresponding $3D$ points representing the blob center in the calibration target with respect to the LiDAR coordinate frame {**L**} and target coordinate frame {**B**}, respectively. The pose of the calibration target with respect to LiDAR is calculated by finding the optimal/best rotation ${}^{L}R_{B}$ and translation ${}^{L}t_{B}$ between these corresponding points so that they are aligned, which is shown in eq. (F.6) for point i.

$$ {}^{L}P^{i} = {}^{L}R_{B}\,{}^{B}P^{i} + {}^{L}t_{B} \tag{F.6} $$

The optimal rigid body transformation of the target coordinate frame with respect

to the LiDAR coordinate frame is found using the following steps:

1. *Calculate the centroid of both datasets.* The centroids of the points in the LiDAR coordinate frame (${}^{L}P^{c}$) and target coordinate frame (${}^{B}P^{c}$) are calculated by the average of points in each dataset as given by eq. (F.7), where $N = 4$ is the total number of points in each coordinate frame.

$$\left.\begin{aligned} {}^{L}P^{c} &= \frac{1}{N}\sum_{i=1}^{N} {}^{L}P^{i} \\ {}^{B}P^{c} &= \frac{1}{N}\sum_{i=1}^{N} {}^{B}P^{i} \end{aligned}\right\} \tag{F.7}$$

2. *Bring both datasets to the origin and calculate the optimal rotation ${}^{L}R_{B}$.* Based on the centroids computed using eq. (F.7) both datasets are re-centered to the origin, which removes the translation component from the datasets leaving only the rotational part between the datasets. Covariance matrix H is calculated using eq. (F.8), where $N = 4$ is the total number of points in each coordinate frame. The optimal rotation ${}^{L}R_{B}$ is calculated using SVD as given by eq. (F.9), where $V' = V$ if the determinant of $VU^{T} > 0$, otherwise V' is obtained by changing the sign of the third column of V.

$$\begin{aligned} H = &\Big[({}^{B}P^{1} - {}^{B}P^{c}) \cdots ({}^{B}P^{i} - {}^{B}P^{c}) \cdots ({}^{B}P^{N} - {}^{B}P^{c})\Big] \cdot \\ &\cdot \Big[({}^{L}P^{1} - {}^{L}P^{c}) \cdots ({}^{L}P^{i} - {}^{L}P^{c}) \cdots ({}^{L}P^{N} - {}^{L}P^{c})\Big]^{T} \end{aligned} \tag{F.8}$$

$$\left.\begin{aligned} \Big[U, S, V\Big] &= SVD(H) \\ {}^{L}R_{B} &= V'U^{T} \end{aligned}\right\} \tag{F.9}$$

3. *Calculate the optimal translation ${}^{L}t_{B}$.* The translation of the target coordinate frame with respect to the LiDAR coordinate frame is calculated using eq. (F.10).

$${}^{L}t_{B} = {}^{L}P^{c} - {}^{L}R_{B}\,{}^{B}P^{c} \tag{F.10}$$

F.2.3 Camera to LiDAR Transform Estimation

Once the transforms of the calibration target coordinate frame $\{\mathbf{B}\}$ with respect to the camera frame $\{\mathbf{C}\}$ ($^{C}T_{B}$) and with respect to the LiDAR frame $\{\mathbf{L}\}$ ($^{L}T_{B}$) are known, the transform of the LiDAR frame with respect to the camera frame ($^{C}T_{L}$) is calculated using eq. (F.11).

$$^{C}T_{L} = {}^{C}T_{B}({}^{L}T_{B})^{-1} \tag{F.11}$$

F.3 Camera-LiDAR Data Fusion

The point cloud in the LiDAR coordinate frame $\{\mathbf{L}\}$ is transformed to the camera coordinate frame $\{\mathbf{C}\}$ using the transformation $^{C}T_{L}$ obtained after calibration. The transformed point cloud with the negative Z-coordinate is filtered out; the points that are only within the field of view of the camera are kept for coloring. Filtering is needed because the points with the positive and negative Z-coordinate with the same X and Y coordinates are projected in the same image pixel coordinates resulting in the false coloring of the point cloud. The transformed point cloud is projected to the image plane using eq. (F.1). The points that are located outside the image pixel size of the camera are filtered out. The colored point cloud is obtained using the RGB values of the image pixel coordinates obtained using eq. (F.5).

F.3.1 Object Detection and Segmentation

Bollard detection and segmentation are done using Mask R-CNN [9]. The use of Mask R-CNN to detect and segment the bollard is presented in [14]. The bounding box coordinates obtained from the segmentation are used to segment the corresponding point cloud belonging to the bounding box. The overall architecture for segmenting the bollard point cloud using the fused camera and LiDAR data is shown in Fig. F.4.

F.3.2 Object Pose Estimation

Fig. F.5 shows the procedure for bollard pose estimation from the segmented bollard point cloud obtained using the proposed camera-LiDAR data fusion technique. The point cloud corresponding to the bollard in the camera coordinate frame $\{\mathbf{C}\}$ is transformed to the robot/world coordinate frame $\{\mathbf{W}\}$ with the known transformation $^{W}T_{C}$ obtained after the extrinsic calibration of the camera [15]. In the transformed bollard point cloud, all the planes perpendicular to the vertical axis (Z-axis pointing up from the ground) are estimated. To avoid processing of the planar point clouds with a number of inliers less than a threshold, such planar clouds are filtered out,

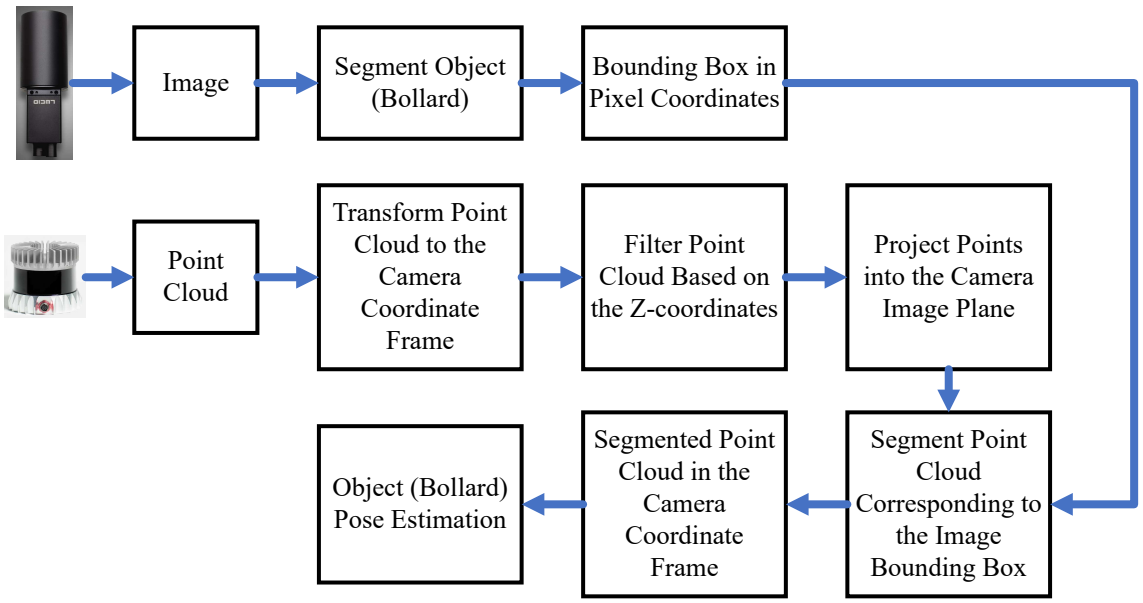

Figure F.4: Block diagram showing the camera-LiDAR data fusion for the object pose estimation

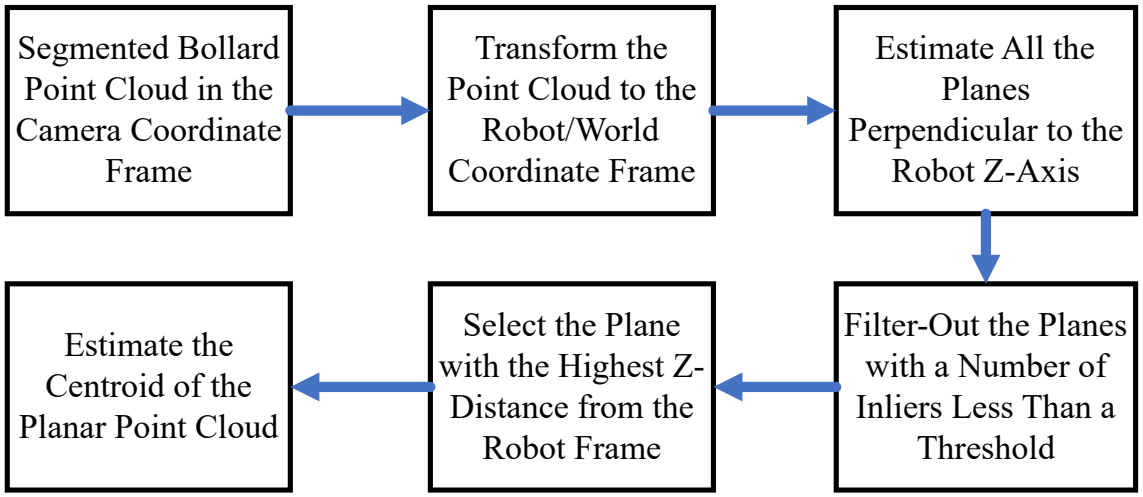

Figure F.5: Block diagram showing the bollard pose estimation

leaving only the planar clouds corresponding to the base and top of the bollard. The planar cloud corresponding to the top of the bollard is selected based on the Z-coordinate of the planes with the known information that the bollard is always located in the direction of the positive Z-coordinate with respect to robot frame. The centroid of thus obtained planar cloud representing bollard's top surface represents the position of the bollard with respect to the robot coordinate frame. The estimation of the orientation of the bollard is not taken into consideration in this work to carry-out the autonomous mooring operation irrespective of the orientation of the bollard.

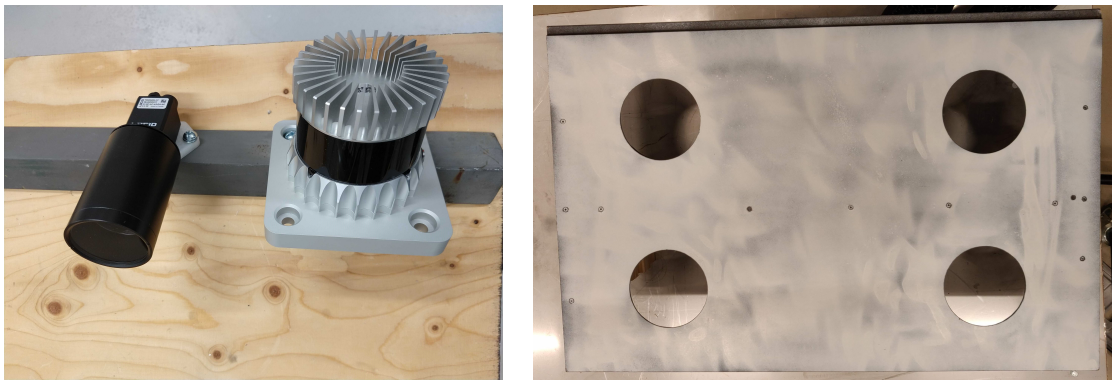

(**a**) Camera-LiDAR setup (**b**) Calibration target

Figure F.6: Camera-LiDAR setup and calibration target

F.4 Results

The performance of the proposed camera-LiDAR data fusion approach is evaluated using 64 channel Ouster OS1-64 LiDAR and 5-megapixel Lucid Triton TRI050S-C color camera. Both sensors are mounted together in a common rig, as shown in Fig. F.6(**a**). Fig. F.6(**b**) shows the calibration target used for the extrinsic calibration of LiDAR with respect to the camera. Dimensions of the calibration target are given in Fig. F.3. The calibration target is placed around 1.4 m away from the camera-LiDAR setup within the overlapping field of view of the camera and LiDAR.

To estimate the pose of the calibration target frame with respect to the LiDAR coordinate frame, four blobs in the calibration target are detected in the LiDAR point cloud. The point cloud corresponding to the calibration target plane is shown in Fig. F.7(**a**). The edges detected in the planar cloud based on the range discontinuities of the points are shown in Fig. F.7(**b**). The blobs detected in the cloud containing the edges of the calibration target and their centroids are shown in Fig. F.7(**c**). The pose of calibration target with respect to the LiDAR calculated using the least-square rigid motion estimation is shown in Fig. F.7(**d**).

The blobs detected in the image and their centroids are shown in Fig. F.8(**a**). The pose of the calibration target with respect to the camera calculated using $3D - 2D$ point correspondences is shown in Fig. F.8(**b**).

Eq. (F.11) is used to calculate the pose of the LiDAR with respect to the camera after determining the pose of the calibration target with respect to the LiDAR and camera. In order to evaluate the calibration accuracy, the re-projection error is calculated. First, the $3D$ circle centers (^{L}P) detected in the LiDAR coordinate frame are transformed to the camera coordinate frame using the transformation ($^{C}T_{L}$) obtained using the proposed calibration method. Thus transformed points (^{C}P) are projected into the image plane using eq. (F.1) to obtain the re-projected circle centers

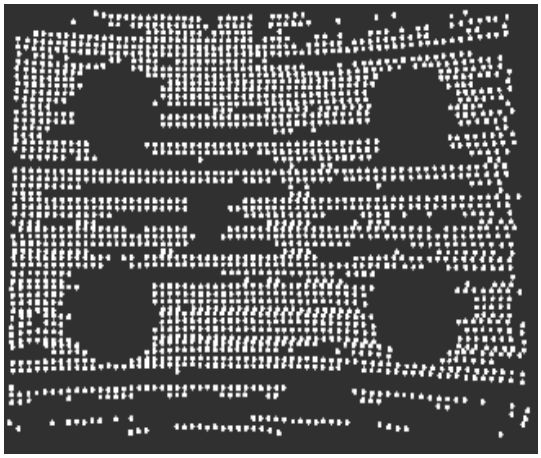

(**a**) Calibration target plane

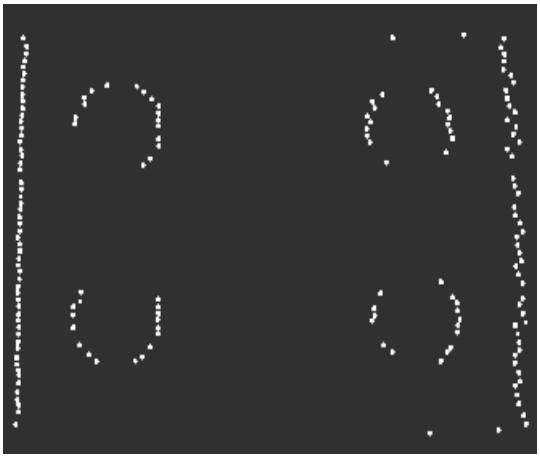

(**b**) Calibration target edges

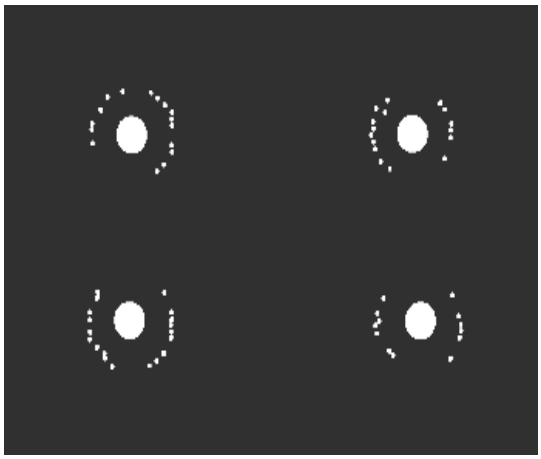

(**c**) Blob detection in the point cloud

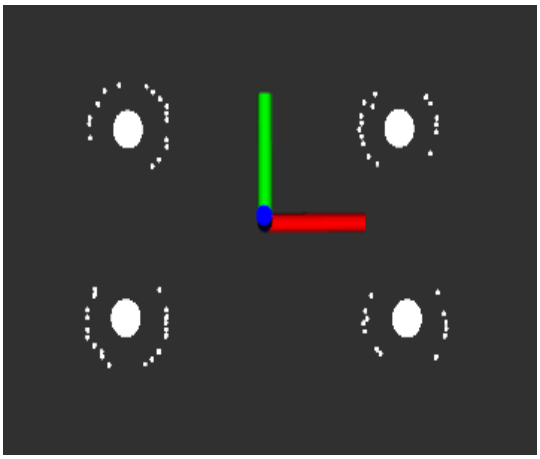

(**d**) Calibration target transform

Figure F.7: Calibration target (blobs) detection in the point cloud

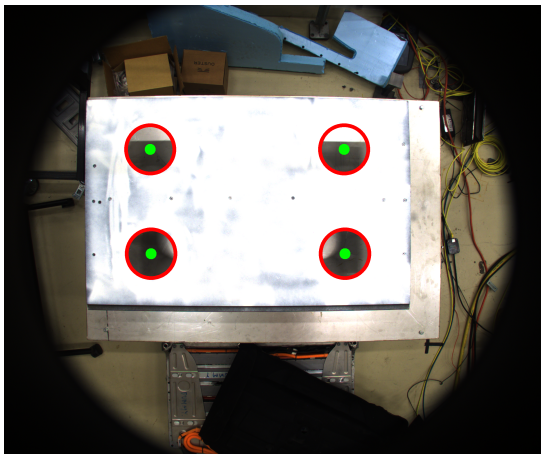

(**a**) Blob detection in the image

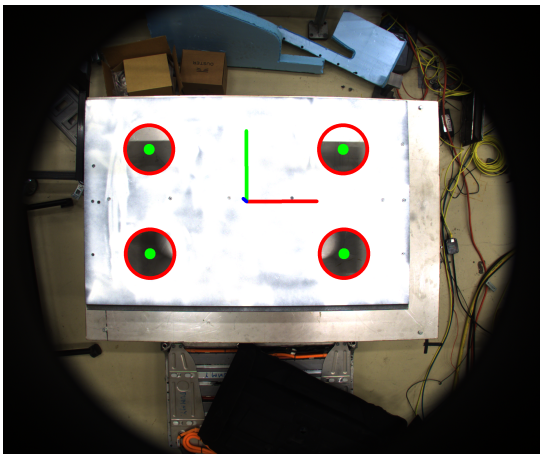

(**b**) Calibration target transform

Figure F.8: Calibration target (blobs) detection in the image

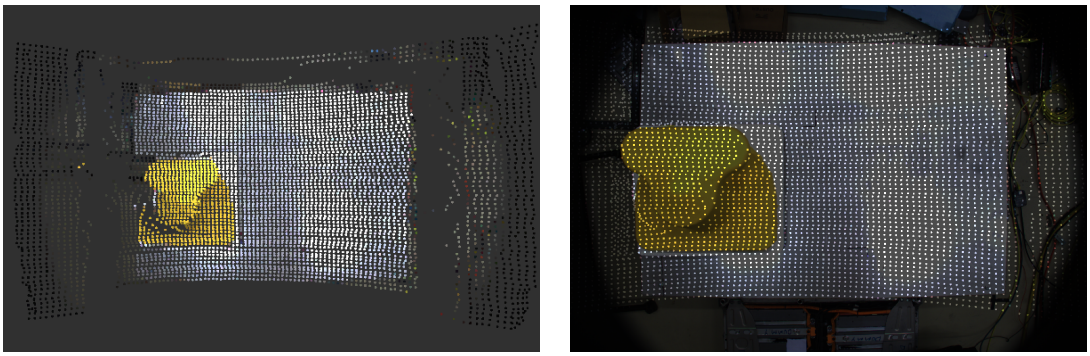

(**a**) Colored point cloud (**b**) Colored point cloud overlaid on the image

Figure F.9: Colored point clouds

(p_L) in pixel coordinates. Then, the re-projection error is calculated using eq. (F.12), where p_{Li} is the i^{th} re-projected circle center, p_{Ci} is the corresponding circle center in the image obtained from the CHT-based blob detection explained in section F.2, and $N = 4$ is the number of circles [7]. The re-projection error (e_{reproj}) obtained in the calibration when placing the calibration target at a distance of approximately 1.4 m is 1.87 $pixels$.

$$e_{reproj} = \sqrt{\frac{1}{N}\sum_{i=1}^{N}(||p_{Li} - p_{Ci}||_{2-norm})^2} \tag{F.12}$$

Fig. F.9(**a**) shows the colored cloud obtained after fusing the data from the camera and LiDAR within the overlapping field of view. The colored point cloud, shown in Fig. F.9(**a**), is overlaid on the image and shown in Fig. F.9(**b**). The bounding box corresponding to the bollard obtained from Mask R-CNN is shown in Fig.F.10(**a**). After fusing the camera and LiDAR data, the segmented colored point cloud overlaid on the image corresponding to the bounding box in the image is shown in Fig.F.10(**b**). To summarize, the segmented colored point cloud belonging to the bollard, shown in Fig.F.11(**b**), is extracted from the raw point cloud from the LiDAR, shown in Fig.F.11(**a**), using the proposed sensor fusion technique. Hence, the image-based segmentation method is used to segment the object, and the corresponding segmented point cloud is extracted using the sensor fusion technique presented in this paper. Thus obtained point cloud is processed to estimate the object pose.

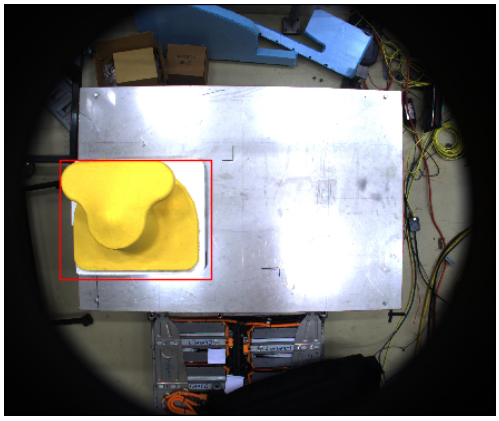

(**a**) Bollard segmentation in the image

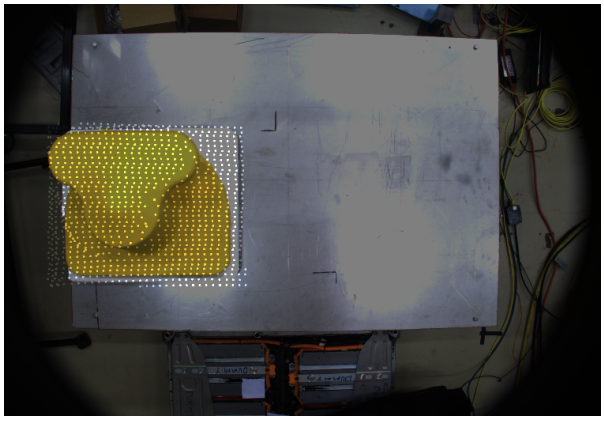

(**b**) Segmented point cloud overlaid on the image

Figure F.10: Bollard segmentation

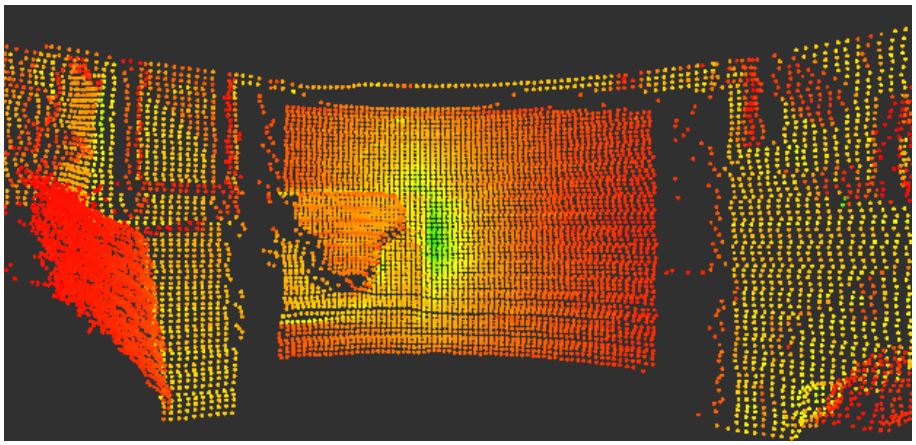

(**a**) Raw point cloud from the LiDAR

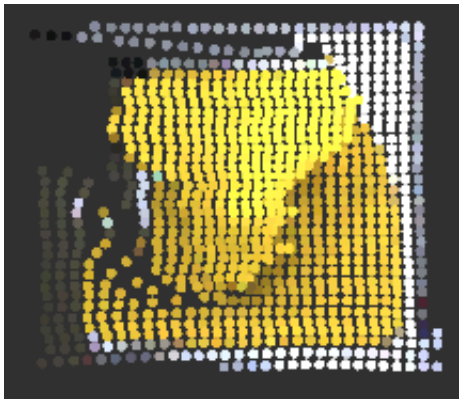

(**b**) Segmented (colored) bollard point cloud

Figure F.11: Point cloud segmentation

F.5 Conclusions and Discussions

The extrinsic calibration of the LiDAR with respect to the camera is presented. The proposed calibration method is used with the dense LiDAR (64 channel Ouster OS1-64) in this paper. The calibration method is suitable for the sparse LiDAR (such as 16 channel Velodyne VLP-16) as well. It is because the circle detection method used in this paper only requires two LiDAR beams to intersect with each of the four circles.

The intrinsic camera parameters and camera to LiDAR extrinsic parameters are used to fuse the data obtained from the camera and LiDAR. The image-based segmentation method is used to segment the object of interest, and the corresponding point cloud is obtained from the presented data fusion technique.

The work will be extended to perform the autonomous mooring operation using the fused data from the camera and LiDAR mounted on a long-reach robotic arm, as shown in Fig. F.1. In addition, it is worth comparing the performance of the detection and pose estimation methods proposed in this paper with other state-of-the-art methods.

Acknowledgment

The work was funded by the Norwegian Research Council, project number 261647/$O$20, and SFI Offshore Mechatronics, project number 237896.

References – Paper F

[1] C. Guindel, J. Beltrán, D. Martín, and F. García. Automatic extrinsic calibration for lidar-stereo vehicle sensor setups. In *2017 IEEE 20th International Conference on Intelligent Transportation Systems (ITSC)*, pages 1–6, Oct 2017. doi: 10.1109/ITSC.2017.8317829.

[2] Jesse Levinson and Sebastian Thrun. Automatic online calibration of cameras and lasers. In *Robotics: Science and Systems*, volume 2, 2013.

[3] Ankit Dhall, Kunal Chelani, Vishnu Radhakrishnan, and K Madhava Krishna. Lidar-camera calibration using 3d-3d point correspondences. *arXiv preprint arXiv:1705.09785*, 2017.

[4] Martin Velas, Michal Spanel, Zdenek Materna, and Adam Herout. Calibration of rgb camera with velodyne lidar. In *WSCG 2014 Communication papers proceedings*, pages 135–144, 2014.

[5] Gaurav Pandey, James R McBride, Silvio Savarese, and Ryan M Eustice. Automatic targetless extrinsic calibration of a 3d lidar and camera by maximizing mutual information. In *Twenty-Sixth AAAI Conference on Artificial Intelligence*, 2012.

[6] Geun-Mo Lee, Ju-Hwan Lee, and Soon-Yong Park. Calibration of vlp-16 lidar and multi-view cameras using a ball for 360 degree 3d color map acquisition. In *2017 IEEE International Conference on Multisensor Fusion and Integration for Intelligent Systems (MFI)*, pages 64–69. IEEE, 2017.

[7] Jun Zhang, Ran Zhang, Yufeng Yue, Chule Yang, Mingxing Wen, and Danwei Wang. Slat-calib: Extrinsic calibration between a sparse 3d lidar and a limited-fov low-resolution thermal camera. In *2019 IEEE International Conference on Robotics and Biomimetics (ROBIO)*, pages 648–653. IEEE, 2019.

[8] Zhong-Qiu Zhao, Peng Zheng, Shou-tao Xu, and Xindong Wu. Object detection with deep learning: A review. *IEEE transactions on neural networks and learning systems*, 2019.

[9] Waleed Abdulla. Mask r-cnn for object detection and instance segmentation on keras and tensorflow. `https://github.com/matterport/Mask_RCNN`, 2017.

[10] Gary Bradski and Adrian Kaehler. Opencv. *Dr. Dobb's journal of software tools*, 3, 2000.

[11] Radu Bogdan Rusu and Steve Cousins. 3d is here: Point cloud library (pcl). In *2011 IEEE international conference on robotics and automation*, pages 1–4. IEEE, 2011.

[12] Olga Sorkine. Least-squares rigid motion using svd. *Technical notes*, 120(3):52, 2009.

[13] K Somani Arun, Thomas S Huang, and Steven D Blostein. Least-squares fitting of two 3-d point sets. *IEEE Transactions on pattern analysis and machine intelligence*, (5):698–700, 1987.

[14] Ajit Jha, Dipendra Subedi, Per-Ove Løvsland, Ilya Tyapin, Linga Reddy Cenkeramaddi, Baltasar Beferull-Lozano, and Geir Hovland. Autonomous mooring towards autonomous maritime navigation and offshore operations. In *2020 15th IEEE Conference on Industrial Electronics and Applications (ICIEA)*, page to appear. IEEE, 2020.

[15] Morris Antonello, Andrea Gobbi, Stefano Michieletto, Stefano Ghidoni, and Emanuele Menegatti. A fully automatic hand-eye calibration system. In *2017 European Conference on Mobile Robots (ECMR)*, pages 1–6. IEEE, 2017.